Volume II

LOW-ENERGY, HIGH-RESOLUTION, VARIABLE ANGLE ELECTRON IMPACT SPECTROSCOPY*

Thesis by

James Kinsey Rice

In Partial Fulfillment of the Requirements

For the Degree of

Doctor of Philosophy

California Institute of Technology

Pasadena, California

1969

(Submitted September 9, 1968)

*Work supported in part by the United States Atomic Energy Commission,

Reporting Code No. CALT-532-39

DISCLAIMER

5. RESULTS AND DISCUSSION

5.1. Introduction

In this section we present the results obtained for six systems: helium, molecular nitrogen, carbon monoxide, molecular hydrogen, acetylene, and ethylene.

Energy-loss spectra, where given, are unretouched X-Y recorder traces obtained from the count-rate-meter (see section 4.3.4.3). The basic data (energy-loss spectra) are obtained as follows:

(1) The instrument is "tuned" and stabilized as discussed in section 4.3.

(2) At some initial scattering angle (usually near 40°) an energy-loss spectrum is recorded.

(3) The scattering angle is increased by 10° and another energy-loss spectrum is obtained. This procedure is repeated until the entire angular range has been scanned from two to eight times.

The error bars assigned to derived quantities (such as peak height ratios and differential cross sections) are determined as follows: If $X_1, X_2, \ldots X_N$ represent a set of measurements of the same quantity, then the quoted value is $\bar{X} \pm \Delta X$ where

$$\bar{X} = \frac{1}{N} \sum_{i=1}^{N} X_i \qquad (5\text{-}1)$$

and ΔX is simply the average error,

$$\Delta X = \frac{1}{N} \sum_{i=1}^{N} |\bar{X} - X_i| \quad . \tag{5-2}$$

The error in the differential cross sections at low angles introduced by the volume correction factor (section 4. 4. 4. 4) is not specifically indicated on the figures but we estimate it to be negligible (i. e. , $\lesssim 5\%$) for angles (θ) greater than 30° and at most 20% for $\theta = 10°$.

5. 2. Helium

5. 2. 1. Introduction

The electron-impact excitation of helium has been the subject of a great many experimental and theoretical investigations[47]. However, relatively few of these dealt specifically with the angular dependencies of inelastic differential scattering cross sections (DCS). Measurements at fixed scattering angles near 0°[129] and 90°[130] over a wide range of incident electron energies disclosed significant differences in the relative DCS for optically allowed and forbidden transitions. It was generally found that the ratios of DCS for forbidden transitions to those for allowed ones were greater for lower impact energies at a fixed scattering angle and for larger scattering angles at a fixed incident energy. The basis for this behavior is qualitatively well understood (refer to section 3) although no theoretical calculations have yet proved reliable in predicting the shape of the various inelastic DCS below about 100 eV (nor above this for exchange excitation[32]). Silverman and Lassettre[131] have shown that the Born approximation prediction of the total cross section

for the $1^1S \rightarrow 3^1P$ transition is significantly in error below about 100 eV. Vriens, et al.[32] have determined that the Born approximation is not valid for predicting DCS below about 200 eV for the $1^1S \rightarrow 2^1P$ transition nor below 400 eV for the $1^1S \rightarrow 2^1S$ one. Also they point out that the DCS for the $1^1S \rightarrow 2^3S$ transition decreases rapidly for angles greater than 5° at incident electron energies between 100 eV and 225 eV. This is in direct contradiction to the Born-Oppenheimer or Ochkur-Rudge exchange approximations (see section 3). It is interesting to note, however, that the Ochkur-Rudge approximation apparently predicts nearly the correct shape (peak near $\theta = 90°$) of the DCS for this transition at impact energies quite close to threshold[66]. It would be of interest to study this DCS as a function of incident energy to determine at what energy it begins to peak forward.

There are only three previous experimental measurements with which we can (and will) compare our results:

(1) The peak intensity ratios for several helium transitions determined by Chamberlain, et al.[27] at a 0° scattering angle and incident energies from 22 eV to 81 eV,

(2) the measurements of Simpson, et al.[31] on the shape of the $1^1S \rightarrow 2^3S$, 2^1S, and 2^1P DCS for $5° \leq \theta \leq 60°$ and 56.5 eV incident energy, and

(3) Ehrhardt and Willmann's[37b] determination of the shape of the $1^1S \rightarrow 2^3S$ DCS as a function of θ at 24 eV.

In addition, the DCS for excitations of the 2^3S, 2^1S, and 2^3P states relative to that of the 2^1P one provide essential information about the differences between the angular dependencies of scattered electron intensities for transitions which are optically spin- and/or symmetry-forbidden and those of an optically allowed one.

5.2.2. Energy Scale Calibration

As noted previously (section 4.4.6), the energy-loss scale is calibrated simply by tuning the instrument on the elastic peak with $V_{SWP} = 0$. The energy-loss in eV is then numerically equal to the sweep voltage without any contact potential corrections (an experimental verification of this is presented in section 5.2.3).

However, there is a contact potential associated with the incident beam (as discussed in section 4.4.3.5). In the present work, this potential was determined experimentally for helium by observing the 57.1 eV and 58.2 eV helium resonances[31]. Although this calibration of the contact potential is necessarily valid only at these particular energies (57-58 eV), it was assumed to be correct throughout the impact-energy range studied ($\sim$ 25 eV to $\sim$ 57 eV). This correction has been applied to all of the quoted impact-energies for helium.

5.2.3. Results and Discussion

Figure 5.2-1 shows an energy-loss spectrum of helium at an impact energy of 34 eV and a scattering angle (θ) of 25°. The resolution (FWHM of the elastic as well as the inelastic peaks) is

Figure 5.2-1. Energy-loss spectrum of helium. Incident beam energy (E_o) = 34 eV; incident beam current (I_o) = 3.2×10^{-8} A; scattering angle (θ) = 25°; scan rate (SR) = .010 V/sec; rate-meter time constant (TC) = .5 sec; scattering chamber pressure (P) = 3×10^{-3} torr.

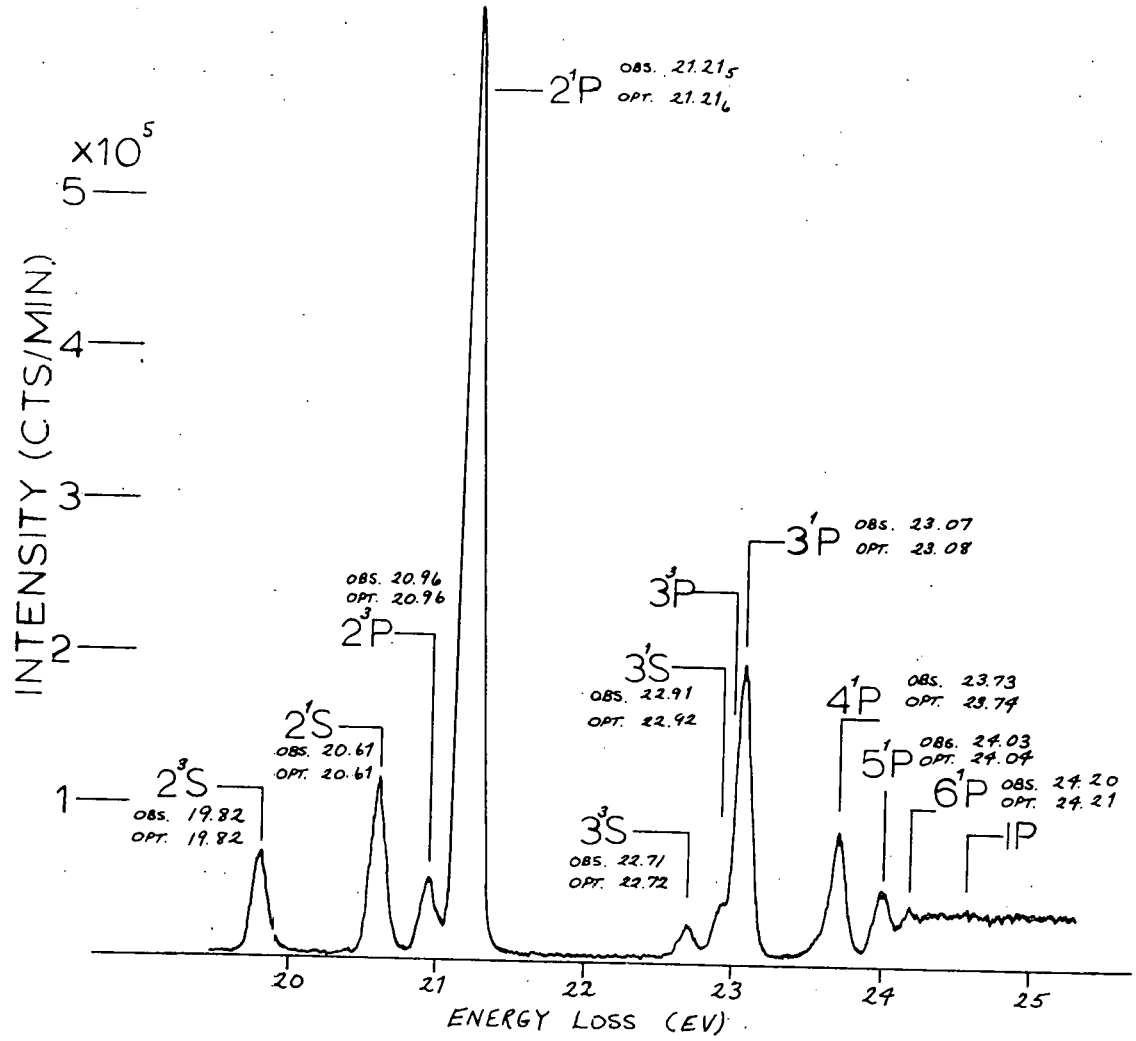
INTENSITY (CTS/MIN.)
x10^5
5
4
3
2
1
2^1P OBS. 21.215 OPT. 21.216
2^3P OBS. 20.96 OPT. 20.96
2^1S OBS. 20.61 OPT. 20.61
2^3S OBS. 19.82 OPT. 19.82
3^1P OBS. 23.07 OPT. 23.08
3^3P
3^1S OBS. 22.91 OPT. 22.92
3^3S OBS. 22.71 OPT. 22.72
4^1P OBS. 23.73 OPT. 23.74
5^1P OBS. 24.03 OPT. 24.04
6^1P OBS. 24.20 OPT. 24.21
IP
20
21
22
23
24
25
ENERGY LOSS (EV)

0.10 eV, which is sufficient to clearly resolve the five lowest-lying transitions. The positions of the centers of the observed peaks are given in eV by the numbers labelled obs. Those labelled opt. were obtained from Moore's table[132] of atomic energy levels (optical data). The agreement between the obs. and opt. values is within the accuracy with which the peak positions can be determined for this resolution. In particular, the very intense 2^1P peak can be located to within .001 eV ($\sim 1\%$ of its FWHM) while the weaker and somewhat overlapping n = 3, 4, . . . , etc. levels can be determined to within .01 eV ($\sim 10\%$ of their FWHM). The pertinent instrumental settings for figure 5.2-1 are given in the figure caption.

Figure 5.2-2 shows three impact spectra of helium collected under identical conditions except for different scattering angles of 0°, 30°, and 60°. The four peaks in these spectra correspond to transitions from the 1^1S ground state to the 2^3S (spin- and symmetry-forbidden), 2^1S (symmetry-forbidden), 2^3P (spin forbidden), and 2^1P (optically allowed) states.

Since the peak shapes are not a function of angle, the respective peak heights are directly proportional to the DCS for that transition. Since the collection efficiency is not a function of energy-loss (section 4.4.4.3), it follows that the ratio of two peak intensities at the same angle is equal to the corresponding ratio of the DCS at that angle. (Note that the volume correction cancels.) Figures 5.2-3, -4, -5, and -6 contain plots of the $2^3S/2^1P$, $2^1S/2^1P$, and $2^3P/2^1P$ peak intensity ratios(and hence the DCS ratios) as a function

Figure 5.2-2. Energy-loss spectra of helium at scattering angles of $\theta = 0°$, $30°$, and $60°$. $E_o = 34$ eV, $I_o = 1 \times 10^{-8}$ A, $P = 2 \times 10^{-3}$ torr.

$\theta = 0°$ scan: SR = .010 V/sec, TC = 0.5 sec.

$\theta = 30°$ scan: SR = .005 V/sec, TC = 1 sec.

$\theta = 60°$ scan: SR = .001 V/sec, TC = 10 sec.

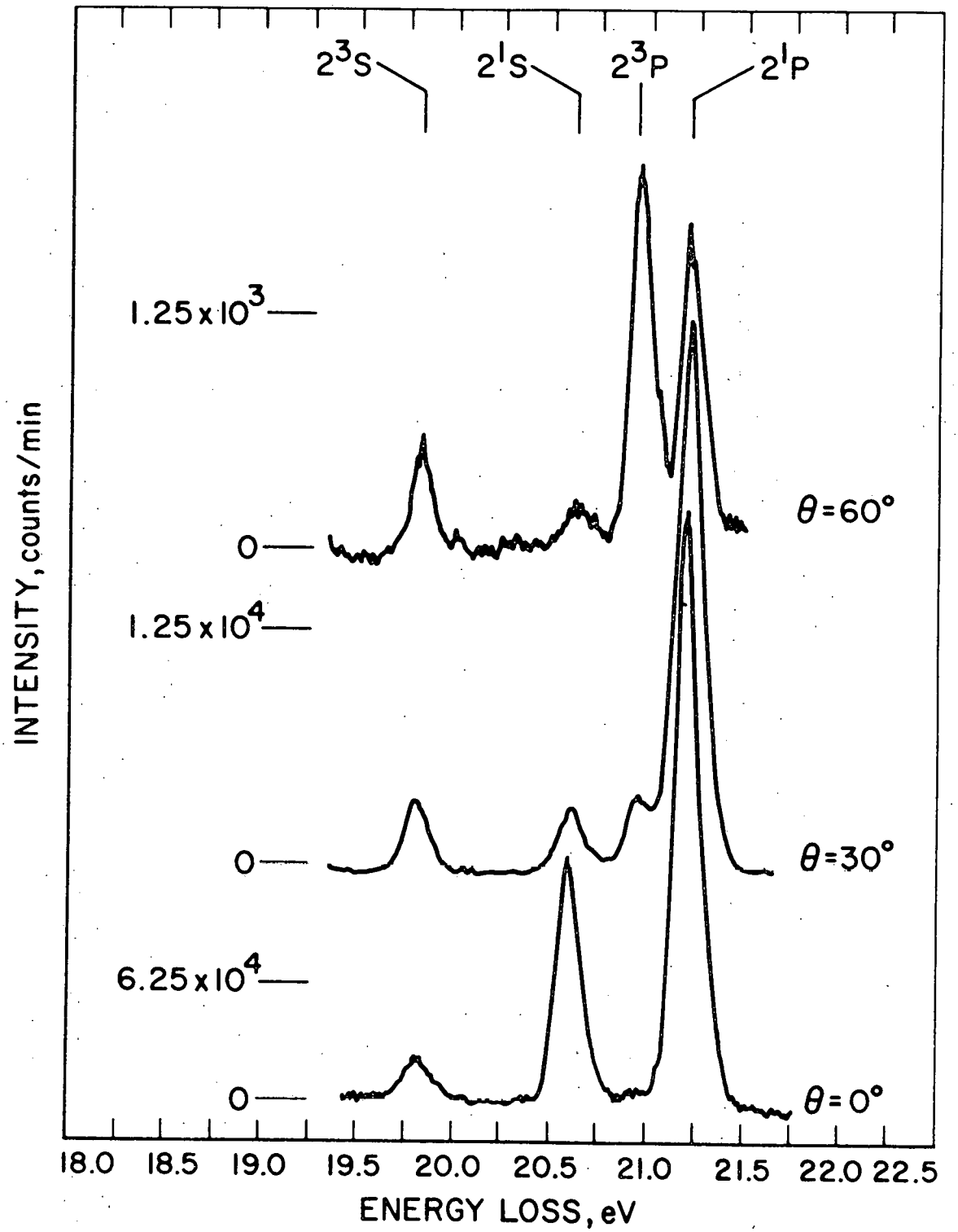
2^3S
2^1S
2^3P
2^1P
1.25×10^3
0
$\theta = 60°$
1.25×10^4
0
$\theta = 30°$
6.25×10^4
0
$\theta = 0°$
INTENSITY, counts/min
18.0 18.5 19.0 19.5 20.0 20.5 21.0 21.5 22.0 22.5
ENERGY LOSS, eV

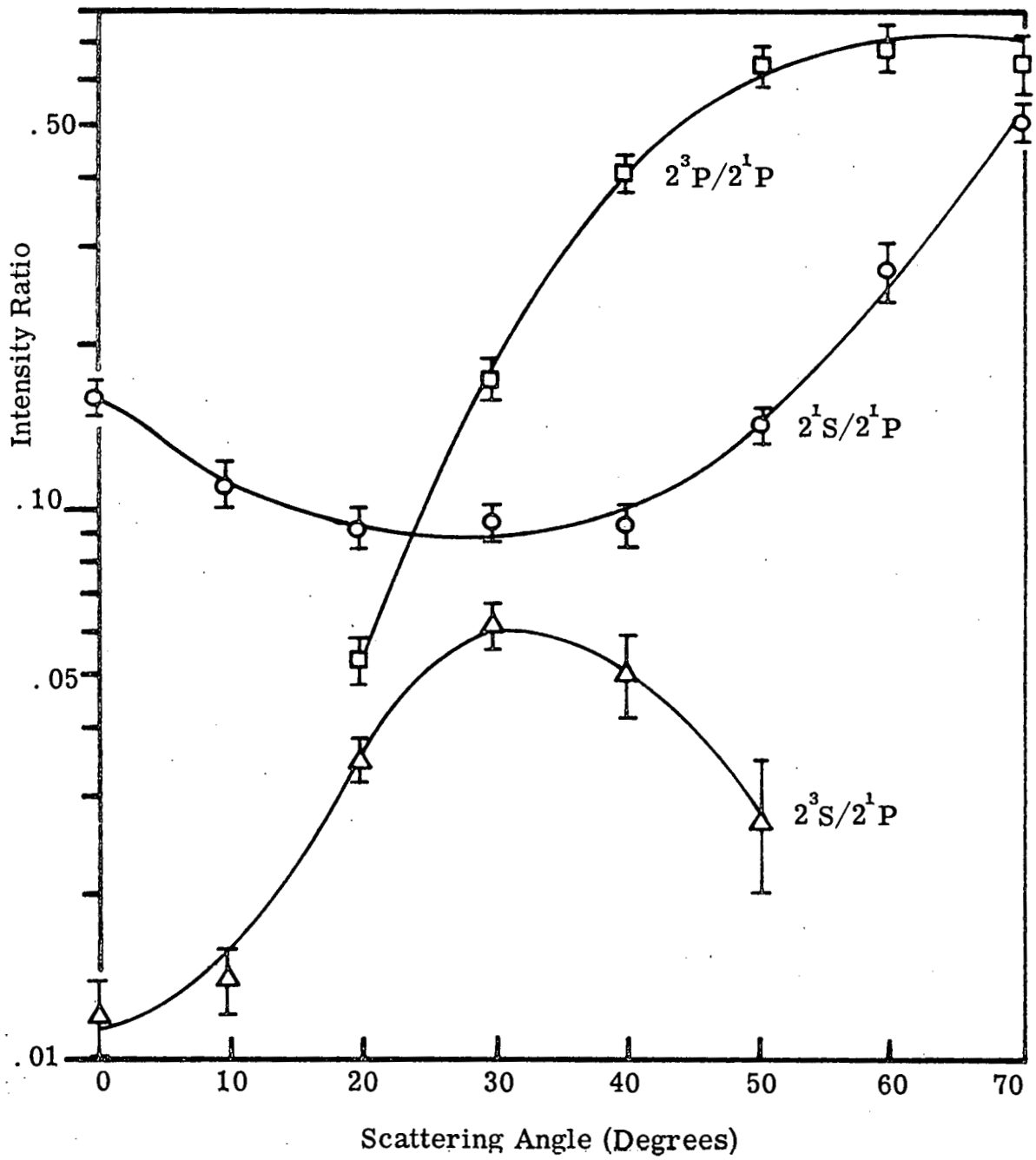

Figure 5.2-3. Ratios of intensities of the $1^1S \rightarrow 2^3S$, 2^1S, and 2^3P transitions in helium to that of the $1^1S \rightarrow 2^1P$ transition as a function of scattering angle. $E_0 = 55.5$ eV. The average of four to six scans at each angle was used to determine the ratios.

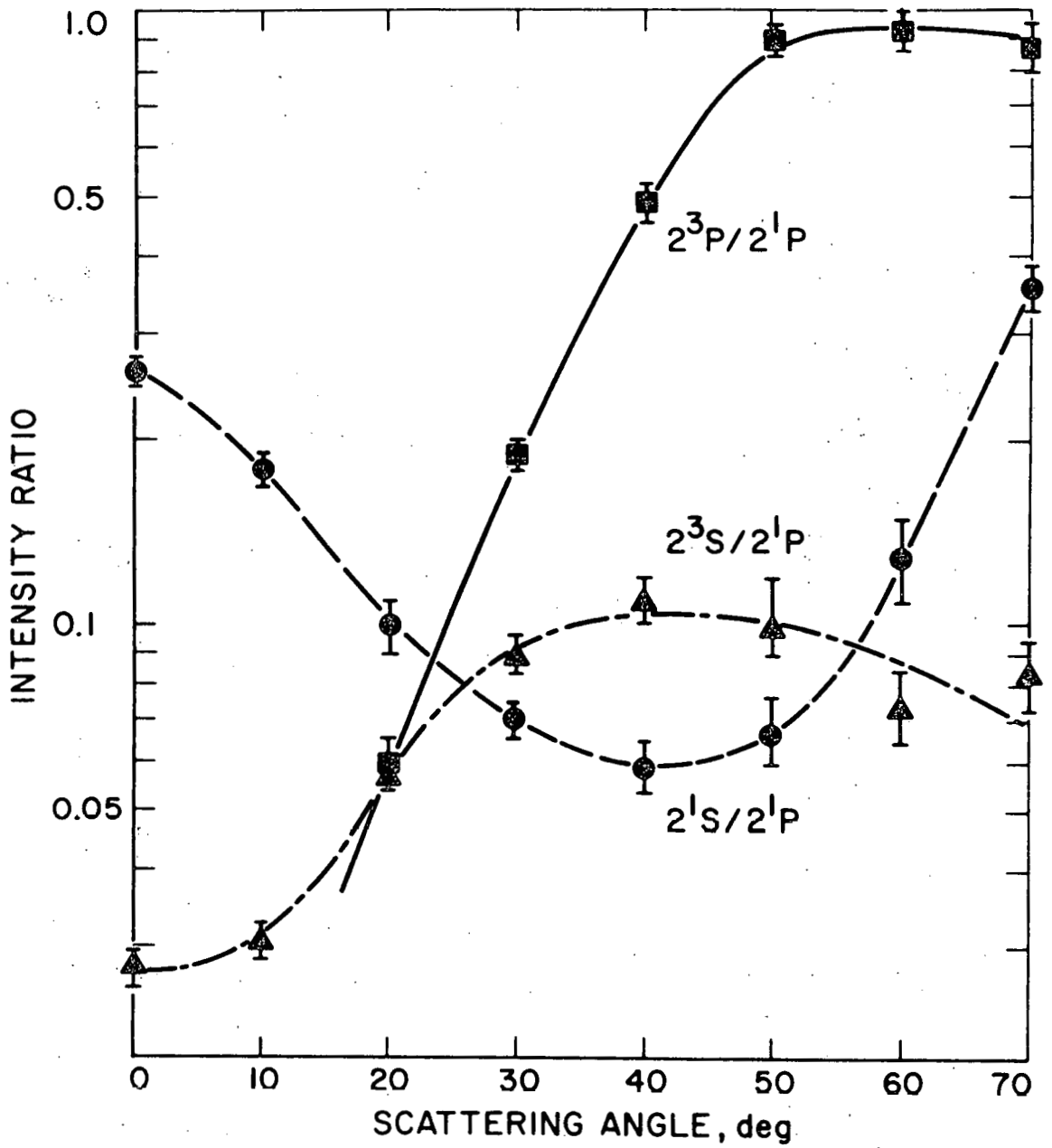

Figure 5.2-4. Same as figure 5.2-3 except that E_o = 44 eV. The average of four to five scans at each angle was used to determine the ratios.

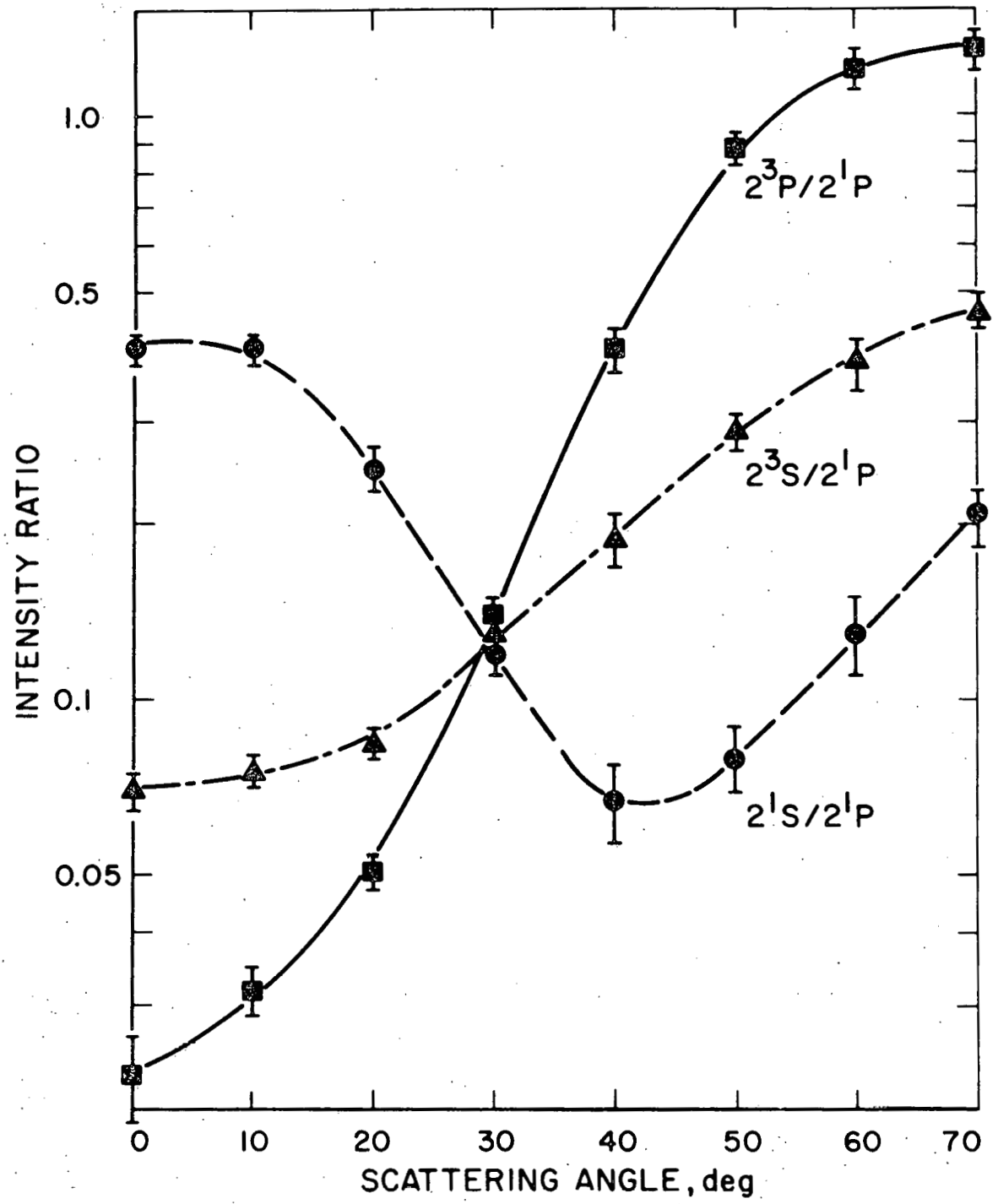

Figure 5.2-5. Same as figure 5.2-3 except that E_o = 34 eV. The average of four scans at each angle was used to determine the ratios.

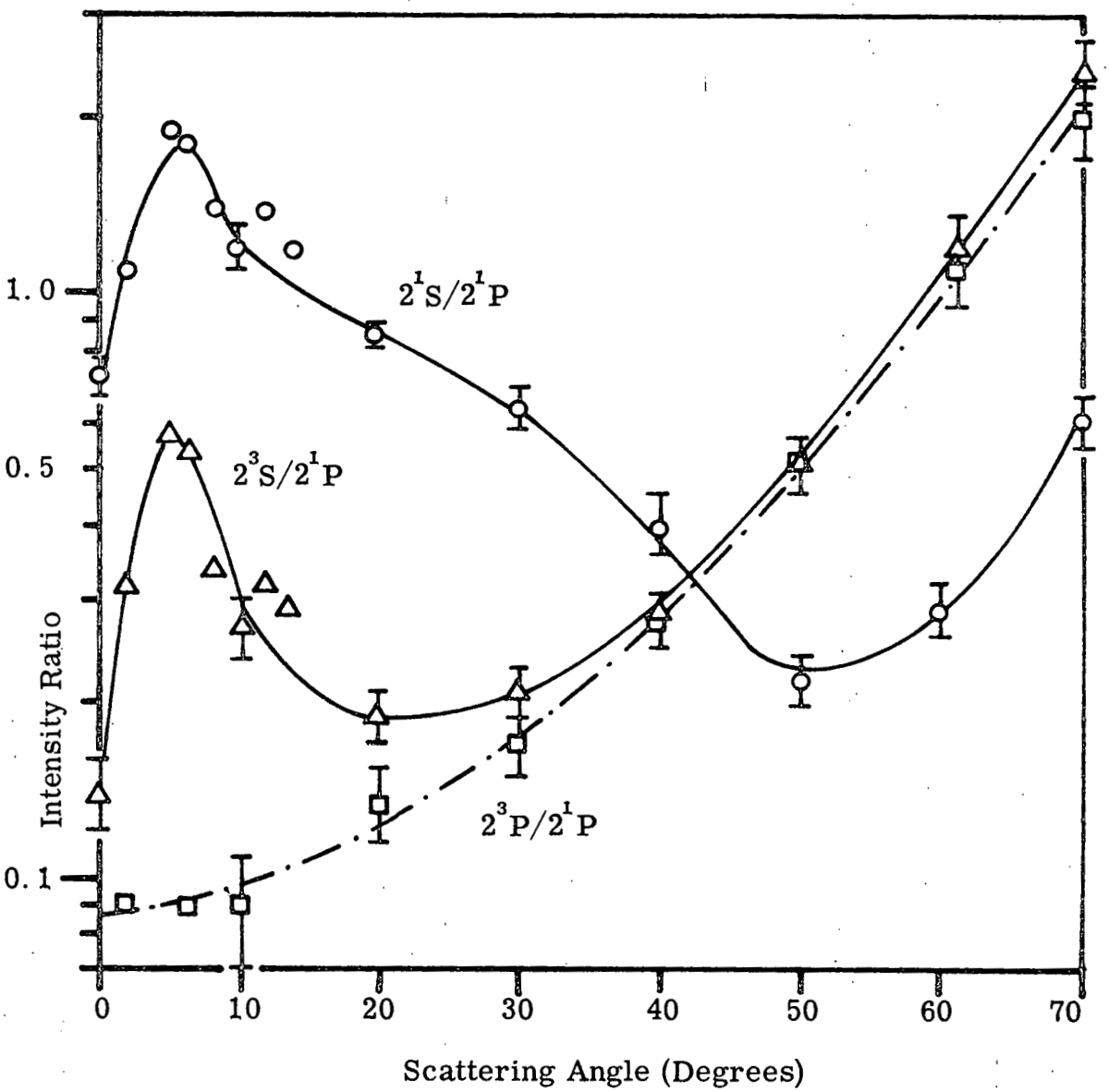

Figure 5.2-6. Same as figure 5.2-3 except that E_o = 26.5 (see text). The points with error bars are the average of four scans. The others are individual scans.

of scattering angle for incident electron energies of 55.5 eV, 44 eV, 34 eV, and 26 eV, respectively. The number of measurements used to determine these ratios is given in the figure captions.

Table 5.2-1 compares the $\theta = 0°$ ratios obtained in this research with those of Chamberlain, et al.[27]. The agreement is excellent except for the $2^1S/2^1P$ ratio at an impact energy of 26 eV. This difference could be satisfactorily accounted for by an inaccuracy in our incident energy calibration of about 0.5 eV at this incident energy (i.e., 26 eV should actually be 26.5 eV). Such an error is not unlikely since the calibration is performed only at $\sim$ 60 eV. The ratios of reference (27) at an impact energy of 26.5 eV are presented in the last row of table 5.2-1.

Figure 5.2-7 shows the $3^3S/2^3S$ ratio at 34 eV as a function of θ from 10° to 70°. Within the accuracy of this determination, log $(\frac{3^3S}{2^3S})$ versus θ is a straight line. The extrapolated value of this ratio at $\theta = 0°$ is 0.15 which implies a $3^3S/2^1P$ ratio of .010. This is also in good agreement with the value (.01) from reference (27). The overall agreement serves to verify that our instrumental collection efficiency is indeed independent of energy-loss from 19.8 eV to 22.7 eV (at least to the same extent as is that of reference (27)).

Figure 5.2-8 compares the angular dependencies of the DCS for excitation of the 2^1P, 2^1S, 2^3P, and 2^3S states obtained from the present work (derived from the same energy-loss scans used for obtaining the data of table 5.2-1 and figure 5.2-3) with those of Simpson, et al.[31]. The two sets of data are normalized by setting

TABLE 5.2-1

Peak intensity ratios at $\theta = 0°$ for several transitions in helium. Column (a) contains the results of this work. Column (b) contains the results of Chamberlain, et al.[27]. The values in column (b) were obtained by plotting the ratio data of reference (27) as $\log_{10}$ (ratio) versus incident energy and fitting the points to a smooth curve. Reference (27) gives no error estimates.

Incident Energy eV	$(2^3S/2^1P) \times 100$		$(2^1S/2^1P) \times 100$		$(2^3P/2^1P) \times 100$	
	(a)	(b)	(a)	(b)	(a)	(b)
55.$_5$	1.2 ± .2	1	16 ± 1	15	-	0
44.	2.9 ± .2	3	26 ± 2	25	-	0
34.	7.0 ± .5	7	40 ± 2	40	2.3 ± .4	2
26.	14 ± 2	14	73 ± 6	85	9 ± 2	8
26.5*		13		79		7

* Refer to text.

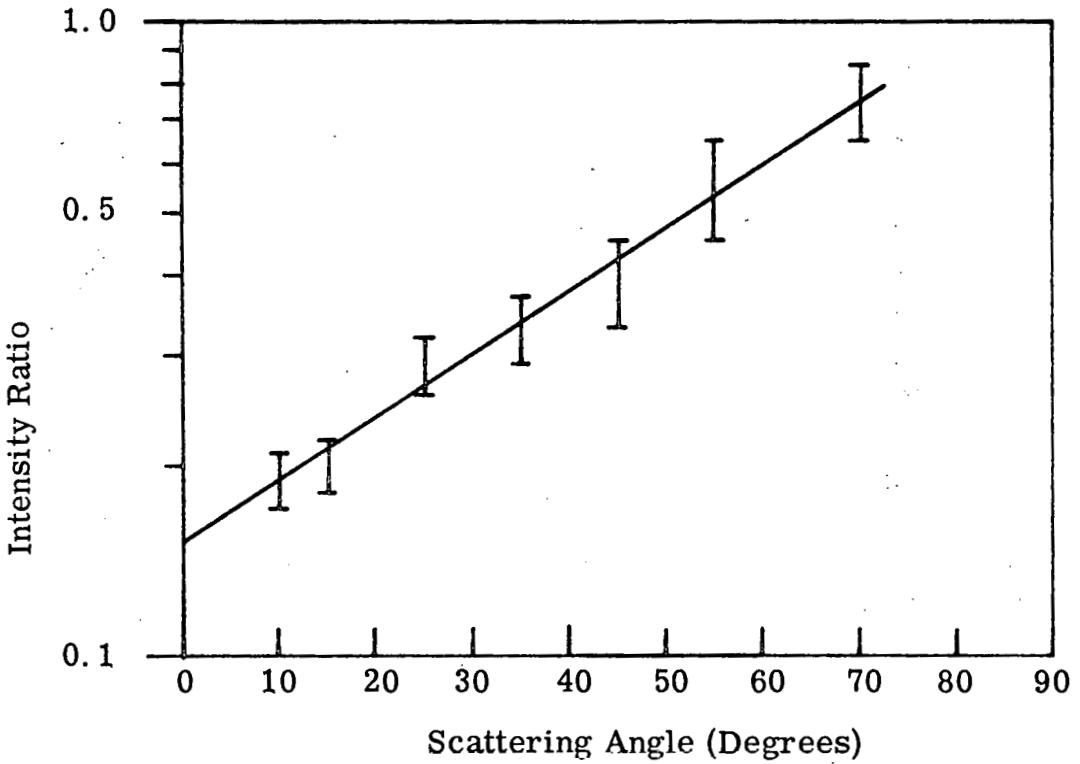

Figure 5.2-7. Ratio of intensity of the $1^1S \rightarrow 3^3S$ transition to that of the $1^1S \rightarrow 2^3S$ transition as a function of scattering angle. E_o = 34 eV. The average of three scans at each angle was used to determine the ratios. The solid line is the best straight line (average ordinate method) through the points.

Figure 5.2-8. Differential scattering cross sections (DCS) in arbitrary units for excitation of the 2^3S, 2^1S, 2^3P, and 2^1P states of helium from its 1^1S ground state. The solid line and data points are from the present research. For clarity, only a few representative error bars are shown. The dashed lines are the results of Simpson[31]. The two sets of data are normalized by setting the $1^1S \rightarrow 2^1P$ DCS equal to 30 (arbitrary units) at $\theta = 10°$. The present data may be placed on an absolute scale (see text) by multiplying the DCS of this figure by 4.7×10^{-3} (see table 5.2-2). $E_o = 55.5$ eV.

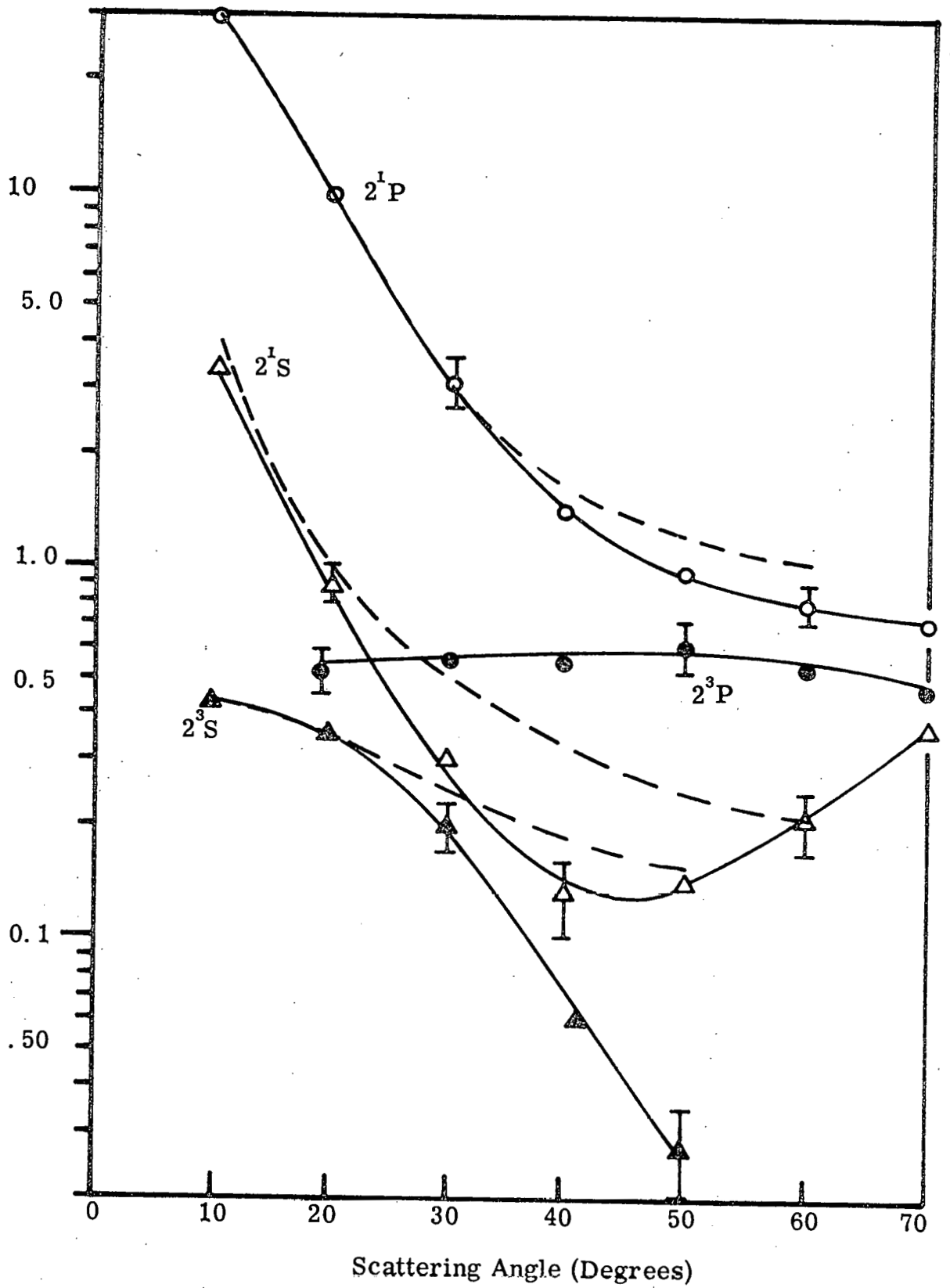
10
5.0
1.0
0.5
0.1
.50
2^1P
2^1S
2^3P
2^3S
0
10
20
30
40
50
60
70
Scattering Angle (Degrees)

the value of the DCS for excitation of the 2^1P state equal to 30 (arbitrary units) at $\theta = 10°$. The relative positions of all of the other points follow from this one requirement.

There are several factors which must be considered in comparing these data sets:

(1) They were obtained at slightly different impact energies--56.5 eV for reference (31) and 55.5 ± .2 for the present work. Since both of these impact energies are in an off-resonance portion of the helium excitation spectrum and are relatively high compared to the inelastic thresholds, this difference should not significantly alter the angular distributions.

(2) Our data are subject to an addition 20% error at $\theta = 10°$ due to the uncertainty of the beam geometry (refer to section 4.4.4.4). The data of reference (31) are not.

(3) Chamberlain, et al.[121] have suggested that it is likely that the scattering intensities of reference (31) are too high at the larger angles due to the effects of double scattering. Such effects are not important in the present research (see section 4.4.4.2).

(4) J. A. Simpson, et al.[31] give no error estimates for their data.

The agreement between this work and that of reference (31) is excellent for $\theta \leq 25°$. This is just the region in which the effects of double scattering should be least important in the data of reference (31) but the uncertainty in the proper volume correction is most significant in our data. Consequently, this good agreement indicates

that our volume correction is probably accurate to within the errors of reference (31) (unknown) and the present work ($\sim 10\%$). The discrepancies in the two data sets at higher angles could be the result of double scattering in the data of reference (31), which tends to enhance the scattered signal. Without additional details concerning the conditions under which those data were obtained, it is fruitless to speculate further.

The final experimental measurement with which we can compare our results is that of Ehrhardt and Willmann[37b]. Figure 5.2-9 shows the angular dependence of the DCS for excitation of the 2^3S state from reference (37b) and the present research at an impact energy of 24 eV. The data of reference (37b) are believed to be quite reliable. Since the target in their case is an atomic beam, the scattered intensity is directly proportional to the DCS without an angle dependent path length correction and double scattering is very unlikely. Further, they have accurately calibrated the incident beam energy ($24.0 \pm .05$ eV for the results in fig. 5.2-9). Our results have been normalized to those of reference (37b) at $\theta = 30°$ (the volume correction for our results should be quite reliable for this angle and larger ones). The agreement is within the errors of the two measurements for scattering angles between about 10° and 50° but there is a significant deviation at higher angles. This discrepancy cannot be due to double scattering nor an improper volume correction. However, as indicated from the comparison in table 5.2-1 for an impact energy of ~ 26 eV, the incident energy in our case may be

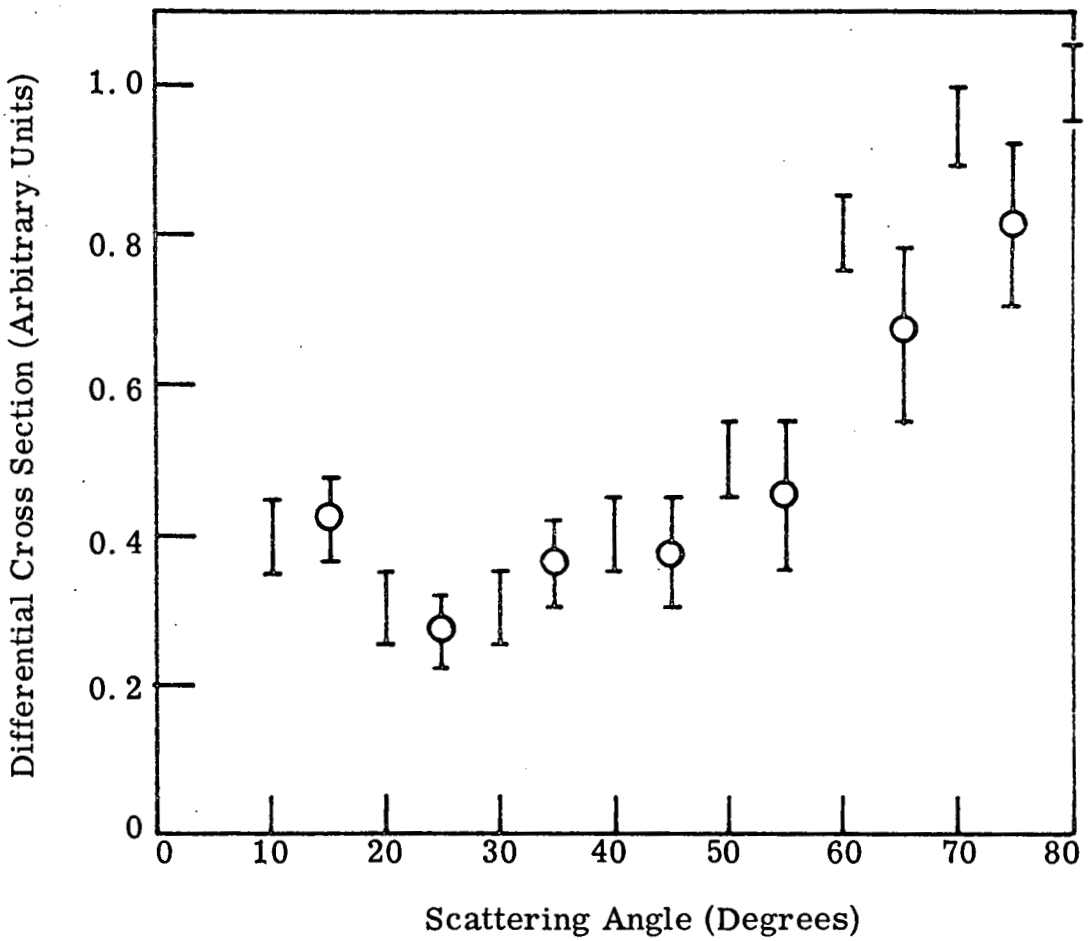

Figure 5.2-9. The $1^1S - 2^3S$ differential scattering cross section (in arbitrary units) for helium at $E_o \approx 24$ eV. The plane error bars are the results of Ehrhardt[37b], the open circles are the present results (average of three scans at each angle). The two sets of data were normalized by setting the DCS equal to 0.30 at $\theta = 30°$. (Refer to the text for other details.)

incorrect by 0.5 eV. Unfortunately, we were not able to obtain reliable data at lower impact energies (24 eV is within 4 eV of the 2^3S excitation threshold which presents some of the difficulties discussed in section 4.4.4.3) nor do Ehrhardt and Willmann present data at higher incident energies. If we assume that the incident energy of 24 eV as determined by observation of the 57.1 eV helium resonance is inaccurate by 0.5 eV in the same sense as indicated by table 5.2-1 for the 26 eV calibration, then the "true" impact energy is probably close to 24.5 eV. Since these impact energies are so near the excitation threshold, a relatively small change in incident energy can make a large change in the angular distribution as shown in figure 5.2-10. The distributions at 22.0 eV (curve 1) and 24.0 eV (curve 2) are taken from reference (37b) while the ones at E (curve 3) ($E \cong 24.5$ if the assumptions above are correct), E + 2.0 (curve 4), and 34 eV (curve 5) are from the present work. All of the distributions have been normalized to 0.30 (arbitrary units) at $\theta = 30°$. For clarity, smooth curves have been drawn through the data points (within the error bars) and one representative error has been indicated on each curve. It is quite clear that increasing the impact energy from 22 eV to 34 eV changes the angular distribution from one that is peaked at angles greater than 70° to one that peaks at angles less than 10°. (Of course, there may be additional peaks beyond 70° which we cannot observe.) This general trend is consistent with $E \cong 24.5$ in curves 3 and 4.

Figure 5.2-10. The $1^1S \rightarrow 2^3S$ differential scattering cross section (in arbitrary units) for helium. Data of reference (37b) at E_o = 22.0 eV (curve 1) and E_o = 24.0 eV (curve 2). Present results at $E_o = E$ (curve 3, see text), $E_o = E + 2$ eV (curve 4), and E_o = 34 eV (curve 5). Each curve is normalized to 0.3 arbitrary units at $\theta = 30°$ and contains one representative error bar.

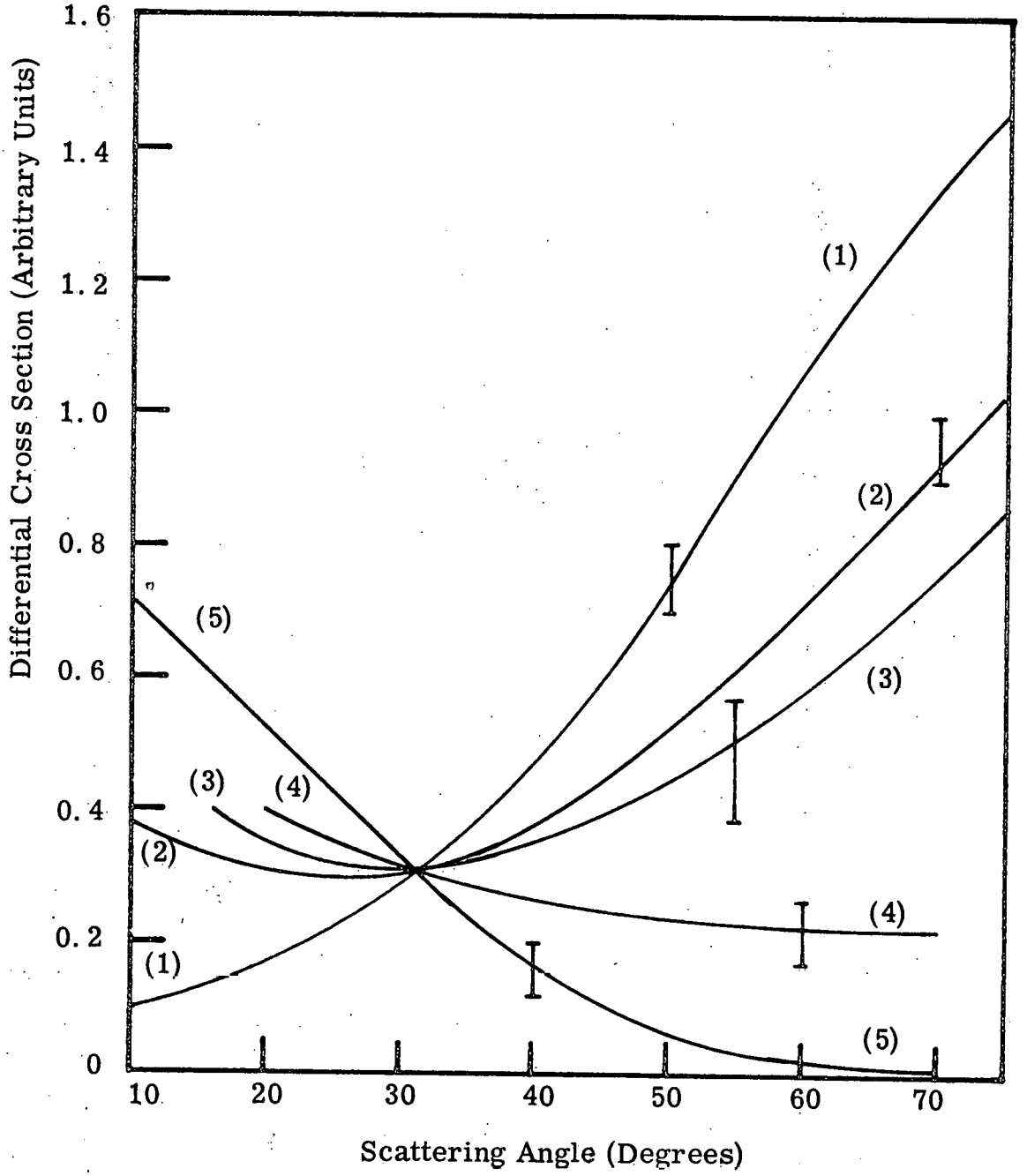
Differential Cross Section (Arbitrary Units)
1.6
1.4
1.2
1.0
0.8
0.6
0.4
0.2
0
10
20
30
40
50
60
70
Scattering Angle (Degrees)
(1)
(2)
(3)
(4)
(5)

Figures 5.2-11, -12, and -13 show the measured DCS (in arbitrary units) at 44 eV, 34 eV, and 26 (26.5 eV), respectively. These data were obtained from the same energy-loss scans which were used to derive the ratio data of table 5.2-1 and figures 5.2-4, -5, and -6.

The data in figures 5.2-8, -11, -12, and -13 can be placed on an absolute scale (but only in an approximate way) as follows. Let $\sigma^{T}_{2^1P}(E,\theta)$ be the "true" differential cross section for excitation of the 2^1P state for an incident energy E and scattering angle θ. Then, the "true" total cross section for this excitation is

$$Q^{T}_{2^1P}(E) = 2\pi \int_0^{\pi} \sigma^{T}_{2^1P}(E,\theta) \sin\theta \, d\theta \qquad (5\text{-}3)$$

Within the experimental uncertainties already discussed (section 4.4.4) the experimental DCS in "arbitrary" units is directly proportional to the "true" one:

$$\sigma^{Arb}_{2^1P}(E,\theta) = K(E)\, \sigma^{T}_{2^1P}(E,\theta) , \qquad (5\text{-}4)$$

where K(E) depends on the incident energy but not on θ. The total experimental cross section in these "arbitrary" units is

$$Q^{Arb}_{2^1P}(E) = 2\pi \int_0^{\pi} \sigma^{Arb}_{2^1P}(E,\theta) \sin\theta \, d\theta \qquad (5\text{-}5)$$

which, together with (5-3) and (5-4), gives

Figure 5.2-11. $1^1S \rightarrow 2^3S$, 2^1S, 2^3P, and 2^1P DCS (in arbitrary units) for helium. E_o = 44 eV. The conversion factor to place these data on an absolute scale (table 5.2-2) is $3.3 \times 10^{-3} \pi a_o^2$/arbitrary unit. For clarity, only a few representative error bars are shown.

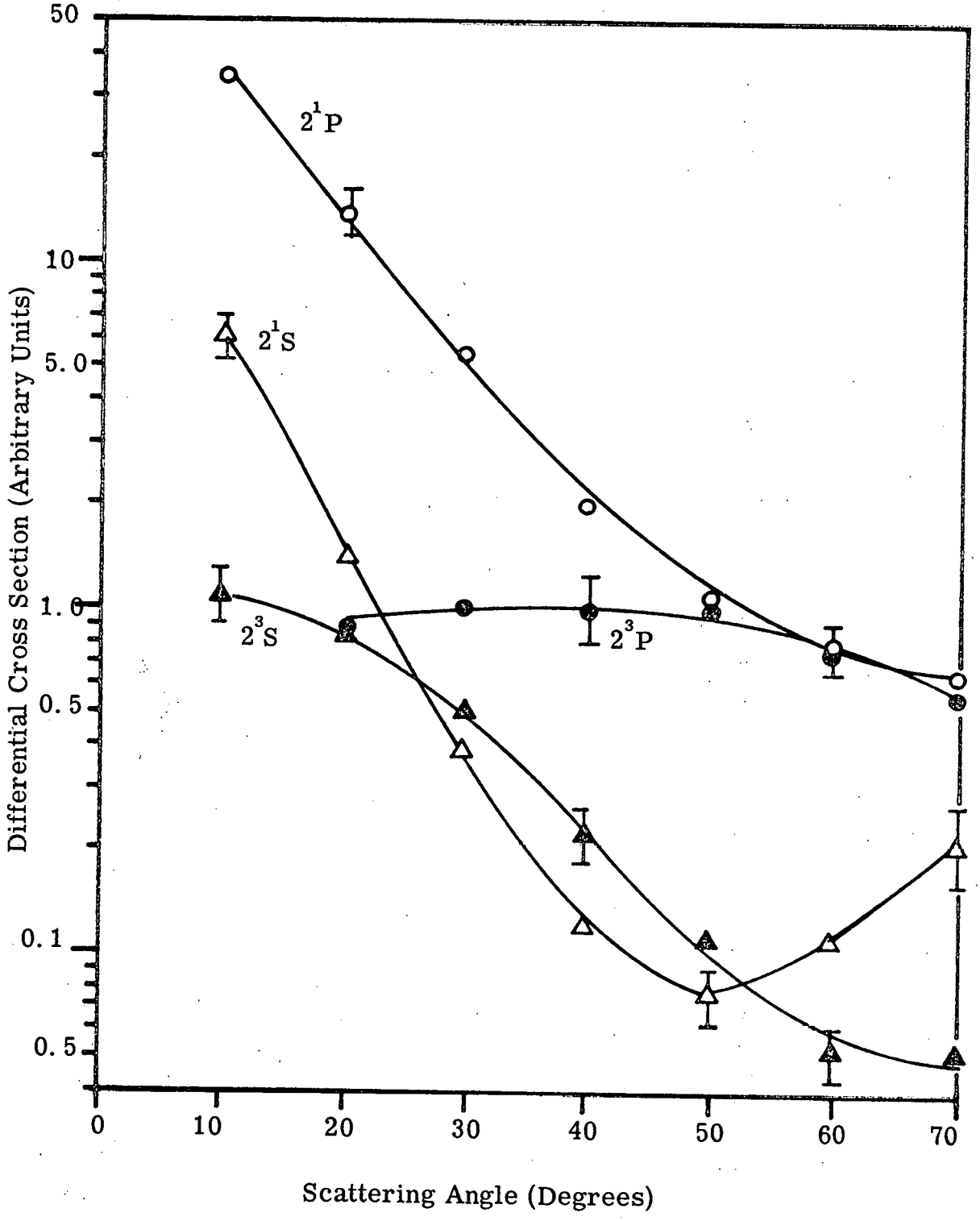
50
10
5.0
1.0
0.5
0.1
0.5
Differential Cross Section (Arbitrary Units)
2^1P
2^1S
2^3S
2^3P
0
10
20
30
40
50
60
70
Scattering Angle (Degrees)

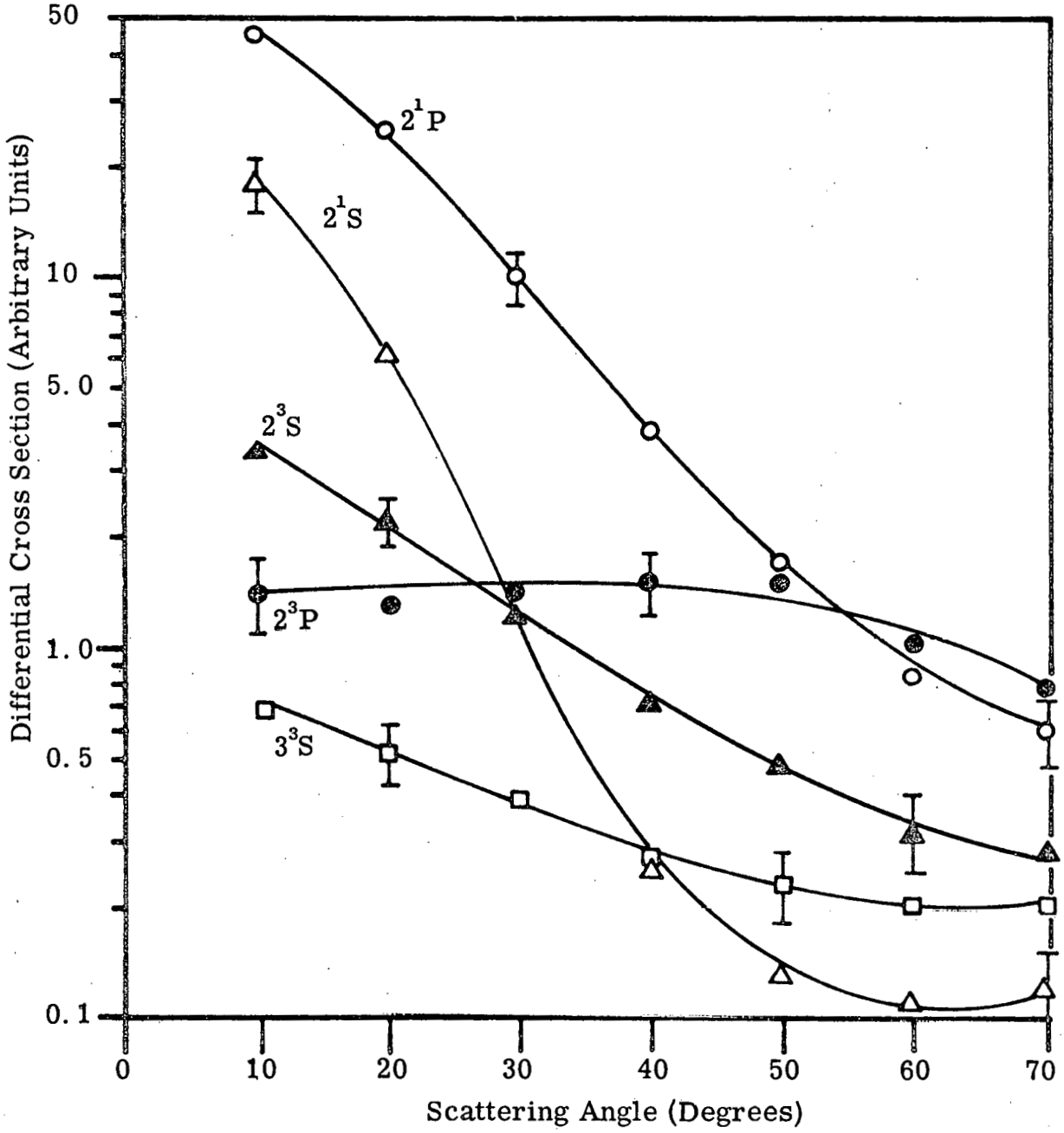

Figure 5.2-12. The same as fig. 5.2-11 except that E_o = 34 eV and the $1^1S \rightarrow 3^3S$ DCS is included. Conversion factor (table 5.2-2) is $1.4 \times 10^{-3} \pi a_o^2$/arbitrary unit.

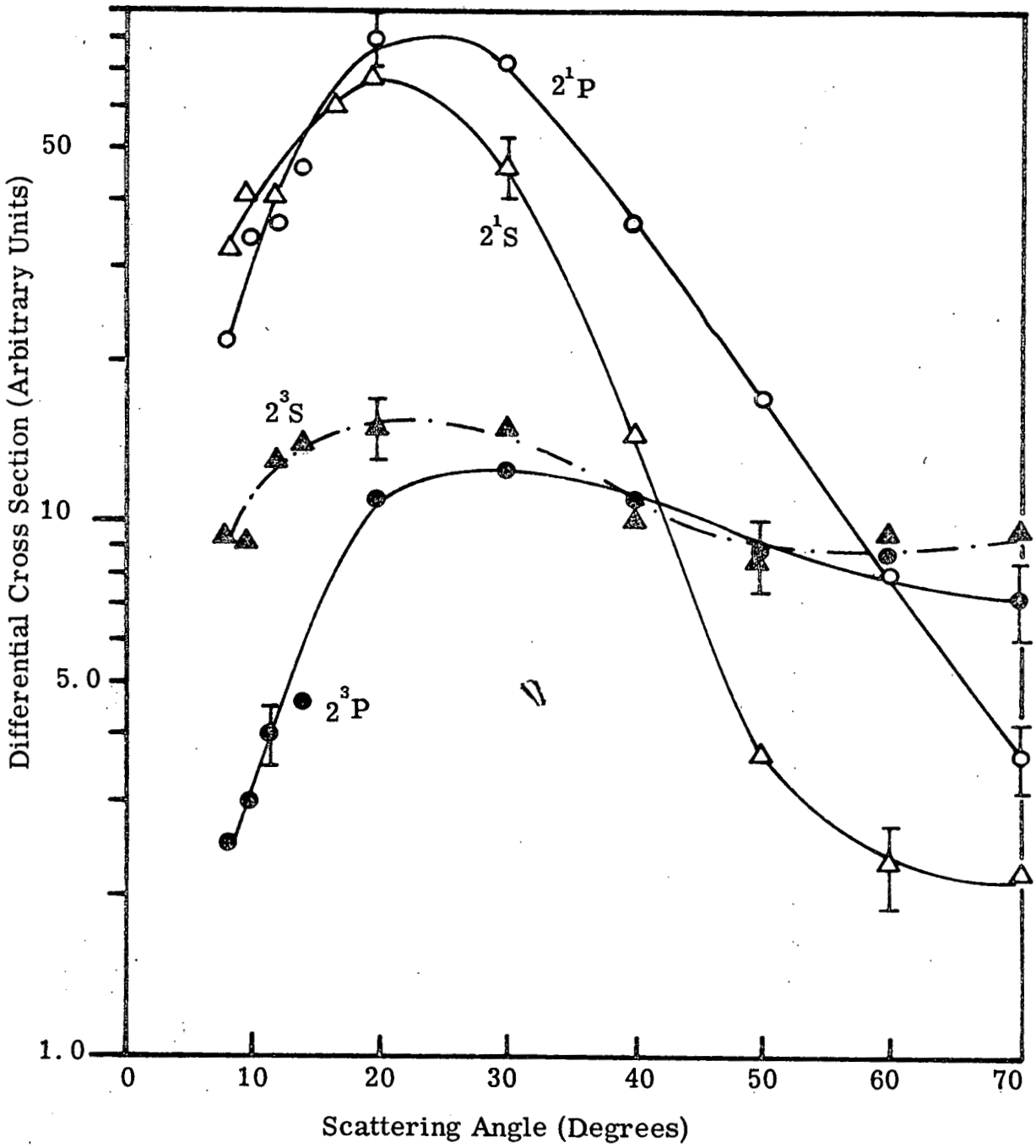

Figure 5.2-13. The same as fig. 5.2-11 except that E_o = 26 (26.5 eV). The conversion factor (table 5.2-2) is $1.3 \times 10^{-3} \pi a_o^2$/arbitrary unit.

$$K(E) = \frac{Q^{Arb}_{2^1P}(E)}{Q^{T}_{2^1P}(E)} \quad (5\text{-}6)$$

Reliable values of $Q^{T}_{2^1P}(E)$ for 22 eV $\leq E \leq$ 450 eV are available[43] and $Q^{Arb}_{2^1P}(E)$ can be calculated from the present data through relation (5-5). Table 5.2-2 gives the results of numerical integration of (5-5) for $\sigma^{Arb}_{2^1P}$ taken from figures 5.2-8, -11, -12, and -13.

A third-order interpolation by Bessel's formula[133] was used to obtain approximately 240 "data" points from an assumed value of $\sigma^{Arb}_{2^1P}$ at $\theta = 0°$ and the $\sigma^{Arb}_{2^1P}$ values at $\theta = 10°, 20°, \ldots, 70°$ from the figures. The uncertainty of the DCS below 10° does not introduce any appreciable error in the integral (5-5) from $\theta = 0°$ to 70° because of the $\sin\theta$ weighting factor. For lack of a better method, the data were extrapolated to $\theta = 180°$ by assuming

$$\sigma^{Arb}_{2^1P}(\theta \geq 70°) = A\, e^{-\theta/\alpha} \quad (5\text{-}7)$$

where A and α were determined by $\sigma^{Arb}_{2^1P}(60°)$ and $\sigma^{Arb}_{2^1P}(70°)$. The respective values of α are given in table 5.2-2. The integral over (5-7) was performed analytically. The uncertainty in the integral (5-5) over the range $\theta = 0°$ to 70° is probably 10-15% since this is the approximate relative error in each experimental value of $\sigma^{Arb}_{2^1P}(E,\theta)$.

TABLE 5.2-2

Quantities related to the calculation of K(E). Refer to the text for the corresponding definitions. Arb stands for arbitrary units.

E (eV)	$Q^{Arb\,0}_{2^1P}$ (Arb) (eq. 5-8)	$Q^{Arb\,1}_{2^1P}$ (Arb) (eq. 5-9)	α (radians) (eq. 5-7)	$Q^{Arb\,2}_{2^1P}$ (Arb) (eq. 5-10)	$Q^{T}_{2^1P}$ $\times 10^{18}$ cm^2 (ref. 43)	$\frac{1}{K(E)}$ (πa_o^2/Arb) (eq. 5-11)	EPE (%) (eq. 5-12)
55.5 (fig. 5.2-8)	15.08	3.90	1.48	6.07	7.9	4.7×10^{-3}	23
44 (fig. 5.2-11)	19.29	2.64	.84	5.48	6.3	3.3×10^{-3}	25
34 (fig. 5.2-12)	29.66	1.76	.52	5.06	3.7	1.4×10^{-3}	23
26 (26.5) (fig. 5.2-13)	125.66	4.78	.22	30.3	1.5	1.3×10^{-4}	31

It is difficult to estimate the overall error in the calculation of $Q^{Arb}_{2^1P}$ since we have no knowledge, either theoretical or experimental, of how $\sigma^{Arb}_{2^1P}$ really varies beyond $\theta = 70°$. In order to obtain some estimate of the possible error in the integral form $\theta = 70°$ to $180°$, we have calculated this integral assuming $\sigma^{Arb}_{2^1P}(\theta \geq 70°) = \sigma^{Arb}_{2^1P}(70°)$. Thus, our estimated error in the determination of $Q^{Arb}_{2^1P}$ is simply the value of the integral between $70°$ and $180°$ assuming this constancy with respect to θ minus its value assuming the θ dependence given by (5-7) plus 12% (uncertainty in the $\theta = 0°$ to $70°$ integral). In summary, the various integral quantities in table 5.2-2 are given by:

$$Q^{Arb\,0}_{2^1P}(E, 0°\text{-}70°) = 2\pi \int_0^{70°} \sigma^{Arb}_{2^1P}(E,\theta) \sin\theta \, d\theta , \qquad (5\text{-}8)$$

$$Q^{Arb\,1}_{2^1P}(E, 70°\text{-}180°) = 2\pi A \int_{70°}^{180°} e^{-\theta/\alpha} \sin\theta \, d\theta , \qquad (5\text{-}9)$$

and

$$Q^{Arb\,2}_{2^1P}(E, 70°\text{-}180°) = 2\pi \, \sigma^{Arb}_{2^1P}(E, 70°) \int_{70°}^{180°} \sin\theta \, d\theta . \qquad (5\text{-}10)$$

The values of $Q^{T}_{2^1P}(E)$ are taken from reference (43). Our best estimate of K(E) (from equation (5-6)) is then

$$K(E) = \frac{Q^{Arb\,0}_{2^1P} + Q^{Arb\,1}_{2^1P}}{Q^{T}_{2^1P}} \qquad (5\text{-}11)$$

with an estimated percent error (EPE) of

$$EPE \equiv \left(\frac{Q^{Arb\,2}_{2^1P} - Q^{Arb\,1}_{2^1P}}{Q^{Arb\,0}_{2^1P} + Q^{Arb\,1}_{2^1P}} \right) \times 100 + 12\%. \qquad (5\text{-}12)$$

The results of this absolute scale calibration can be compared, at least within a factor of 2, with the absolute calculations of Heideman and Vriens[73] based on the Bethe-Born approximation, for $\sigma_{2^1P}(E, 0°)$. Table 5.2-3 summarizes this comparison. The values of $\sigma_{2^1P}(E, 0°)$ in column (a) were obtained by extrapolating the $\sigma^{Arb}_{2^1P}$ data of figures 5.2-8, -11, -12, and -13 to $\theta = 0°$ and multiplying the result by the corresponding 1/K(E) from table 5.2-2. It is evident that the resulting DCS could be incorrect by as much as a factor of 2 from a combination of the error in the extrapolation and the absolute calibration (EPE). Further, the application of a high-energy approximation to this low-energy region can introduce errors of this same magnitude[73]. The fact that the values of column (a) are lower than those of column (b) is to be expected since the Bethe-Born approximation (and all other approximations which ignore back-coupling of the states, see section 3.3.3)

TABLE 5.2-3

Zero-angle differential cross sections from this work (column a) and reference (73) (column b) for the $1^1S \rightarrow 2^1P$ transition in helium. E is the incident electron energy.

E (ev)	$\sigma_{2^1P}(E, 0°)/\pi a_o^2$	
	(a)	(b)
55.5	.21	.70
44	.18	.44
34	.084	.21
(26.5)	.039	.071

consistently over estimates cross sections at lower impact energies.

There is a further theoretical comparison of interest. Cartwright[66] has calculated the DCS for the $1^1S \rightarrow 2^3S$ and 2^3P transitions in helium using the Ochkur-Rudge (OR) method. Figures 5.2-14 and -15 show the results of the present experimental work and these calculations for two different impact-energies. The agreement between the general magnitudes of the cross sections is remarkable but the lack of similarity in the shapes represents a definite failure of the OR approximation. At higher impact-energies (100 eV → 225 eV) the deviations between the experimental shapes[32] and those predicted by the OR and Born-Oppenheimer approximations[67] become even more pronounced. Finally, figure 5.2-16 shows the ratio of the DCS for excitation of the 2^3S state to that of the 2^3P state according to the OR approximation (reference (66)) and the present work. Again, the calculated ratios are of the correct order of magnitude, but their variations with θ bear little resemblance to the experimental ones.

In summary, the comparisons of this section indicate that:

(1) the data obtained with this instrument are consistent with the results of previous investigators, and

(2) the usual first order exchange approximations (OR, Born-Oppenheimer) are not reliable for predicting the detailed shape of DCS curves for excitation of the 2^3S and 2^3P states of helium in this low-energy range.

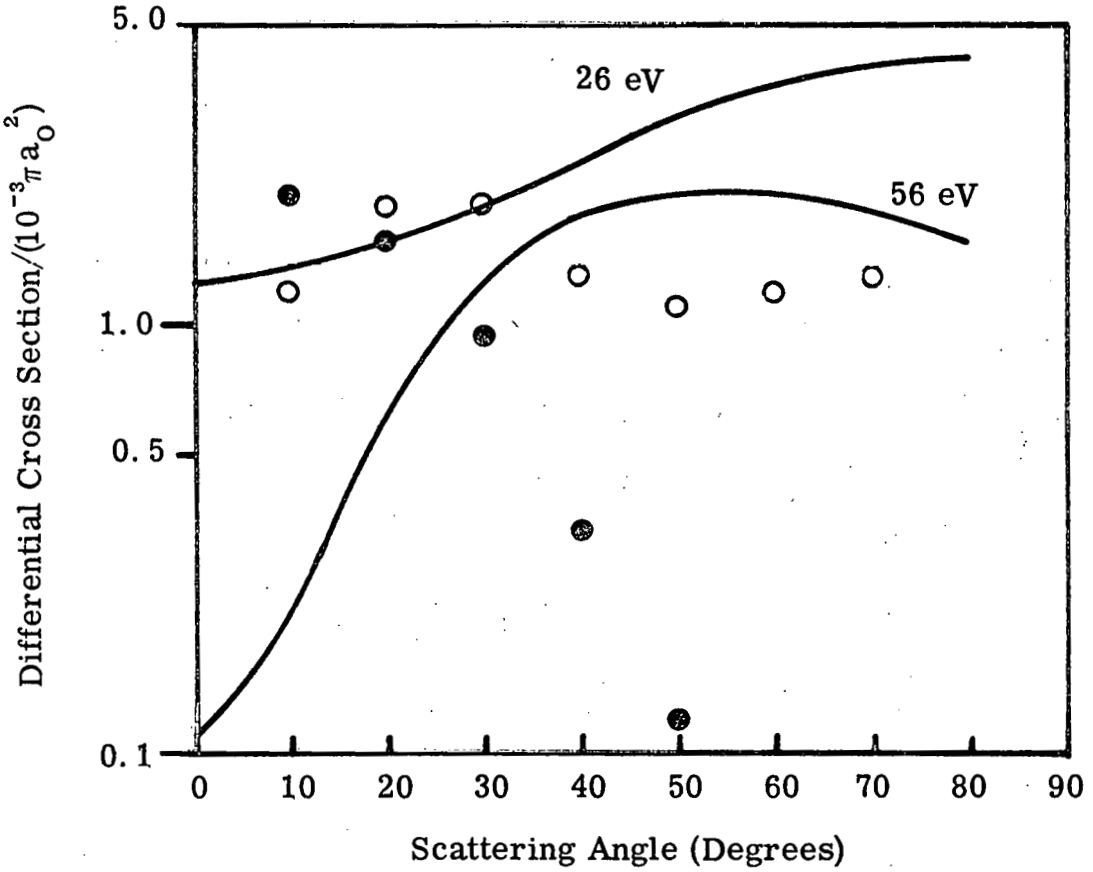

Figure 5.2-14. The $1^1S \rightarrow 2^3S$ DCS for helium. The solid lines are the calculations of reference (66) at E_o = 26 eV and 56 eV. The present results are given at E_o = 26.5 eV (open circles) and at E_o = 55.5 eV (filled circles). Absolute units have been placed on the present results as discussed in the text. The relative error in the experimental data can be found in figures 5.2-8, -13.

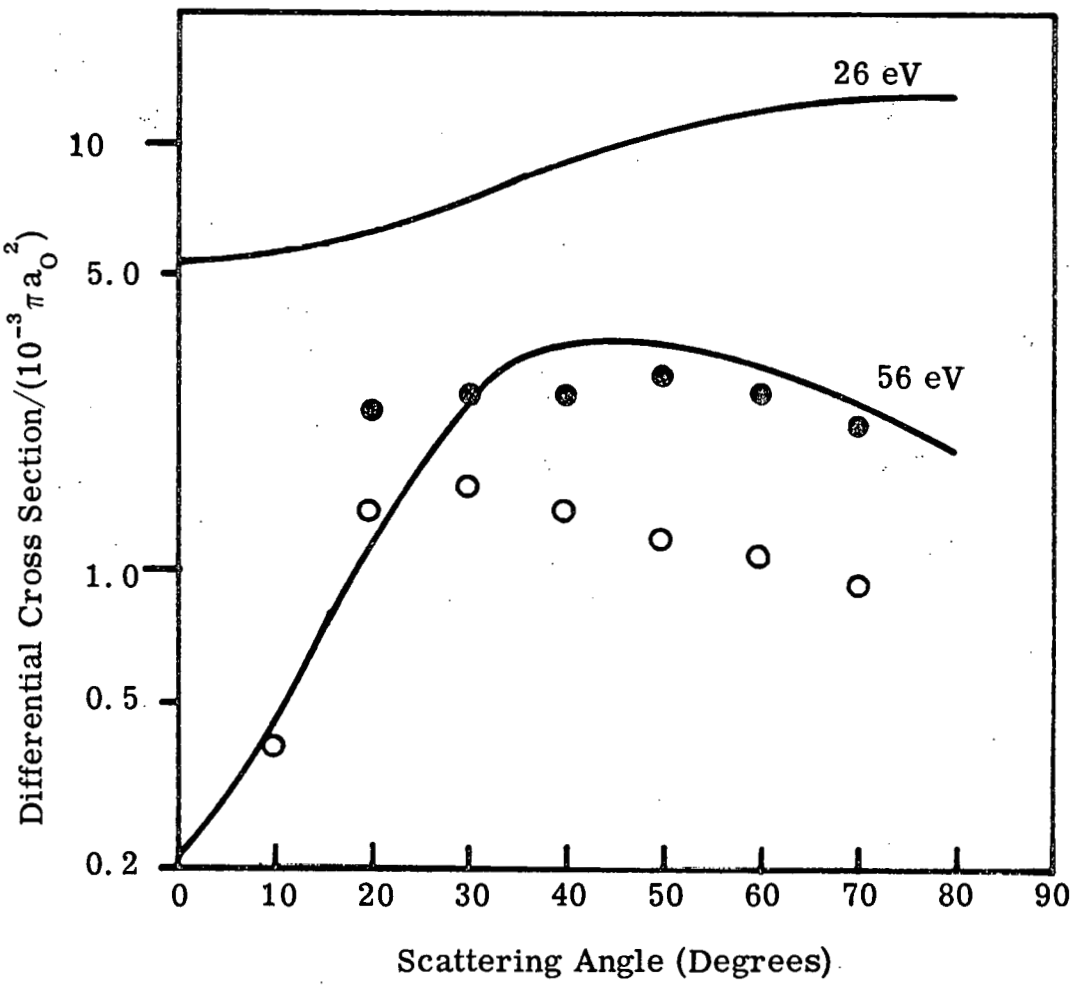

Figure 5.2-15. $1^1S - 2^3P$ DCS for helium. The solid lines are the calculations of reference (66) at E_o = 26 eV and 56 eV. The present results are given at E_o = 26.5 eV (open circles) and 55.5 eV (filled circles) and have been put on an absolute scale as discussed in the text. The relative error in the experimental data is indicated in figures 5.2-8, -13.

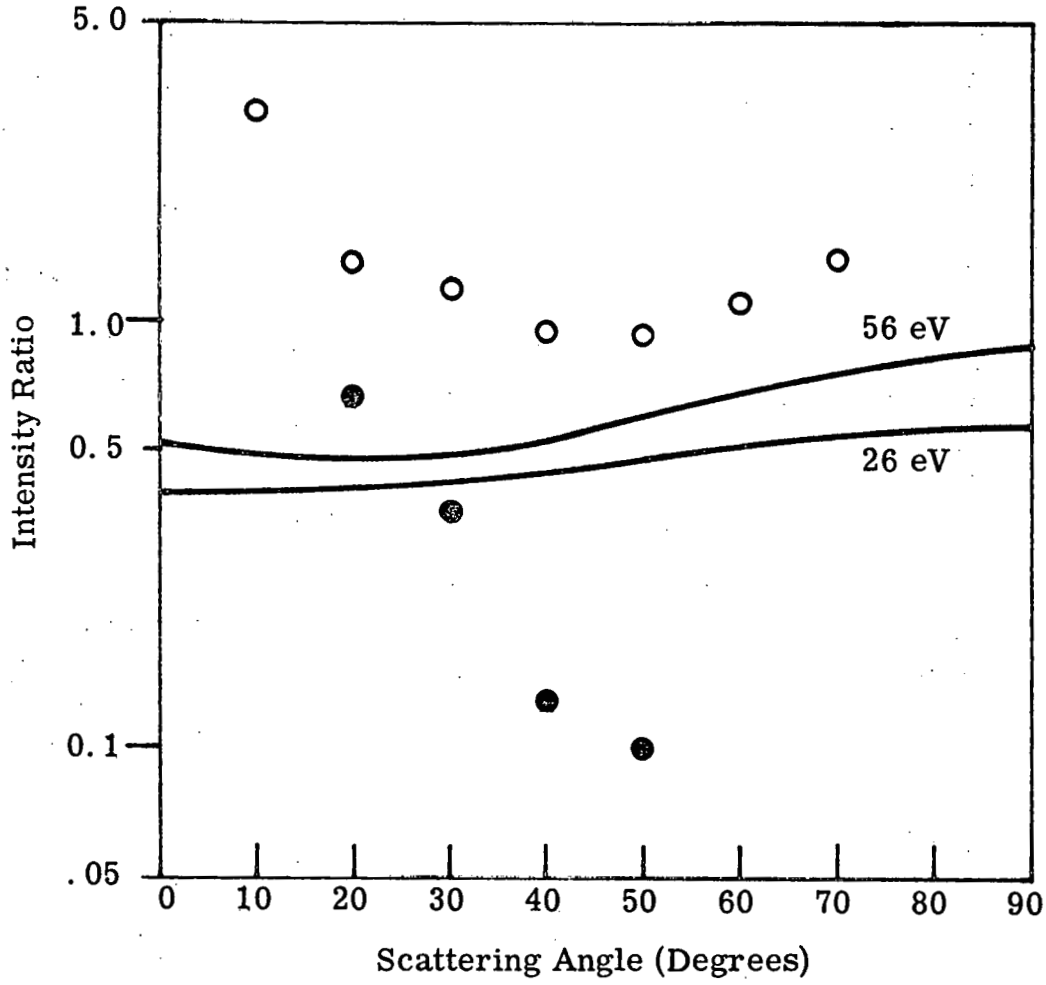

Figure 5.2-16. Ratio of intensity of the $1^1S \rightarrow 2^3S$ transition to that of the $1^1S \rightarrow 2^3P$ transition for helium. The solid lines are derived from the calculations of reference (66) at E_o = 26 eV and 56 eV. The present results are given at E_o = 26.5 eV (open circles) and 55.5 eV (filled circles). The error in the data can be obtained from figures 5.2-3, -6.

5.2.4. Further Discussion

As mentioned earlier, our primary concern is to use electron scattering data to determine the nature of a given transition (i.e., to determine whether it is spin- and/or symmetry-forbidden) for cases in which this information may not be available from optical studies. From our present understanding of the scattering process (refer to section 3), it is expected that the angular distribution of electrons scattered after causing optically forbidden transitions will be quite different from that of electrons causing allowed ones. These differences can be enhanced by studying the DCS ratios (rather than the DCS themselves) as a function of angle. (Further, such a study eliminates one source of experimental error, the angle dependent volume correction.)

Indeed, the DCS ratios given in figures 5.2-3, -4, -5, and -6 show such characteristic differences. The most generally consistent behavior, at all energies studied, is that of the $2^3P/2^1P$ DCS ratio (spin-forbidden only/ optically allowed). In all cases, it increases by about two orders of magnitude from $\theta = 0°$ to 70°. The variation of the $2^3S/2^1P$ DCS ratio (spin- and symmetry-forbidden/allowed) is less uniform with changes in the incident energy. Generally, this ratio increases with increasing angles, reaching a maximum which shifts to higher angles at lower incident energies. Its maximum increase over the 0° to 70° angular range is usually significantly less than that of the $2^3P/2^1P$ ratio. Finally, the $2^1S/2^1P$ DCS ratio (symmetry-forbidden only/allowed) generally decreases with

increasing angle, reaching a broad minimum at about 40°, and thereafter increases. Silverman and Lassettre[15] have reported that the $2^1S/2^1P$ DCS ratio increases by a factor of about 10 from $\theta = 3.8°$ to $\theta = 15.3°$ at an incident energy of 500 eV. It is interesting to note that at intermediate energies (34 eV to 56 eV), this ratio decreases over the same angular range but that at 26.5 eV it increases sharply from $\theta = 0°$ to about 6° and thereafter decreases. This same effect is noted in the $2^3S/2^1P$ DCS ratio at this energy, but not in the $2^3P/2^1P$ one.

In addition to the characteristic variation of these triplet/singlet ratios with angle, they exhibit a dependence on incident energy which (in some cases) is to be expected from the considerations of section 3. As the incident energy is lowered toward threshold, spin-forbidden total cross sections are usually enhanced relative to spin allowed ones. We might expect the respective differential cross sections to vary in a similar way. Then, the triplet/singlet ratios should increase with decreasing energy more rapidly than the singlet/singlet one. This behavior is evident for $\theta = 0°$ from table 5.2-1. However, the magnitude of this effect is sensitive to the particular θ considered. Table 5.2-4 presents the ratios at $\theta = 40°$ for which the $2^3P/2^1P$ ratio is nearly constant. The enhancement with decreasing energy of the triplet/singlet ratios compared to the $2^1S/2^1P$ one is most evident in the region of low ($\theta \approx 0°$) and high ($\theta \approx 70°$) scattering angles.

TABLE 5.2-4

Peak intensity ratios in helium at $\theta = 40°$.

E_o (eV)	$2^3S/2^1P$	$2^1S/2^1P$	$2^3P/2^1P$
55.5	.050	.093	.40
44	.11	.059	.49
34	.19	.067	.40
(26.5)	.28	.40	.29*

* See reference (134).

The DCS themselves for the various transitions also show a number of interesting features. First, the 2^1S and 2^1P DCS are more sharply peaked forward than the 2^3S or 2^3P DCS (as expected). Second, as the incident energy is decreased the 2^1P and 2^3S DCS become more isotropic (recall section 3.4). The 2^3P DCS is relatively flat over a wide range of angles at all of these energies. Third, the behavior of the 2^1S DCS presents an interesting variation. At 55.5 eV it reaches a distinct minimum at about 40° while at 44 eV and 34 eV the minimum moves out to 50° and 60°, respectively, and apparently lies beyond 70° at 26.5 eV. This behavior is similar to the diffraction effects observed in both elastic and inelastic scattering from atoms[44g]. Qualitatively, the present effect can be explained as follows. Recall equation (3-114) of section 3 which relates the phase shifts η_ℓ to the angular dependence of the DCS. Suppose that $\eta_0 > \eta_1 > \eta_2 > \eta_3 >$ etc. as indicated by equation (3-117) and that $\eta_3 \cong \frac{\pi}{2}$ for a certain incident energy $\hbar^2k^2/2m$. In this case, the DCS $\sigma(k,\theta)$ will be dominated by the P_3 partial wave.

Hence,

$$\sigma(k,\theta) \simeq \text{const.} \{P_3(\cos\theta)\}^2 \quad ,$$

which has a minimum at $\theta = 40°$ (and 90°). This seems to correspond approximately to the 2^1S DCS of figure 5.2-8 at 55.5 eV. Now, suppose the incident energy is lowered. From (3-117) we expect all of the η_ℓ's to decrease. In particular, η_2 may decrease to $\simeq \frac{\pi}{2}$. Thus, at this lower impact energy

$$\sigma(k',\theta) \cong \text{const}\{P_2(\cos\theta)\}^2 \quad ,$$

which has a minimum at $\theta = 55°$. From a comparison of figures 5.2-11 and -12, this case would correspond to an incident energy intermediate between 44 eV and 34 eV. In a similar way, as the impact energy is lowered further, the first η_ℓ to reach $\sim\frac{\pi}{2}$ corresponds to a lower ℓ value and the minimum is expected to move toward larger angles. As an illustrative example, the 2^1S DCS at 55.5 eV (fig. 5.2-8) has been compared with $\{P_3(\cos\theta)\}^2$ in figure 5.2-17. Of course, partial waves other than P_3 contribute to the DCS, but the general agreement in shape is noteworthy.

Finally, the behavior of the 2^1P, 2^1S, and 2^3P DCS at 26.5 eV (fig. 5.2-13) for $\theta \lesssim 20°$ is unique in that these DCS appear to decrease markedly toward smaller angles. This effect is probably not due to a resonance, since none have been observed in this region[31,135], nor can it be explained by the preceding arguments.

5.3. Nitrogen

5.3.1. Introduction

In the excitation energy range from about 6 eV to 13 eV, N_2 exhibits a number of features which we can observe via electron impact. Table 5.3-1 lists the optical excitation energies for some of these transitions and the energy-losses at which we observe them. Notice that our values agree quite well with the optical ones.

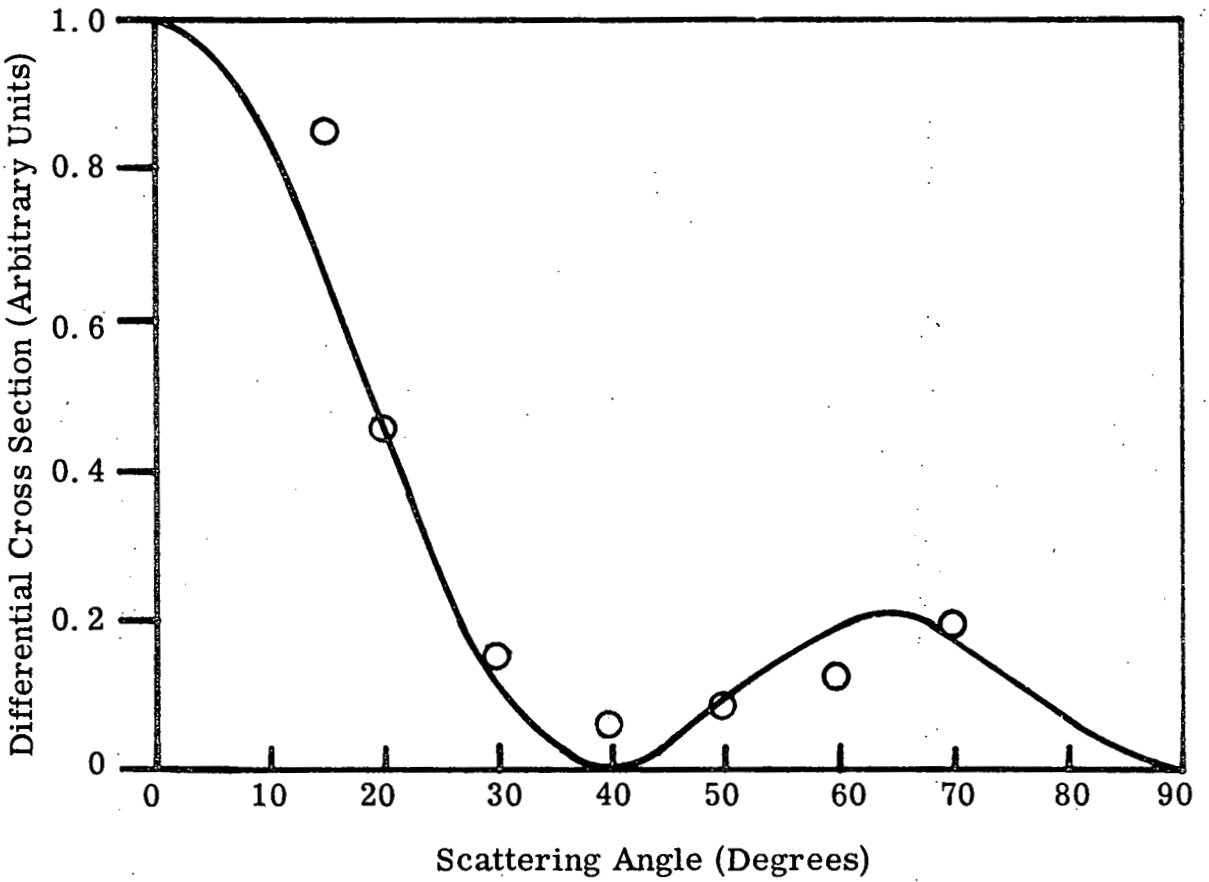

Figure 5.2-17. Comparison of the measured $1^1S \rightarrow 2^1S$ DCS of helium at E_o = 55.5 eV (circles) with $|P_3(\cos\theta)|^2$ (solid line). The data have been normalized to the arbitrary value of .45 at $\theta = 20°$.

TABLE 5.3-1

Transitions from the $X^1\Sigma^+$ (ν = o) ground electronic and vibrational state of N_2 to various electronic and vibrational states in the range from 6 eV to 13.3 eV. The column labelled UES contains the upper electronic state designation, the one labelled UVS lists the upper vibrational state, OPT. EE is the optical excitation energy, and OBS.EE is the excitation energy (energy-loss) observed in the present work.

UES[a]	UVS	OPT. EE[b] (eV)	OBS. EE[c] (eV)
$A^3\Sigma_u^+$	0	6.17	-
	1	6.35	-
	2	6.52	6.50
	3	6.69	6.71
	4	6.86	6.84
	5	7.02	7.02
	6	7.18	7.19
$B^3\Pi_g$	0	7.35	7.36
	1	7.56	7.57
	2	7.77	7.77
	3	7.98	7.97
	4	8.18	8.17
	5	8.38	8.37
$a^1\Pi_g$	0	8.55	8.56
	1	8.76	8.77
	2	8.96	8.97
	3	9.16	9.16
	4	9.35	9.35
	5	9.55	9.54
	6	9.74	9.73
	7	9.92	9.91
	8	10.10	10.09
	9	10.28	10.30
	10	10.46	10.48
$C^3\Pi_u$	0	11.03	11.03
	1	11.28	11.29
	2	11.52	11.51

TABLE 5.3-1 (continued

UES[a]	UVS	OPT. EE[b] (eV)	OBS. EE[c] (eV)
$(E\,^3\Sigma_g^+)$[d]	0	11.87	11.87
$(^1\Sigma_g^+)$[e]	0	-	12.26
$b\,^1\Pi_u$	0	12.58	
	1	12.66	
	2	12.75	
	3	12.84	
	4	12.93	(12.92)[f]
$p'\,^1\Sigma_u^+$	0	12.93	
	1	13.20	(13.21)[g]

[a] State designations are taken from reference (2b) pp 551-553, except as indicated.

[b] Calculated from the data of (a) above.

[c] The observed excitation energies from this research are believed to be accurate to $\pm .01_5$ eV in most cases. The given energy-losses were determined from scans in which the feature was most clearly observed (i. e., low angles for the singlets and high ones for the triplets).

[d] This state is listed in (a) above as E. Our use of this assignment is discussed in the text.

[e] This state is not listed in (a) above. Its assignment is discussed in the text.

[f] The vibrational features are not resolved in our spectra. The peak we observe should correspond nearly to $\nu' = 4$.

TABLE 5.3-1 (continued)

[g] The vibrational structure is not resolved in our spectra. The peak position at 13.18 eV should correspond with the $\nu' = 1$ level although there may be contributions from several other states. See reference (39).

The transition from the $X^1\Sigma_g^+$ ground state of N_2 to the $b^1\Pi_u$ state is the first optically allowed one. Transitions to the lower lying states are forbidden by symmetry ($g \not\to g$, e.g., $a^1\Pi_g$, $^1\Sigma_g^+$), electron spin multiplicity ($1 \not\to 3$, e.g., $A^3\Sigma_u^+$, $C^3\Pi_u$) or both (e.g., $B^3\Pi_g$, $E^3\Sigma_g^+$). Excitation of the $p'\ ^1\Sigma_u$ (or $b^1\Pi_u$) state is electric-dipole allowed while transitions to the symmetry forbidden states are electric-quadrupole allowed. Gilmore[136] has summarized the potential energy curves for most of these states.

The electron-impact excitation of N_2 has been studied at both low and high angles at a number of incident energies. All of the electronic states of table 5.3-1 have been observed by previous investigators although the assignment of the $E^3\Sigma_g^+$ one has been in question.

Lassettre and Krasnow[16] investigated the change with scattering angle (0° to 15°) of the unresolved $X^1\Sigma_g^+ \to a^1\Pi_g$ (Lyman-Birge-Hopfield) transition at 500 eV. They found that the ratio of the DCS for excitation of the $a^1\Pi_g$ state to that of the $b^1\Pi_u$ one varied from about .05 at $\theta = 4°$ to 0.3 at $\theta = 10°$. Later these studies were extended[17c] to lower energies (60 eV) and higher resolution but at low angles ($\theta \lesssim 2.5°$). Recently, Skerbele, et al.[22a] reported high resolution spectra of N_2 at 50 eV and 36 eV ($\theta \approx 0$ to 12°). In this case, transitions to all of the electronic states of table 5.3-1 were observed although singlet → triplet transitions were a minor part of the overall spectrum.

Heideman, et al.[29] obtained energy-loss spectra for $\theta = 0°$ at incident energies of 15.7 eV and 35 eV. Neither the A nor B states were observed at either energy while the C state was evident at the lower one. Transitions to the other electronic states in table 5.3-1 could be seen at both energies.

Doering and Williams[36c] have presented lower resolution energy-loss spectra at impact energies down to 16.1 eV for $\theta = 90°$. As expected, the singlet → triplet transitions comprise a major part of the N_2 spectrum under these conditions. No vibrational structure was resolved, but transitions to the $B^3\Pi_g$, $a^1\Pi_g$, $C^3\Pi_u$, and $b^1\Pi_u$ states were evident.

The N_2 excitation spectrum has also been studied by Brongersma and Oosterhoff[11] and Compton, et al.[13] using a trapped-electron technique. Although the reported spectra of these authors are similar in appearance, their state assignments are quite different. This is probably the result of an energy calibration error in the results of Compton, et al.[13]. Brongersma[11] was able to verify the identity of the B state by resolving its vibrational structure. It is interesting to note that these threshold studies do not reveal excitations to the A or C states but are dominated by transitions to the B and E ones (all four of these states are triplets).

5.3.2. Results and Discussion

Figures 5.3-1 and -2 show energy-loss spectra of nitrogen taken at an impact energy of 40 eV (uncalibrated) and scattering angles of $\theta = 20°$ and $80°$, respectively. The low angle spectrum

Figure 5.3-1. Energy-loss spectrum of N_2. E_o = 40 eV, $I_o = 2 \times 10^{-8}$ A, $\theta = 20°$, SR = .01 V/sec, TC = .5 sec, $P = 1 \times 10^{-3}$ torr.

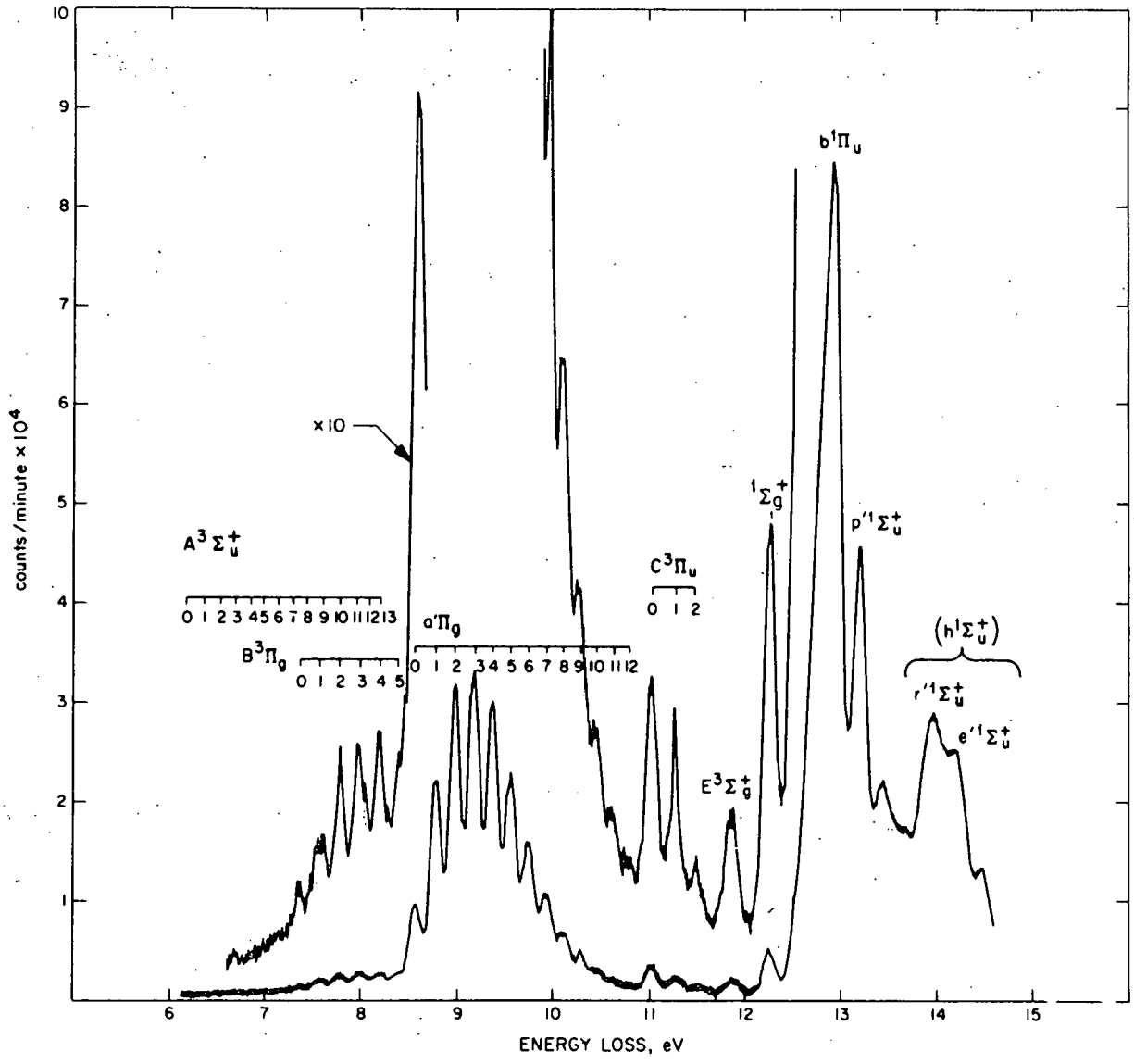
counts / minute x 10^4
ENERGY LOSS, eV
×10
A³Σu+
B³Πg
a'Πg
C³Πu
E³Σg+
¹Σg+
b¹Πu
p'¹Σu+
(h¹Σu+)
r'¹Σu+
e'¹Σu+

Figure 5.3-2. Energy-loss spectrum of N_2. E_o = 40 eV, $I_o = 2 \times 10^{-8}$ A, $\theta = 80°$, SR = .002 V/sec, TC = 10 sec, $P = 1 \times 10^{-3}$ torr.

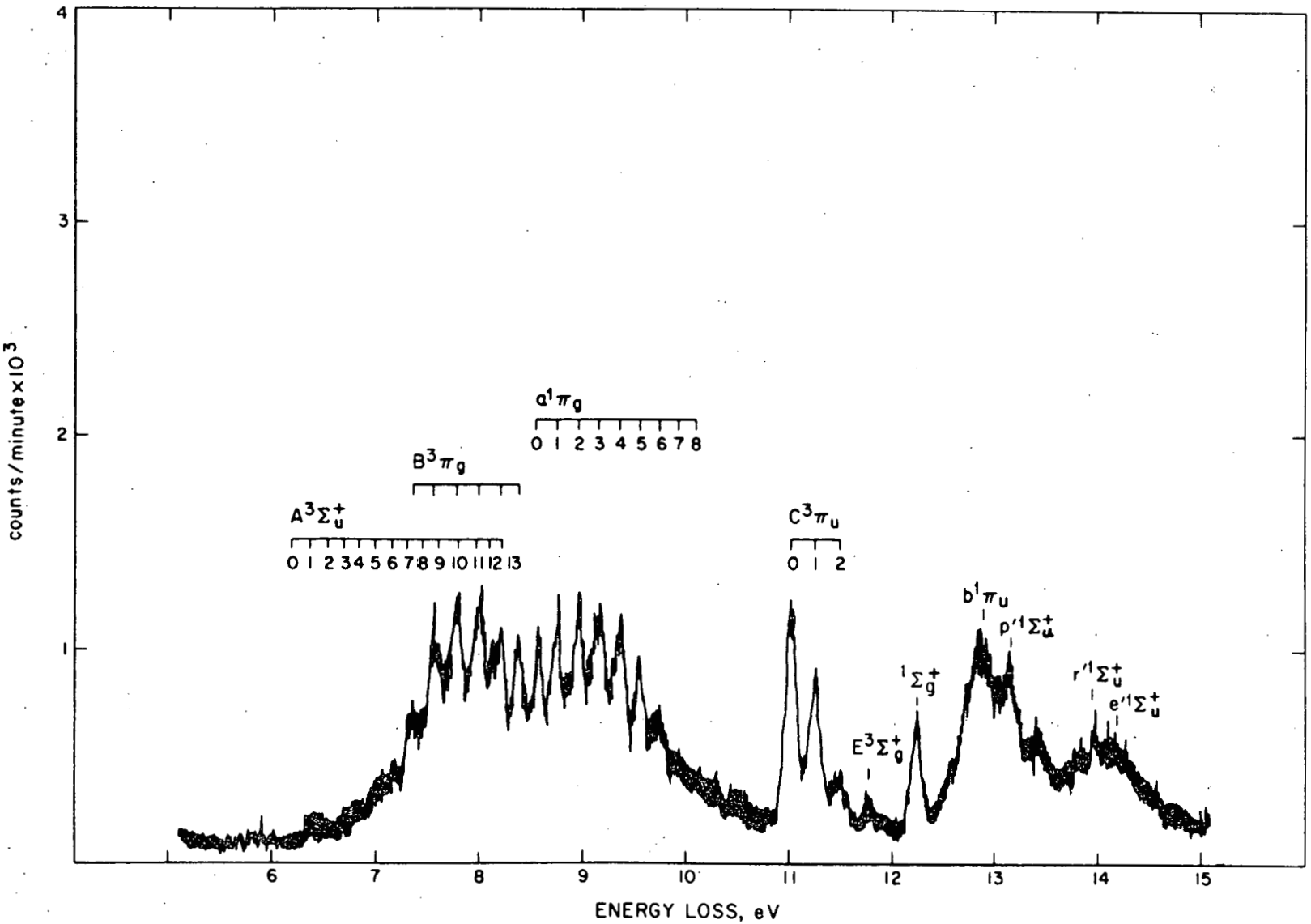
counts/minute×10³
4
3
2
1
6
7
8
9
10
11
12
13
14
15
ENERGY LOSS, eV
a¹πg
0 1 2 3 4 5 6 7 8
B³πg
A³Σu+
0 1 2 3 4 5 6 7 8 9 10 11 12 13
C³πu
0 1 2
E³Σg+
¹Σg+
b¹πu
p'¹Σu+
r'¹Σu+
e'¹Σu+

agrees with that of reference (22a) (although our resolution is not as good) while the high angle one is similar to the one of reference (36c) except that our resolution is much better. Figure 5.3-3 shows a separate scan at $\theta = 80°$ of the energy-loss region from about 6 eV to 11.5 eV. In this figure, transitions to several of the $A^3\Sigma_u^+$ vibrational levels can be weakly observed.

It is of interest to first consider the validity of the Franck-Condon factor considerations discussed in section 3.3.7.1. If they are valid, we expect the relative vibrational peak intensities (after application of the suitable correction, see section 3.3.7.1) to be (1) independent of incident energy, (2) independent of scattering angle, and (3) in accord with the results from optical measurements and reliable calculations. The $C^3\Pi_u$ state is a good "test" case since its vibrational levels are well resolved and the electronic band itself is relatively isolated. Table 5.3-2 summarizes the relative intensity data obtained in this research as well as the calculations of Benesch, et al.[137]. The error limits in the table are calculated according to equation (5-2). They do not contain a possible systematic error due to the background correction. Since the base line was determined below 6 eV, a rising background in the vicinity of 11 eV would increase the measured relative intensities. This effect would be most severe for the smallest peak, i.e., the $\nu' = 2$ one. Within the errors of this determination there is no change with scattering angle and the overall average is in reasonable agreement with the calculations[137] without the use of $C^{ED}_{\nu\nu 0}$. The

Figure 5.3-3. Energy-loss spectrum of N_2 (6 eV to 9.5 eV). E_o = 35 eV, $I_o = 3 \times 10^{-8}$ A, $\theta = 80°$, SR = .002 V/sec, TC = 10 sec, $P = 2 \times 10^{-3}$ torr.

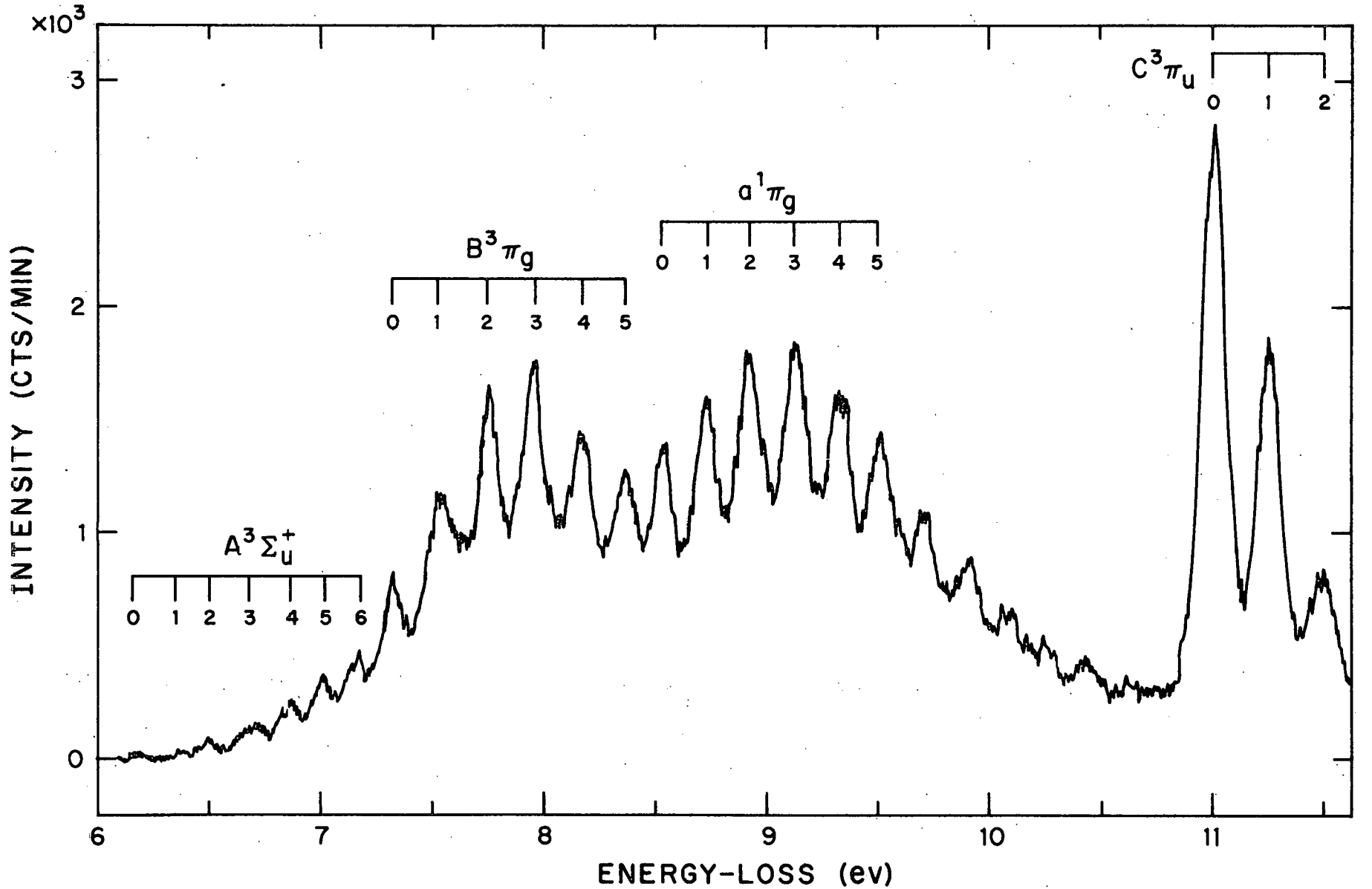
×10³
3
2
1
0
INTENSITY (CTS/MIN)
A³Σu⁺
0 1 2 3 4 5 6
B³πg
0 1 2 3 4 5
a¹πg
0 1 2 3 4 5
C³πu
0 1 2
6
7
8
9
10
11
ENERGY-LOSS (ev)

TABLE 5.3-2

Relative intensity distribution of the $X^1\Sigma_g^+(\nu = o) \rightarrow C^3\Pi_u$ ($\nu' = 0,1,2$) transitions of N_2. The incident energy is 25 eV. The $\nu' = 0$ peak intensity is normalized to 1.00. Columns 2 and 3 contain the relative peak intensities. Columns 5 and 6 contain the factor indicated in equation (3-74) (section 3.3.7.1).

Scattering Angle (degrees)	ν' 1	ν' 2	Number of Scans	C_{10}^{ED}	C_{20}^{ED}
10	.61 ± .05	.21 ± .04	4	1.028	1.056
20	.62 ± .04	.21 ± .04	4	1.008	1.016
30	.60 ± .04	.20 ± .02	5	.997	.994
40	.59 ± .04	.22 ± .03	4	.991	.983
50	.66 ± .07	.22 ± .03	4	.989	.978
60	.68 ± .03	.24 ± .03	4	.987	.974
70	.64 ± .03	.27 ± .03	4	.986	.972
80	.68 ± .04	.27 ± .02	6	.985	.970
Average over all angles	.63 ± .03	.23 ± .02	35	.996	.993
Calculated values[a]	.558	.193			

[a] Reference (137).

precision in the measurements is not sufficient to determine whether the small trend ($\sim 4\%$) in angle, predicted by equation (3-74), is correct. If anything, this trend seems opposite to that indicated (possibly) by the data (i.e., dividing the relative intensities by C_{10}^{ED} or C_{20}^{ED} would enhance the slight deviation with angle rather than decrease it). Since the relative intensity of the $\nu' = 2$ peak is only $\sim 10\%$ larger than the calculated value, the background problem mentioned above is apparently not significant (assuming the reliability of the calculation[137]).

A similar determination was performed for an impact energy of 35 eV. An average of 28 scans at angles from 10° to 80° yielded a $\nu' = 1$ relative intensity of $0.60 \pm .03$ and a $\nu' = 2$ relative intensity of $0.21 \pm .03$. Notice that the relative intensities are also independent of incident energy (at least in this 25 - 35 eV energy range).

The relative vibrational intensities within the $a^1\Pi_g$ band have been measured by other investigators at $\theta = 0°$. We cannot reliably measure these intensities at large angles because of the overlapping $B^3\Pi_g$ state. However, six low-angle scans ($\theta \lesssim 15°$) were used to determine the relative intensities summarized in table 5.3-3. The agreement with the calculated values is quite good, except possibly for $\nu' = 0$. The $\nu' = 9$ and 10 relative intensities of this research are in better agreement with theory than those of reference (17c), presumably because the background problem encountered in that work was not evident in ours. There is an

TABLE 5.3-3

Intensity distribution in the $a^1\Pi_g$ band of N_2. The $X^1\Sigma_g^+(\nu = o) \rightarrow a^1\Pi_g(\nu' = 3)$ transition intensity is normalized to 1. $C^{DQ}_{\nu'3}$ has been calculated for an incident energy of 25 eV.

		Incident Energy (eV)				
ν'	$C^{DQ}_{\nu'3}$	400[a]	60[a]	35[b]	25 (This Research)	Calcd.[c]
0	1.019	.37 ± .03	.28 ± .02	.28	.27 ± .02	.235
1	1.012	.68 ± .04	.63 ± .05	.69	.64 ± .04	.630
2	1.006	.96 ± .07	.91 ± .03	.93	.93 ± .05	.932
3	1.00	1.00	1.00	1.00	1.00	1.00
4	.994	.83 ± .04	.85 ± .04	.84	.86 ± .03	.873
5	.998	.66 ± .01	.61 ± .05	.65	.62 ± .04	.664
6	.981	.48 ± .03	.42 ± .03	.45	.45 ± .03	.453
7	.975	.37 ± .02	.26 ± .03	.30	.28 ± .03	.287
8	.970	.27 ± .04	.17 ± .01	.22	.19 ± .02	.172
9	.965	.18 ± .01	.11 ± .01	-	.097 ± .008	.097
10	.959	.12 ± .01	(.07)	-	.04 ± .01	.054

[a] Reference (17c).

[b] Derived from the spectra of reference (29).

[c] Reference (137).

optically determined[138] set of relative intensities with which the data of table 5.3-3 can also be compared, but the relative precision of the optical measurements is too low for a meaningful comparison[139]. Again, the precision of the data is not sufficient to test the predictions of equation (3-73). The C_{03}^{DQ} value, although greater than unity, is not nearly large enough to lower the relative intensity of the $\nu' = 0$ peak by the required 10% (if this value is to agree with the calculations of reference (137)).

As mentioned in section 2, the only doubtful state assignment in this energy-loss region is that of the E one (at 11.87 eV). The state at 12.26 eV seems clearly to be a $^1\Sigma_g^+$ one[18] while the one at 11.87 eV may be either a $^1\Sigma_g^+$ (references (17a, 19)) or $^3\Sigma_g^+$ (reference (29)). Meyer and Lassettre[17a] and Lassettre, et al.[17c] argue for the former (singlet) assignment primarily because they observe it at an impact energy of 400 eV. Heideman, et al.[29] prefer the latter assignment since the $\theta = 0°$ excitation function of this state is sharply peaked near threshold--a behavior indicative of a singlet → triplet transition. This disagreement can be resolved by comparing the relative angular dependencies of the DCS for excitation of the 11.87 eV and 12.26 eV states. Figure 5.3-4 shows the peak intensity ratios of the $E^3\Sigma_g^+$ (11.87 eV), $^1\Sigma_g^+$ (12.26 eV), $p'^1\Sigma_u$ (13.21 eV) and $C^3\Pi_u$ (11.03) excitations with respect to the $b^1\Pi_u$ (12.92 eV) one as a function of scattering angle from $\theta = -30°$ to $+80°$ for $E_o = 35$ eV (uncalibrated). The $C^3\Pi_u$ intensity is the sum of the $\nu' = 0$, 1, and 2 vibrational level peak intensities while the

Figure 5.3-4. Ratios of intensities of the $X^1\Sigma_g^+ \rightarrow E^3\Sigma_g^+$ (11.87 eV), ■; $^1\Sigma_g^+$ (12.26 eV), ○; $C^3\Pi_u$ (11.03 eV), △; and $p'^1\Sigma_u^+$ (13.21 eV), □ transitions to that of the $b^1\Pi_u$ (12.92 eV) one in N_2 as a function of scattering angle. E_o = 35 eV. Peak intensities were used for the E, $^1\Sigma_g^+$, p', and b states while the sum of the $\nu' = 0, 1, 2$ vibrational level peak intensities was used for the C state. Each data point is an average of three to four scans at each angle. For clarity, only a few representative error bars are shown.

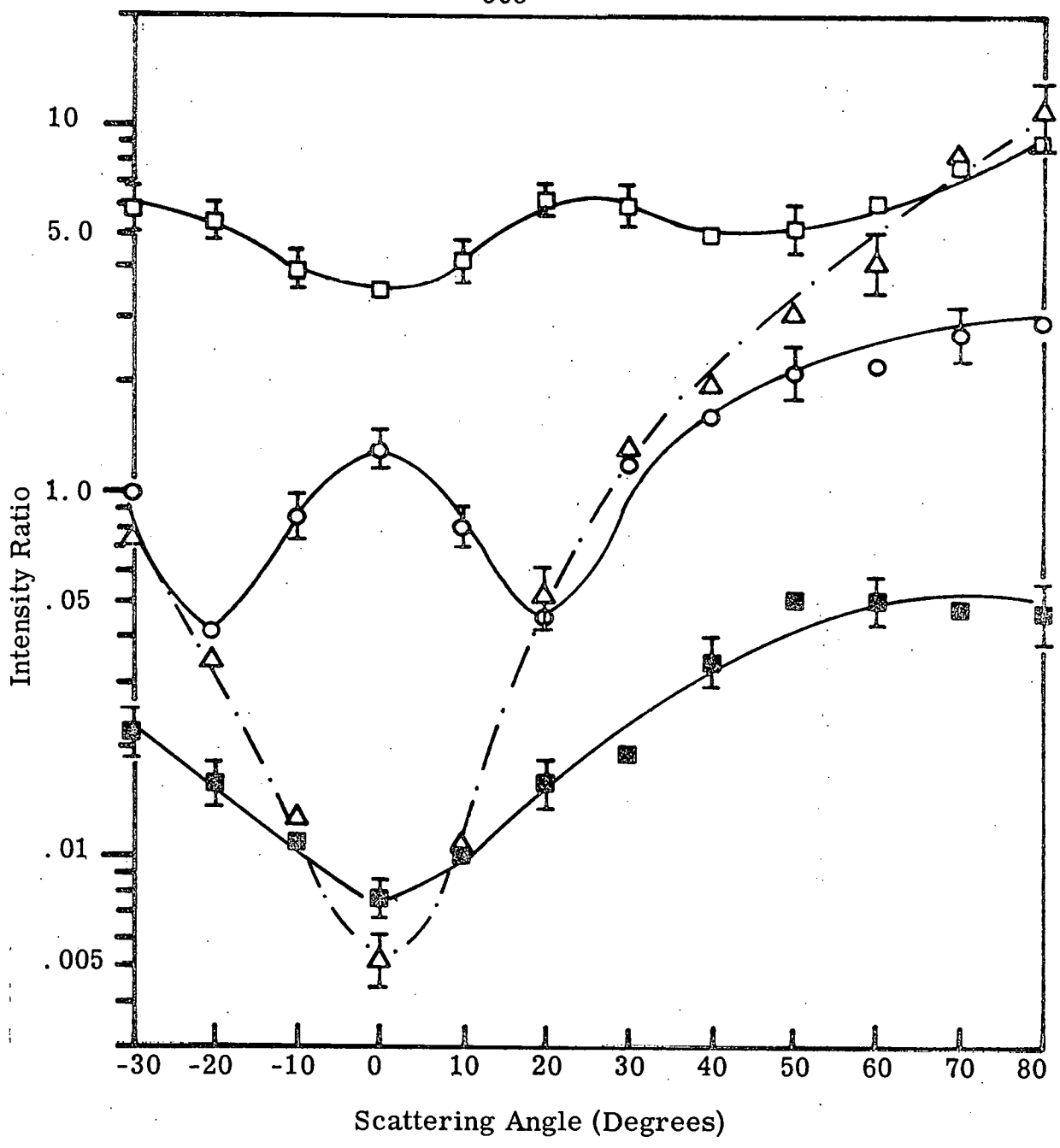
10
5.0
1.0
.05
.01
.005
Intensity Ratio
-30
-20
-10
0
10
20
30
40
50
60
70
80
Scattering Angle (Degrees)

intensity of the others are measured at their respective peaks. This figure clearly shows the expected symmetry of these ratios about $\theta = 0°$ (see section 4.4.3.2). Since the relative intensities of the vibrational levels within a given electronic band seem to be independent of angle (or incident energy), these ratios are equal to the "true" DCS ratios times a constant (independent of angle but dependent upon resolution). Of prime importance is the fact that the variation with θ of these plotted ratios is the same as that of the "true" DCS ratios. It is clear that the triplet/singlet ratios behave with θ as we expect (qualitatively) from theory and agree with our observations in helium.

The X → b transition in N_2 and the $1^1S \rightarrow 2^1P$ transition in helium are similar in that the change in orbital angular momentum ($\Delta\Lambda$) is 1 while the change in spin angular momentum (ΔS) is 0. Likewise, the X → C (N_2) and $1^1S \rightarrow 2^3P$ (He) transitions have $\Delta\Lambda = 1$ and $\Delta S = 1$. Thus, we might expect the C/b (N_2) and $2^3P/2^1P$ (He) ratios to behave in a similar manner with angle for impact energies which are higher than their corresponding threshold energies by about the same amount. A comparison of figure 5.3-4 (the incident energy is ~ 24 eV above threshold) and figure 5.2-4 (of section 5.2) shows this to be the case. In an analogous way, we expect the $^1\Sigma_g^+$ (12.26 eV)/b and $2^1S/2^1P$ ratios to exhibit similar behavior with θ. This also is evident in the comparison of these two figures. Finally, the assignment of the 11.87 eV transition as $E^3\Sigma_g^+$ is completely consistent with the similarity in the behavior of the $2^3S/2^1P$ and $E^3\Sigma_g^+$ (11.87)/b ratios ($\Delta\Lambda = 0$, $\Delta S = 1$ for both upper

states). Even if these somewhat qualitative comparisons are not convincing, it is clear from figure 5.3-4 that the 11.87 eV and 12.26 eV transitions are fundamentally different. Further, the assignment of the 11.87 eV transition as a singlet would be entirely inconsistent with our understanding of the way in which singlet/singlet and triplet/singlet ratios differ with θ. The results obtained for the isoelectronic molecule CO (see section 5.4) provide an additional justification for assigning the 11.87 eV state as a triplet.

Figure 5.3-5 shows the same peak intensity ratios of figure 5.3-4 for a lower impact energy (25 eV, uncalibrated). Note that both the E/b and C/b ratios increase by about the same amount relative to the $^1\Sigma_g^+$/b ratio. This also indicates the singlet → triplet nature of the 11.87 eV transition.

Figure 5.3-6 shows the p' $^1\Sigma_u^+$ (peak)/b $^1\Pi_u$ (peak), B $^3\Pi_g$ (ν' = 4)/b $^1\Pi_u$, and a $^1\Pi_g$ (ν' = 3)/b $^1\Pi_u$ ratios as a function of θ at 40 eV (uncalibrated). The B/b ratio behavior is nearly identical to that of the C/b one. Since the X → B and X → C transitions have $\Delta\Lambda = 1$ and $\Delta S = 1$ in common but different "even-odd" symmetries (i.e., X → B is g → g while X → C is g → u), this similarity may indicate that the latter distinction is less important in determining the angular dependence of the DCS than the former ones. However, this does not seem to be the case when $\Delta S = 0$. The $^1\Sigma_g^+$/b and p' $^1\Sigma_u^+$/b ratios both oscillate between 0° and 80° but with opposite initial slopes. Also, the a/b ratio oscillates with nearly the same frequency and phase as the p'/b one but with a larger amplitude. Note that the

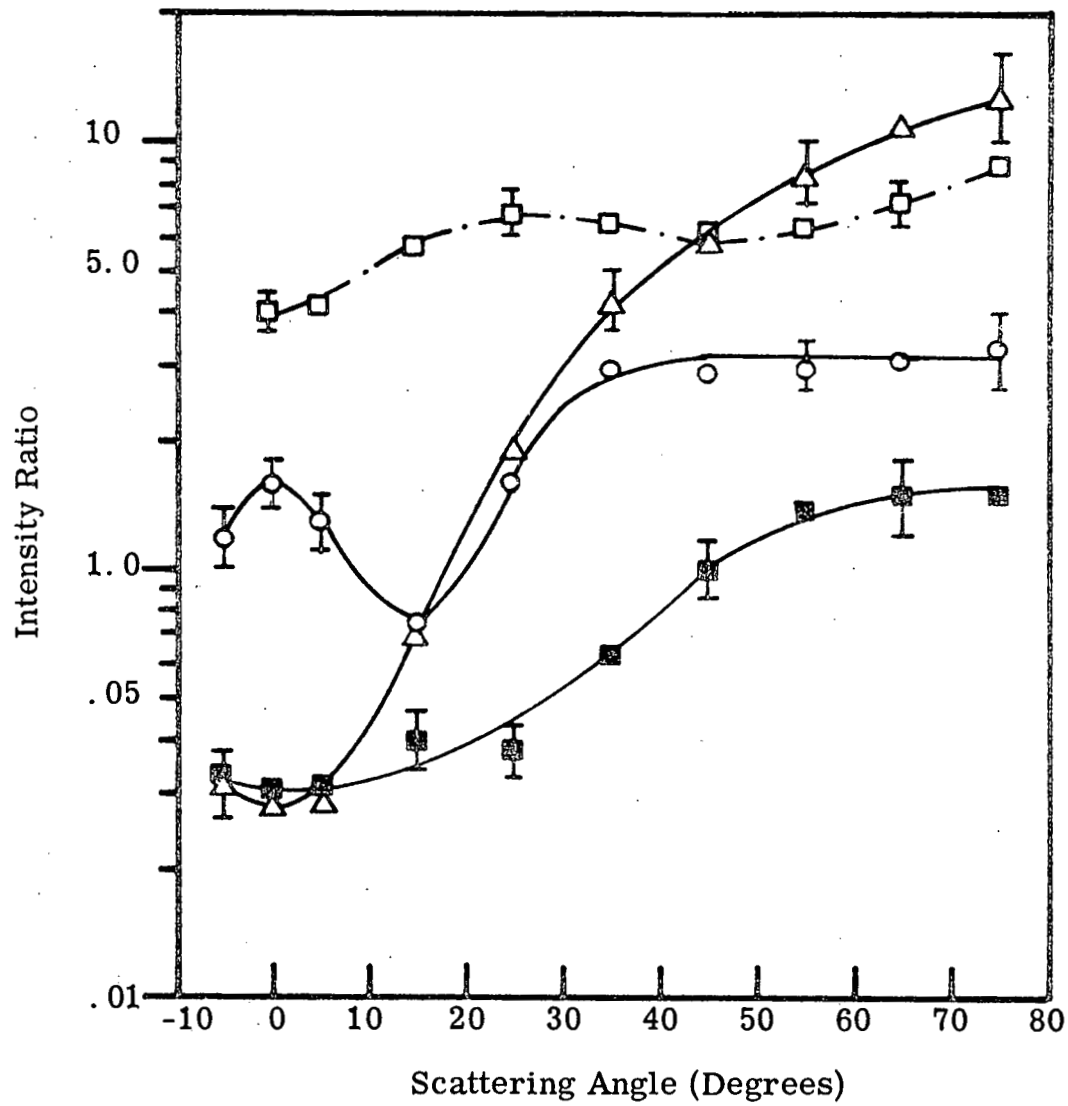

Figure 5.3-5. Ratios of intensities of the $X^1\Sigma_g^+ - E^3\Sigma_g^+$, ■; $^1\Sigma_g^+$, ○; $C^3\Pi_u$, △; and $p'^1\Sigma_u^+$, □ transitions to that of the $b^1\Pi_u$ one in N_2 (see the caption of fig. 5.3-4). E_o = 25 eV. Each data point is an average of four to six scans (as listed in table 5.3-2).

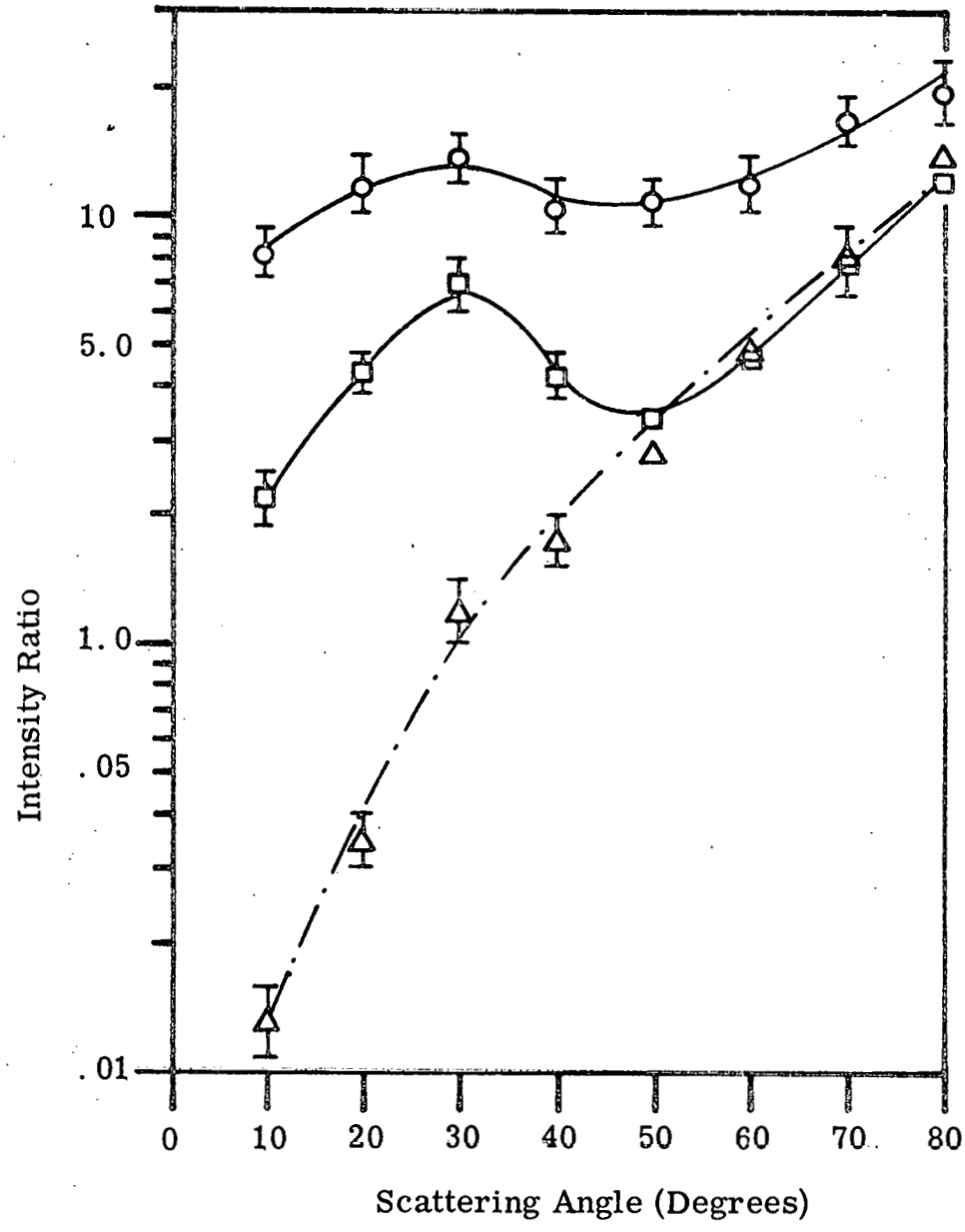

Figure 5.3-6. Ratios of intensities of the $X^1\Sigma_g^+ \rightarrow B^3\Pi_g$ ($\nu' = 4$), △; $a^1\Pi_g$ ($\nu' = 3$), □; and $p'^1\Sigma_u^+$ (peak), ○ transitions with respect to that of the $b^1\Pi_u$(peak) one in N_2. E_o = 40 eV. Each data point is an average of three scans.

$X \rightarrow p'$ and $X \rightarrow a$ transitions are $g \rightarrow u$, $\Delta\Lambda = 0$, $\Delta S = 0$ and $g \rightarrow g$, $\Delta\Lambda = 1$, $\Delta S = 0$, respectively, while the $X \rightarrow {}^1\Sigma_g^+$ one is $g \rightarrow g, \Delta\Lambda = 0, \Delta S = 0$.

Figure 5.3-7 contains the DCS (in arbitrary units) for the transitions in figure 5.3-4 (35 eV) while figure 5.3-8 presents them for the transitions in figure 5.3-6 (40 eV). Notice that as expected all of the singlet DCS are more sharply peaked forward than any of the triplet ones.

These DCS cannot be placed on an absolute scale primarily because there is no absolute determination of $Q^T_{b\,{}^1\Pi_u}(E)$ with which the $Q^{Arb}_{b\,{}^1\Pi_u}(E)$ can be normalized for E less than about 100 eV[140]. Also, the lack of equal vibrational resolution of the various electronic bands (i.e., the vibrational structure of the $a\,{}^1\Pi_g$ state is resolved while that of the $b\,{}^1\Pi_u$ one is not) complicates the relation of peak intensity ratios to DCS ratios. The first difficulty could be overcome by using a mixture of He and N_2 (of known concentration) in the scattering chamber. The N_2 DCS could then be determined using He as a standard.

5.4. Carbon Monoxide

5.4.1. Introduction

CO is isoelectronic with N_2 and as expected exhibits a somewhat similar energy-loss spectrum under electron impact. Table 5.4-1 summarizes the electronic and vibrational transitions we can observe below an excitation energy of about 12 eV. Transitions from the $X\,{}^1\Sigma^+$ ground state to the $a\,{}^3\Pi$ and $b\,{}^3\Sigma^+$ states are spin-forbidden

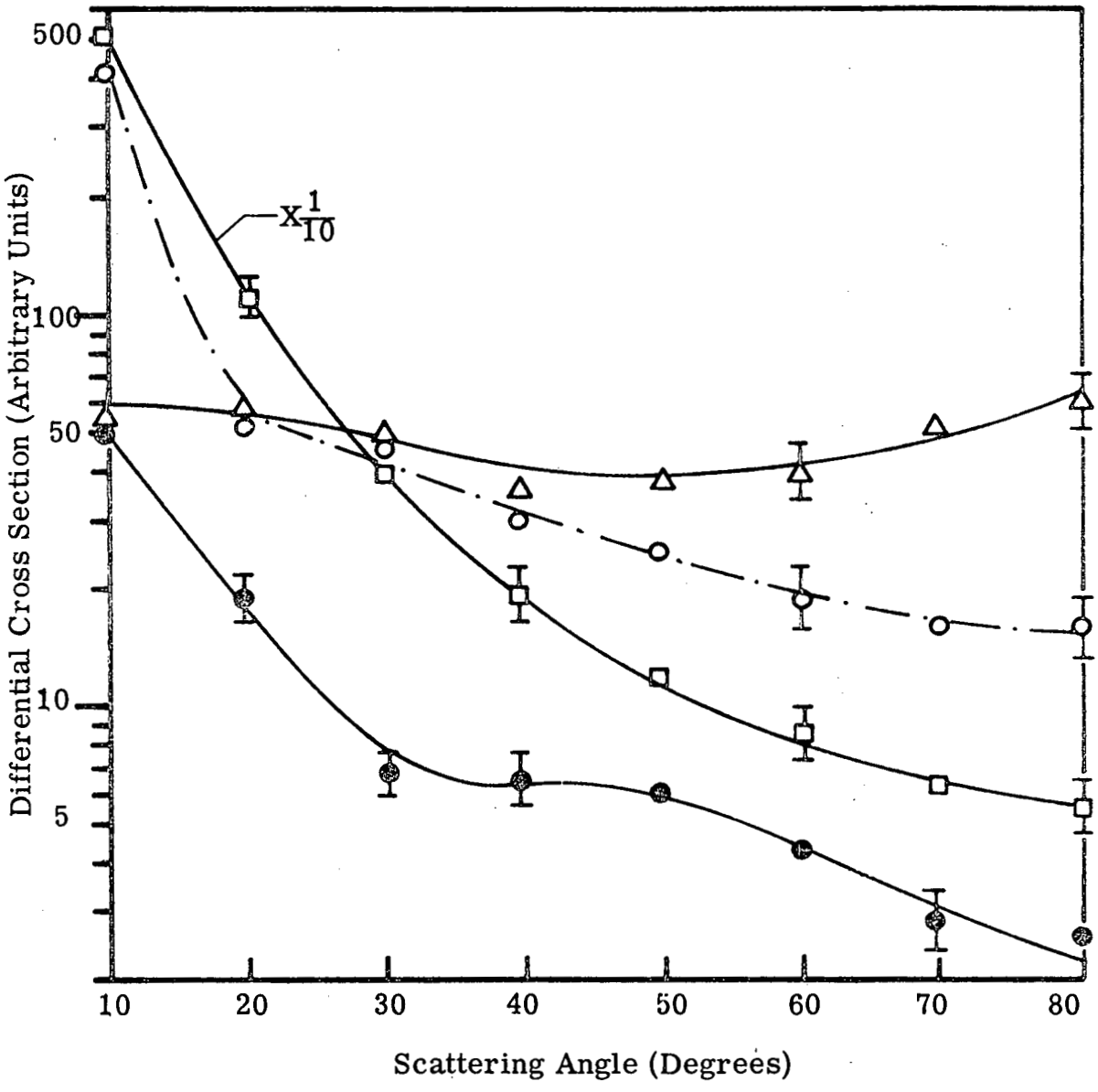

Figure 5.3-7. Differential cross section (arbitrary units) for excitation of the $E\,^3\Sigma_g^+$, ●; $^1\Sigma_g^+$, ○; $C\,^3\Pi_u$, △; and $b\,^1\Pi_u$, □ states in N_2. E_o = 35 eV. For clarity, only a few representative error bars are shown.

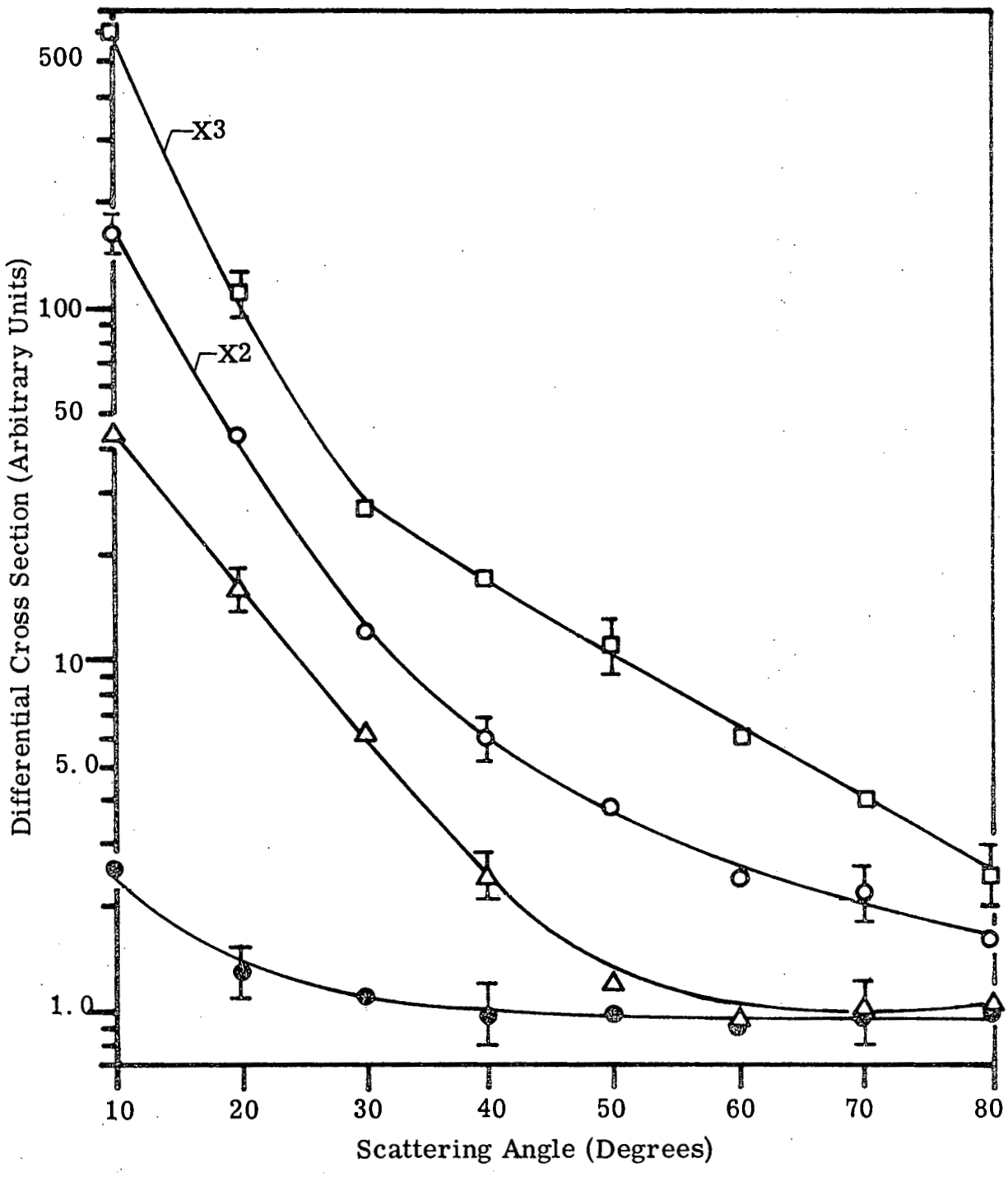

Figure 5.3-8. Differential cross section (arbitrary units) for excitation of the $B^3\Pi_g(\nu' = 4)$, ●; $a^1\Pi_g(\nu' = 3)$, △; $p'^1\Sigma_u^+$, ○; and $b^1\Pi_u$, □ states in N_2. E_o = 40 eV.

TABLE 5.4-1

Transitions from the $X^1\Sigma^+$ ($\nu = 0$) ground state of CO to various electronic and vibrational states below 12 eV. The abbreviations are defined in table 5.3-1.

UES[a]	UVS	OPT. EE[b] (eV)	OBS. EE[c] (eV)
$a^3\Pi$	0	6.01	6.01
	1	6.22	6.22
	2	6.43	6.43
	3	6.63	6.64
	4	6.84	6.85
$A^1\Pi$	0	8.03	8.03
	1	8.21	8.21
	2	8.39	8.39
	3	8.56	8.57
	4	8.74	8.73
	5	8.90	8.90
	6	9.06	9.07
	7	9.22	-
$b^3\Sigma^+$	0	10.39	10.40
	1	10.67	-
	2	10.94	-
$B^1\Sigma^+$	0	10.78	10.77
	1	11.03	11.03
	2	11.29	-
$C^1\Sigma^+$	0	11.40	11.40
	1	11.66	
$(E^1\Pi)$[d]	0	11.52	(11.50)[e]
	1	11.78	

[a] State designations are from reference (2b), pp 520-522.

[b] Calculated from the data of reference (a) above.

[c] The values are believed to be accurate to about ± .01 eV.

[d] This state designation is given by S. G. Tilford, J. T. Vanderslice,

TABLE 5.4-1 (continued)

and P. G. Wilkinson, Can. J. Phys., 43, 450 (1965).

[e] Observed as a shoulder on the $C^1\Sigma^+$ ($\nu' = 0$) peak.

while all other transitions in table 5.4-1 are optically allowed. Potential energy curves for these states and a summary of available optical data on CO can be found in the review of Krupenie[141].

The electron-impact excitation spectrum of CO was first obtained by Schulz[9a] using the trapped-electron technique. Transitions to the $a^3\Pi$ state (Cameron bands) were the most intense feature in his spectrum. Brongersma and Oosterhoff[11], with an improvement of this same technique, were able to resolve some vibrational structure in the $a^3\Pi$ state. Transitions to the $A^1\Pi$ state were not observed while those to the $B^1\Sigma^+$ and $b^3\Sigma^+$ ones were relatively intense.

Lassettre and coworkers[142] first studied the X → A transition in the energy-loss spectrum of CO at an incident energy of 500 eV and $\theta \leq 15°$. Lassettre and Silverman[143] expanded this study to the angular dependence of the X → B and X → C transitions ($\theta \lesssim 15°$). In a later publication[144] they compared the envelope shape of the unresolved X → A transition with theoretically calculated Franck-Condon factors. The agreement was quite good. Meyer, et al.[21] were able to resolve the X → A vibrational structure with an improved spectrometer. They again compared the relative intensities within this band to calculated Franck-Condon factors. However, noticeable discrepancies were found for higher vibrational levels. This led them to suggest that the intensity distributions within the $A^1\Pi$ band might be energy-dependent, approaching the calculated values at higher (> 200 eV) impact energies. Skerbele,

et al.[145] reinvestigated the $A^1\Pi$ band at 200 eV and 400 eV incident energy ($\theta \lesssim 6°$). They found that the relative intensities of the vibrational levels were independent of angle but differed from calculated Franck-Condon values at higher ν'. Also a slight trend in the relative intensity distribution as a function of impact energy was noted.

Recently, Skerbele, et al.[22b] reported a high resolution study of CO at 50 eV impact energy in which excitations of the $a^3\Pi$ and $b^3\Sigma^+$ states were observed in addition to those of the $A^1\Pi$, $B^1\Sigma^+$, $C^1\Sigma^+$, $E^1\Pi$, and $F^1\Pi$ ones. The relative vibrational intensities within the $a^3\Pi$ band agreed well with the calculations of Nicholls[146].

5.4.2. Results and Discussion

Figures 5.4-1 and -2 show electron energy-loss spectra of CO at an impact energy of 25 eV (uncalibrated) and $\theta = 10°$ and 75°, respectively. Since the vibrational structure of both the $a^3\Pi$ and $A^1\Pi$ states is clearly resolved, we can compare the relative peak intensities within these bands with calculations[146] and the results of other investigators[21, 22b, 145]. Table 5.4-2 summarizes the results obtained at 25 eV and 35 eV for the $A^1\Pi$ band. Since we observed no angle dependence in the relative intensities (within the error of this data), all of the scans at each energy are averaged together. However, from equation (3-72) (section 3.3.7.1), we would expect a rather significant difference in the distribution of relative intensities at $\theta = 0°$ from those at $\theta = 80°$. In particular

Figure 5.4-1. Energy-loss spectrum of CO. E_o = 25 eV, $I_o = 1 \times 10^{-8}$ A, $\theta = 10°$, S.R. = .01 V/sec, TC = 1 sec, $P = 2 \times 10^{-3}$ torr.

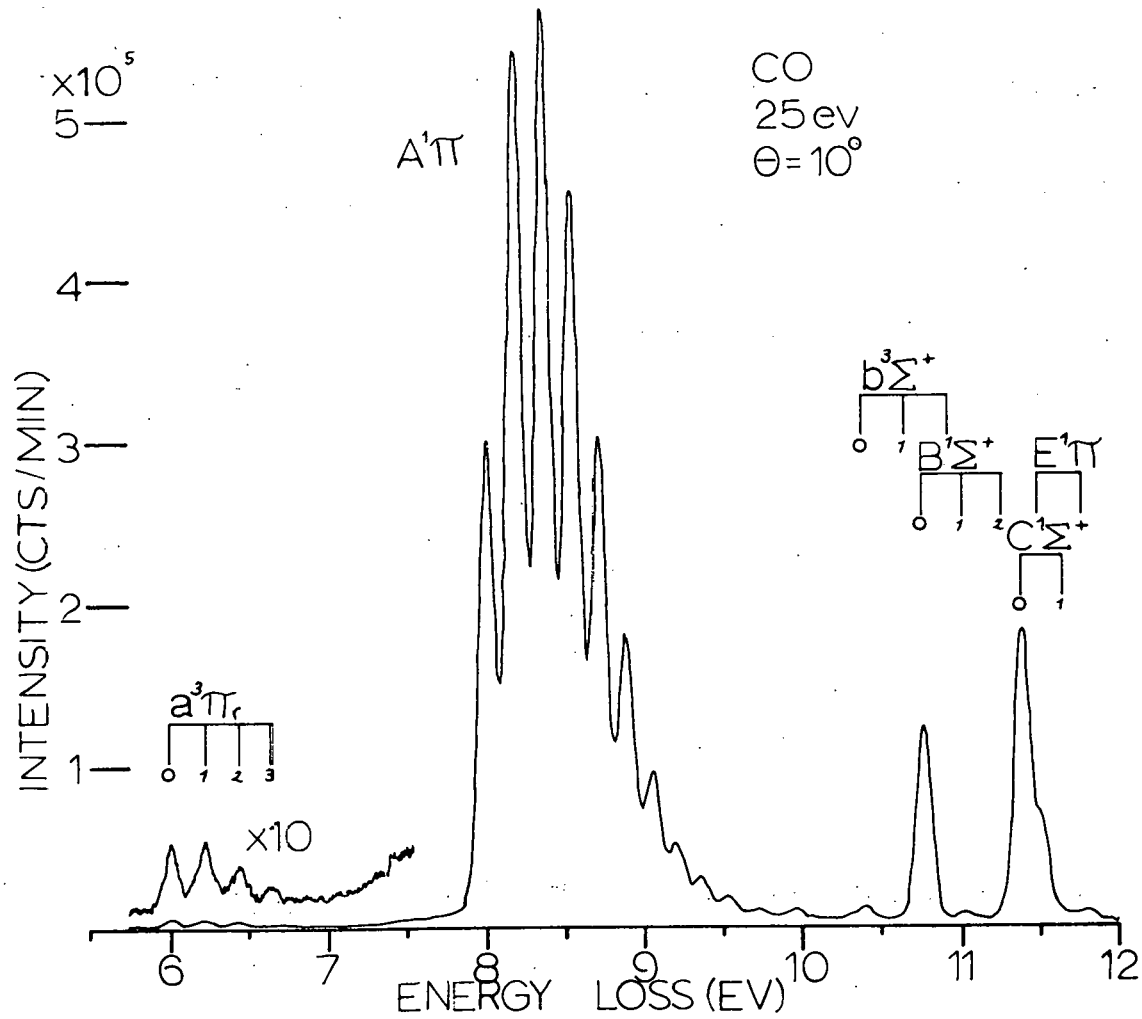
CO
25 ev
θ = 10°
A¹Π
b³Σ⁺
B¹Σ⁺
E¹Π
C¹Σ⁺
a³Π
x10
x10⁵
INTENSITY (CTS/MIN)
ENERGY LOSS (EV)

Figure 5.4-2. Energy-loss spectrum of CO. E_o = 25 eV, $I_o = 1 \times 10^{-8}$ A, $\theta = 75°$, S.R. = .002 V/sec, TC = 10 sec, $P = 2 \times 10^{-3}$ torr.

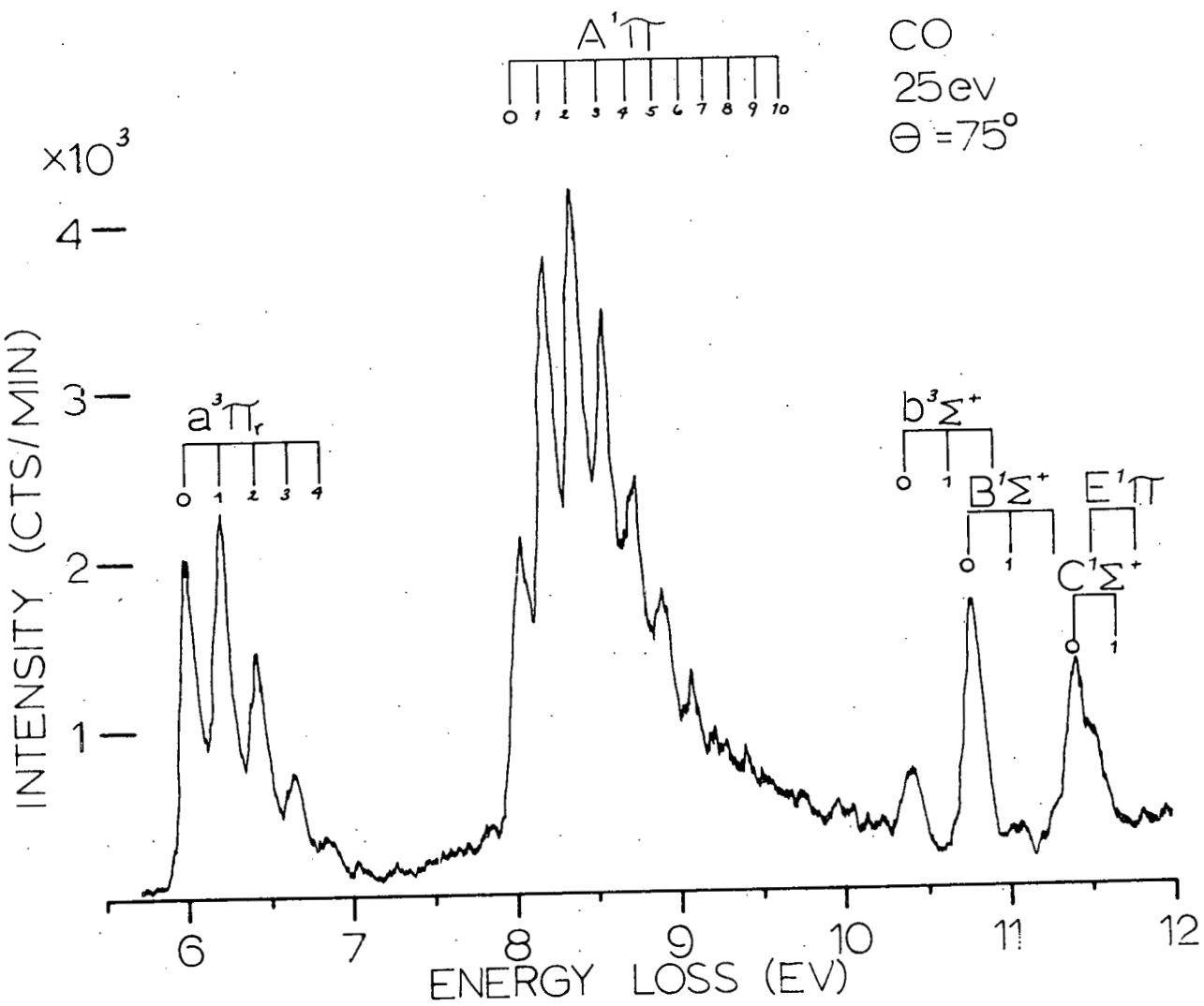
A¹Π
0 1 2 3 4 5 6 7 8 9 10
CO
25ev
Θ = 75°
×10³
4
3
2
1
INTENSITY (CTS/MIN)
a³Π_r
0 1 2 3 4
b³Σ⁺
0 1
B¹Σ⁺
0 1
E¹Π
C¹Σ⁺
0 1
6
7
8
9
10
11
12
ENERGY LOSS (EV)

TABLE 5.4-2

Relative vibrational intensity distribution in the $A^1\Pi$ band of CO. The $X^1\Sigma^+$ ($\nu = 0$) → $A^1\Pi$($\nu' = 2$) transition intensity is normalized to 1.

ν'	Incident Energy (eV)					Calculations[f]
	400[a]	200[b]	50[c]	35[d]	25[e]	
0	.44 ± .02	.45 ± .02	.55	.48 ± .02	.51 ± .02	.492
1	.87 ± .02	.89 ± .02	.94	.95 ± .03	.94 ± .02	.940
2	1.00	1.00	1.00	1.00	1.00	1.00
3	.83 ± .03	.88 ± .02	.80	.81 ± .04	.78 ± .03	.788
4	.56 ± .03	.62 ± .02	.52	.54 ± .03	.52 ± .03	.517
5	.34 ± .01	.39 ± .02	.32	.34 ± .04	.31 ± .02	.299
6	.20 ± .01	.24 ± .02	.17	-	.16 ± .02	.159

[a] Reference (145).

[b] Reference (21).

[c] Derived from the spectrum of reference (22b).

[d] This research, average of 8 scans.

[e] This research, average of 11 scans.

[f] Reference (146).

equation (3-72) predicts that, at $\theta = 0°$

$$C_{02}^{DD} = 1.092 \text{ and } C_{62}^{DD} = .857 \text{ while at } \theta = 80°$$

$$C_{02}^{DD} = 1.005 \text{ and } C_{62}^{DD} = .991.$$

The fact that the angular resolution is only about 2° will not change these numbers (to 3 significant digits). Although the data do not indicate the trend predicted by equation (3-72), their precision is barely adequate for a valid comparison. It is interesting to note that the low-energy data of this research and reference (22b) agree much better with the calculations than do the high-energy data[21, 145]. ($C_{\nu 2}^{DD}$ is essentially 1.00 under the high-energy conditions.)

Table 5.4-3 presents the relative intensities with the $a^3\Pi$ band. The "correction" factor predicted by equation (3-74) is not shown since it exhibits even less deviation from 1.00 than that predicted for the $C^3\Pi_u$ state of N_2. Again, the relative intensities were independent of angle and the average is presented in the table. It is noteworthy that the agreement of these relative intensities with calculations[146] is good even for impact energies within .05 eV of threshold (trapped-electron results[11]). To make equation (3-74) consistent with the trapped-electron method, q^2 and q_0^2 must be integrated over all angles before dividing them. This yields a vibrational level peak intensity ratio of

$$R_{\nu 0}^{\nu} = \breve{C}_{\nu\nu 0} \frac{G_{00}^{n\nu}}{G_{00}^{n\nu 0}} \qquad (5\text{-}13)$$

TABLE 5.4-3

Relative vibrational peak intensities in the $a^3\Pi$ (Cameron) band of CO. The $X^1\Sigma^+$ ($\nu = 0$) → $a^3\Pi$ ($\nu' = 1$) transition intensity is normalized to 1.

ν'	Incident Energy (eV)				Calculations[e]
	50[a]	Threshold[b] (+.05 eV)	35[c]	25[d]	
0	.84 ± .03	$1._0$	.88 ± .07	.84 ± .04	.835
1	1.00	1.00	1.00	1.00	1.00
2	.74 ± .03	$.6_8$	.75 ± .10	.64 ± .04	.686
3	.39 ± .10	$.3_4$	.44 ± .12	.34 ± .04	.357
4	-	.2	-	.16 ± .02	.158

[a] Reference (22b).

[b] Derived from the trapped-electron spectrum of reference (11) without an overlap correction.

[c] This research, average of angles from 0° to 75°, 8 scans.

[d] This research, average of angles from 0° to 80°, 15 scans.

[e] Reference (146).

where

$$\tilde{C}_{\nu\nu o} = \frac{k_\nu (k^2 + k_\nu^2)}{k_{\nu o}(k_o^2 + k_{\nu o}^2)} \quad ,$$

k^2 is proportional to the incident energy which excites the ν^{th} vibration, and k_o^2 is proportional to that for the νo^{th} one. However, each peak in the excitation spectrum of reference (11) corresponds approximately to the same electron energy after the scattering event. Thus, with $k_\nu = k_{\nu o} \equiv \lambda$, $\tilde{C}$ of equation (5-13) becomes

$$\tilde{C}_{\nu\nu o} \cong \frac{k^2 + \lambda^2}{k_o^2 + \lambda^2} \quad . \tag{5-14}$$

Since $\frac{\hbar^2\lambda^2}{2m}$ is approximately .05 eV while $\frac{\hbar^2 k_o^2}{2m}$ and $\frac{\hbar^2 k^2}{2m}$ are ~ 6 eV,

$$\tilde{C}_{\nu\nu o} \cong \frac{k^2}{k_o^2} \cong \frac{W_\nu}{W_{\nu o}} \quad . \tag{5-15}$$

Consequently, the high-energy form of the Ochkur approximation predicts only a ~10% distortion in the relative peak intensities at threshold. (Of course, it is very doubtful that this set of approximations has any validity whatsoever at threshold.)

Figures 5.4-3 and -4 show the relative angular dependence of the DCS for excitation of the $a^3\Pi(\nu' = 0 + 1 + 2)$, $b^3\Sigma^+(\nu' = 0)$, $B^1\Sigma^+(\nu' = 0)$, and $C^1\Sigma^+(\nu' = 0)$ states with respect to that of the $A^1\Pi(\nu' = 0 + 1 + 2)$ one at incident energies of 35 eV and 25 eV, respectively. The a/A intensity ratio is quite characteristic of a

Figure 5.4-3. Ratios of intensities of the $X^1\Sigma^+(\nu = 0) \rightarrow C^1\Sigma^+$ ($\nu' = 0$), curve (a); $B^1\Sigma^+$ ($\nu' = 0$), curve (b); $a^3\Pi(\nu' = 0,1,2)$, curve (c); and $b^3\Sigma^+$ ($\nu' = 0$), curve (d) transitions to that of the $X \rightarrow A^1\Pi$ ($\nu' = 0,1,2$) one in CO. $E_o = 35$ eV. Each data point is an average of three to four scans at each angle.

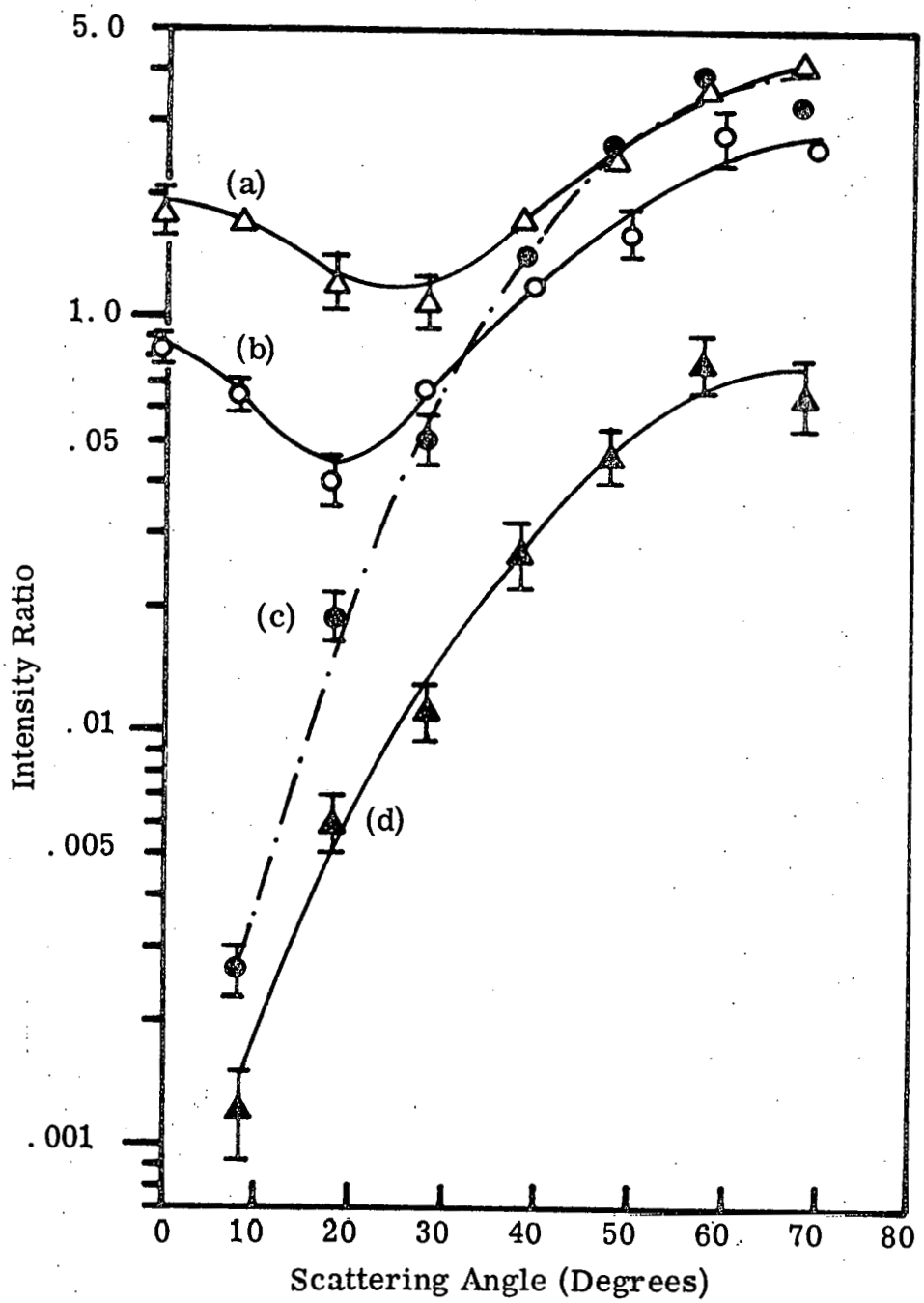
5.0
1.0
.05
.01
.005
.001
Intensity Ratio
(a)
(b)
(c)
(d)
0
10
20
30
40
50
60
70
80
Scattering Angle (Degrees)

Figure 5.4-4. Ratios of intensities as defined in figure 5.4-3. E_o = 25 eV. Each data point is an average of four scans at each angle.

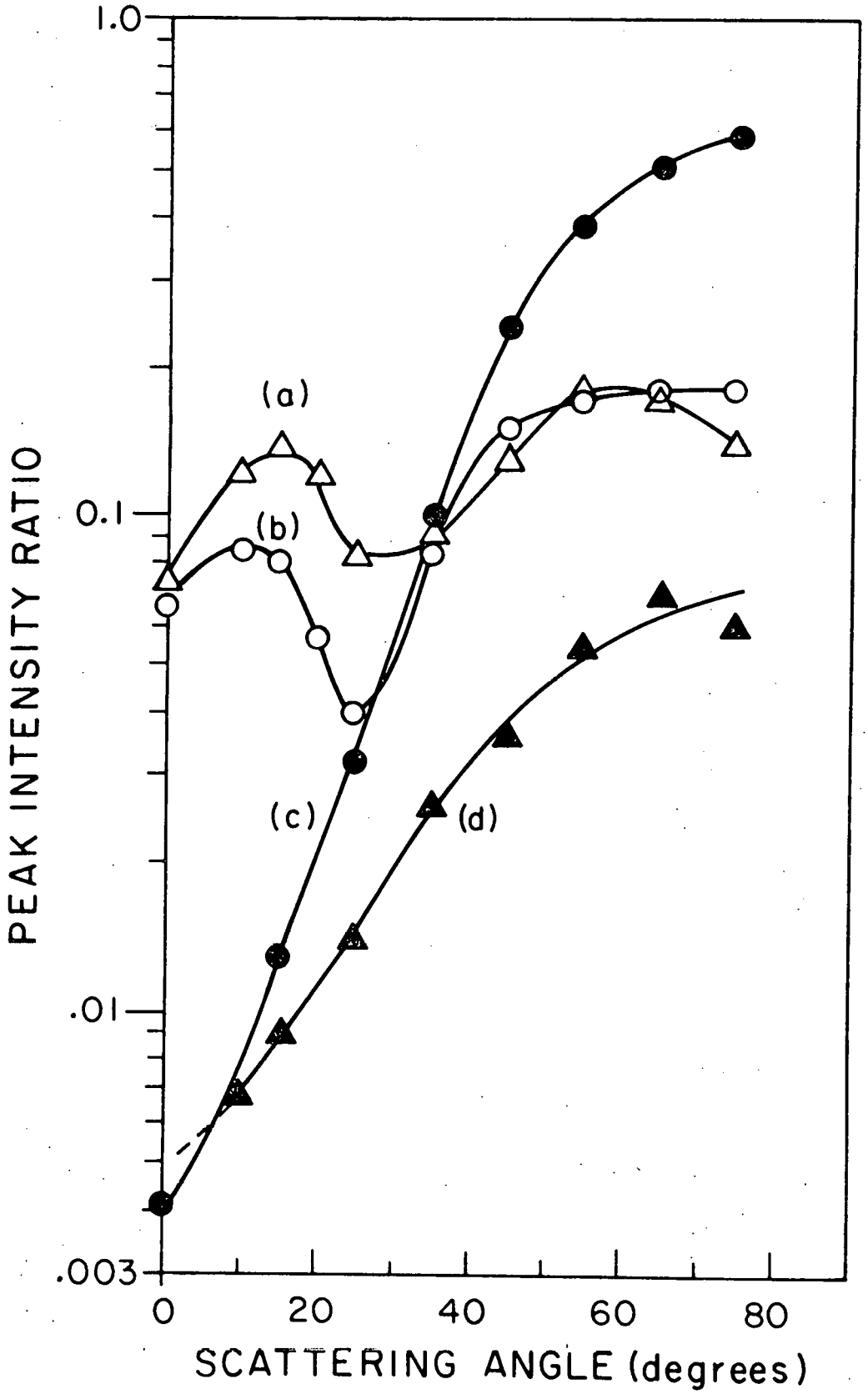
1.0
0.1
.01
.003
PEAK INTENSITY RATIO
(a)
(b)
(c)
(d)
0
20
40
60
80
SCATTERING ANGLE (degrees)

(singlet → triplet)/(singlet → singlet) ratio as evidenced by the $2^3P/2^1P$ ratio of helium and the $B^3\Pi_g/b^1\Pi_u$ and $C^3\Pi_u/b^1\Pi_u$ ratios of N_2. Also the b/A intensity ratio is quite similar to the $E^3\Sigma_g^+/b^1\Pi_u$ one of N_2 and the $2^3S/2^1P$ ratio of helium. This striking similarity with the E/b ratio of N_2 provides an additional confirmation of the triplet designation of that E state. The B/A and C/A intensity ratios exhibit a more complex behavior. At 35 eV they closely resemble the $^1\Sigma_g^+/b^1\Pi_u$ ratio of N_2 while at 25 eV they are more like the $a^1\Pi_g/b^1\Pi_u$ and $p'^1\Sigma_u^+/b^1\Pi_u$ ratios of N_2. In any case, they exhibit the oscillatory behavior which seems characteristic of ($\Delta S = 0$, $\Delta\Lambda = 0$, symmetry-forbidden)/($\Delta S = 0$, $\Delta\Lambda = 1$, allowed) intensity ratios.

Herzberg[2b] lists a $c^3\Sigma^+$ state with a 0 → 0 excitation energy of 11.415 eV. Also, Brongersma[11] observes a relatively intense feature at 11.42 eV in the threshold excitation spectrum. This transition is practically coincident with the $C^1\Sigma^+$ ($\nu' = 0$) transition (11.396 eV) which we observe and which may be responsible for the peak in reference (11). If excitation of the $c^3\Sigma^+$ state were important under our experimental conditions, we would expect the measured $C^1\Sigma^+/A^1\Pi$ ratio to increase abnormally (compared to the B/A ratio, for example) at larger scattering angles. This behavior is not evident in the data (figures 5.4-3 and -4). (A case in which a singlet → singlet transition intensity is distorted by an underlying singlet → triplet one is discussed in section 5.5).

Figure 5.4-5 gives the DCS at 25 eV(in arbitrary units) for the

Figure 5.4-5. Differential cross section (arbitrary units) for excitation of the $A^1\Pi(\nu' = 0, 1, 2)$, ○; $a^3\Pi$ $(\nu' = 0, 1, 2)$, ●; $b^3\Sigma^+$ $(\nu' = 0)$, △; and $B^1\Sigma^+$ $(\nu' = 0)$, □ states of CO. E_0 = 25 eV.

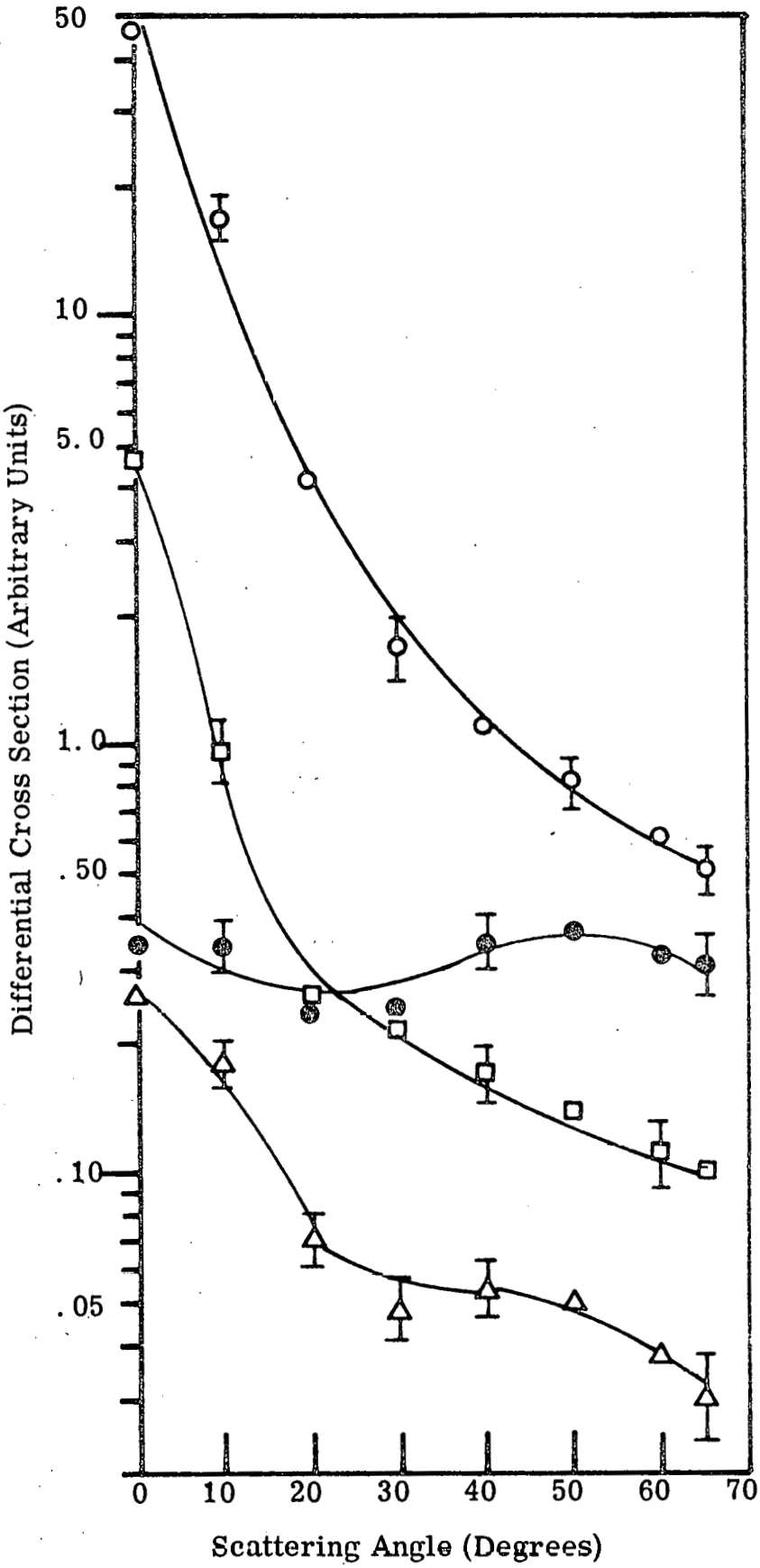
50
10
5.0
1.0
.50
.10
.05
Differential Cross Section (Arbitrary Units)
0
10
20
30
40
50
60
70
Scattering Angle (Degrees)

transitions of figure 5.4-4. The singlet DCS are sharply peaked forward while the $a^3\Pi$ DCS is relatively isotropic. The $b^3\Sigma^+$ DCS is quite similar to that of the $E^3\Sigma_g^+$ state of N_2. All of these comparisons are as expected.

5.5. Hydrogen

5.5.1. Introduction

H_2 has been exhaustively studied by optical methods (reference (2b), pp 530-32). Relatively few electron-impact studies of H_2 have been reported, although excitations from the $X^1\Sigma_g^+$ ground state to the $b^3\Sigma_u^+$, $B^1\Sigma_g^+$, $C^1\Pi_u$, $c^3\Pi_u$, and $D^1\Pi_u$ have been observed.

Schulz[149] used a trapped-electron technique to observe excitations to the $b^3\Sigma_u^+$ (repulsive) state and a second band, peaked at about 12 eV, which he assigned as X → B, C, D (singlets). In view of the recent high-resolution trapped-electron work of Dowell and Sharp[12], this 12 eV peak probably contained substantial contributions from the $c^3\Pi_u$ state.

Kuppermann and Raff[35a] observed transitions to $b^3\Sigma_u^+$ state as well as several of the unresolved singlets using a retarding field method of energy analysis and the collection of electrons scattered between $22° \leq \theta \leq 112°$ (with the $\theta = 90°$ direction being preferred). Lassettre and coworkers[147,148] have reported unresolved energy-loss spectra at impact energies from 300 eV to 500 eV and $0° < \theta < 5°$. No forbidden excitations were observed, nor was any vibrational structure in the B, C, D, etc. states resolved.

Kuyatt, et al.[150] and Heideman, et al.[30] were able to resolve many vibrational levels in the B, C, and D states at incident energies from 90 eV to 13.7 eV at $\theta \cong 0°$. They did not observe excitation of the $b^3\Sigma_u^+$ state. However, below about 30 eV, transitions to the $c^3\Pi_u$ and/or a $^3\Sigma_g^+$ state (unresolved) were noted.

At an incident energy of 25 KeV ($\theta \approx 0°$), Geiger[151] reported a well-resolved energy-loss spectrum of H_2. Transitions to the singlet states (B, C, and D) are clearly evident but no forbidden excitations were observed (nor are they expected to be at this high energy).

5.5.2. Results and Discussion

Our results on the exchange excitation of the lowest triplet state of H_2 ($b^3\Sigma_u^+$) are given in the attached preprint (appendix III). However, there are a number of additional aspects of this study which will be discussed below. (Figures 5.5-1 through -6 are in the attached preprint.) Table 5.5-1 gives the observed excitation energies of H_2 in the same format as used for N_2 and CO.

Since we were able to resolve several vibrational members of the $B^1\Sigma_u^+$ and $C^1\Pi_u$ states at 40 eV, it is of interest to compare the relative vibrational peak heights within each band to the Franck-Condon factor ratios as discussed in section 3.3.7.1. However, H_2 presents an extremely unfavorable case in which to obtain a meaningful comparison. As is evident from figures 5.5-1, -2, and -3, transitions from the $X^1\Sigma_g^+$ ground state to the $b^3\Sigma_u^+$ state overlap those to the $B^1\Sigma_u^+$, which in turn overlap those to the $C^1\Pi_u$ state.

TABLE 5.5-1

Excitation energies in H_2 for transitions from the $X^1\Sigma_g^+$ ($\nu = 0$) ground state. The abbreviations are defined in Table 5.3-1.

UES[a]	UVS	OPT. EE[b] (eV)	OBS. EE[c] (eV)
$b^3\Sigma_u^+$	(repulsive)	-	$10.0 \pm .2$[d]
$B^1\Sigma_u^+$	0	11.18	11.18
	1	11.34	11.35
	2	11.50	11.50
	3	11.66	11.65
	4	11.81	11.81
	5	11.96	11.95
	6	12.10	12.10
$C^1\Pi_u$	0	12.29	12.29
	1	12.58	12.58
	2	12.85	12.85
	3	13.10	13.10
	4	13.34	13.35
	5	13.56	13.55
$a^3\Sigma_g^+$	0	11.79	(11.80)[e]
	1	12.10	(12.08)
	2	12.40	
	3	12.68	
	4	12.94	
	5	13.19	
$c^3\Pi_u$	0	11.75	(11.80)
	1	12.04	(12.08)
	2	12.32	
	3	12.58	
	4	12.82	
	5	13.05	

[a] Reference (2b) pp. 530-32.

[b] Optical excitation energies for the $C^1\Pi_u$, $c^3\Pi_u$, and $a^3\Sigma_g^+$ are from table I of reference (12). Those for the $B^1\Sigma_u^+$ are from reference (154).

TABLE 5.5-1 (continued)

[c] This research. Accurate to within ± .01 eV except as indicated.

[d] Energy-loss corresponding to the peak intensity.

[e] Values in parentheses refer to excitations which were observed as abnormal increases in the $B^1\Sigma_u^+$ ($\nu' = 4, 6$) intensities.

In addition, transitions to the $a^3\Sigma_g^+$ and $c^3\Pi_u$ states overlap part of the $B^1\Sigma_u^+$ band and all of the $C^1\Pi_u$ one. Consequently, each particular peak height is proportional to the sum of a number of DCS, each one contributing an amount which depends on the resolution and scattering angle. It would require a resolution which is well beyond the present "state of the art" to separate all of these excitations.

The results discussed below are for an impact-energy of 40 eV (uncalibrated). This value is chosen because (1) our highest resolution (FWHM = .04 eV) data were obtained at this energy and (2) excitations to the a, b, and c triplet states, although observable, cause relatively little distortion of the strong X → B, C transitions. This latter condition is required if we are to make any meaningful Franck-Condon factor comparisons.

First, let us examine the relative peak intensities within the $C^1\Pi_u$ band. The intensity ratios should be related to the ratio of respective Franck-Condon factors according to equation (3-72) (Bethe-Born approximation). If the X → C (ν') peak intensities are determined relative to that of the X → C ($\nu' = 1$), the $C^{DD}_{\nu' 1}$ (of equation (3-72)) differs from unity by less than ~ 5% over the range of ν' we can measure. Since the relative precision of the data is only ~ 5-10%, $C^{DD}_{\nu' 1}$ will be neglected. The relative peak intensities were measured for scattering angles from $\theta = 0°$ to $\theta = 80°$. No change in relative intensity was noted (within the accuracy of these measurements). If the transitions to the triplet states (a, c) were

contributing significantly to the $C^1\Pi_u$ band intensity, we would expect some distortion of the relative intensity distribution in this band. Such affects would presumably become more noticeable at higher angles since the ratio of triplet to singlet DCS generally increases markedly with angle (see sections 5.2, 5.3, 5.4). The distortion of the $C^1\Pi_u$ (ν') relative intensities due to the incompletely resolved $B^1\Sigma_u^+$ vibrational peaks should be less dependent on angle since the $B^1\Sigma_u^+/C^1\Pi_u$ DCS ratio does not change much with this variable (see below).

Table 5.5-2 summarizes the average (over all θ's) relative intensities and presents as a comparison the high-energy data of Geiger[151] and the calculations of Hutchisson[152]. The agreement in all cases is quite good, with the exception of the $\nu' = 0$ relative intensity. This is to be expected since the $B^1\Sigma_u^+$ ($\nu' = 7$) level is practically coincident with the $C^1\Pi_u$ ($\nu' = 0$) one.

The measurement and interpretation of the relative vibrational intensity distribution within the $B^1\Sigma_u^+$ band is somewhat more complicated. From figure 5.5-3 it is quite clear that at $\theta = 80°$ the intensities of both the $\nu' = 4$ and 6 levels are strongly enhanced by the $a^3\Sigma_g^+$ ($\nu' = 0, 1$) and/or $c^3\Pi_u$ ($\nu' = 0, 1$) levels, respectively. Further the intensity of the lower ν' members of the $B^1\Sigma_u^+$ state may be significantly increased at higher angles by the $b^3\Sigma_u^+$ state (see figure 5.5-1). Apparently, the least affected level (which we can observe) will be the $B^1\Sigma_u^+$ ($\nu' = 5$) one. Thus, table 5.5-3 presents the relative vibrational intensities within the $B^1\Sigma_u^+$ state

TABLE 5.5-2

Relative vibrational peak intensity distribution for the $X^1\Sigma_g^+$ ($\nu = 0$) → $C^1\Pi_u$ ($\nu' = 0$ to 5) transitions. The intensity of the $X(\nu = 0) \rightarrow C(\nu' = 1)$ transition is normalized to 1.00. The data from all angles have been averaged together (16 scans).

Investigator	ν'					
	0	1	2	3	4	5
This research (40 eV)	.72 ± .02	1.00	.91 ± .03	.67 ± .03	.43 ± .02	.26 ± .02
Geiger[151] (25 KeV)	.62	1.00	.96	.62	.40	.23
Hutchisson[152] (calculation)	.635	1.00	.961	.697	.411	.236

TABLE 5.5-3

Relative vibrational peak intensity distribution for the $X^1\Sigma_g^+$ ($\nu = 0$) → $B^1\Sigma_u^+$ ($\nu' = 0$ to 6) transitions. The intensity of the X($\nu = 0$) → B($\nu' = 5$) transition is normalized to 1.00. The scans for $\theta = 0°$ to 10° and 15° to 20° have been averaged together as indicated.

	ν'							No. of
θ	0	1	2	3	4	5	6	Scans
<0°-10°>	.08 ± .01	.24 ± .02	.47 ± .03	.72 ± .03	.91 ± .04	1.00	1.06 ± .05	4
<15°-20°>	.08 ± .01	.22 ± .03	.51 ± .03	.72 ± .04	.92 ± .04	1.00	1.09 ± .05	4
30°	.08	.25	.47	.73	.95	1.00	1.2_0	2
40°	.12 ± .02	.25 ± .04	.52 ± .04	.74 ± .03	.95 ± .04	1.00	1.19 ± .04	3
50°	.16	.32	.57	.78	.90	1.00	1.2	1
60°	.21	.33	.63	.79	1.2_5	1.00	1.4_5	2
80°	.22	.36	.56	.73	1.2	1.00	1.3_5	2
Geiger[151] (25 KeV, $\theta = 0°$)	.10	.19	.38	.59	.84	1.00	1.06	
Hutchisson[152] (calculation)	.082	.345	.860	1.246	1.316	1.00	.556	

(with respect to that of the $\nu' = 5$ level) obtained from this research, the work by Geiger[151], and calculations[152]. (Since Geiger used 25 KeV incident electrons, only singlet → singlet transitions were observed.)

It is clear that neither the results of Geiger[151] nor of this research agree with the calculations[152] (except fortuitously perhaps at $\nu' = 0$). We would expect the agreement of this work with that of Geiger to be best at the lowest angles, since the ratio of triplets to singlets is smallest there. Our results seem consistently high by about 10% (except $\nu' = 0$ and 6) for $\theta \lesssim 20°$. This is probably not due to the overlapping $b^3\Sigma_u^+$ state since the b/B DCS ratio changes by more than a factor of 10 in the same angular range (see below). (Further, below $\theta \approx 30°$ we did not observe excitation of the $b^3\Sigma_u^+$ state in these high resolution scans.) This discrepancy cannot be accounted for by the correction factor $C^{DD}_{\nu\nu 0}$ of equation (3-72) since $C^{DD}_{\nu\nu 0}$ is within about 5% of unity at these angles. In any case, for angles greater than $\sim 40°$, the enhancement of the $\nu' = 0$ and 1 peak intensities (due to excitation of the $b^3\Sigma_u^+$ state); the $\nu' = 4$ intensity (due to transitions to the $a^3\Sigma_g^+$ ($\nu' = 0$) and/or $c^3\Pi_u$ ($\nu' = 0$) levels); and the $\nu' = 6$ peak intensity (due to excitation of the $a^3\Sigma_g^+$ ($\nu' = 1$) and/or $c^3\Pi_u$ ($\nu' = 1$) states) is clearly evident. This distortion with angle of the relative vibrational intensity distribution within an electronic band can presumably be used to detect forbidden transitions which are strongly masked by overlapping allowed ones[153].

Let us next consider the variation with scattering angle of the relative DCS for excitation of the $b^3\Sigma_u^+$, $B^1\Sigma_u^+$, and $C^1\Pi_u$ states. Figure 5.5-7 shows the peak intensity ratios of the $X^1\Sigma_g^+$ ($\nu = 0$) → $b^3\Sigma_u^+$ and $B^1\Sigma_u^+$ ($\nu' = 5$) transitions with respect to that of the $X^1\Sigma_g^+$ ($\nu = 0$) → $C^1\Pi_u$ ($\nu' = 1$) one. The $B^1\Sigma_u^+$ ($\nu' = 5$)/$C^1\Pi_u$ ($\nu' = 1$) intensity ratio was determined from the same high-resolution data used to obtain the results presented in tables 5.5-2 and -3. The $b^3\Sigma_u^+/C^1\Pi_u$ ($\nu' = 1$) intensity ratio was obtained from lower resolution (FWHM ≈ .10 eV) scans (at the same 40 eV impact energy). Both the b/C ($\nu' = 1$) and B ($\nu' = 5$)/C ($\nu' = 1$) peak intensity ratios are directly proportional to the corresponding DCS ratios. Since the proportionality constant depends somewhat on the resolution, but not on the angle, the magnitude of the ratios are not directly comparable although their relative angular dependencies are. As expected, the b/C intensity ratio increases rapidly with angle while the B/C one is practically constant (within the errors of this determination). The angular variation of the b/C ratio is quite similar to the $^3\Sigma^+/\Pi$ ratios already noted (N_2, CO). This tends to reinforce the tentative hypothesis (see section 5.3)) that for $\Delta S = 1$, the value of $\Delta\Lambda$ (0 or 1) is more important in determining the relative angular distribution than is the g → g or u nature of the transition. The $B^1\Sigma_u^+/C^1\Pi_u$ intensity ratio does not exhibit the oscillations noted in the previous $^1\Sigma/\Pi$ ratios. Although the $X^1\Sigma_g^+$ → $B^1\Sigma_u^+$ transition in H_2 is the only case we have examined of a $\Delta\Lambda = 0$, g → u, $\Delta S = 0$ transition, the fact that its intensity, relative to that of the $^1\Pi_u$ one, does not

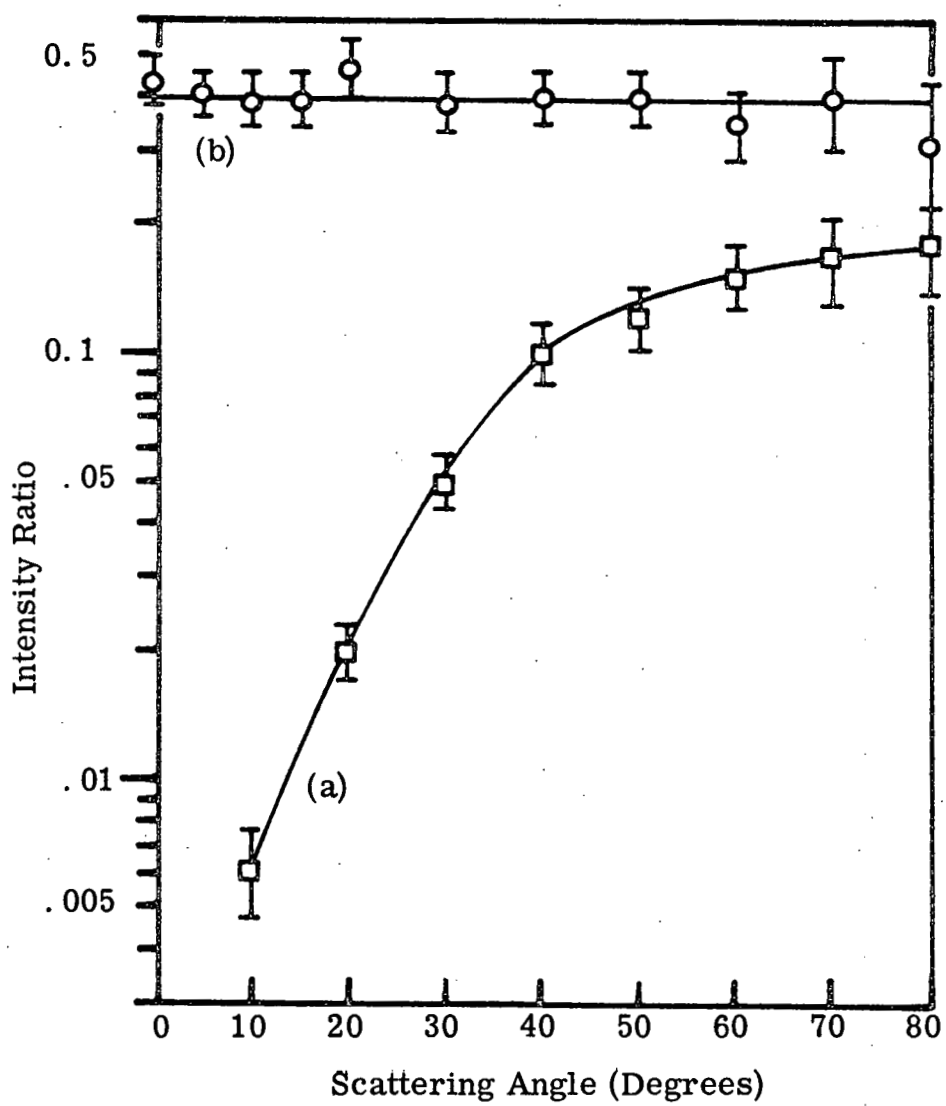

Figure 5.5-7. Ratios of intensities of the $X^1\Sigma_g^+ \rightarrow b^3\Sigma_u^+$ (peak) curve (a) and $B^1\Sigma_u^+$ ($\nu' = 5$) curve (b) transitions to that of the $X \rightarrow C^1\Pi_u$ ($\nu' = 1$) one in H_2. $E_o = 40$ eV. Each data point is an average of two to four scans at each angle.

oscillate as do those of the $\Delta\Lambda = 0$ or 1, g → g, $\Delta S = 0$ transitions (N_2) is consistent with the conjecture (section 5.3) that for $\Delta S = 0$, the g → g or u nature of the transition is more important in determining the relative angular distribution than is the $\Delta\Lambda$ value.

Finally, figure 5.5-8 shows the DCS (in arbitrary units) for excitation of the $C^1\Pi_u$ ($\nu' = 1$) and $b^3\Sigma_u^+$ states at 40 eV for $\theta = 10°$ to 80°. As expected, the singlet → singlet DCS is sharply forward peaked, while the singlet → triplet one is more isotropic.

5.6. Acetylene

5.6.1. Introduction

Since acetylene (C_2H_2) is isoelectronic with N_2 and CO. we might expect that it would exhibit a similar energy-loss spectrum. The only previous electron-impact study of C_2H_2 was reported by Bowman and Miller[10] using the trapped-electron method. A comparison of their result with those of Schulz[155] for CO and N_2 does indeed show this similarity. However, the tentative state assignments of reference (10) do not reflect this similarity, particularly with regard to the feature peaking at 6.2 eV. In both N_2 and CO a low-lying triplet state ($B^3\Pi_g$ in N_2 and $a^3\Pi$ in CO) was responsible for the peak which appears to correspond to the 6.2 eV transition observed by Bowman and Miller. Ingold and King[156] had observed a weak singlet → singlet transition ($\tilde{X}^1\Sigma_g^+ \rightarrow \tilde{A}^1A_u$) in absorption peaking at about 6 eV. Since the observation of a trapped-electron excitation spectrum is not sufficient to identify a transition as singlet → singlet or triplet[157], Bowman and Miller apparently

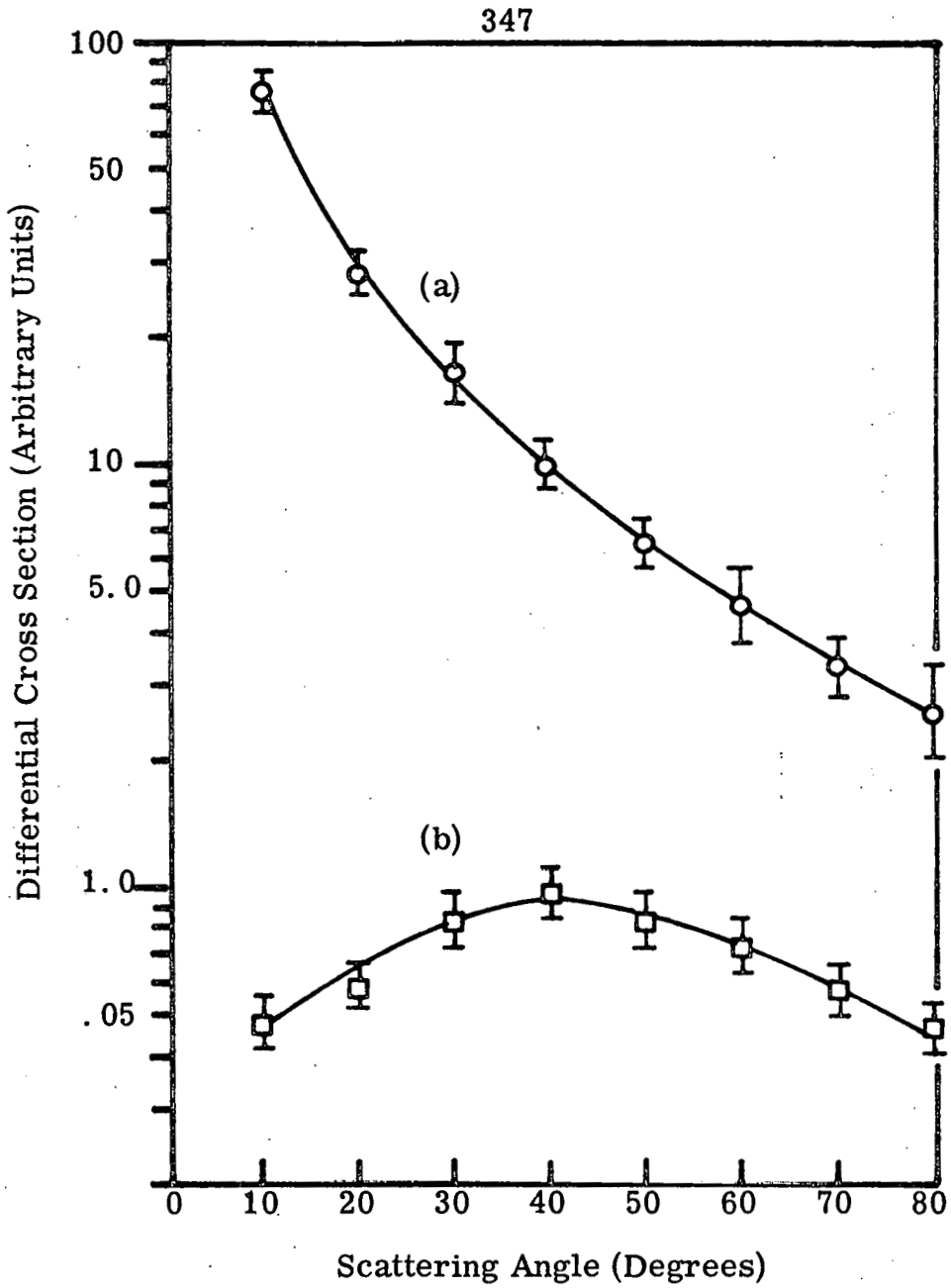

Figure 5.5-8. Differential cross section (arbitrary units) for excitation of the $C^1\Pi_u$ ($\nu' = 1$) curve (a) and $b^3\Sigma_u^+$ curve (b) states in H_2. E_o = 40 eV.

assumed that they were observing the $\tilde{X} \rightarrow \tilde{A}$ excitation.

The attached reprint (appendix IV) discusses our investigation of the energy-loss spectrum of C_2H_2 (from about 1 eV to 9.5 eV) and identification of two singlet → triplet transitions, with peak intensities at 5.2 eV and 6.1 eV. Some additional aspects of this study are discussed below.

5.6.2. Additional Results and Discussion

Figure 5.6-3 (figures 5.6-1 and -2 are in the reprint) shows an energy-loss spectrum of acetylene from about 5 eV to 12 eV for an impact energy of 45 eV and a scattering angle $\theta = 10°$. It is similar in appearance to the optical absorption spectrum obtained by Nakayama and Watanabe[158]. The energy-losses of the main features of figure 5.6-3 are listed in table 5.6-1 along with possible state assignments. Beyond 9 eV the UV absorption spectrum is too complex for these correspondences to be more than tentative.

Figure 5.6-2 (see appendix IV) contains the peak ratios of several states at 25 eV. Similar measurements were made at 35 eV as shown in figure 5.6-4. As before (preprint) the singlet → triplet/singlet → singlet ratios are sharply increasing functions of angle while the singlet → singlet/singlet → singlet ones vary much more slowly.

Note that in both figures 5.6-2 and -4 the $\tilde{C}^1\Pi_u$ ($\nu_2 = 1$)/$\tilde{C}^1\Pi_u$ ($\nu_2 = 0$) intensity ratios gradually increase with angle. This is not expected, since these peaks arise from transitions to two vibrational members of the same electronic state. The 70% change

Figure 5.6-3. Energy-loss spectrum of acetylene. E_o = 45 eV, $I_o = 5 \times 10^{-8}$ A, $\theta = 10°$, SR = .010 V/sec; TC = .5 sec, P = 1.2×10^{-3} torr. The excitation energies for the numbered features are listed in table 5.6-1.

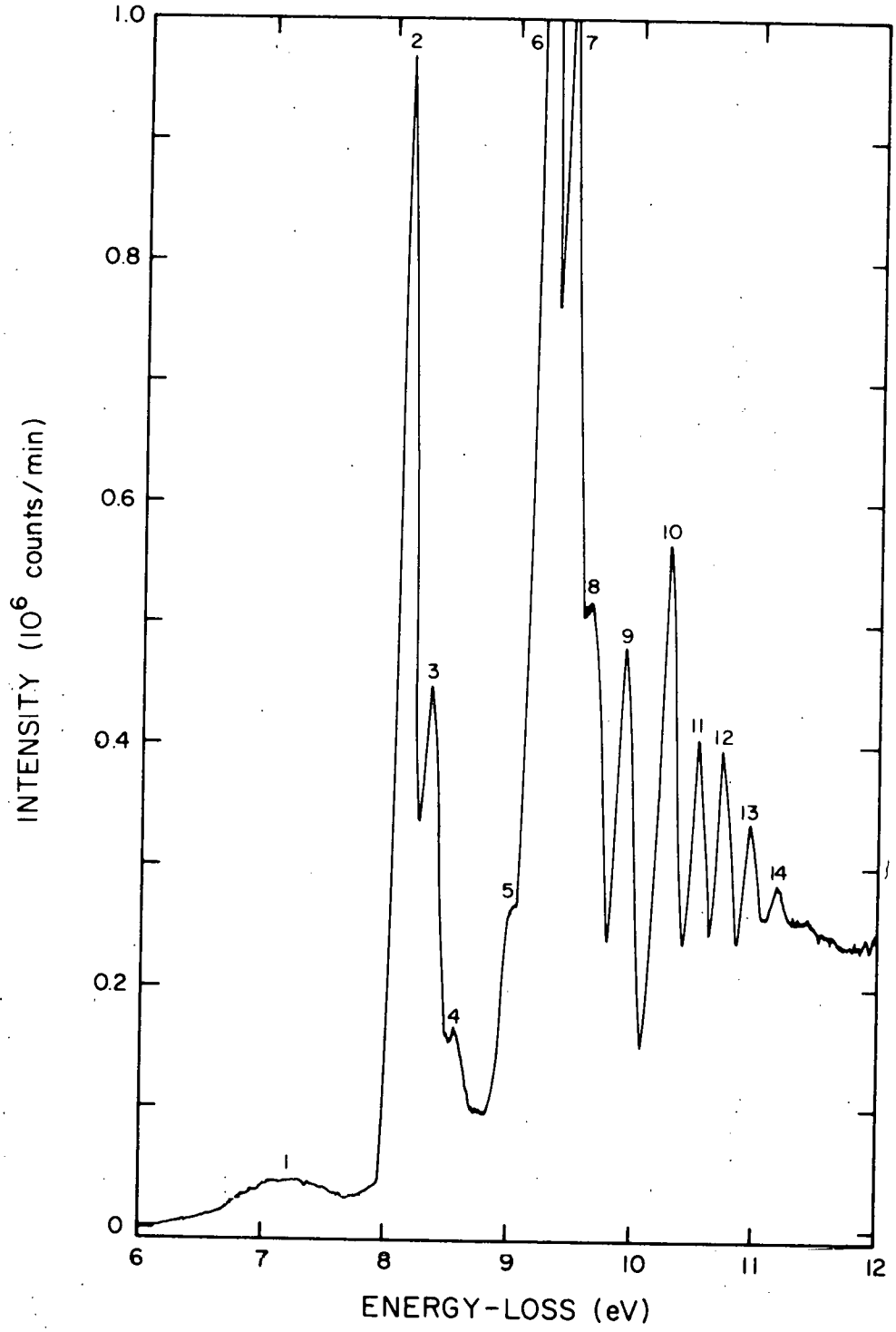
1.0
0.8
0.6
0.4
0.2
0
INTENSITY (10^6 counts/min)
6
7
8
9
10
11
12
ENERGY-LOSS (eV)
1
2
3
4
5
6
7
8
9
10
11
12
13
14

TABLE 5.6-1

Excitation energies observed in the electron impact spectrum of acetylene. The first column is the peak identification number from figure 5.6-3. The second column is the energy-loss at which the peak is observed in the present work, the third column is the most likely corresponding optical excitation energy, and the fourth column is the assignment of the upper state (the ground state is $\tilde{X}\,^1\Sigma_g^+$, point group $D_{\infty h}$).

Peak Number	Energy Loss (eV)	Optical Excitation Energy[a]	Assignment[b]		
			Point Group	State	Vibrational Level
	$5.2 \pm .1$[c]			$\tilde{a}$ (triplet)	unresolved
	$6.1 \pm .1$[c]			$\tilde{b}$ (triplet)	unresolved
1	$7.2 \pm .1$	(7.3) (broad)		$\tilde{B}$	(diffuse, unassigned bands)
2	$8.16 \pm .01$	8.16	$D_{\infty h}$	$\tilde{C}(^1\Pi_u)$, [3R]	ν_{00}
3	$8.37 \pm .01$	8.38	$D_{\infty h}$	$\tilde{C}(^1\Pi_u)$, [3R]	ν_2
4	$8.61 \pm .01$	8.62	$D_{\infty h}$	$\tilde{C}(^1\Pi_u)$, [3R]	$2\nu_2$
5	$9.02 \pm .02$				
6	$9.26 \pm .01$	9.24	$D_{\infty h}$	$\tilde{D}$, [3R′]	ν_{00}

TABLE 5.6-1 (continued)

Peak Number	Energy Loss (eV)	Optical Excitation Energy[a]	Assignment[b]		
			Point Group	State	Vibrational Level
		9.25	C_{2h}	$\tilde{E}, \{B\}$	ν_{oo}
		9.27	C_{2h}	$\tilde{F}, \{C\}$	ν_{oo}
7	9.47 ± .01	9.46	$D_{\infty h}$	$\tilde{D}, [3R']$	ν_2
		9.48	C_{2h}	$\tilde{F}, \{C\}$	ν_2
8	9.66 ± .02	9.68	$D_{\infty h}$	$\tilde{D}, [3R']$	$2\nu_2$
		(9.68)	C_{2h}	$\tilde{F}, \{C\}$	$2\nu_2$
9	9.94 ± .01	(9.93)	$D_{\infty h}$	[4R]	ν_{oo}
10	10.29 ± .01	(10.28)	$D_{\infty h}$	[4R']	ν_{oo}
11	10.54 ± .02	(10.52)	$D_{\infty h}$	[4R']	ν_2
12	10.74 ± .02				
13	10.96 ± .02	Probably Rydberg states [nR] , [nR'].			
14	11.19 ± .03				

TABLE 5.6-1 (continued)

[a] Optical excitation energies in parentheses were determined from fig. 1 of reference (158).

[b] States in square brackets [ ] are from Price[164], those in { } are from Wilkinson[165], the other designations are from Herzberg[2c].

[c] Refer to figure 1 of the reprint, appendix IV.

Figure 5.6-4. Peak intensity ratios in acetylene for E_o = 35 eV. The peak ratios are labelled according to their number designations in figure 5.6-3. The curves labelled $\tilde{a}/2$ and $\tilde{b}/2$ are the triplet intensity ratios (with respect to peak 2) times 10. For clarity, only a few representative error bars are shown for each ratio. Each data point is an average of three scans.

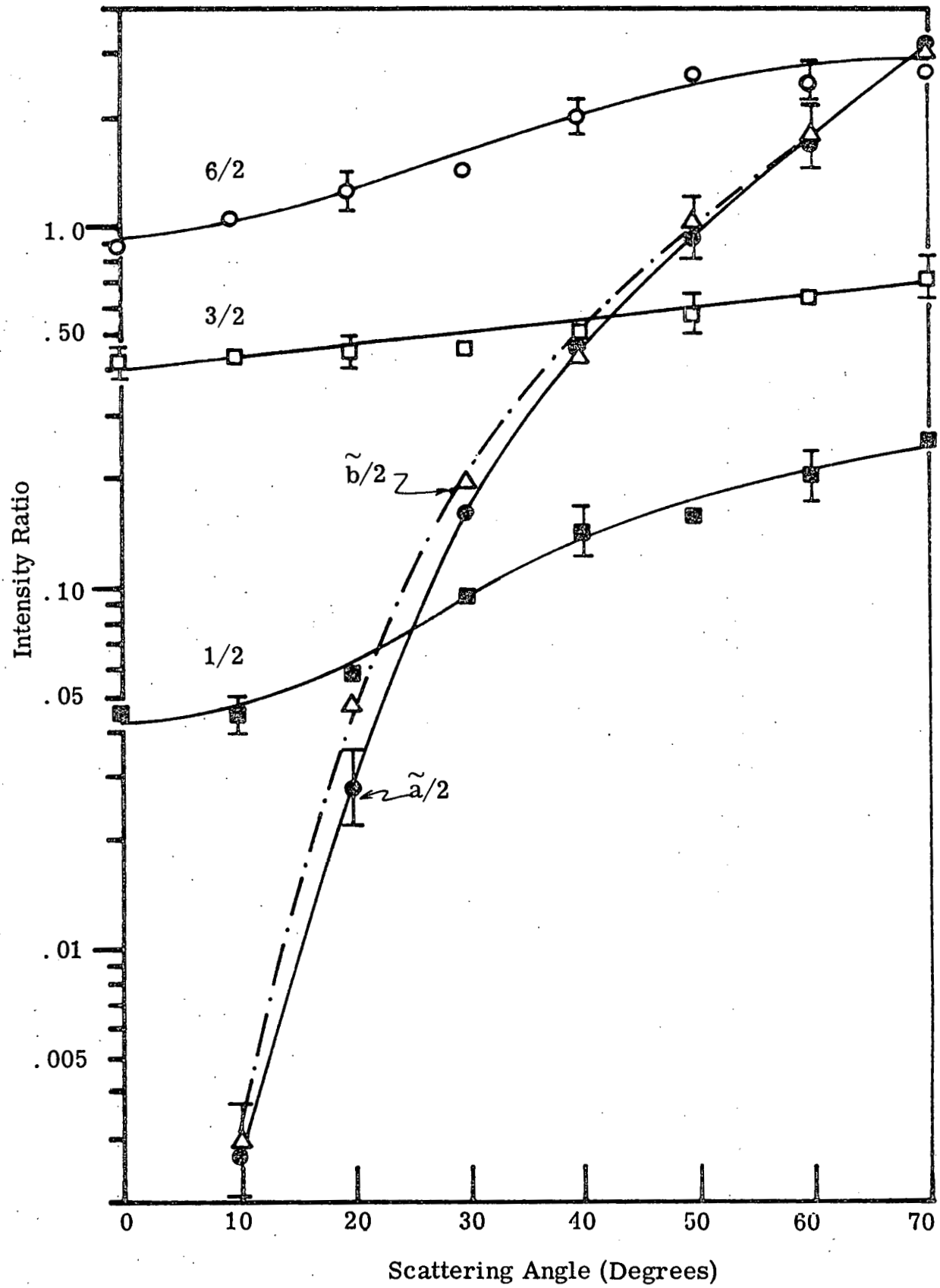
6/2
3/2
1/2
b̃/2
ã/2
1.0
.50
.10
.05
.01
.005
Intensity Ratio
0
10
20
30
40
50
60
70
Scattering Angle (Degrees)

at both E_o = 35 eV and 25 eV for θ = 0° to 70° is well outside the reasonable error limits of the data. This leaves two possible explanations: (1) the Franck-Condon factor considerations of section 3.3.7.1 are not valid[159], and (2) there is an underlying excitation (probably forbidden) which enhances the $\nu_2 = 1$ peak relative to the $\nu_2 = 0$ one. As to the first possibility, we can only point out that in all reported cases (only six transitions, including the present work), no significant ($> \sim 5\%$) deviations in relative vibrational intensities have been noted as a function of angle. The second possibility has been clearly demonstrated for one case in H_2 (refer to section 5.5). Based on this evidence (meager though it is), the second explanation seems to be the most likely one. Referring to reference (10), we note that the most intense excitation occurs at ~ 8.2 eV. From the results of Schulz[9a] and Brongersma[11], we note that the most intense features (excluding negative ion formation) in the trapped-electron spectra of both CO and N_2 are due to singlet → triplet transitions. In particular, the $X \rightarrow B^3\Pi_g$ and $X \rightarrow E^3\Sigma_g^+$ transitions are the most intense in N_2 while the $X \rightarrow a^3\Pi$ and $X \rightarrow b^3\Sigma^+$ are the most intense in CO. In view of these comparisons, it is not unlikely that the excitation observed at 8.2 eV in reference (10) is due to a singlet → triplet transition, analogous to the $^1\Sigma \rightarrow {}^3\Sigma$ transitions of N_2 and CO. In order to explain the intensity ratio variation we have observed in the $\tilde{C}^1\Pi_u$ band of C_2H_2, the maximum transition intensity for this hypothetical triplet state should lie somewhat higher than 8.16 eV, in agreement with reference (10). Without additional data, further speculation seems unwarranted.

The steeply rising (with increasing θ) $\tilde{a}/\tilde{C}$ and $\tilde{b}/\tilde{C}$ intensity ratios are quite similar in behavior to the previously observed intensity ratios for which the singlet → triplet transitions have $\Delta S = 1$ and $\Delta\Lambda = 1$. (All of the reference excitations for the intensity ratios have been chosen to be transitions in which $\Delta S = 0$, $\Delta\Lambda = 1$, and g → u (where applicable).) Thus, we tentatively suggest that $\tilde{a}$ and $\tilde{b}$ are Π states (Λ of ground state = 0, plus $\Delta\Lambda = 1$ implies Λ of excited state = 1). In analogy with N_2, they might correspond to the $B\,^3\Pi_g$ and $C\,^3\Pi_u$ states. These would be states of a linear C_2H_2 configuration. It is also possible that the excited state is "bent" (a possibility which does not exist for N_2). In this case a $^3\Pi_{g(u)}$ state of the linear molecule (point group $D_{\infty h}$) would correlate with $^3A_{g(u)} + {}^3B_{g(u)}$ states of the "trans-bent" (point group C_{2h}) molecule[160]. (We have neglected the "cis-bent" configuration and the possibility of spin-orbit coupling mixing singlets with triplets.) Essentially, the potential function for the degenerate Π electronic state of the linear molecule splits into two when the molecule is bent. The magnitude of this splitting depends on the magnitude of the vibronic interaction (Renner-Teller effect)[161].

From the present data, we cannot decide between the possibilities of (1) excitation of the two $^3\Pi$ states of the linear molecule (probably a $^3\Pi_g$ and a $^3\Pi_u$), or (2) excitation of a single $^3\Pi_{g(u)}$ state of the linear molecule which splits into an $^3A_{g(u)}$ and $^3B_{g(u)}$ state of the "bent" system.

The transitions we observe do not seem to be of the type $^1\Sigma \rightarrow {}^3\Sigma$. The $\tilde{a}$ and $\tilde{b}$/singlet ratios are sharply rising functions of θ as are the $^3\Pi$ and ^3P/singlet ratios already discussed. In particular, all of these ratios are much steeper than are the $^3\Sigma$/singlet ratios we have observed. This apparently eliminates the possibility that we observed a $\pi \rightarrow \pi^*$ transition, since the resulting electron configuration ($\pi^3\pi$) leads only to Σ and Δ states[162]. Π states can be obtained by either promoting an electron from a σ orbital into a π orbital or viceversa. Since MO calculations[163] predict that a $^3\Sigma$ is the lowest triplet state (as in N_2), apparently we have not observed the lowest triplet in C_2H_2. Bowman and Miller's tentative assignment of the lowest triplet state at 2.0 eV is not inconsistent with the present work, even though we failed to observe an energy-loss feature at 2.0 eV.

Figures 5.6-5 and -6 present the DCS (in arbitrary units) for the excitations shown (in ratio form) in figures 5.6-2 and -4, respectively. The $\tilde{a}$ and $\tilde{b}$ DCS are quite similar to the 2^3P (He), $a^3\Pi$(CO), and $C^3\Pi_u$ (N_2) ones, as expected. The singlet cross sections are sharply peaked forward, more so at 35 eV than at 25 eV incident energy (recall the discussion of section 3.4).

As already noted in table 5.6-1, the peak labelled 6 in figure 5.6-3 could contain substantial contributions from the non-Rydberg $\tilde{E}$ (ν_{00}) and $\tilde{F}$ (ν_{00}) states. Likewise, peak 7 could be a composite of $\tilde{D}$ ($\nu_2 = 1$) and $\tilde{F}$ ($\nu_2 = 1$) excitations. Thus, it is of interest to compare the relative intensity of these two peaks as a

Figure 5.6-5. Differential cross sections (arbitrary units) for excitation of the $\tilde{a}$, $\tilde{b}$, $\tilde{B}$ (1), $\tilde{C}$ ($\nu_2 = 0$) (2), and $\tilde{D}$ ($\nu_2 = 0$) (6) states of acetylene. $E_o = 25$ eV. Each data point is an average of three scans.

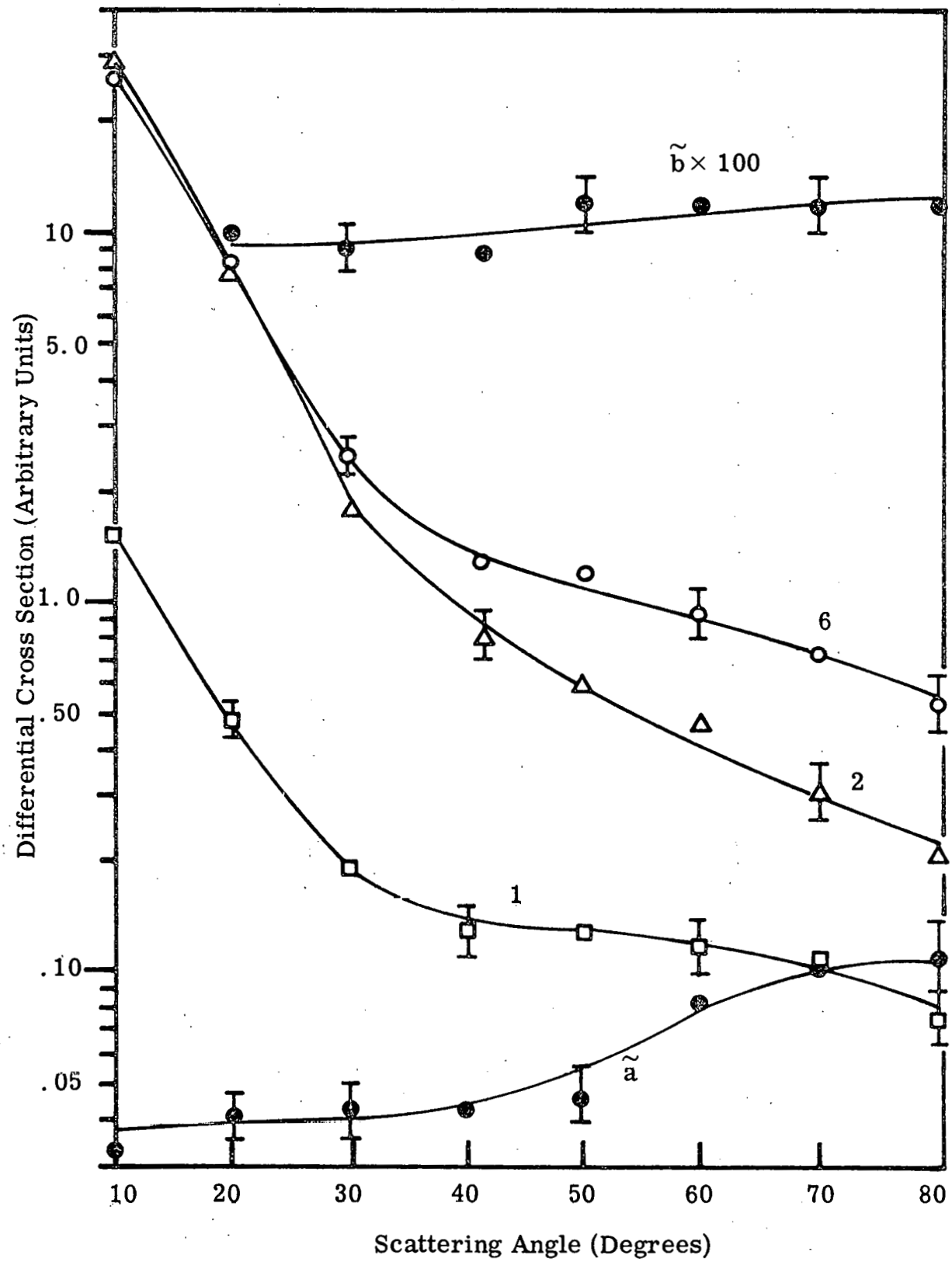
$\tilde{b} \times 100$
6
2
1
$\tilde{a}$
10
5.0
1.0
.50
.10
.05
Differential Cross Section (Arbitrary Units)
10
20
30
40
50
60
70
80
Scattering Angle (Degrees)

Figure 5.6-6. Differential cross sections (arbitrary units) for excitation of the $\tilde{a}$, $\tilde{b}$, $\tilde{B}$ (1), $\tilde{C}$ ($\nu_2 = 0$) (2), and $\tilde{D}$ ($\nu_2 = 0$) (6) states of acetylene. E_o = 35 eV. Each point is an average of three scans.

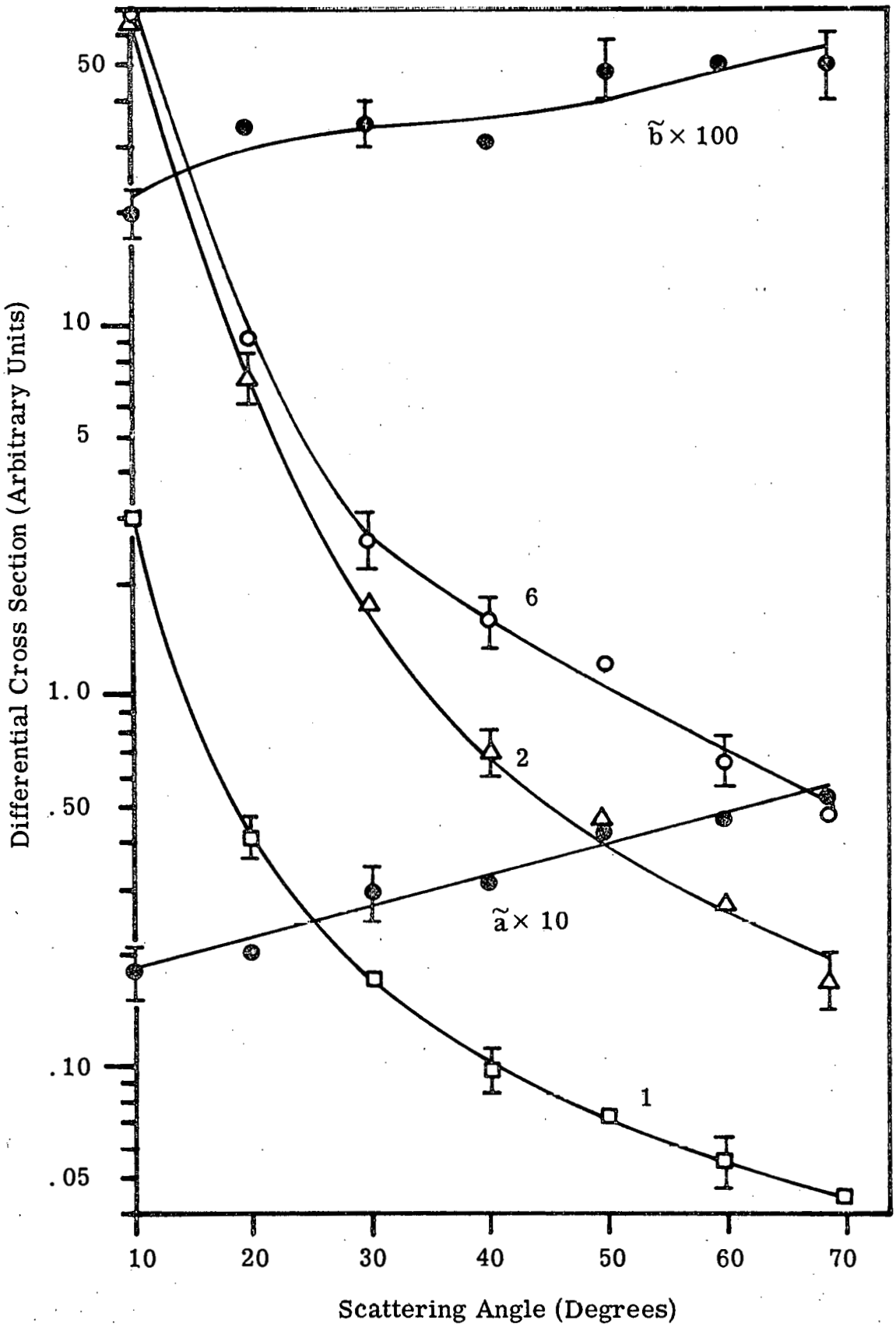
50
10
5
1.0
.50
.10
.05
Differential Cross Section (Arbitrary Units)
$\tilde{b} \times 100$
6
2
$\tilde{a} \times 10$
1
10
20
30
40
50
60
70
Scattering Angle (Degrees)

function of angle. Table 5.6-2 presents the results of such a comparison for an impact energy of 35 eV. $C^{DD}_{\nu\nu 0}(\theta)$ has been included in the table, primarily because in this one case it seems to improve the constancy of the ratio (perhaps fortuitously). The invariance of this peak intensity ratio with angle indicates that either the three electronic states mentioned above vary with angle in nearly the same way or that we only observe transitions to one of the states (either $\tilde{F}$ or $\tilde{D}$). Without higher-resolution studies, we cannot decide between these alternatives.

5.7. Ethylene

5.7.1. Introduction

Ethylene is a molecule of considerable interest to both theoretical and experimental chemists. Since C_2H_4 is an example of the simplest pi-electron system, it has been used extensively as a model for testing theoretical calculations. Unfortunately, the overlapping nature of its electronic bands has complicated experimental investigations[166] while ab initio calculations have as yet been somewhat limited by the computational effort involved[167].

The optical absorption spectrum of ethylene has been studied by a number of investigators in the solid[168], liquid[82], and gaseous state[169]. The optically observed transitions (from the $\tilde{X}\,^1A_g$ planar ground state, N state of Mulliken[170]) can be briefly summarized as follows:

(1) At long wave lengths (low energy), a progression of extremely weak diffuse bands, beginning at about 3.6 eV and peaking

TABLE 5.6-2

Ratio of the peak intensity of peak number 7 (figure 5.6-3) to that of peak number 6 as a function of scattering angle θ. E_o = 35 eV.

θ (degrees)	7/6 Peak Intensity Ratio (I_R)	C_{10}^{DD}	$\frac{I_R}{C_{10}^{DD}}$	No. of Scans Used
0°	.85 ± .05	.958	.89	2
10°	.87 ± .05	.979	.89	2
20°	.86 ± .04	.991	.85	2
30°	.90 ± .04	.995	.90	3
40°	.86 ± .03	.997	.86	3
50°	.88 ± .04	.998	.88	2
60°	.90 ± .05	.999	.90	2
70°	.88 ± .04	.999	.88	3
Average of all angles	.88 ± .02		.88 ± .01	19

at ~ 4.6 eV is observed[171]. The upper state for this system is the lowest triplet $\tilde{a}^3B_{1u}$[172] (Mulliken's T state[170]).

(2) A stronger absorption consisting of a progression of diffuse bands beginning at about 5 eV, merging into a continuum at about 7 eV, and reaching a flat maximum at ~ 7.6 eV occurs next. It is generally agreed[172] that the upper state is the first excited singlet, $^1B_{1u}$ (V state of Mulliken[170]).

(3) At 7.11 eV, the first Rydberg transition is observed[173] (R state of Mulliken). Nearly all features observed at higher energies can be attributed to additional Rydberg transitions[166].

(4) The first ionization potential is found to be 10.50$_7$ eV[173]. The relative intensities and order of these transitions from 6.2 eV to 11.64 eV are conveniently shown in the figures of Zelikoff and Watanabe[174].

Kuppermann and Raff[35] were the first to observe electronic excitation of ethylene via electron-impact. The peaks they observed at 4.6 eV and 7.7 eV correlate well with the N → T and N → V (or R) transitions observed optically. Trapped-electron spectra reported by Brongersma[87] and Bowman and Miller[10] show peaks at nearly these same locations as well as one at ~ 9.2 eV (and negative ion formation at lower energies). Doering's[36c] investigations at large scattering angles (θ = 90°) and low energies (down to 10.9 eV) revealed approximately these same features (4.4 eV, 7.7 eV, and 9.3 eV). At somewhat higher energies (50 eV) and θ = 0°, Simpson and Mielczarek[26] observed energy-loss peaks which coincided

with several Rydberg transitions. The 4.4 (4.6) eV transition was not observed and the broad peak near 7.7 (actually peaking at 7.5 eV) was clearly due to the lowest N → R transition. The energy-loss spectrum of Lassettre and Francis[147], obtained at an incident energy of ~ 400 eV and $\theta \approx 0°$, was quite similar to that of reference (26) (except that the resolution of the former was about 0.6 eV while that of the latter was 0.1 eV).

Significantly higher resolution studies have been reported by Geiger and Wittmaack[40] (FWHM ≈ .025 eV, $E_0 \approx$ 33 KeV, $\theta \approx 0°$) and Ross and Lassettre[23] (FWHM ≈ .03, $E_0 \approx$ 150 eV, $\theta \approx 0°$). Neither the N → T nor N → V transitions are observed, but the N → R and higher Rydberg transitions are clearly evident. The highest energy results[40] agreed in detail[175] with optical absorption data[174]. However, the data of references (26) and (147) indicate a maximum in the N → R (plus underlying N → V) transition intensity at 7.5 eV whereas the optical absorption reaches a maximum at 7.28 eV. Ross and Lassettre[23] have attributed this anomaly to an underlying quadrupole-allowed (but dipole-forbidden) electronic transition.

In summary, electron-impact and optical absorption studies generally agree, with the exceptions that (1) the N → V transition, which is distinctly observed in absorption, has not been seen explicitly via electron-impact (i.e., it is masked by the stronger overlapping N → R transition) and (2) there is electron-impact evidence for an $\tilde{X}\,^1A_g \rightarrow (^1B_{1g})$[176] (quadrupole-allowed) transition

which has not been observed optically. It is generally agreed[177] that no other features have been revealed by electron-impact.

5.7.2. Results and Discussion

Figure 5.7-1 shows an energy-loss spectrum of ethylene under low resolution (FWHM of elastic peak = 0.15 eV) at $\theta = 40°$ and $E_o = 40$ eV. The N → T and N → R (or V) transitions are clearly evident as well as higher Rydberg transitions. Figure 5.7-2 shows the energy-loss region from about 7 eV to 10 eV under relatively high resolution (FWHM $\approx$ .05 eV) at $E_o = 40$ eV and $\theta = 10°$. The peaks observed in these figures along with their probable assignment are listed in table 5.7-1 (all peaks except that of the N → T transition were taken from figure 5.7-2). These spectra agree quite well with the previous results. In particular, the relative intensities within the N → R band agree with those of Ross and Lassettre[23], although the resolution is not as good. Unfortunately, the signal level at this resolution (FWHM = .05 eV) was not sufficient to scan a very large range of angles. The R band relative intensities are summarized in table 5.7-2. Our low angle results at 40 eV are the same (within the error limits)as the $\theta = 0°$, 150 eV results of Ross and Lassettre[23]. At higher angles, the enhancement of the peaks of the $\nu_2 = 2$ and 3 levels relative to that of the $\nu_2 = 1$ is quite clear. This reinforces the hypothesis[23] that at least one forbidden transition (hereafter labelled as N → Z) underlies the N → R transition at about 7.5 eV energy-loss (and higher). The energy-dependence

Figure 5.7-1. Energy-loss spectrum of ethylene. E_o = 40 eV, I_o = 3×10^{-8} A, θ = 40°, SR = .002 V/sec, TC = 5 sec, P = 1.0×10^{-3} torr. FWHM of the elastic peak = 0.15 eV.

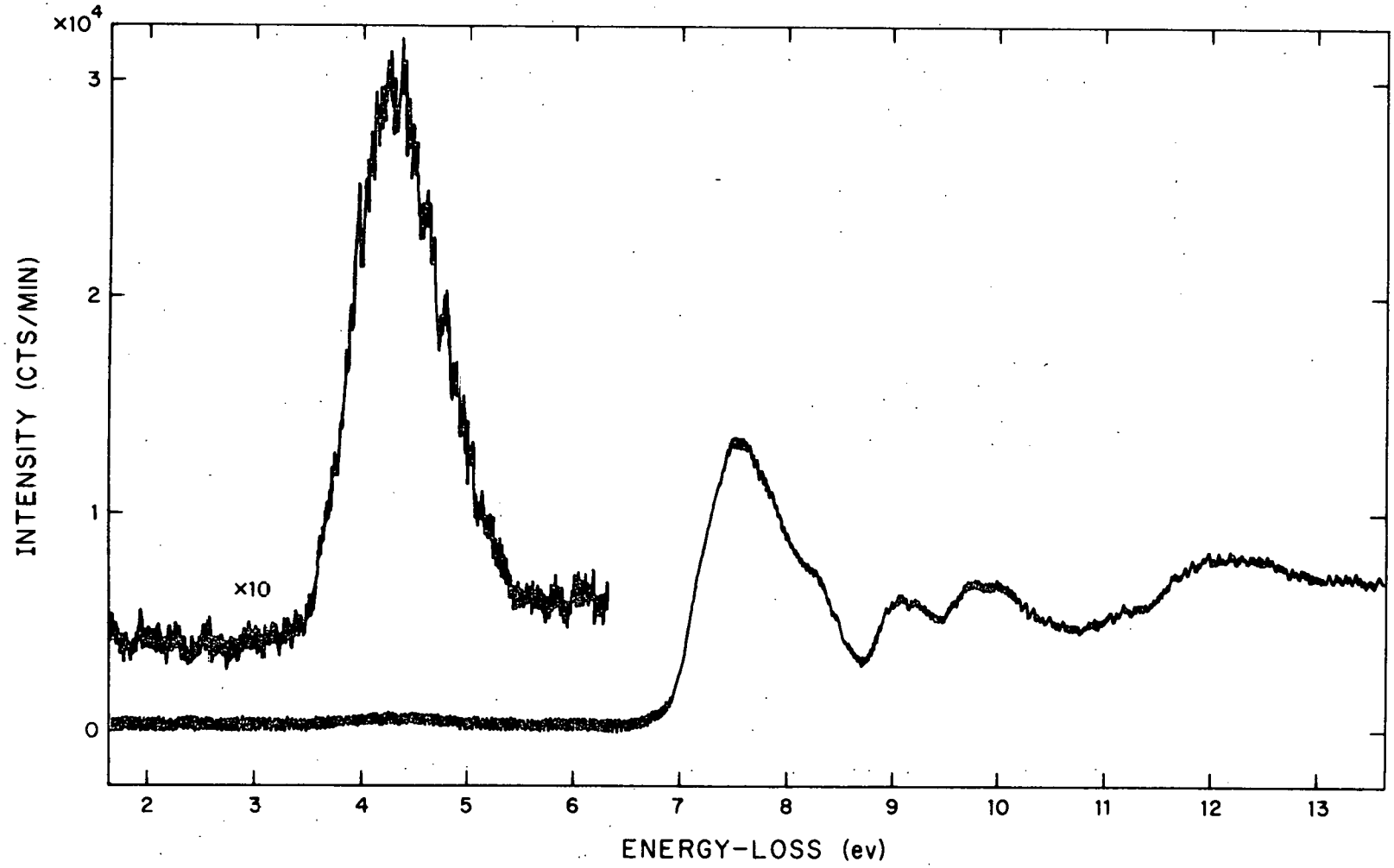
×10^4
3
2
1
0
INTENSITY (CTS/MIN)
×10
2
3
4
5
6
7
8
9
10
11
12
13
ENERGY-LOSS (ev)

Figure 5.7-2. Energy-loss spectrum of ethylene. E_o = 40 eV, I_o = 1×10^{-9} A, θ = 10°, SR = .008 V/sec, TC = 1 sec, P = 1.2×10^{-3} torr. FWHM of the elastic peak is .05 eV.

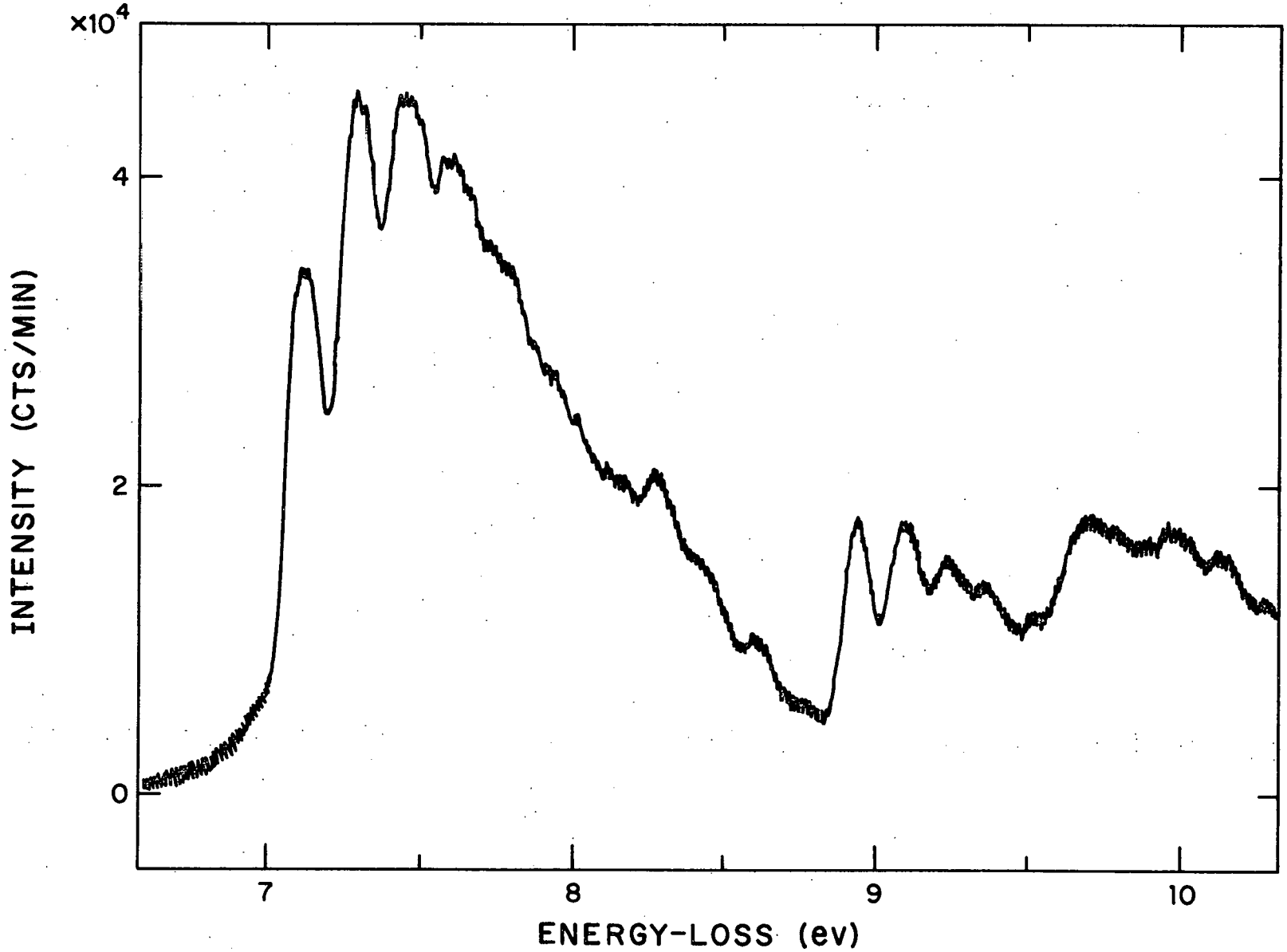
×10^4
4
2
0
INTENSITY (CTS/MIN)
7
8
9
10
ENERGY-LOSS (ev)

TABLE 5.7-1

Energy-loss peak locations in the electron-impact spectrum of C_2H_4. The first column lists the excitation energies (below ionization) of the peaks in figure 5.7-2; the second column lists the corresponding optical values; and the third column presents the upper state assignment corresponding to the optical values. The ground electronic state of ethylene is $\tilde{X}\,^1A_g$ (point group D_{2h})

Excitation Energy From This Research (eV)	Optical Excitation Energy[a] (eV)	Assignment of Upper State		
		Electronic[b]	Vibration[c]	
4.4 ± .1		$\tilde{a}\,^3B_{1u}$		
(onset : 3.4 ± .1	<3.6)			
			ν_2	ν_4
7.12 ± .01	7.11	$\tilde{B}$, (2R)	0	0
	7.17		0	2
7.30 ± .01	7.28		1	0
	7.34		1	2
7.46 ± .01	7.45		2	0
	7.50		2	2
7.59 ± .02	7.61		3	0
	7.67		3	2
(7.79)[d]	7.77		4	0

TABLE 5.7-1 (continued

Excitation Energy From This Research (eV)	Optical Excitation Energy[a] (eV)	Assignment of Upper State		
		Electronic[b]	Vibration[c]	
			ν_2	ν_4
8.27 ± .01	8.26	$\tilde{C}$, (3R′)	0	0
	8.32		0	2
(8.41)[d]	8.42		1	0
8.60 ± .02	8.62	$\tilde{D}$, (3R″)	0	0
8.93 ± .01	8.90	$\tilde{E}$, (3R)	0	0
	8.95		0	2
9.08 ± .02	9.08		1	0
	9.13		1	2
9.24 ± .02	9.25		2	0
9.36 ± .02	9.36	(4R′)	0	0
9.70 ± .02				

[a] Optical excitation energies for the $\tilde{a}$ state are from reference (84), those for the $\tilde{B}$ from reference (169), and all others from reference (166).

[b] Electronic states in parentheses are from references (169) and (266); the others are from reference (2c), p. 629.

[c] The vibrational assignments are from references (169) and (166).

[d] Shoulder.

TABLE 5.7-2

Relative intensity distribution for the first Rydberg transition (N → R) in ethylene. The third, fourth, and fifth columns are the results of other investigators. These authors resolved the ν_2 and $2\nu_4$ excitations, but to compare with our results (column six), in which they are not resolved, these peaks have been averaged together.

ν_2	ν_4	$(I/I_{\nu_2 = 1})^{(a)}$	$(I/I_{\nu_2 = 1})^{(b)}$	$(I/I_{\nu_2 = 1})^{(c)}$	$(I/I_{\nu_1 = 1})^{(d)}$	
					$\theta = 10°$	$\theta = 40°$
0	0	.88	.78	.76 ± .05	.75 ± .06	.72 ± .05
0	2					
1	0	1.00	1.00	1.00	1.00	1.00
1	2					
2	0	.85	.90	1.00 ± .02	1.00 ± .05	1.15 ± .05
2	2					
3	0	.74	.80	.92 ± .02	.91 ± .06	1.10 ± .05
3	2					

[a] Reference (174). [b] Reference (40). [c] Reference (23). [d] Present results, $E_o = 40$ eV, average of three scans.

of this increase in the $\nu_2 = 2$ (and $\nu_2 = 3$) relative intensity can provide a clue to the nature of the N → Z transition. To this end, the intensity ratios of the $\nu_2 = 2$ to $\nu_2 = 1$ peaks from Geiger[40], Ross[23], and Simpson[26] are listed below:

θ =	0°	0°	0°
E_0 =	33,000 eV	150 eV	50 eV
(I_2/I_1) =	.90	1.00	(1.09)[178]

Ross argued that the ratio increase from 33,000 eV to 150 eV is consistent with an underlying quadrupole transition, but did not point out that Simpson's data are quantitatively in agreement with this suggestion[179].

Our angular measurements (meager though they are) may also provide an indication of the nature of this N → Z transition. Let us assume that the 7.46 eV transition intensity is the sum of three components: the N → R ($\nu_2 = 2$) intensity (IR_2), the N → V continuum intensity (IV_2), and the N → Z intensity (IZ_2). Presumably, the 7.12 eV and 7.30 eV peak intensities are equal to $IR_0 + IV_0$ and $IR_1 + IV_1$, respectively. Although IR_0/IR_1 and IV_0/IV_1 are expected to be independent of angle from our previous Franck-Condon factor considerations, $IR_0 + IV_0/IR_1 + IV_1$ will depend on θ if the N → R and N → V DCS have different angular dependencies. The latter ratio will be independent of θ if $IV_0 \ll IR_0$ and $IV_1 \ll IR_1$ (a likely case). Since the data (Table 5.7-2) indicate that this ratio is nearly constant between $\theta = 10°$ and 40°, we can

tentatively conclude that (1) the N → R and N → V DCS behave in nearly the same way with angle or (2) the N → V DCS is negligible compared to the N → R one. For simplicity we shall assume the latter to be true (although the following arguments do not depend on this assumption). Thus, from the data of table 5.7-2 we have:

$$\frac{IR_2 + IZ_2}{IR_1} \cong 1.00 \text{ at } \theta = 10^\circ$$

and

$$\cong 1.15 \text{ at } \theta = 40^\circ.$$

But $IR_2/IR_1 \cong .90$ from the 33 KeV data of Geiger for which IZ is certainly negligible. (Recall that IR_2/IR_1 is most likely independent of angle and energy since it is a relative intensity within a single electronic band.) Thus,

$$\frac{IZ_2}{IR_1} \cong 0.1 \text{ at } \theta = 10^\circ$$

and

$$\cong 0.25 \text{ at } \theta = 40^\circ.$$

This factor of 2.5 increase from 10° to 40° is not inconsistent with a "quadrupole"/"dipole" intensity ratio (e.g., $^1\Sigma_g^+/b^1\Pi_u$ of N_2), but it is also similar to a "spin- and symmetry forbidden"/"dipole allowed" ratio (e.g., $E^3\Sigma_g^+/b^1\Pi_u$ of N_2). These results are certainly not definitive, but they indicate the utility of angular measurements as well as a need for more complete high resolution studies as a function of angle. In summary, we can only note that all of the arguments above are consistent with Z being either a "singlet" or "triplet" "g" state[180].

Figure 5.7-3 shows the intensity ratios for the peaks of the N → T, N → R, and N → 3R′ ($\nu_2 = 0$) transitions to that of the N → 3R ($\nu_2 = 0$) one. These data were obtained from scans of intermediate resolution (FWHM = .10 eV). The N → 3R ($\nu_2 = 0$) peak intensity was used as a reference because: (1) the resolution was not sufficient to use the N → R ($\nu_2 = 0$) peak intensity as a reference (the most "logical" choice), (2) the peak of the N → R transition could not be used since the N → Z transition might enhance it at higher angles, (3) the N → 3R′($\nu_2 = 0$)/N → 3R ($\nu_2 = 0$) intensity ratio is nearly constant with angle, indicating that both transitions are most likely "isolated" from underlying forbidden transitions and (4) the N → 3R ($\nu_2 = 0$) transition is not strongly overlapped as is the N → 3R′ one.

As expected, the singlet/singlet ratios are relatively flat while the triplet/singlet one increases markedly with angle. The latter ratio is quite characteristic of those for which transitions to the upper state have $\Delta S = 1$, $\Delta\Lambda = 0$. Since this transition is a $\pi \rightarrow \pi^*$ type, our conclusion concerning the acetylene triplets (i.e., they are not $\pi \rightarrow \pi^*$) is consistent with these results. The $\tilde{a}$ (or $\tilde{b}$)/$\tilde{C}$ ratio in acetylene increased by a factor $> 10^2$ from $\theta = 10°$ to 80° while the $\tilde{a}$/3R ratio in ethylene only increases by a factor of about 30 over the same angular range and at nearly the same incident energy above threshold.

The (N → R)/(N → 3R ($\nu_2 = 0$)) intensity ratio is not enhanced at higher angles as we might expect from the higher resolution data.

Figure 5.7-3. Peak intensity ratios in ethylene for E_o = 25 eV. The peak labels can be correlated with energy-losses from table 5.7-1. Each data point is an average of three scans. The FWHM of the elastic peak was 0.10 eV for these data.

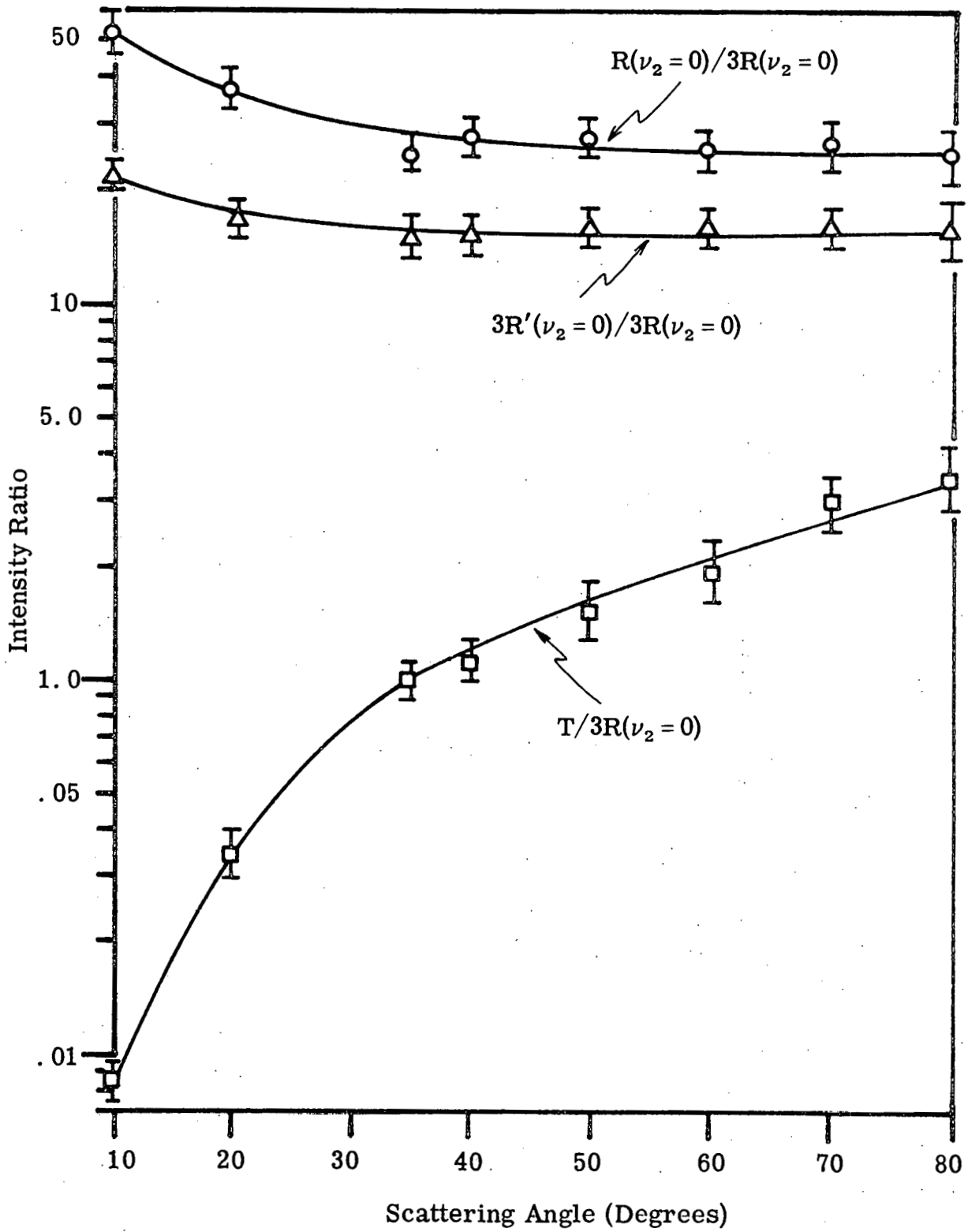
50
10
5.0
1.0
.05
.01
Intensity Ratio
$R(\nu_2 = 0)/3R(\nu_2 = 0)$
$3R'(\nu_2 = 0)/3R(\nu_2 = 0)$
$T/3R(\nu_2 = 0)$
10
20
30
40
50
60
70
80
Scattering Angle (Degrees)

However, there is a noticeable shift in the location of the N → R peak from 7.46 ± .01 eV at $\theta = 10°$ to 7.58 ± .05 eV at $\theta = 80°$ which attests to an underlying forbidden transition. The location of the N → 3R′ ($\nu_2 = 0$) peak does not change with angle.

Figure 5.7-4 shows a comparison of the shape of the N → T DCS calculated in section 3.3.7.2 with that of the experimentally determined one at 25 eV. The agreement is not very good. This is not unexpected since rather crude approximations have been used in the calculation. Figure 5.7-5 shows the calculated distributions at a few additional energies simply to indicate the predicted trends with energy and angle. The curves exhibit a rather unusual shape compared to other calculations on helium and hydrogen[66] using the same approximation. This is probably an artifact of the simple wave functions used in the present case. Inspection of equation (3-92a) shows that the DCS is zero whenever $q \cong 1.453\ a_o^{-1}$. Thus, if $K_o < .843\ a_o^{-1}$ ($E_o < 9.66$ eV), then the DCS will not be zero in the 0° to 180° angular range; if $R_o = .843$, then the DCS is zero at $\theta = 180°$; and if $k_o > .843$, the zero in the DCS moves toward smaller angles, varying as $\theta \approx \frac{1.45}{k_o}$ for $k_o \gg 1.45\ a_o^{-1}$ ($E_o \gg$ 28.6 eV).

Figure 5.7-6 gives the DCS (in arbitrary units) for the N → R (peak), N → 3R ($\nu_2 = 0$), and N → 3R′ ($\nu_2 = 0$) transitions at 25 eV. As expected, these singlet → singlet Rydberg transitions are strongly peaked in the forward direction with very similar shapes. (The latter, of course, was evident from the ratios.)

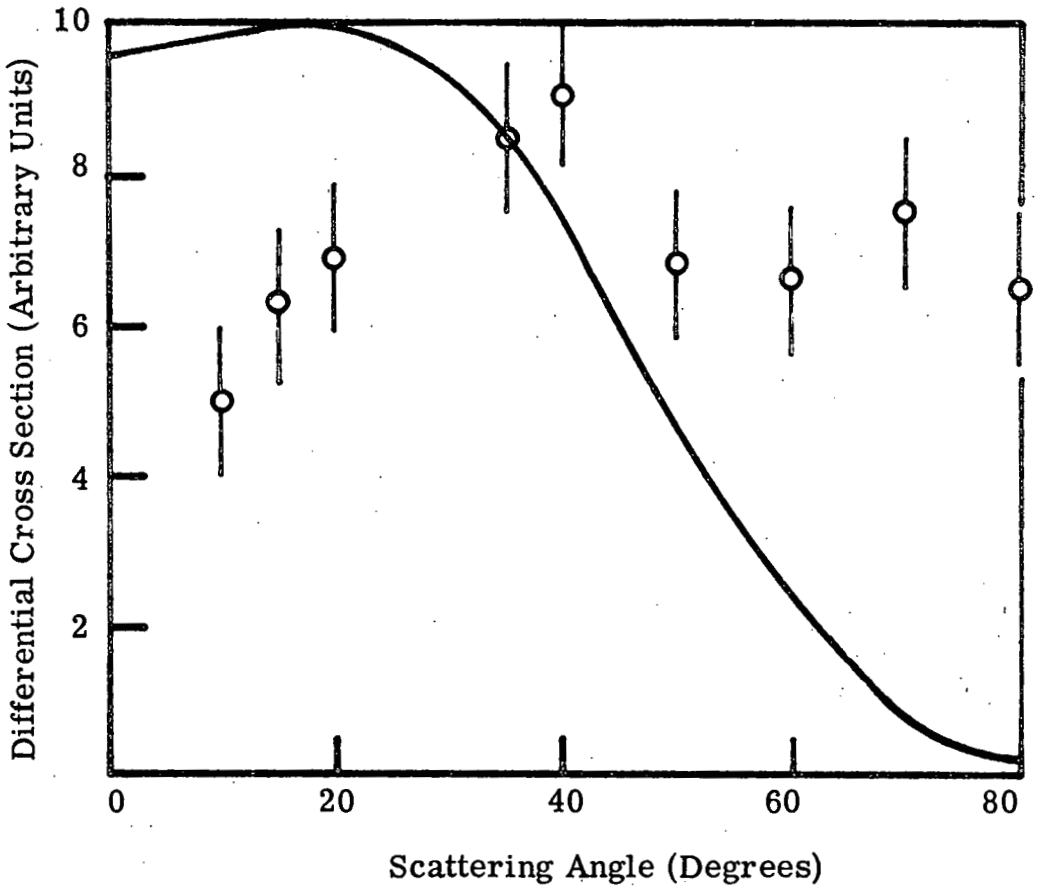

Figure 5.7-4. Differential cross section (arbitrary units) for the N → T transition in ethylene. The circles are experimental points for E_o = 25 eV (average of three scans). The solid line was calculated according to section 3.3.7.2. The data and calculations are normalized to the same value at θ = 35°.

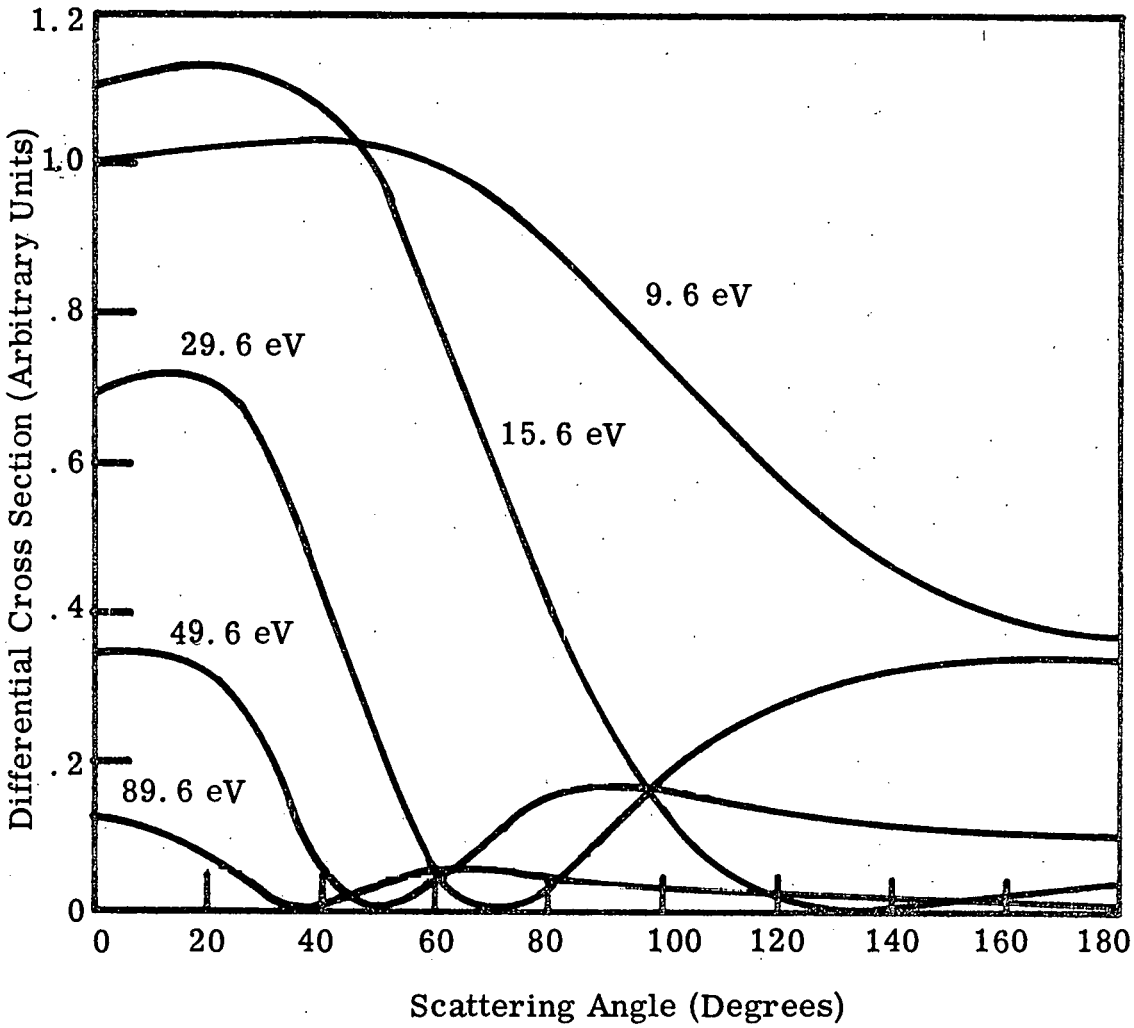

Figure 5.7-5. Differential cross section (arbitrary units) for the N → T transition in ethylene calculated according to section 3.3.7.2 for several incident energies. The relative scale for all of the curves is determined by normalizing the DCS at E_o = 9.6 eV and θ = 0° to 1.0.

Figure 5. 7-6. Differential cross section (arbitrary units) for several transitions in ethylene. E_o = 25 eV. Each data point represents an average of three scans.

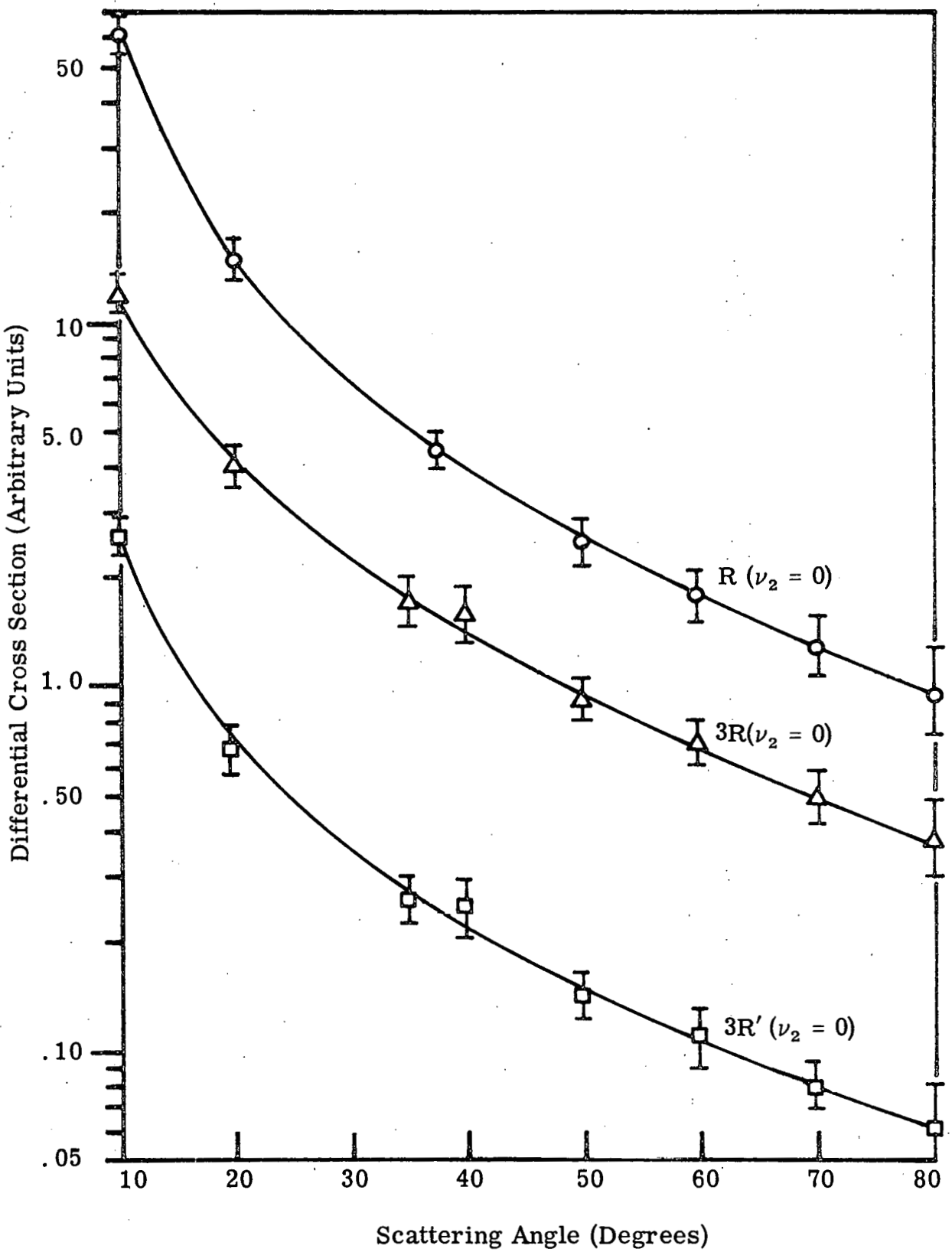
Differential Cross Section (Arbitrary Units)
50
10
5.0
1.0
.50
.10
.05
10
20
30
40
50
60
70
80
Scattering Angle (Degrees)
R (ν_2 = 0)
3R(ν_2 = 0)
3R′ (ν_2 = 0)

6. CONCLUSIONS

The work described in this thesis represents the first use of the measurement of electron-impact differential cross sections (DCS) as a function of scattering angle (θ) to characterize and identify singlet → triplet (spin-forbidden) transitions. We are hampered in our endeavor to draw general "spectroscopic rules" for the identification of such transitions from these DCS measurements by two things:

(1) The theory of electron-molecule scattering, though formally well developed, has not been applied with much success to DCS in the low-energy region (a few tens of eV's above threshold) in which exchange excitations are important; and

(2) practically all of the available experimental measurements of DCS angular dependencies (in this low-energy region) have been made by us during the course of this research on the few systems reported here. These handicaps mean that our "rules" are a self-consistent set of generalizations based primarily on a limited set of empirical results. Nevertheless, it is worth reiterating the consistent trends we have noted in sections 5.2 through 5.7.

The character of an excited state (of the target molecule) is reflected in the corresponding DCS. Differences in the behavior with θ of the DCS for the excitation of states of different character can be enhanced by comparing cross section ratios. This has been done for all of the transitions we studied. The DCS for an optically-allowed transition (usually the lowest lying such transition) in each

molecule was used consistently as a "standard" for ratio comparisons. Let DCSA be the DCS for excitation of the optically-allowed "standard" state (A) of some molecule and DCSB be the DCS for excitation of some other state (B) of the same molecule. Then, we will designate the quantity "DCSB/DCSA" (DCS ratio as used before in sections 5.2 through 5.7) simply by "the B ratio."

Table 6-1 presents a summary of some of the ratio data already discussed in sections 5.2 through 5.7 for singlet → triplet ($\Delta S = 1$) transitions. An examination of this table and the actual behavior with θ of various triplet state ratios leads us to the following conclusions:

(1) Triplet state ratios increase markedly with increasing $\theta (0° \leq \theta \leq 80°)$ for impact energies that are 20 to 30 eV above threshold. This behavior clearly distinguishes them from singlet state ratios.

(2) The magnitude of the triplet state ratio increase is sensitive to the value of $\Delta\Lambda$ associated with the singlet → triplet transition. Notice that the ratios for which $\Delta\Lambda = 1$ increase sharply by about two orders of magnitude over the angular range above in a manner that is independent of the g → g (or u) nature of the transition. On the other hand, triplet state ratios for which $\Delta\Lambda = 0$ increase by about one order of magnitude. From the examples of this latter type, those which are symmetry- allowed (SA) increase by about a factor of five more than those which are symmetry-forbidden (SF). Further, these $\Delta S = 1$, $\Delta\Lambda = 0$ ratios tend to reach a plateau at

TABLE 6-1

Summary of some pertinent data on all of the singlet → triplet transition ratios we have investigated. The first column lists the molecule (atom) and the transition whose DCS is used as a reference for the ratio determination (state A). The second column gives the B state associated with the factor increase (B ratio at high angle limit divided by B ratio at low angle limit) listed in the third column. The fourth, fifth, and sixth columns give the value of $\Delta\Lambda$, the impact-energy above threshold, and the limits of the angular range used to determine the factor increase, respectively.

Molecule (Atom)	B State	Factor Increase	$\Delta\Lambda$	Impact Energy Above Threshold (eV)	Angular Range (degrees)
He	2^3S	6	0	24	0 - 70
$1^1S \rightarrow 2^1P$	2^3P	60	1	23	0 - 70
N_2	$E^3\Sigma_g^+$	6	0	23	10 - 80
$X^1\Sigma_g^+ \rightarrow b^1\Pi_u$	$C^3\Pi_u$	100	1	24	10 - 80
	$B^3\Pi_g$	100	1	32	10 - 80
CO	$b^3\Sigma^+$	30	0	25	10 - 80
$X^1\Sigma^+ \rightarrow A^1\Pi$	$a^3\Pi$	100	1	29	10 - 80

TABLE 6-1 (Continued)

Molecule (Atom)	B State	Factor Increase	$\Delta\Lambda$	Impact Energy Above Threshold (eV)	Angular Range (degrees)
C_2H_2	$\tilde{a}$	1000	(1)[a]	30	10 - 80
$\tilde{X}^1\Sigma_g^+ \rightarrow \tilde{C}^1\Pi_u$	$\tilde{b}$	1000	(1)[a]	29	10 - 80
C_2H_4	T	35	0	21	10 - 80
(N → 3R)					
H_2	$b^3\Sigma_u^+$	30	0	30	10 - 80
$X^1\Sigma_g^+ \rightarrow C^1\Pi_u$					

[a] Presumably, $\Delta\Lambda = 1$ for these two transitions. See text, section 5.6.

intermediate angles, in contradistinction to the $\Delta S = 1$, $\Delta\Lambda = 1$ ratios.

In summary, triplet state excitations as a whole can be clearly identified by their ratio behavior (11 examples). The determination of $\Delta\Lambda$ from the ratio behavior also seems reasonably reliable (5 examples of $\Delta\Lambda = 0$ and presumably 6 examples of $\Delta\Lambda = 1$). There is no apparent difference in the ratio dependencies of SA and SF ratios for $\Delta\Lambda = 1$ (at least 1 SF example and 2 SA examples), while for $\Delta\Lambda = 0$, the SF ratios seem to increase less than do the SA ones (1 SF example and 3 SA examples). The reliability of these generalizations can be judged by the number of examples.

For singlet state ratios ($\Delta S = 0$), the situation seems more complex. In particular, these ratios do not exhibit any general trend with angle as do the triplet ones (this in itself, however, points up the $\Delta S = 0$ character of the former). Some singlet ratios are practically constant while others oscillate with either positive or negative slopes at small θ. In the case of CO, the signs of the initial slopes of the $^1\Sigma^+$ ratios change from negative to positive as the impact energy is lowered from 35 eV to 25 eV while a similar singlet state ratio ($p'\,^1\Sigma_u^+$) in N_2 has the same behavior at 25 eV that it has at 40 eV.

Consequently, we do not feel that any meaningful correlations between the ratio behavior and the value of Λ or the symmetry of the excited state can be derived from these investigations without additional data.

One diatomic molecule of special interest for future work is O_2. Since it has a triplet ground state, transitions to singlet states are spin-forbidden. This, of course, is simply the reverse of the excitations we have studied so far. In addition, O_2 has a low-lying singlet state with $\Lambda = 2$ (i.e., $a^1\Delta_g$) which, if we could observe it, would provide information about $\Delta S = 1$, $\Delta\Lambda = 2$ transitions (we have observed no other $\Delta\Lambda = 2$ transitions). The list of interesting polyatomic molecules is practically endless since the scattering from none other than those reported here have been studied as a function of angle at low energy. The study of methyl substituted ethylenes may help elucidate the nature of the olefinic "mystery band"[181]. Also the search for the low-lying triplet states of small molecules such as H_2O, CO_2, formaldehyde, etc. is worthwhile for future investigation.

APPENDIX I

OVERLAP OF TWO GAUSSIANS

Consider one energy analyzer (monochromator) for which $f(E)\,dE$ is the fraction of electrons of energy E transmitted in the energy range $E \rightarrow E + dE$ and a second analyzer (selector) for which $g(E - T)$ is the fraction of electrons of energy E transmitted per unit energy range. We assume that $f(E)$ and $g(E - T)$ have maxima at $E = 0$ and $E = T$, respectively, and are normalized so that

$$\int_{-\infty}^{\infty} f(E)\,dE = \int_{-\infty}^{\infty} g(E - T)\,dE = 1. \qquad \text{(I-1)}$$

If the output of the monochromator is directed into the selector, the fraction of electrons per unit energy range $F(T)$ that will be collected, apparently with energy T, at the selector output is

$$F(T) = \int_{-\infty}^{\infty} f(E)\, g(E - T)\,dE \ . \qquad \text{(I-2)}$$

For the present analyzer system, f and g can be adequately approximated by Gaussians (see section 4. 4. 3. 3) as

$$f(E) = \frac{1}{A\sqrt{\pi}}\, e^{-E^2/A^2} \qquad \text{(I-3)}$$

and

$$g(E - T) = \frac{1}{B\sqrt{\Pi}} \; e^{-(E - T)^2/B^2} \qquad \text{(I-4)}$$

where

$$A = \frac{\Delta E_{\frac{1}{2}}^{m}}{2\sqrt{\ell n 2}} \qquad \text{and}$$

$$B = \frac{\Delta E_{\frac{1}{2}}^{s}}{2\sqrt{\ell n 2}} \; .$$

$\Delta E_{\frac{1}{2}}^{m}$ and $\Delta E_{\frac{1}{2}}^{s}$ are the full-width at half-maximum (FWHM) of the monochromator and selector transmission functions, respectively.

Substitution of (I-3) and (I-4) into (I-2) and integration over E yields

$$F(T) = \frac{1}{\sqrt{\pi(A^2 + B^2)}} \; e^{-T^2/(A^2 + B^2)} \; . \qquad \text{(I-5)}$$

Consequently, the overall transmission function of this two analyzer system is Gaussian with a FWHM of

$$\Delta E_{\frac{1}{2}} = \left[(\Delta E_{\frac{1}{2}}^{m})^2 + (\Delta E_{\frac{1}{2}}^{s})^2 \right]^{\frac{1}{2}} \; . \qquad \text{(I-6)}$$

If both analyzers are operated with the same resolution (FWHM), then the FWHM of the beam leaving the monochromator as observed by the selector is $\sqrt{2}\,\Delta E_{\frac{1}{2}}^{m}$.

APPENDIX II

SPECIFICATIONS OF THE 1024 CHANNEL NUCLEAR DATA ANALYZER SYSTEM

1. Introduction

The system is a modified version of the ND-181 FM-ITB system described in Nuclear Data Inc.'s brochures entitled:

a. - ND-180 512 Channel Analyzer System
ND-181 1024 Channel Analyzer System

b. - Instruction Manual, ND-180 FM Pulse Height Analyzer System (November, 1964)

c. - Model ND-180 ITB Integrator and Time Base Unit Instruction Manual (February, 1965)

The main standard features are described in those brochures and are summarized below. The modifications of this system which are desired are described in Section 3 following. Section 4 lists the main components of the system.

2. General Description

2.1 Modes of Operation: A. Pulse Height Analysis (PHA)
B. Multi Channel Scaling (MCS)
C. Signal Averaging (SA). Wave Form Comparison Method

2.2 Number of channels: 1024

2.3 Count capacity per channel: 10^6

2.4 Count rate up to 10^6 per second in MCS.

2.5 Memory dividable into halves and quarters.

2.6 Capability of 2 and 4 detector operation by external routing in Modes PHA, Normal MCS, and Mode B-IV.

2.7 Transfer from any quadrant to any quadrant, bidirectional.

2.8 Coincidence and anticoincidence operation in all modes except in SA. Jacks on front panel for monitoring coincidence or anticoincidence and detector output signals to determine their time relationships.

2.9 Upper and lower level discriminator.

2.10 Display: Analog: CRT and X-Y Recorder.
Digital: Serial Print and Paper Punch.

2.11 Horizontal display position control on front panel to allow user to look at last portion of spectrum when spectrum is greatly expanded on external oscilloscope.

2.12 Auto repeat capability.

2.13 Time Base Unit with channel dwell times, 50, 100, 200, 500, 1000, 2000 μ sec., 5, 10, 20, 50, 100, 200 m sec., 0.5, 1, 2 seconds for MCS and SA.

2.14 Magnetic core memory "Live Time."

2.15 Live Time in steps of 1, 2, 4, 8, 10, 20, 40, 80, 100, 200, 400, 800, 1000 and infinity (minutes) in PIIA. Possibility of use of external oscillator. Live Time is always printed in first channel of memory.

2.16 Sweep triggering (MCS and Averaging): Internal, Recurrent, External. Plus or Minus, AC or DC triggering.

2.17 Sweep delay: 0, 1, 2, 4, or 8 times the selected sweep period.

2.18 Data and address lights.

2.19 Dead time meter.

2.20 Test mode.

2.21 Capability of overlapping quarters and halves.

2.22 Capability of normalizing data in each half of memory when in overlapping position.

2.23 Calibration capability to add 1000 counts to all memory channels.

2.24 Manual address advance (one channel at a time) for digital readout of channels of interest.

3. Modifications

In addition to the standard features mentioned in Sections 1 and 2 above, the following modifications are included.

3.1 Forward and Forward-Backward Address Scaler. Either type of operation can be selected in modes of operation PHA and MCS.

3.2 In Multi-Channel Scaling Mode, besides the normal operation mode, called hereafter MCS-I, an additional mode is required, labeled MCS-II.

3.2.1 Mode MCS-II

In this mode the Nuclear Data System will be attached to an electron scattering apparatus. This apparatus has an electron detector system (ED), an electron beam chopper (EBC), and an

electrostatic energy analyzer (EA).

3.2.1.1 General Description of MCS-II Mode

The Time Base Generator (TBG) in the Nuclear Data ITB Unit supplies appropriate pulses to Square Wave Generator (SWG). SWG makes the voltage across terminals P_1 and P_2 change alternately between 0 and 10 volts at a frequency determined by the dwell time (Δt) selected by the ITB. (P_1 and P_2 are not grounded.) TBG also supplies the appropriate pulses to Translator (TR) in such a way that when the electron beam is on (voltage difference between P_1 and P_2 (V_1) is zero), the incoming counts are routed into the first half of the memory of ND-181 FM and when the electron beam is off (V_1 = 10 V), the incoming counts are routed into the second half of the memory.

The Raytheon DAC-20-10 Unit (incorporated by Nuclear Data as part of the analyzer system) supplies an analog voltage (range 0-10 V) which is proportional to the channel number in the first half of the memory if First/Direct Switch (FD-S), incorporated into the system by Nuclear Data, is in First position, and strictly proportional to the channel number into which counts are being accumulated if FD-S is in Direct position. For Mode MCS-II this switch is in the First position. During the time in which counts are being accumulated in channel 1 (first half of the memory) and then into the matching channel 513 (in the second half of the memory) the analog voltage has the same value. A differential amplifier system (supplied by Nuclear Data as part of the system) with an amplification range of

0-10 (with steps 1.0, 2.0, 3.0, 4.0, 5.0, 6.0, 7.0, 8.0, 9.0, and 10.0) amplifies the analog signal supplied by the DAC. The amplified signal, V_2, is available for external use across terminals P_3 and P_4. (P_3 and P_4 are not grounded.) The stability and reproducibility for these voltages are given later in this Section.

A block diagram of this mode is shown in Figure II-1. Figure II-2 shows the various voltages and time relations.

3.2.1.2 Step by Step Description of MCS-II Mode

Step 0. System is not counting (standby position), but TBG is operating and the square wave signal appears across P_1 and P_2. Operator command (manual setting of control switch to start position) causes counting to begin as per Step 1 without disturbing the square wave in any way.

Step 1. When counting is initiated, counts are accumulated in channel number i (i = 1 to start) in the first half of the memory for time Δt, beginning precisely (within 1 μ sec.) when the square wave on terminals P_1 and P_2 goes to zero. The analog voltage across P_2 and $P_3(V_2) = 0$.

Step 2. Counts are accumulated in channel 513 for time Δt beginning precisely (within 4 μ sec.) when $V_1 = 10$ volts. V_2 is left unchanged.

Step 3. i is increased by one and Steps 1 and 2 are repeated until channel 1024 is reached. When channel 1024 is reached, a Full cycle has been completed.

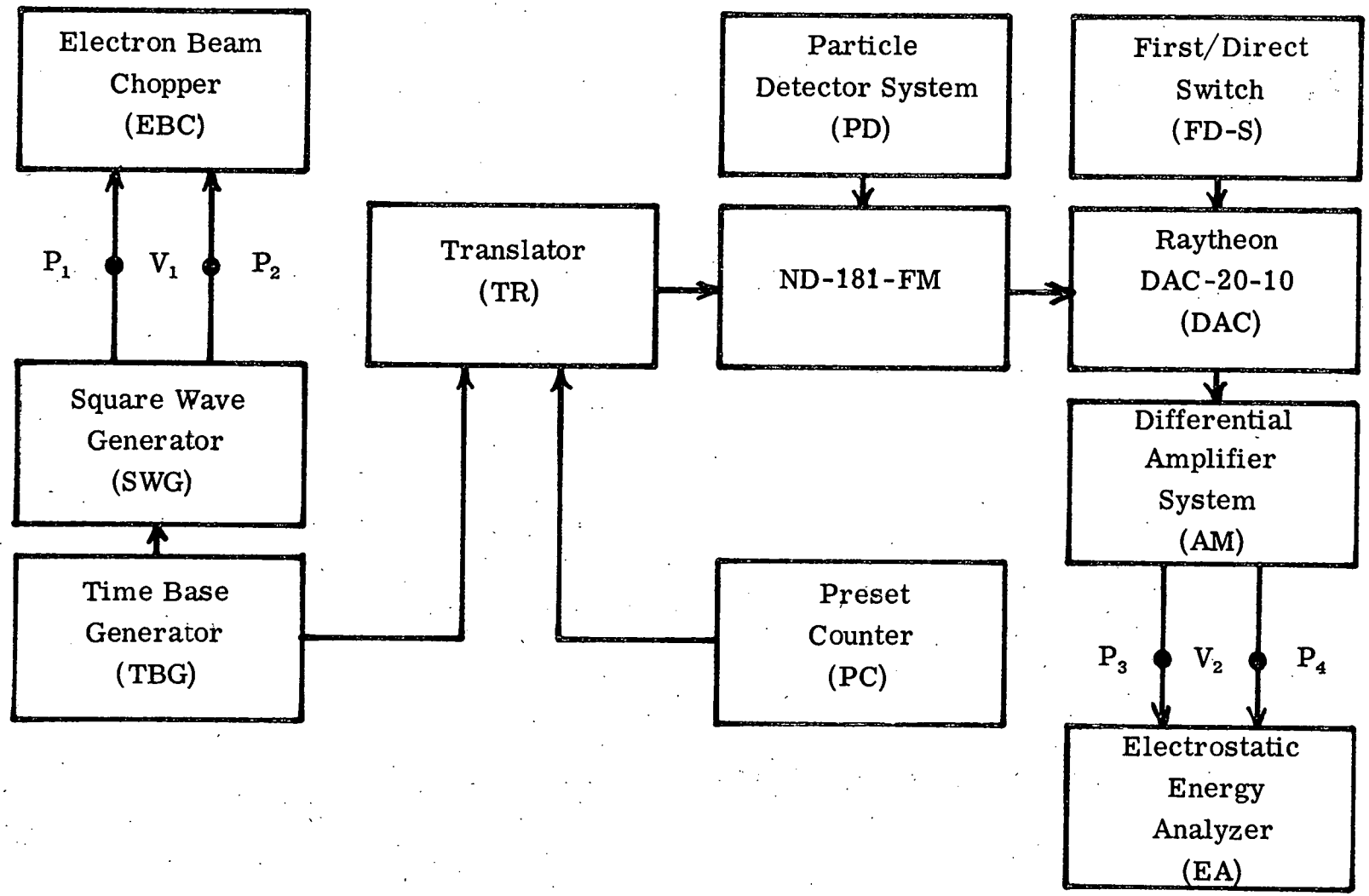

Figure II-1. Block schematic diagram for Mode MCS-II.

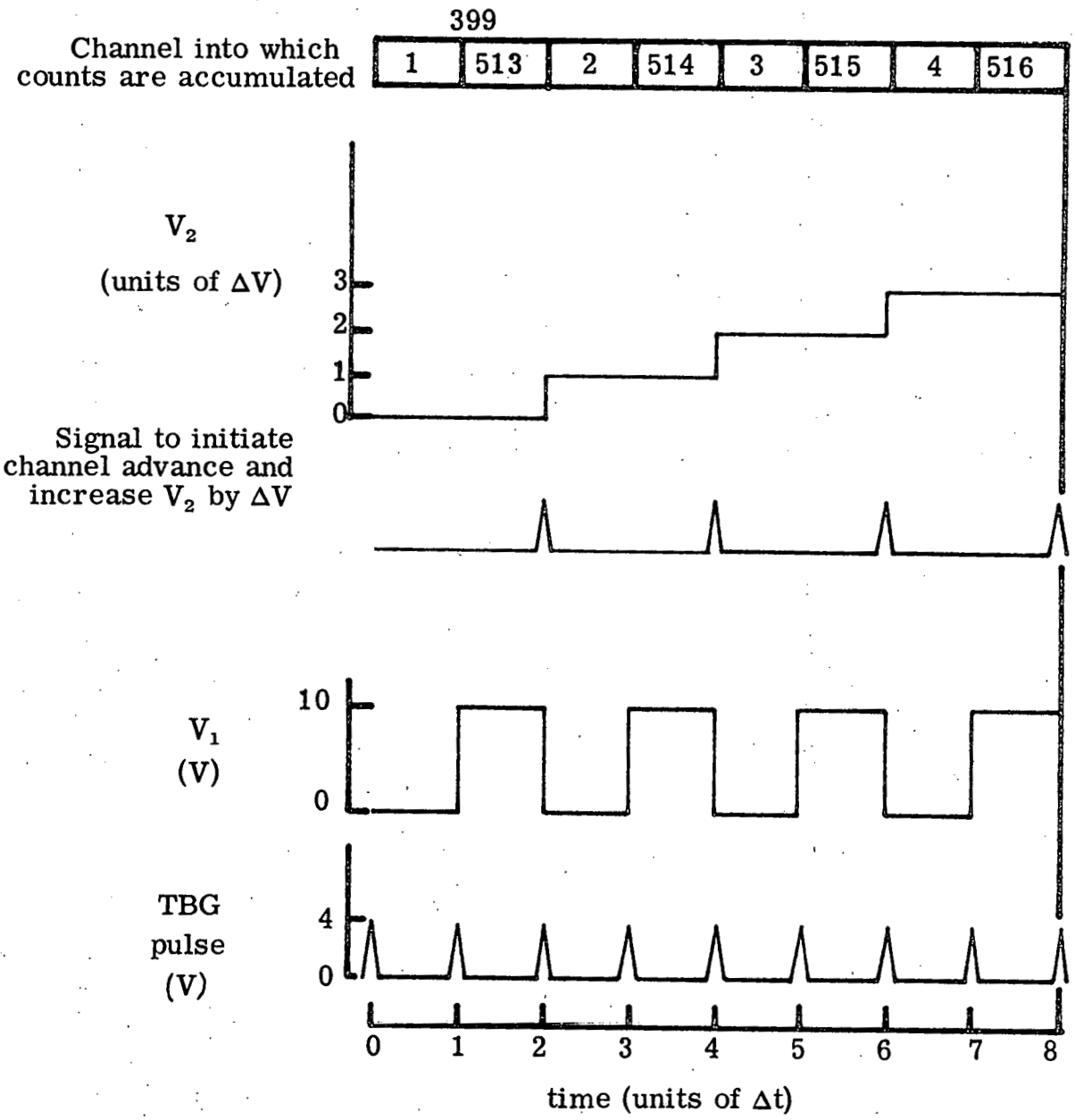

Figure II-2. Time signal relations for Mode MCS-II.

Step 4. Full cycle is repeated as many times as selected on the 5-digit present counter (PC) incorporated into the system by Nuclear Data.

3.2.1.3 Specifications for Mode MCS-II

a. - V_1 is 0 or 10 volts within 0.1 volts. The rise time and decay time for switching between these two values is less that 4 μ sec.

b. - V_2 is proportional to the channel number in the first half of the memory or to the channel number into which counts are being accumulated depending on whether FD-S in in First or Direct position, respectively. When the differential amplifier is set at gain 1, the range of V_2 is 0.000 to 10.240 V with a deviation from linearity that is less than 1 mV and reproducibility better than 1 mV in the entire range. When the amplifier gain is 10, the range is 0.00 to 102.40 V and deviation from linearity and reproducibility is less than 10 mV in the entire range. As the channel address is increased by one, the time for V_2 to reach its new value (to within 0.01%) is 1 μ sec. or less. As this address is switched from 1024 to 1, the time for V_2 to drop to less than 1 mV is 10 μ sec. or less.

c. - Δv, the voltage step, is 10, 20, 30, 40, 50, 60, 70, 80, 90, or 100 mV corresponding to gain 1, 2, 3, 4, 5, 6, 7, 8, 9, or 10 of the differential amplifier.

d. - Δt, the dwell time selected on ITB: see Section 2.13.

e. - DAC-20-10 Unit: see Raytheon Booklet SP-171C, pp. 6 and 7.

f. - Output impedence is $\leq$ 1000 ohms for both V_1 and V_2.

g. - Synchronization between ITB pulses and changes in V_1 and V_2 is 1 μ sec.

h. - Dwell times in corresponding channels of two halves of the memory (for example, channels 2 and 514) are equal to within 0.25 microseconds or 1 part in 10^5, whichever is larger.

4. Components

The major components of which the system is composed are:

a. - ND-181-F

b. - ND-181-M

c. - ND-180-ITB

d. - ND-312 Teletype

e. - Raytheon DAC-20-10

f. - Differential Amplifier System

g. - Translator

h. - Preset Counter

i. - Modification of ITB

APPENDIX III

Angular Dependence of Low-Energy Electron Impact Excitation Cross Section of the Lowest Triplet States of H_2

by

S. Trajmar,* D. C. Cartwright,†‡ J. K. Rice,† R. T. Brinkmann,* and A. Kuppermann†

California Institute of Technology, Pasadena, California

(Received 12 July 1968)

ABSTRACT

The differential cross sections for the electron impact excitation of the lowest triplet states of molecular hydrogen ($b^3\Sigma_u^+$, $a^3\Sigma_g^+$) have been calculated from threshold to 85 eV impact energy using the Ochkur-Rudge theory. For the $X^1\Sigma_g^+ \rightarrow b^3\Sigma_u^+$ transition, the relative differential cross sections

---

*Jet Propulsion Laboratory. Work supported in part by the National Aeronautics and Space Administration, Contract NAS7-100.

†Albert Amos Noyes Laboratory of Chemical Physics, contribution number 3705. Work supported in part by the U. S. Atomic Energy Commission. Report Code CALT 532-33.

‡Present address: The Max Planck Institute for Physics and Astrophysics, Institute for Extraterrestrial Physics, 8046 Munich, Germany.

were measured with a low-energy, high-resolution electron impact spectrometer from 10° to 80° scattering angle and impact energies of 25, 35, 40, 50, and 60 eV. Theory and experiment are in good agreement for the shape of the differential cross section for energies of 35 eV and above. However, at 25 eV, the theory continues to predict a rather well developed maximum in the cross section at around 40° while the experimental cross sections are more isotropic. An appreciable contribution to the inelastic scattering in the energy loss region from 11 to 14 eV due to excitation to the $a^3\Sigma_g^+$ and/or $c^3\pi_u$ states is definitely established from the observed angular distributions. A quantitative evaluation of the individual angular behavior of the excitations in this region, however, would require a resolution higher than the presently available one of 0.030 eV.

1. INTRODUCTION

Low-energy electron impact spectroscopy has been found to be a very powerful tool for locating and identifying energy levels of molecules, especially those to which transitions from the ground state are forbidden by optical selection rules.[1-9] (The low-energy range as defined here is from a few eV up to 100 eV. This corresponds to the binding energy of outer electrons in atoms and molecules and is a very important region from the point of view of spectroscopy, photochemistry, plasma physics, and for many atmospheric phenomena.) Both the energy and angular dependencies of the differential cross section are important in identifying a given transition. The energy dependence of the differential cross section has been investigated to some degree in the past.[1-9] However, there is very little information available on the angular dependence of excitation cross sections at low impact energies. The Born-Oppenheimer approximation is not valid at these impact energies; in fact, no theory has proved reliable in predicting the energy and angular dependencies of differential cross sections for even the simplest system of electron-atomic hydrogen.

Recent studies of He,[9a] C_2H_2,[9b] H_2, N_2, CO, CO_2, H_2O, and C_2H_4,[10] indicate that the measurement of the differential cross section at a fixed incident energy and variable scattering angle yields more information about the nature of the electronic excitation than does the measurement of the energy dependence of the differential cross section at a fixed scattering angle. In order to learn more about the angular behavior of differential cross sections for different types of electronic

excitations, it is important to carry out experiments on transitions of known character. The information obtained from such studies is useful in the evaluation of different approximate theories and may lead to rules for assigning unknown transitions.

The hydrogen molecule, being the molecule most amenable to theoretical calculation, was the natural selection for comparison between theory and experiment. Cartwright and Kuppermann[11] have calculated total cross sections for the electron impact excitation of the two lowest triplet states of molecular hydrogen using the Ochkur-Rudge (OR) theory.[12] These cross sections agree well with Corrigan's experimental electron impact dissociation cross sections[13] from threshold to about 50 eV. A comparison between the theoretical and experimental angular distributions as functions of incident energy provides an additional and more sensitive test of the theory, since integration of the differential cross section may conceal a failure of the theory while still leading to the correct total cross section. Green[14] has pointed out that the arguments of Rudge[12c,d] and Crothers[12e] justifying Rudge's modification of the Ochkur theory are of doubtful validity and the best test of these theories is comparison with experimental differential cross sections. Hence, the (OR) approximation has been used to calculate the differential cross sections for the $X^1\Sigma_g^+ \rightarrow b^3\Sigma_u^+$ and $X^1\Sigma_g^+ \rightarrow a^3\Sigma_g^+$ excitations for comparison with the equivalent experimental measurements. The singlet-triplet transition provides an unambiguous test of rearrangement scattering theories since they are due entirely to exchange excitation with no contribution from direct process.

A broad feature in the electron impact spectrum of H_2 corresponding to the $X^1\Sigma_g^+ \rightarrow b^3\Sigma_u^+$ transition has been observed by Schulz[2a] and Dowell and Sharp[15] using the trapped-electron method. By this method the total cross section is measured very near threshold energy. Kuppermann and Raff[4c] also observed the $X^1\Sigma_g^+ \rightarrow b^3\Sigma_u^+$ transition at 60 eV impact energy with an apparatus which collected scattered electrons from 22° to 112°, the collection efficiency being highest at 90°. To our knowledge there are no experimental or theoretical differential cross sections for electron-exchange processes in molecular hydrogen to which our results can be compared.

2. THEORY

Most previous calculations of the exchange excitation of atoms by low energy electrons have been performed in the Born-Oppenheimer (BO) approximation.[16] The results of such calculations, however, indicate that the (BO) approximation fails badly for incident electron energies below about 100 eV.[17] The calculation of similar exchange processes involving diatomic molecules has been limited by the mathematical difficulty of treating the noncentral molecular force field and the nuclear motion. Ochkur[12b] and Rudge[12c] have proposed modifications of the (BO) approximation which have been found to give reliable total cross sections for exchange processes in atomic systems. Recently, this (OR) approximation was employed to calculate total cross sections for excitation of the $(b^3\Sigma_u^+)$ and $(a^3\Sigma_g^+)$ states of molecular hydrogen.[11] The methods used in the cross section calculations reported here are very similar to the ones used in the total cross section calculations and consequently are only briefly outlined.

Within the framework of the (BO) separation of nuclear and electronic motion [18] and the (OR) approximation to the exchange scattering amplitude of an electron by a diatomic molecule, the differential cross section for exchange excitation from initial state $i(n,\nu,J,M)$ to final state $f(n',\nu',J',M')$ can be written as

$$I_i^f(k_o,\theta,\varphi) = \frac{3k'}{k_o} \left| \int_{R,\Omega} \xi_{n',\nu'J'}^{*}(R)\, Y_{J'}^{M'*}(\chi,\phi)\, T_i^f\, \xi_{n\nu J}(R)\, Y_J^M(\chi,\phi) R^2 dR d\Omega \right|^2, \quad (1)$$

where

$$T_i^f(k_o,\theta,\varphi;R,\chi,\phi) \equiv \frac{2a_o}{\left[a_o k' - i\left(I_n/\mathcal{R}\right)^{\frac{1}{2}}\right]^2}$$

$$\times \int e^{i\vec{q}\cdot\vec{r}_1}\, \psi_{n'}^{*}(\vec{r}_1,\vec{r}_2;R)\, \psi_n(\vec{r}_1,\vec{r}_2;R) d\vec{r}_1\, d\vec{r}_2 \quad (2)$$

In Eqs. (1) and (2), ψ,ξ, and Y are the spatial electronic vibrational and rotational wave functions; I_n is the ionization energy of state n; $\mathcal{R}$ is the Rydberg energy; a_o is the Bohr radius; R the internuclear distance; χ,ϕ the polar orientation angles of the internuclear axis with respect to a space-fixed coordinate system; $d\Omega$ is the element of solid angle in the direction of the internuclear axis; θ and φ are polar angles defining the direction of scattering with respect to the direction of the incoming free electron; $\vec{r}_1$ and $\vec{r}_2$ are the coordinates of the bound electrons in the molecule fixed coordinate system; n,ν, and J are the electronic, vibrational and rotational quantum numbers; $\vec{k}_o$, $\vec{k}'$ are the initial and final wave number vectors of the free electron which are related by

$$k'(k_o, i, f) = \left[k_o^2 - (2m/\hbar^2)(E_f - E_i)\right]^{\frac{1}{2}} \quad (3)$$

where E_i and E_f represent the total energy of the molecule before and after collision, and finally

$$\vec{q} = \vec{k}_o - \vec{k}'$$

The factor of 3 in Eq. (1) comes from integration over spin variables. Since the presently available experimental energy resolution is not sufficient to resolve rotational transitions, only rotationally averaged differential cross sections will be considered here. If the temperature of molecular hydrogen is appreciably higher than its rotational characteristic temperature (174°K), then the rotationally averaged differential cross section for a gaseous thermal target is given by

$$I_{n\nu}^{n'\nu'}(k_o,\theta,\varphi) = \frac{3k''}{k_o}\int_\Omega \left|\int_R \left[R\xi_{n'\nu'}(R)\right]^* T_{n\nu}^{n'\nu'}(k_o,\theta,\varphi;R,\chi,\phi)\left[R\xi_{n\nu}(R)\right]dR\right|^2 \frac{d\Omega}{4\pi} \quad (4)$$

where

$$k''(k_o,n,\nu,n',\nu') = \left[k_o^2 - (2m/\hbar^2)(E_{n'\nu'} - E_{n\nu})\right]^{\frac{1}{2}} \quad (5)$$

In the derivation of (4), the vibrational wave functions and the wave number of the scattered electron were assumed independent of J and J'. This assumption is consistent with present experimental energy resolution capabilities.

The excited ($b^3\Sigma_u^+$) state is unbound and hence there is a continuum of ν'-vibrational states. The differential cross section for excitation to all final vibrational states is formed from (4) by "summing" over ν'. Application of the delta-function approximation[19] to (4) leads to a rotationally averaged differential cross section for excitation from the

ground vibrational state to all excited vibrational states which is given by

$$I^{(1)}(k_o,\theta,\varphi) = \frac{3k''}{k_o} \int_{D_o}^{E_o} P^{(1)}(E_1) \langle |T_{v'}^{(1)} R^{(1)}(E_1)|^2 \rangle dE_1 \qquad (6)$$

where

$$P^{(1)}(E_1) \equiv \frac{|R^{(1)}(E_1)\xi_o^{(o)}[R^{(1)}(E_1)]|^2}{\int_{D_o}^{\infty} |R^{(1)}(E_1)\xi_o^{(o)}[R^{(1)}(E_1)]|^2 \, dE_1} \qquad (7)$$

In the above, D_o is the dissociation energy of the ground electronic state; E_o is the energy of the incident electron; $\xi_o^{(o)}$ is the lowest vibrational wave function of the ground electronic state; and the angular brackets represent an average over all orientations of the internuclear axis with respect to the incident electron beam. The integration over the internuclear distance R has been transformed to an integration over the corresponding potential energy E_1. E_1 (R) is the expression for the potential energy of the $b^3\Sigma_u^+$ state as a function of internuclear distance and $R^{(1)}(E_1)$ is the inverse of this function.

The $a^3\Sigma_g^+$ state is bound (dissociation energy 2.91 eV) and has about 16 vibrational states and no continuum whose left classical turning points fall within the Frank-Condon vertical band from the ground electronic-vibrational state. The calculation of the differential cross section for this state is performed similarly to that of the $b^3\Sigma_u^+$ state.

In the calculations reported here, the electronic wave functions used were those of Weinbaum[20] for the ground state, Phillipson-Mulliken[21] for the $b^3\Sigma_u^+$ state, and a two parameter Hartree-Fock wave function for the

$a^3\Sigma_g^+$ state. The numerical methods used were similar to those discussed previously[11] and the results reported here are believed to have computation errors of less than 10%.

3. MEASUREMENT OF THE CROSS SECTIONS

3.1 Apparatus

The low-energy electron-impact spectrometer used in these experiments is basically the same type as the one described by Simpson[22] and Kuyatt and Simpson.[23] It consists of a low-energy electron gun, a scattering chamber, two hemispherical electrostatic analyzers (for generating a monochromatic electron beam and energy-analyzing the scattered electrons), and a detector. The resolution of each of the two electrostatic analyzers is variable in the 0.030 to 0.300 energy range by appropriately adjusting the sphere potentials. The scattering chamber is a welded-bellows cylinder which allows a variation in scattering angle from -30° to $+90^\circ$. The convolutions of the bellows have an "s" shape and form an electron trap which reduces the effect of wall scattering which could seriously interfere with the measurements at higher angles. The scattering chamber sample pressure is normally in the 10^{-5} to 10^{-2} torr region. The pressure is measured with miniature ion and thermocouple gauges and is kept constant during an experiment by a variable leak and a pressure controlling system. Temperature control of the target gas is possible by introducing cooling or heating media into the area between the scattering chamber and a second bellows which surrounds it. The second electrostatic energy analyzer is tuned to pass electrons with the same energy as the first energy selector. A sweep voltage is applied between scattering chamber and center of the second analyzer.

When this voltage is zero, electrons that did not lose any energy during the scattering will pass this analyzer and reach the detector, a twenty stage electron multiplier. The multiplier output can be coupled to a count-rate-meter or a 1024 channel scaler. As the sweep voltage is gradually increased, electrons that have lost the corresponding energy in exciting the molecular target will reach the detector. The number of electrons counted per unit time versus the sweep voltage furnishes an energy-loss spectrum. The energy-loss sweep voltage is controlled either by a sweep generator or by the multichannel scaler whose memory channel number (into which counting occurs) is converted to an analog voltage. External field effects are eliminated with appropriate radio frequency and magnetic shielding. The entire apparatus is bakable to 400° C. A more detailed description of the system is given elsewhere.[24]

3.2 Experimental

In these experiments the electron current scattered into a given solid angle of approximately 10^{-3} steradian was measured as a function of energy loss at a fixed electron impact energy. A typical energy-loss spectrum is shown in Fig. 1. It is an X-Y recording of the count-rate-meter output. The X-axis represents the energy-loss of the electrons and the Y-axis corresponds to the number of electrons per minute reaching the detector with each particular energy loss. This spectrum was obtained with an electron impact energy of 50 eV and a scattering angle of 40°. The elastic peak shown on the left-hand side determines the zero energy loss point.

The apparatus for the $b^3\Sigma_u^+$ excitation was tuned to about 0.2 eV resolution (full width at half-maximum FWHM of the elastic peak). This was a reasonable choice to insure high signal level and partial resolution of the vibrational structure of the $X^1\Sigma_g^+ \rightarrow C^1\pi_u$ transition. Most of the measurements were made with a count-rate-meter with a time constant that varied from 0.5 sec for the elastic peak to 10 sec for the triplet transition at high angles. The energy-loss sweep-rate was adjusted accordingly to give an undistorted reproduction of the features. The energy-loss scale is absolute, being measured with a digital voltmeter with respect to the center of the elastic peak. Its accuracy (about 10 meV) is verified by the optical values of the portions of the vibrational bands of the $C^1\pi_u$ excitation.

For the experiments in the 11-14 eV energy loss region the instrument was retuned to obtain an overall resolution of about 0.040 eV (FWHM). Typical spectra at this resolution are shown on Figs. 2 and 3 and discussed below.

In order to monitor the conditions at different angles during the experiment, and check the overall instrument stability, the pressure and the beam current in the scattering chamber were measured and the elastic peak was scanned before and after each energy loss spectrum was taken. The pressure of H_2 was kept constant (to within about 5%) at a value between 1 and 2 millitorr during each experiment and the linearity of the scattered current with pressure was established from 0.1μ up to 2μ.

3.3 Scattering Volume Correction and Error Estimation.

Measurements taken at different scattering angles correspond to different scattering geometry. If one wants to compare cross sections at different angles, a normalization of all measurements to the same

scattering geometry is necessary. It is customary[25] to carry out this normalization by multiplying the scattered current by sin θ where θ is is the scattering angle. This procedure yields proper normalization only if the electron beams entering the scattering chamber and the electron optics of the detector system have small diameter and angular divergence.

In our instrument circular apertures are used for collimating and focusing the electron beam. The scattering geometry is shown on Fig. 4. Both the electron beam entering the scattering chamber and the directions viewed by the electron optics at the exit of this chamber are represented by cones. Typical values for the incident beam and exit viewing cone half angles are 3° and 4.5° respectively. The intersection of these two cones defines the volume from which scattered particles can reach the detector. The solid angle extended by the detector varies from point to point within this volume in fact it drops to zero at the extremes. One has to average therefore, the solid angle over this volume to get an effective value of (scattering length) x (solid angle) $\equiv (\ell d\Omega)_{eff}$. This problem has been discussed by G. Breit, H. M. Thaxton and L. Eisenbud[26a] and by C. L. Critchfield and D. C. Dodder.[26b] Every differential volume element within this volume has to be properly weighted for electron density and solid angle subtended at the entrance of the detector optics. For normalizing our measurements, the incoming beam was considered as a cone with a truncated Gaussian electron density distribution having its maximum along the cone axis. The density weighted volume elements of the beam cone were integrated within the limits defined by the surface of the view cone. Each element was also weighted by the inverse square of the distance from the entrance aperture of the detector to allow for the solid angle of the detector at the volume element. The value of $(\ell d\Omega)_{eff}$ at

each angle was normalized to the value at 90°. The differential scattering cross section for a particular excitation is proportional to the peak height (after correction for scattering geometry) provided that the cross section is independent of angle within the range defined by the view cone and that the line shape is independent of angle. At $\theta = 10°$, the difference between these calculations and the approximate sin θ correction is about 10%.

The errors inherent in the reduced measurements are of three types:

1. Random fluctuations and background noise. If the number of counts per second reaching the detector is N, then from the statistical nature of the counting process, the uncertainty in N (one standard deviation) is $\pm\sqrt{N/\tau}$ where τ is the time constant (in sec) of the rate meter.[27] This fluctuation was always less than 5% for the $X^1\Sigma_g^+ \rightarrow b^3\Sigma_u^+$ peak. In addition, there is a background noise due to stray electrons, electronic noise, and cosmic rays. This noise is relatively independent of scattering angle and amounts to about 2 counts per sec.

2. Effective scattering volume correction. Another source of error arising from the effective volume correction is due to the ±1° uncertainty in the scattering angle and the uncertainties in the beam and view cone angles. These latter angles cannot be determined directly with the present experimental setup. The latter, however, can be estimated from the electron optics with satisfactory accuracy. The beam cone angle is then obtained from the direct beam intensity profile as measured on the first dynode of the multiplier as a function of scattering angle. (The peak position of this curve defines the zero scattering angle.)

3. Instrumental error. This includes all effects associated with the variation of pressure, beam intensity, and overall instrument detection efficiency during the measurements. The constancy of these quantities is monitored during each energy-loss sweep but a significant change of instrument detection efficiency with scattering angle could go undetected. The fact that the optimum tuning conditions are found to be the same at any angle and that the scattering intensity is symmetric around zero angle, indicates that this effect is negligible.

The error bars assigned to the measurements include estimated contributions from these three sources of error.

4. RESULTS AND DISCUSSION

As seen in Fig. 1, the inelastic feature corresponding to the $X^1\Sigma_g^+ \rightarrow b^3\Sigma_u^+$ transition has a maximum at about 10 eV energy loss. Since the $b^3\Sigma_u^+$ state of H_2 is unstable with respect to dissociation into two hydrogen atoms, the transition is represented by a broad feature whose shape seems to be determined[11] by the Frank-Condon overlap integrals.[28a] In the 11 to 14 eV energy loss region several singlet and triplet transitions overlap.[28b] The optical vibrational band progression for the $X^1\Sigma_g^+ \rightarrow C^1\Pi$ transition is shown.

To determine the angular dependence of the differential cross section for this transition, the corresponding maximum ordinate was read off the energy loss spectrum at each angle and normalized to the same scattering volume with the calculated effective scattering volume described above. Using this peak height instead of the area under the band does not introduce any error if the line shape is the same at all

angles. We found that this was indeed the case for both the elastic and inelastic features of the energy loss spectra. In order to compare the absolute theoretical and relative experimental cross sections, the latter are multiplied at each energy, by a factor which is the average of the ratios of the calculated absolute and experimental relative cross sections at each angle. The possibility of appreciable contribution from the strong $C^1\pi_u$ tail was eliminated by plotting the cross sections obtained not only from the maximum ordinate measurements, but from measurements at 0.5 and 1.0 eV away from that maximum. No change in the shape of the curves of relative cross section versus scattering angle was observed.

Figure 5 compares the theoretical and experimental differential cross sections at 25, 35, 40, 50, and 60 eV impact energies. The solid curves are the calculated ones. Each experimental point was obtained from a spectrum similar to the one shown in Fig. 1.

At 50 and 60 eV the calculated and observed curves agree quite well. As one goes to lower impact energies, however, the disagreement between theory and experiment increases. While the theory predicts well-formed maxima at around 40° for low impact energies, the experiment shows fairly isotropic scattering below 35 eV. Although the measured differential cross sections are in arbitrary units, the absolute values obtained from them by the procedure described above should be close to the correct ones at 50 and 60 eV impact energies, since for them the experimental and calculated differential cross sections agree very well and the total cross section obtained from the integration of the calculated differential cross sections agrees approximately with Corrigan's measurement.[11,13] In

calculating the total cross section, Cartwright and Kuppermann[11] neglected the contribution from the excitation to the $c^3\pi_u$ state. Inclusion of this contribution may improve this agreement.

The validity of the Ochkur (O) and (OR) theories of electron exchange scattering can be tested only in a very few cases due to the lack of experimental data and/or more accurate theoretical calculations. The (O) approximation may be considered as an (OR) approximation with improper normalization of the wave function. For the 2^3S excitation of He the shape of the experimental differential cross section of Ehrhardt and Willman[7b] agrees with the OR predictions at 24 eV from 20° to 120°.[29] The experimental data of Simpson, Menderez, and Mielczarek[6b] at 56.5 eV (5°-50°) and Vriens, Simpson, and Mielczarek[25] in the 100 to 225 eV energy range (5° - 15°) are in complete disagreement with the (OR) and (O) curves for the same excitation. In the case of atomic hydrogen, a comparison of the (OR) differential exchange cross sections for elastic scattering and the 1s → 2s excitation to the accurate close coupling calculation of Burke, Shey and Smith[30] has been made by Truhlar, Cartwright, and Kuppermann.[31] They find that the (OR) angular distributions are in qualitative agreement with the close coupling results at intermediate energies but at low energies the agreement is very poor.

It is somewhat surprising, especially in light of the above discrepancies, that the (OR) approximation predicts as well as it does the shape of the angular distribution for the $X^1\Sigma_g^+ - b^3\Sigma_u^+$ transition in H_2 for energies as low as 40 eV. Since the theory is based on first order perturbation principles, the above comparison between theory and experiment implies that for the angular regions and impact energies considered

here the deviation of the interactions from first order are not important or that the agreement is simply an accident. It is important therefore to do additional comparisons between experiment and theory before the usefulness of the (OR) approximation can be determined.

Figures 2 and 3 show the energy loss spectrum of H_2 in the 11 to 14 eV region with a resolution (FWHM) of about 0.040 eV at 20° and 80° respectively. The electron impact energy was 40 eV for these experiments. Many of the vibrational features of the $B^1\Sigma_u^+$ and $C^1\pi_u$ excitation are separated and they account practically for all the intensity at 20°. At higher angles, however, contribution to the inelastic scattering from the $a^3\Sigma_g^+$ and/or $c^3\pi_u$ state is definitely observable. The intensity envelope of the $B^1\Sigma_u^+$ vibrational bands is easily recognized on Fig. 2. The intensity of consecutive vibrational features follows this envelope smoothly. At 80° however the bands with $\nu' = 4$ and 6 are much more intense than they should be according to this intensity envelope. The extra intensity comes from the contribution of the $\nu' = 0$ and 1 bands of the $a^3\Sigma_g^+$ and/or $c^3\pi_u$ excitations. Dowell and Sharp[15] argue that in their electron-trap threshold spectra the dominant features in H_2 are associated with the $c^3\pi_u$ excitation and that all other contributions are negligible. It is not possible to tell from our spectra whether the $a^3\Sigma_u^+$ or $c^3\pi_u$ scattering is responsible for the intensity enhancement we observe. At 40 eV electron energy the singlet bands are stronger than the triplet ones even at high angles and their interference prohibits a definite conclusion. It would require a much better resolution to separate the $a^3\Sigma_u^+$ and $c^3\pi_u$ features from the overlapping singlet ones.

The differential cross sections calculated for the $X^1\Sigma_g^+ \rightarrow a^3\Sigma_g^+$ excitation are shown in Fig. 6. No experimental data are available for comparison, for the reasons just given.

5. ACKNOWLEDGMENT

The authors are grateful to Drs. J. A. Simpson and C. E. Kuyatt for valuable advice concerning the design of the instrument and to Mr. G. Steffensen for his help in carrying out the measurements. They would also like to acknowledge helpful discussions with Professors R. M. Pitzer and W. A. Goddard, and Mr. D. G. Truhlar of the California Institute of Technology concerning certain aspects of the theoretical work.

REFERENCES

1. For a review of early work in this field see H. S. W. Massey and E. H. S. Burhop, Electronic and Atomic Impact Phenomena (Oxford University Press, London, 1952).
2. a) G. J. Schulz, Phys. Rev. 112, 150 (1958); b) G. J. Schulz and J. W. Philbrick, Phys. Rev. Letters 13, 477 (1964).
3. a) E. N. Lassettre, Rad. Res. Supplement 1, 530 (1959); b) A. Skerbele, M. A. Dillon, and E. N. Lassettre, J. Chem. Phys. 46, 4161 (1967); c) ibid, 46, 4162 (1967).
4. a) A. Kuppermann and L. M. Raff, J. Chem. Phys. 37, 2497 (1962); b) ibid, 39, 1607 (1963); c) Discussions of the Faraday Soc. 35 30 (1963).
5. a) F. H. Read and G. L. Whiterod, Proc. Phys. Soc. 82, 434 (1963); b) ibid, 83, 619 (1964); c) ibid, 85, 71 (1965).
6. a) H. G. M. Heideman, C. E. Kuyatt, and G. E. Chamberlain, J. Chem. Phys. 44, 355 (1966); b) J. A. Simpson, M. G. Menendez and S. R. Mielczarek, Phys. Rev. 150, 76 (1966); c) G. E. Chamberlain, Phys. Rev. 155, 46 (1967).
7. a) H. Ehrhardt and F. Linder, Z. Naturfosschg. 22a, 11 (1967); b) H. Ehrhardt and K. Willman, Z. Physik, 203, 1 (1967).
8. J. P. Doering and A. J. Williams III, J. Chem. Phys. 47, 4180 (1967).
9. a) J. K. Rice, A. Kuppermann, and S. Trajmar, J. Chem. Phys. 48, 945 (1968); b) S. Trajmar, J. K. Rice, P. S. P. Wei, and A. Kuppermann, Chem. Phys. Letters 1, 703 (1968).
10. Under investigation in our laboratories.

11. D. C. Cartwright and A. Kuppermann, Phys. Rev. 163, 861 (1967).

12. a) R. A. Bonham, J. Chem. Phys. 36, 2360 (1964); b) V. I. Ochkur, Soviet Physics-JETP 18, 503 (1964); c) M. R. H. Rudge, Proc. Phys. Soc. 85, 607 (1965); d) ibid. 86, 763 (1965); e) D. S. F. Crothers, Proc. Phys. Soc. 87, 1003 (1966).

13. S. J. B. Corrigan, J. Chem. Phys. 43, 4381 (1965).

14. T. A. Green, Proc. Phys. Soc. 92, 1144 (1967).

15. J. T. Dowell and T. E. Sharp, J. Chem. Phys. 47, 5068 (1967).

16. J. R. Oppenheimer, Phys. Rev. 32, 361 (1928).

17. D. R. Bates, A. Fundaminsky, J. W. Leech, and H. S. W. Massey, Trans. Roy. Soc. A243, 117 (1950).

18. M. Born and R. Oppenheimer, Ann. Physik 84, 457 (1927).

19. a) A. S. Coolidge, H. M. James, and R. D. Present, J. Chem. Phys. 4, 193 (1936); b) H. M. James and A. S. Coolidge, Phys. Rev. 55, 186, (1939).

20. C. Weinbaum, J. Chem. Phys. 1, 593 (1933).

21. P. E. Phillipson and R. S. Mulliken, J. Chem. Phys. 28, 1248 (1958).

22. J. A. Simpson, Rev. Sci. Instr. 35, 1698 (1964).

23. C. E. Kuyatt and J. A. Simpson, Rev. Sci. Instr. 38, 103 (1967).

24. S. Trajmar, J. K. Rice, and A. Kuppermann, JPL Tech. Memo. No. 33-373.

25. L. Vriens, J. A. Simpson, and S. R. Mielczarek, Phys. Rev. 165, 7 (1968).

26. a) G. Breit, H. M. Thaxton, and L. Eisenbud, Phys. Rev. 55, 1018 (1939); b) C. L. Crithfield and D. C. Dodder, ibid. 75, 419 (1949).

27. R. D. Evans, The Atomic Nucleus, p. 807 (McGraw-Hill, 1955).

28. a) G. Herzberg, Spectra of Diatomic Molecules, 2nd ed., p. 387 (Van Nostrand, 1953); b) ibid. p. 530.

29. D. C. Cartwright, thesis, California Institute of Technology, Pasadena, California (June 1967), unpublished.

30. a) P. G. Burke, H. M. Schey, Phys. Rev. 126, 147 (1962); b) P. G. Burke, H. M. Schey, and K. Smith, ibid., 129, 1256 (1963).

31. D. C. Truhlar, D. C. Cartwright and A. Kuppermann (to be published).

FIGURE CAPTIONS

Fig. 1. (5.5-1) Electron impact energy-loss spectrum of molecular hydrogen at 50 eV impact energy and 40° scattering angle. Ion gauge reading (uncalibrated): 2×10^{-3} torr. Incident beam current: 2.8×10^{-8} A. Elastic peak FWHM: 0.22 eV.

Fig. 2. (5.5-2) Electron impact spectrum of H_2 in the 11 to 14 eV energy-loss range at 40 eV impact energy and 20° scattering angle. Incident beam current: 1.0×10^{-8} amps. Elastic peak FWHM: 0.040 eV.

Fig. 3. (5.5-3) Electron impact spectrum of H_2 in the 11 to 14 eV energy-loss region at 80° scattering angle. The experimental conditions are the same as for Fig. 2.

Fig. 4. See figure 4.4-10 of thesis.

Fig. 5. (5.5-5) Differential cross section of $X^1\Sigma_g^+ - b^3\Sigma_u^+$ transition in H_2 as a function of scattering angle. Solid curves are theoretical and points are experimental. Different symbols indicate different experiments, conducted over a period of seven months. Incident energies are: (a) 25 eV: ●, ■, ▲. (b) 35 eV: +. (c) 40 eV: ○, □, △. (d) 50 eV: ⊙, ⊡, ◬. (e) 60 eV: ×.

Fig. 6. (5.5-6) Differential cross sections calculated for the $X^1\Sigma_g^+ - a^3\Sigma_g^+$ excitation. The numbers over the curves represent the electron impact energy in eV.

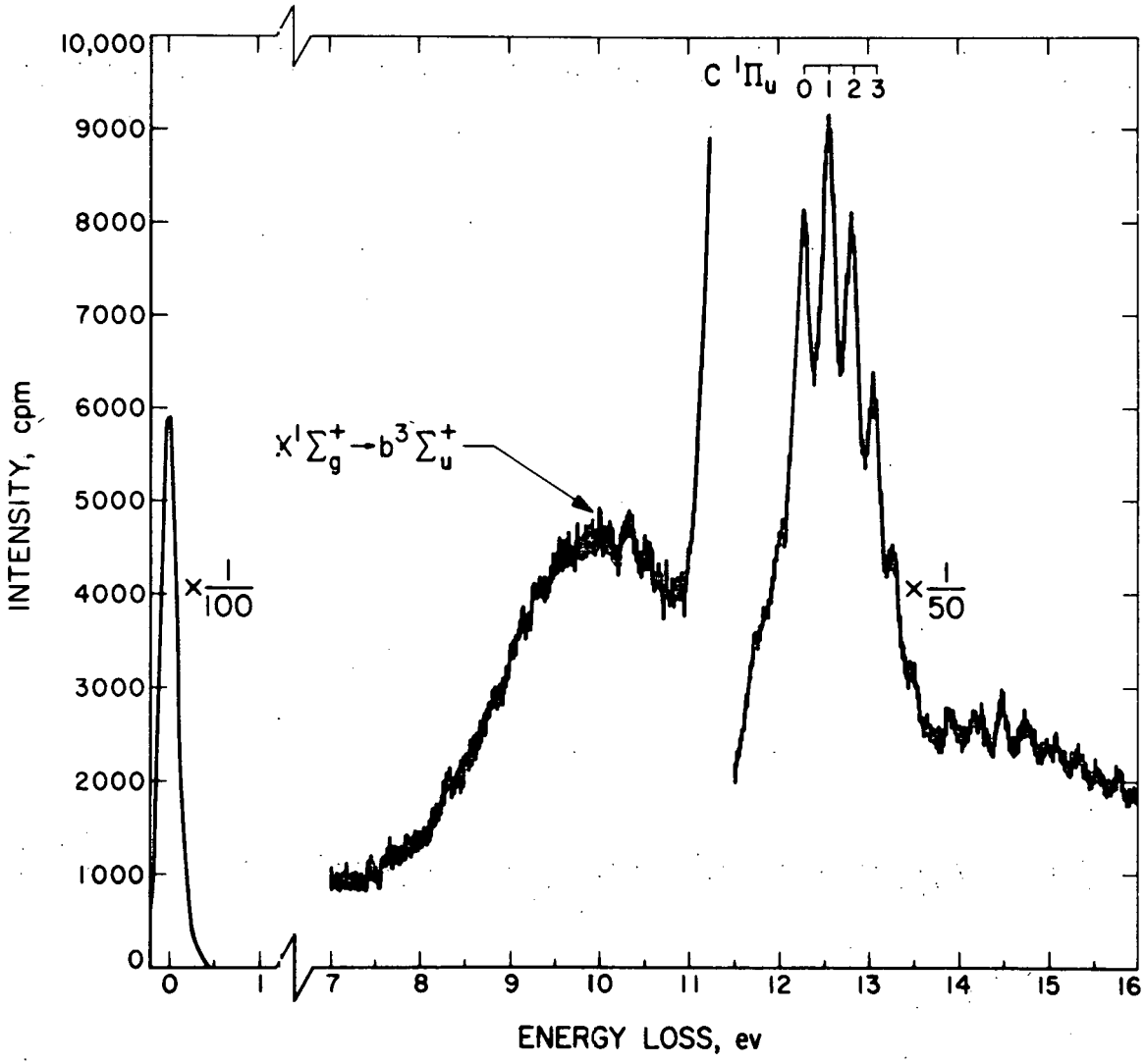
10,000
9000
8000
7000
6000
5000
4000
3000
2000
1000
0
INTENSITY, cpm
C $^1\Pi_u$ 0 1 2 3
$X^1\Sigma_g^+ \rightarrow b^3\Sigma_u^+$
$\times\frac{1}{100}$
$\times\frac{1}{50}$
0
1
7
8
9
10
11
12
13
14
15
16
ENERGY LOSS, ev

Figure 1.

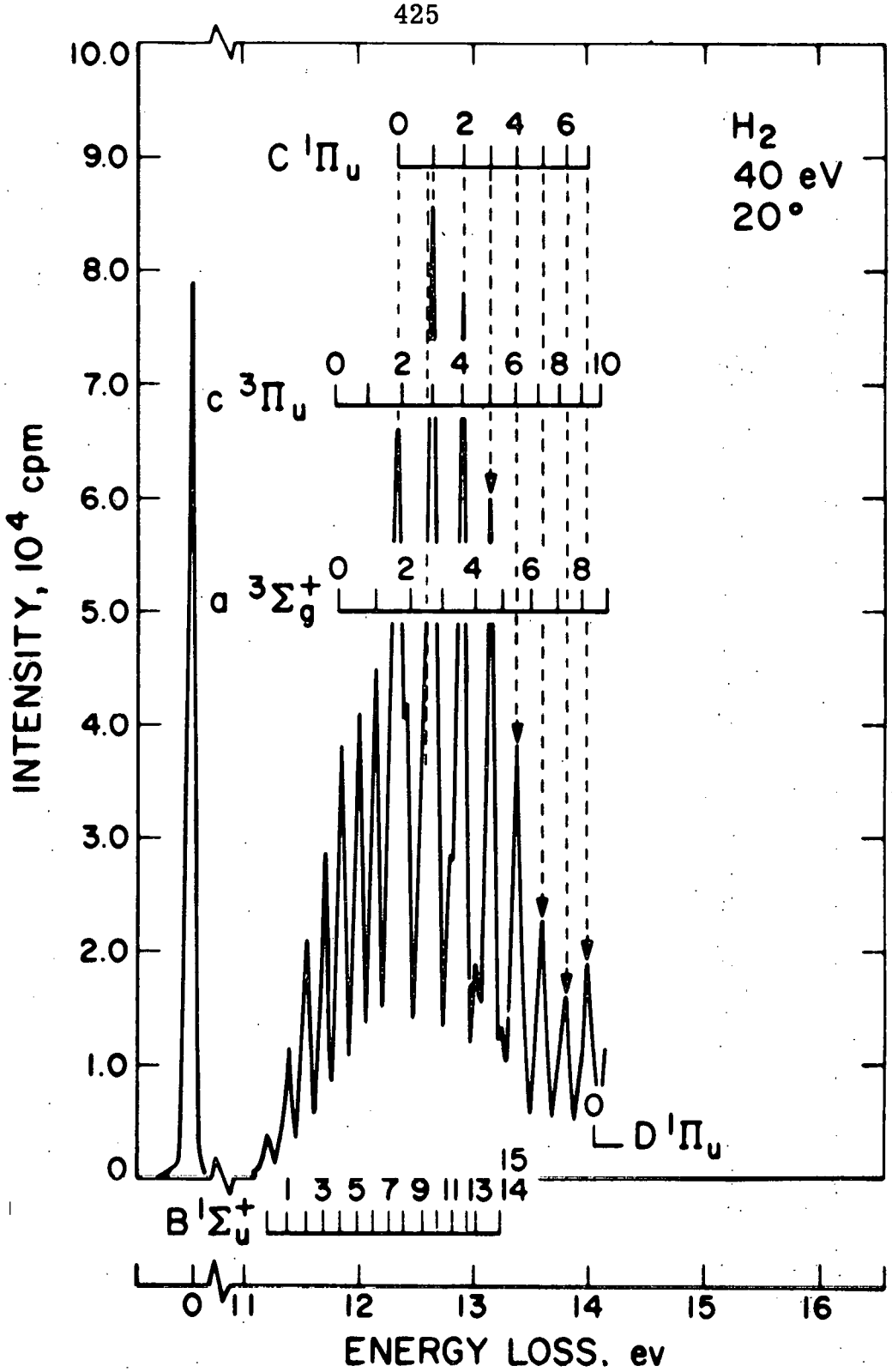
INTENSITY, 10^4 cpm
ENERGY LOSS. ev
H_2
40 eV
20°
C $^1\Pi_u$
c $^3\Pi_u$
a $^3\Sigma_g^+$
B $^1\Sigma_u^+$
D $^1\Pi_u$
0 2 4 6
0 2 4 6 8 10
0 2 4 6 8
1 3 5 7 9 11 13 14 15
0
10.0
9.0
8.0
7.0
6.0
5.0
4.0
3.0
2.0
1.0
0
11
12
13
14
15
16

Figure 2.

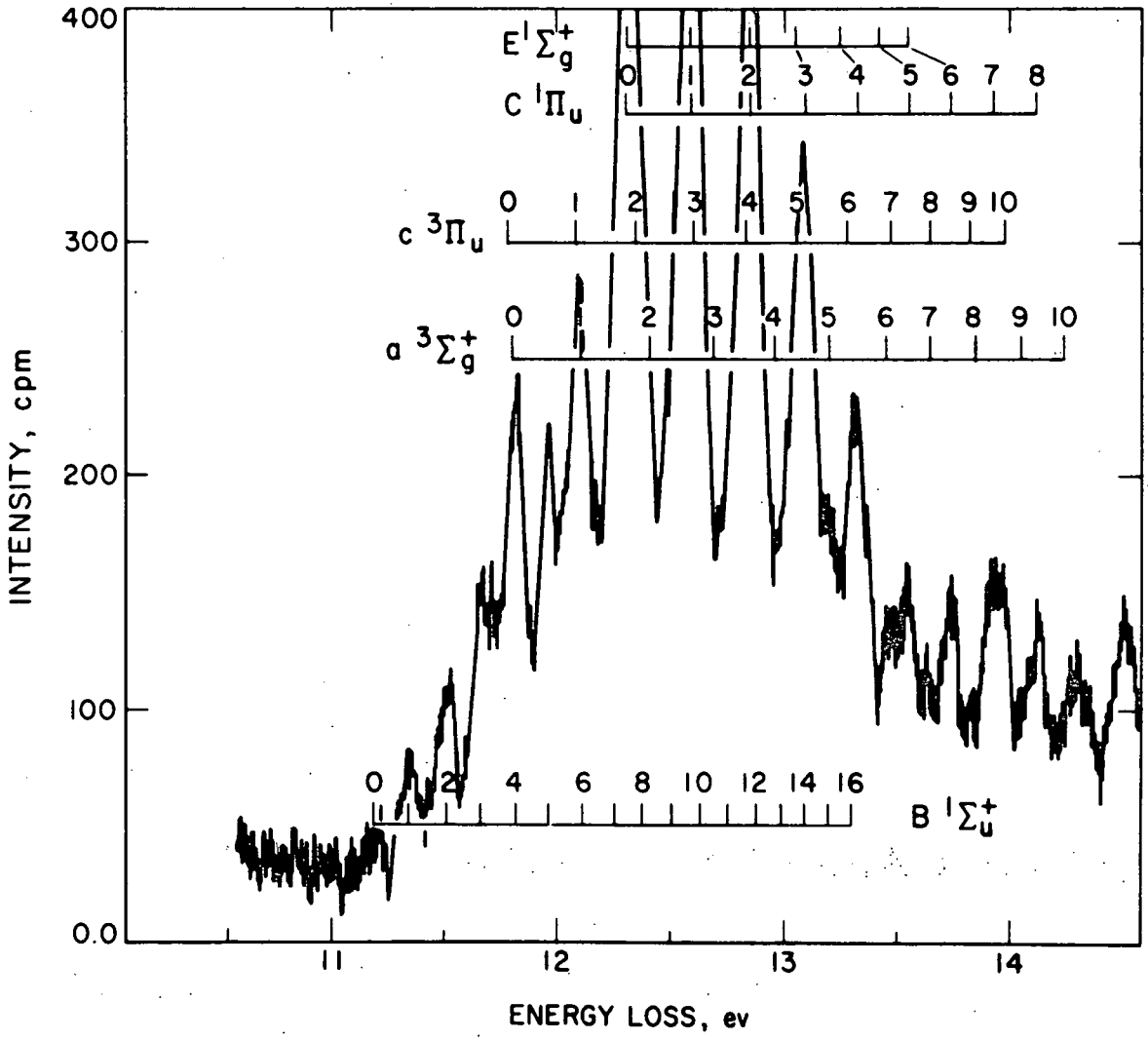
400
300
200
100
0.0
INTENSITY, cpm
11
12
13
14
ENERGY LOSS, ev
E $^1\Sigma_g^+$
C $^1\Pi_u$
c $^3\Pi_u$
a $^3\Sigma_g^+$
B $^1\Sigma_u^+$
0 1 2 3 4 5 6 7 8
0 1 2 3 4 5 6 7 8 9 10
0 2 3 4 5 6 7 8 9 10
0 2 4 6 8 10 12 14 16

Figure 3.

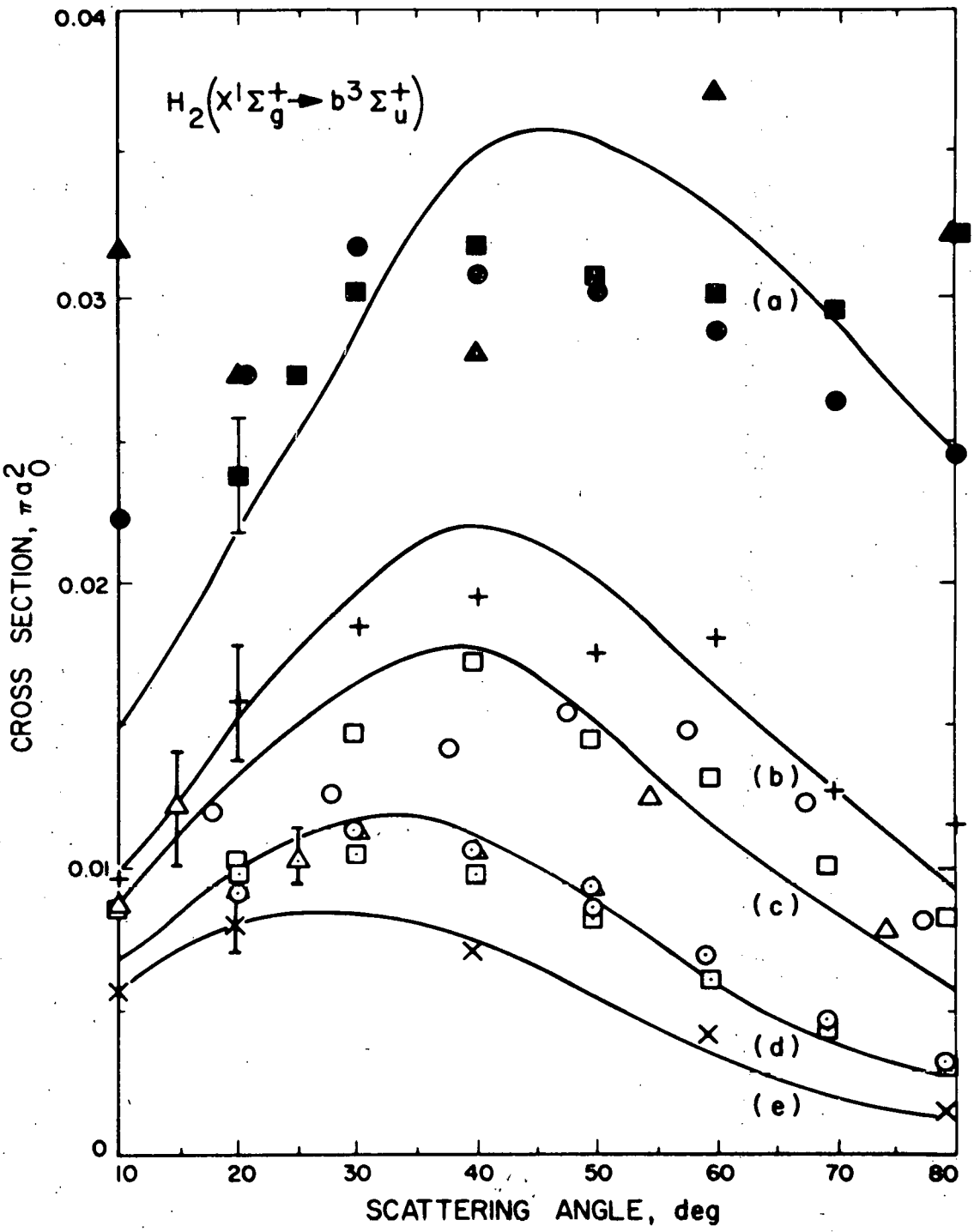
$H_2(X^1\Sigma_g^+ \rightarrow b^3\Sigma_u^+)$
CROSS SECTION, πa_0^2
SCATTERING ANGLE, deg
0.04
0.03
0.02
0.01
0
10
20
30
40
50
60
70
80
(a)
(b)
(c)
(d)
(e)

Figure 4.

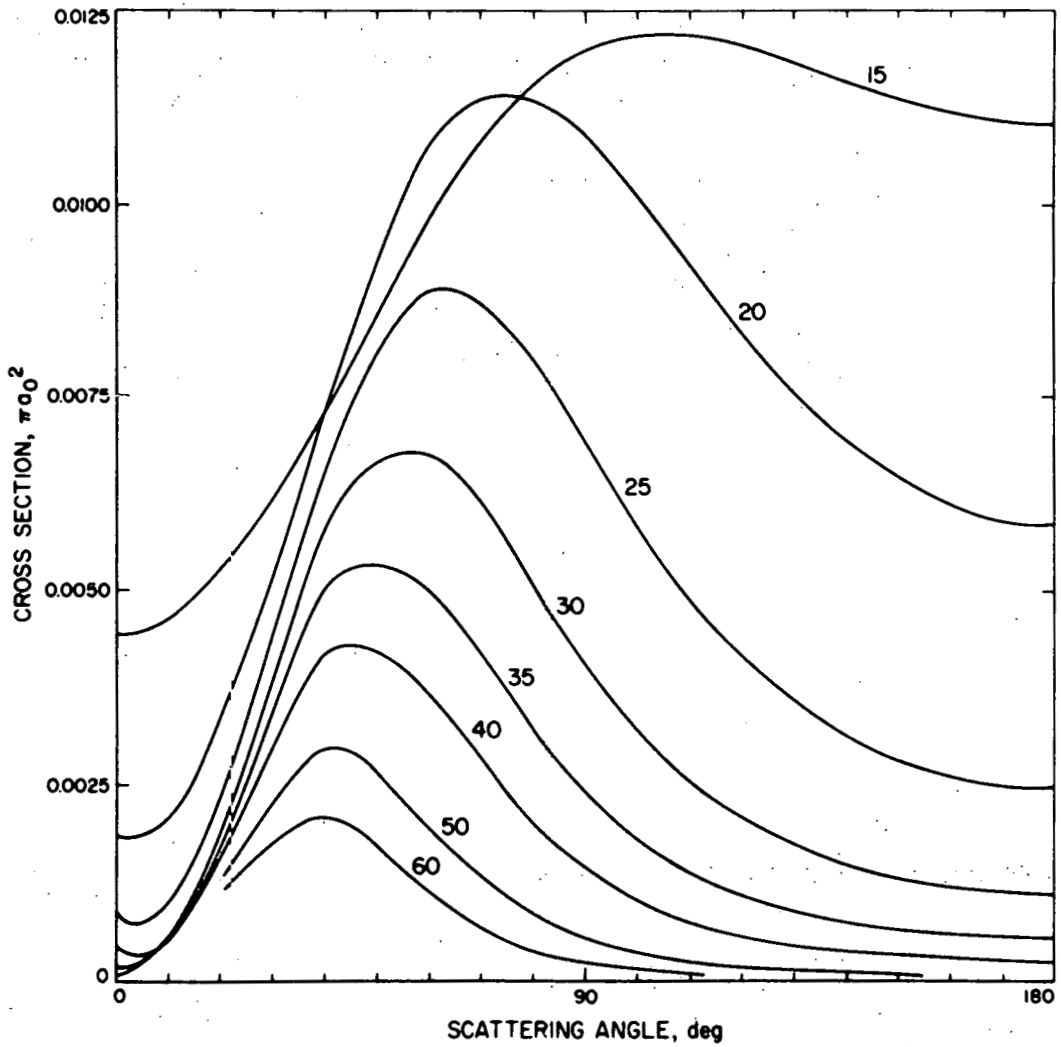
0.0125
0.0100
0.0075
0.0050
0.0025
0
CROSS SECTION, πa_0^2
0
90
180
SCATTERING ANGLE, deg
15
20
25
30
35
40
50
60

Figure 6.

CHEMICAL PHYSICS LETTERS 1 (1968) 703-705. NORTH-HOLLAND PUBLISHING COMPANY, AMSTERDAM

TRIPLET STATES OF ACETYLENE BY ELECTRON IMPACT *

S. TRAJMAR**, J. K. RICE, P. S. P. WEI*** and A. KUPPERMANN
Gates and Crellin Laboratories of Chemistry †,
California Institute of Technology, Pasadena, California 91109, *USA*

Received 18 March 1968

Low-energy electron-impact spectroscopy has revealed two previously unknown low-lying triplet states in acetylene at 5.2 eV and 6.1 eV. The basis for this identification and the disparity in the electron energy-loss and optical absorption spectra are discussed.

The triplet states of acetylene have long eluded detection [1]. A study of the electron-impact energy loss spectrum of C_2H_2 as a function of scattering angle and incident electron energy with an instrument described previously [2] has now unequivocally revealed at least two low-lying triplet states with maximum transition intensities at 5.2 eV (onset at 4.5 eV) ($\tilde{a}$) and 6.1 eV ($\tilde{b}$) (see fig. 1). This identification is based on

* Work supported in part by the U.S. Atomic Energy Commission, Report Code No. CALT-532-24.
** Jet Propulsion Laboratory; supported by the National Aeronautics and Space Administration, Contract No. NAS-7-100.

*** Present address: Bell Telephone Laboratories, Murray Hill, New Jersey 07971.
† Contribution No. 3638.

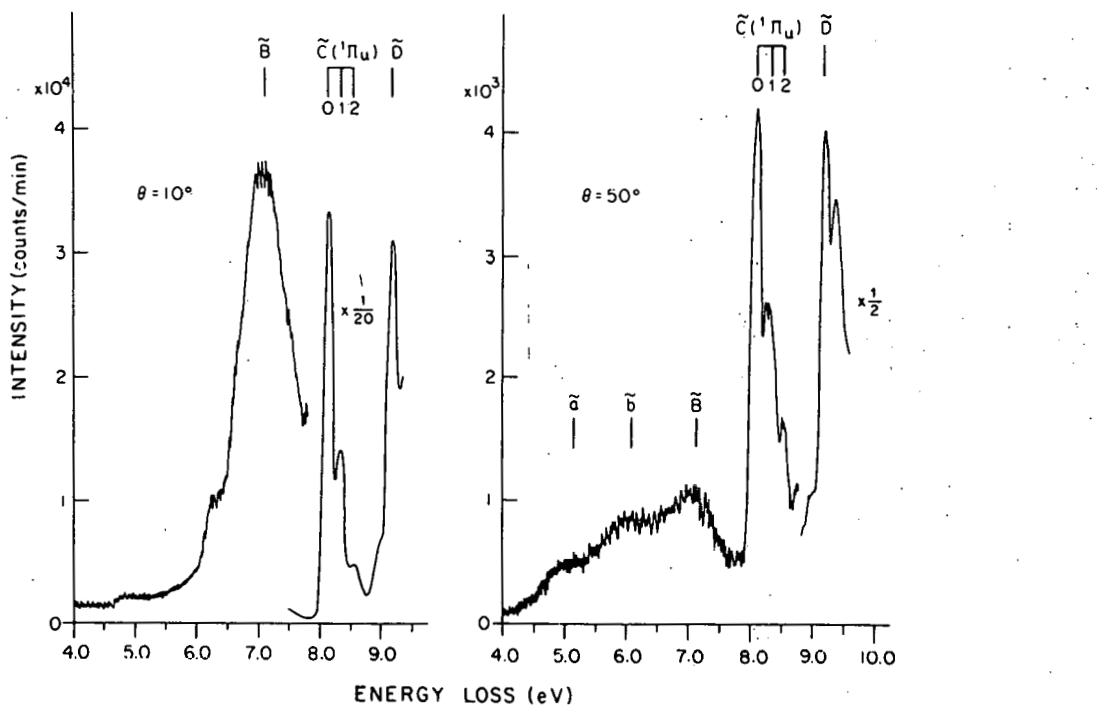

Fig. 1. Energy loss spectra of acetylene at 10° and 50° scattering angles. Pressure gauge reading 8 millitorr; impact energy 25 eV; incident electron current 1×10^{-8} A. The $\times \frac{1}{20}$ and $\times \frac{1}{2}$ are the factors by which intensities were multiplied before plotting.

rules derived from our investigation of the energy and angular dependencies of differential scattering cross sections for 10 singlet ← singlet and 9 triplet ← singlet known transitions in He [2], H_2 [3], N_2 [4], and CO [4].

Fig. 2 shows peak intensity ratios as a function of angle for the indicated states of acetylene [5]. It also illustrates one of the characteristic differences between the angular dependence of singlet/singlet and triplet/singlet intensity ratios. The latter are much steeper functions of angle than the former. Another distinguishing feature we observed is that decreasing the impact energy toward threshold enhances the triplet/singlet ratio over most of its measured angular range (0^o to 80^o) significantly more than any singlet/singlet ratio. The $\tilde{a}$ or $\tilde{b}$/singlet intensity ratios exhibit both of these characteristic "fingerprints" and, hence, $\tilde{a}$ and $\tilde{b}$ are identified as triplet states.

The UV absorption spectrum begins at 5.23 eV with a weak absorption ($f \sim 0.8 \times 10^{-4}$) [6] peaking at ~ 6 eV. Ingold and King [7] have shown that the upper state has A_u symmetry (trans-"bent"). Its singlet nature seems certain from the absence of Zeeman splitting [8] and several observations of Hougen and Watson [9]. The weakness of the absorption is attributed to unfavorable Franck-Condon overlap.

In this case, optical triplet ← singlet transitions are probably much weaker than even the $\tilde{A}^1A_u \leftarrow \tilde{X}^1\Sigma_g^+$ transition due to the absence of appreciable spin-orbit coupling and, as a consequence, excitation to the $\tilde{a}$ and $\tilde{b}$ states have not been observed in the optical absorption spectrum. It has been shown, however, that low-energy electron-impact is quite effective in causing triplet ← singlet transitions but that relative Franck-Condon factors are independent of incident energy and scattering angle [10] even for impact energies low enough for the Born approximation to fail. Since the optical $\tilde{A} \leftarrow \tilde{X}$ transition is 10^{-3} to 10^{-4} times as intense as an ordinary electric-dipole transition (e.g., $\tilde{C} \leftarrow \tilde{X}$) for "geometrical" reasons [7], we would expect this same relative intensity in the electron energy-loss spectrum at any scattering angle. Thus, the electron-impact differential scattering cross sections for excitation of the spin-forbidden $\tilde{a}$ and $\tilde{b}$ states are much larger than that for excitation of the spin-allowed but "Franck-Condon forbidden" $\tilde{A}$ state at scattering angles greater than 10^o. For this reason transitions to the $\tilde{a}$ and $\tilde{b}$ states but not to the $\tilde{A}$ one are seen by low-energy electron scattering, whereas in optical absorption spectroscopy the reverse is

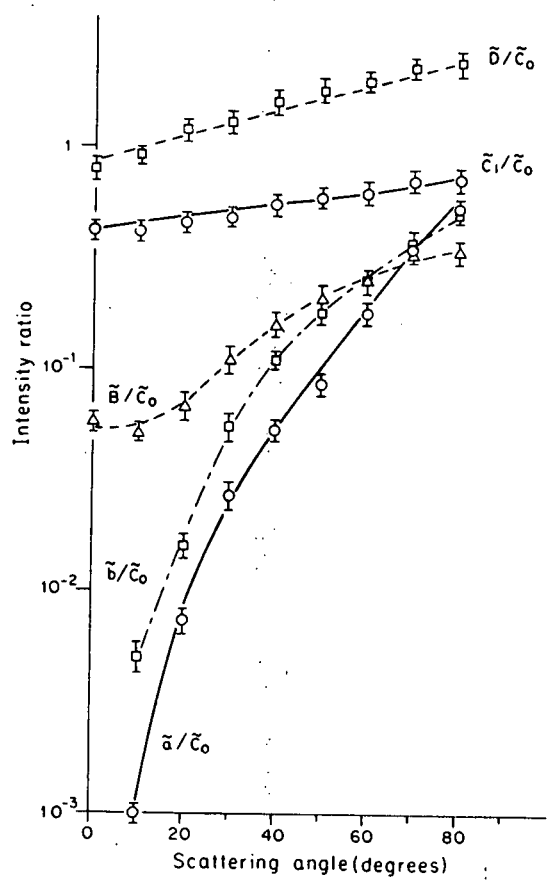

Fig. 2. Peak intensity ratios. $\tilde{C}_0$ refers to the $v = 0$ vibrational level of the $\tilde{C}$ state. $\tilde{C}_1$ refers to the $v = 1$ level.

true. This interpretation would predict that a careful analysis of the optical lines of the $\tilde{A}^1\tilde{A}_u$ state might reveal perturbations due to interaction with the triplet $\tilde{b}$ state. In addition, electron impact at incident energies above 100 eV should make transitions to $\tilde{a}$ and $\tilde{b}$ much weaker than those to $\tilde{A}$.

Bowman and Miller [11] have studied the excitation spectrum of acetylene by the trapped-electron technique. They observed a broad excitation peaking at 6.2 eV which they assigned as $\tilde{A}^1A_u \leftarrow \tilde{X}^1\Sigma_g^+$. This feature might actually be due to transitions to the $\tilde{a}$ and $\tilde{b}$ states. They also reported a transition peaking at 2.0 eV which was tentatively assigned to a low-lying triplet state. We searched carefully for a transition in that region, but found none. The sensitivity of our instrument was sufficient to have revealed features as small as 1/30 of the $\tilde{a}$ and $\tilde{b}$ peaks.

The transition peaking at 7.15 eV has been assigned by Herzberg [1] as $\tilde{B} \leftarrow \tilde{X}$ in analogy to the quadrupole allowed a $^1\Pi_g \leftarrow X^1\Sigma_g^+$ transition in N_2. An extension of this analogy suggests a possible correlation of $\tilde{a}$ and $\tilde{b}$ with the $A^3\Sigma_u^+$ and $B^3\Pi_g$ states of N_2, respectively. The location of these two triplet states should be useful in the evaluation of theoretical energy level calculations in acetylene [12-15].

References

[1] G. Herzberg, Molecular spectra and molecular structure, Vol. III, Electronic spectra and electronic structure of polyatomic molecules (D. Van Nostrand Co., New York. 1966).
[2] J. K. Rice, A. Kuppermann and S. Trajmar, J. Chem. Phys., in press.
[3] S. Trajmar, D. C. Cartwright, J. K. Rice and A. Kuppermann, 20th Annual Gaseous Electronics Conference, October, 1967.
[4] Forthcoming.
[5] See ref. 1 for identification of these states.
[6] G. W. King and C. K. Ingold, Nature 169 (1952) 1101.
[7] C. K. Ingold and G. W. King, J. Chem. Soc. 1953 (1953) 2702.
[8] A. E. Douglas, unpublished, see ref. 1, p. 517.
[9] J. T. Hougen and J. K. G. Watson, Can. J. Phys. 43 (1965) 298.
[10] A. Skerbele, M. A. Dillon and E. N. Lassettre, J. Chem. Phys. 46 (1967) 4162;
A. Skerbele, V. D. Meyer and E. N. Lassettre, ibid. 44 (1966) 4069.
[11] C. R. Bowman and W. D. Miller, J. Chem. Phys. 42 (1965) 681.
[12] I. G. Ross, Trans. Faraday Soc. 48 (1952) 973.
[13] (a) J. Serre, J. Chim. Phys. 52 (1955) 331; (b) C. R. Acad. Sci., Paris, 242 (1956) 1469.
[14] M. J. S. Dewar and N. L. Hojvat, Proc. Roy. Soc., London. A264 (1961) 431.
[15] M. Barfield, J. Chem. Phys. 47 (1967) 3831.

APPENDIX V

LIST OF VENDORS AND/OR MANUFACTURERS

Allied Electronics
2085 E. Foothill Boulevard
Pasadena, California

Assembly Products, Inc.
5770 N. Rosemead Boulevard
Temple City, California

Beckman Instruments
Helipot Division
2400 Harbor Boulevard
Fullerton, California

Carl Herman Associates Industries
1245 E. Walnut Street
Pasadena, California
Representative of Granville-Phillips, F. J. Cooke, and Hastings.

C. E. Howard Corporation
9001 Rayo Avenue
South Gate, California

Centralab
6446 Telegraph Road
Los Angeles, California

Ceramaseal Incorporated
New Lebanon Center
New York, New York

Chester Paul Company
1605 Victory Boulevard
Glendale, California
Representative of Hanson Manufacturing Company.

Dow Radio
1759 E. Colorado Boulevard
Pasadena, California

Dynamics Associates
2615 South Senta Street
Los Angeles, California

Edwards High Vacuum Corporation
6151 W. Century Boulevard
Los Angeles, California

Electronics Measurement Company
Eatontown, New Jersey

Fairchild Instrumentation
5410 West Imperial Boulevard
Los Angeles, California

Fibros Seal
Culver City, California
Representative of United Aircraft Products, Incorporated.

General Electric Company
Vacuum Products Operation
Schenectady, New York

General Radio Corporation
1000 N. Seward Street
Los Angeles, California

Hasco
8318½ W. Third Street
Los Angeles 48, California

Hewlett-Packard
Neely Sales Division
3939 Lankershim Boulevard
North Hollywood, California

Hoskins Manufacturing Company
5935 E. Sheila Street
Los Angeles, California

Industrial Tectronics, Incorporated
3686 Jackson Road
Ann Arbor, Michigan

Kenneth C. Holloway, Incorporated
135 North Halstead Avenue
Pasadena, California

Ladish Pacific Division
3321 East Slauson
Los Angeles, California

Leeds and Northrop Company
5111 Via Corona Avenue
Los Angeles, California

Metal Bellows Corporation
20977 Knapp Street
Chatsworth, California

Miniature Precision Bearings, Incorporated
Precision Park
Keene, New Hampshire

Molycote Corporation
65 Harvard Avenue
Stamford, Connecticut

Mycalex Corporation of America
125 Clifton Boulevard
Clifton, New Jersey

Nuclear Chicago
1053 West Colorado Boulevard
Los Angeles, California

Nuclear Data, Incorporated
P. O. Box 88
San Rafael, California

Nuclide Corporation
642 East College Avenue
State College, Pennsylvania

Pace Engineering Company
13035 Saticoy Street
North Hollywood, California

Parker Seal Company
10567 Jefferson Boulevard
Culver City, California

Paul Nurches Company
2396 Foothill Boulevard
Pasadena, California
Representative of Pamona Electronics and Bell.

Photocon Research
421 North Altadena Drive
Pasadena, California

PIC Design Corporation
East Rockaway, New York

Picker-Nuclear
Los Angeles, California

Princeton Applied Research Corporation
Box 565
Princeton, New Jersey

Ratron
P. O. Box 282
Northridge, California

Radio Corporation of America
Electronic Components and Devices
Lancaster, Pennsylvania

Scientific Atlanta, Incorporated
Box 13654
Atlanta, Georgia

The Carborundum Company
Electronics Division
2240 South Yates Avenue
Los Angeles, California

The Wilkinson Company
P. O. Box 303
Santa Monica, California

T. L. Snitzer Company
5354 West Pico Boulevard
Los Angeles 19, California
Representative of Keithley Instruments.

U. S. Flexible Metallic Tubing Company
454 East Third Street
Los Angeles, California

Vacuum Accessories Corporation of America
P. O. Box 134
Greenlawn, Long Island, New York

Vacuum Research Corporation
420 Market Street
San Francisco 11, California

Varian Associates
Vacuum Products Division
611 Hansen Way
Palo Alto, California

Veeco
86 Denton Avenue
New Hyde Park, Long Island, New York

V. T. Rupp Company

307 Park Avenue

Los Angeles, California

Representative of Kepco, Incorporated

W. D. Wilson

1118 Mission Street

South Pasadena, California

Representative of Swagelok, Cajon, Nupro, and Whitey.

REFERENCES

1. A. Messiah, Quantum Mechanics, Vols. I and II (John Wiley and Sons, Inc., New York, 1961): (a) p. 833; (b) p. 836; (c) p. 867; (d) p. 348.
2. The optical selection rules for atomic systems are summarized in:
   (a) G. Herzberg, Atomic Spectra and Atomic Structure (Dover Publications, New York, 1944), pp. 27-28, 50-54, 153-159.
   Those for diatomic molecules are presented in:
   (b) G. Herzberg, Spectra of Diatomic Molecules (Second Edition, D. Van Nostrand, Inc., 1950), pp. 240-280.
   Those for polyatomic molecules are discussed in:
   (c) G. Herzberg, Electronic Spectra of Polyatomic Molecules (D. Van Nostrand, Inc., 1966), pp. 128-142.
3. J. Franck and G. Hertz, Verk. dtsh. Physik Ges., 16, 457 (1914).
4. E. G. Dymond, Phys. Rev., 29, 433 (1927).
5. J. R. Oppenheimer, Phys. Rev., 32, 361 (1928).
6. H. S. W. Massey and E. H. S. Burhop, Electronic and Ionic Impact Phenomena (Clarendon Press, Oxford, 1952): (a) p. 146, (b) pp. 93-99, (c) p. 189, (d) p. 91, (e) p. 10.
7. E. W. McDaniel, Collision Phenomena in Ionized Gases (John Wiley and Sons, Inc., New York, 1964).
8. G. J. Schulz, Phys. Rev., 112, 150 (1958).

9. G. J. Schulz, (a) Phys Rev., 116, 1141 (1959); (b) 125, 229 (1962); (c) 135, A988 (1964); (d) 136, A650 (1964): (e) J. Chem. Phys., 33, 1661 (1960); (f) 34, 1778 (1961): (g) Phys. Rev. Letters, 10, 104 (1963); (h) 13, 583 (1964).

10. C. R. Bowman and W. D. Miller, J. Chem. Phys., 42, 681 (1965).

11. H. H. Brongersma and L. J. Oosterhoff, Chem. Phys. Letters, 1, 169 (1967).

12. J. T. Dowell and T. E. Sharp, J. Chem. Phys., 47, 5068 (1967).

13. R. N. Compton, R. H. Huebner, P. W. Reinhardt, and L. G. Christophorou, J. Chem. Phys., 48, 901 (1968).

14. Their early work (prior to 1959) has been reviewed by:
(a) E. N. Lassettre, Rad. Res. Supplement, 1, 530 (1959).
A later series of 10 papers appeared in 1964:
(b) E. N. Lassettre, et al., J. Chem. Phys., 40, 1208-1275 (1964).

15. S. M. Silverman and E. N. Lassettre, J. Chem. Phys., 40, 1265 (1964).

16. E. N. Lassettre and M. E. Krasnow, J. Chem. Phys., 40, 1248 (1964).

17. (a) V. D. Meyer and E. N. Lassettre, J. Chem. Phys., 44, 2535 (1966).
(b) A. Skerbele and E. N. Lassettre, J. Chem. Phys., 42, 395 (1965).

(c) E. N. Lassettre, A. Skerbele, and V. D. Meyer, J. Chem. Phys., 45, 3214 (1966).

18. K. Dressler and B. L. Lutz, Phys. Rev. Letters, 19, 1219 (1967).

19. V. Cermák, J. Chem. Phys., 44, 1318 (1966).

20. H. G. M. Heideman, C. E. Kuyatt, and G. E. Chamberlain, J. Chem. Phys., 44, 355 (1966).

21. V. D. Meyer, A. Skerbele, and E. N. Lassettre, J. Chem. Phys., 43, 805 (1965).

22. A. Skerbele, M. A. Dillion, and E. N. Lassettre, (a) J. Chem. Phys., 46, 4161 (1967); (b) 46, 4162 (1967).

23. K. J. Ross and E. N. Lassettre, J. Chem. Phys., 44, 4633 (1966).

24. J. A. Simpson, Rev. Sci. Instr., 35, 1698 (1964).

25. C. E. Kuyatt and J. A. Simpson, Rev. Sci. Instr., 38, 103 (1967).

26. J. A. Simpson and S. R. Mielczarek, J. Chem. Phys., 39, 1606 (1963).

27. G. E. Chamberlain, H. G. M. Heideman, J. A. Simpson, and C. E. Kuyatt, Fourth International Conference on the Physics of Electronic and Atomic Collisions, Abstracts (Science Book Crafters, Inc., Hastings-on-Hudson, New York (1965)), pp. 378-381.

28. C. E. Kuyatt, J. A. Simpson, and S. R. Mielczarek, Bull. Am. Phys. Soc., 9, 266 (1964).

29. H. G. M. Heideman, C. E. Kuyatt, and G. E. Chamberlain, J. Chem. Phys., 44, 355 (1966).

30. H. G. M. Heideman, C. E. Kuyatt, and G. E. Chamberlain, J. Chem. Phys., 44, 440 (1966).

31. J. A. Simpson, M. G. Menendez, and S. R. Mielczarek, Phys. Rev., 150, 76 (1966).

32. L. Vriens, J. A. Simpson, and S. R. Mielczarek, Phys. Rev., 165, 7 (1968).

33. A recent study containing references to their earlier work is: F. M. J. Pichanick and J. A. Simpson, Phys. Rev., 168, 64 (1968).

34. Refer to section 4.1 of this thesis.

35. (a) A. Kuppermann and L. Raff, J. Chem. Phys., 37, 2497 (1962).

(b) A. Kuppermann and L. Raff, Disc. Farad. Soc., 35, 30 (1963),

(c) A. Kuppermann and L. Raff, J. Chem. Phys., 39, 1067 (1963).

36. (a) J. P. Doering, J. Chem. Phys., 45, 1065 (1966).

(b) J. P. Doering, J. Chem. Phys., 46, 1194 (1967).

(c) J. P. Doering and A. J. Williams, IV, J. Chem. Phys., 47, 4180 (1967).

37. (a) D. Andrick and H. Ehrhardt, Z. Phys., 192, 99 (1966).

(b) H. Ehrhardt and K. Willmann, Z. Phys., 203, 1 (1967).

(c) H. Ehrhardt and K. Willmann, Z. Phys., 204, 462 (1967).

38. J. Geiger, Z. Phys., 180, 415 (1964).

39. J. Geiger and W. Stickel, J. Chem. Phys., 43, 4535 (1965).

40. J. Geiger and K. Wittmaack, Z. Naturforsch, 20A, 628 (1965).

41. A discrepancy between the optical data of R. E. Huffman, Y. Tanaka, and J. C. Larrabee [J. Chem. Phys., 39, 910 (1963)] and the electron impact data of E. N. Lassettre, F. M. Glaser, V. D. Meyer, and A. Skerbele [J. Chem. Phys., 42, 3429 (1965)]; V. D. Meyer, A. Skerbele, and E. N. Lassettre [J. Chem. Phys., 43, 3769 (1965)]; Lassettre, et al.[17c]; and Geiger and Stickel[39] had been noted in the relative intensities of the $X^1\Sigma_g^+$ ($\nu = 0$)–$b^1\Pi_u(\nu' = 2)$ and $b^1\Pi_u(\nu' = 3)$ transitions in N_2. However, this anomaly has been resolved by the recent optical work of G. M. Lawrence, D. L. Mickey, and K. Dressler [J. Chem. Phys., 48, 1989 (1968)].

42. D. R. Bates, A. Fundaminsky, J. W. Leech, and H. S. W. Massey, Trans. Roy. Soc., A243, 93 (1950).

43. J. D. Jobe and R. M. St. John, Phys. Rev., 164, 117 (1967).

44. N. F. Mott and H. S. W. Massey, The Theory of Atomic Collisions (Clarendon Press, Oxford (1965)): (a) p. 421, (b) p. 463, (c) pp. 19-28, (d) p. 420, (e) p. 28, (f) Chp. I § 7, etc., (g) p. 593, pp. 571-573.

45. T. Y. Wu and T. Ohmura, Quantum Theory of Scattering (Prentice Hall, Inc., New Jersey (1962)).

46. M. L. Goldberger and K. M. Watson, Collision Theory (John Wiley and Sons, Inc., New York (1964)).

47. L. J. Kieffer, "Bibliography of Low Energy Electron Collision Cross Section Data," National Bureau of Standards Miscellaneous Publication 289, March 10, 1967.

48. We have ignored the explicit consideration of nuclear spin since low-energy electrons are not effective in causing nuclear spin "flips." However, it is important to note that the nuclear spin state of homonuclear diatomic molecules (such as H_2) may affect the excitation probability of certain rotational levels.

49. L. Pauling and E. B. Wilson, Introduction to Quantum Mechanics (McGraw-Hill Book Company, Inc., New York 1935): (a) Chpt. VIII, (b) p. 210, (c) p. 138.

50. It has been pointed out be F. S. Levin, Phys. Rev, 140, B1099 (1965) that the expansion (3-15) and asymptotic form (3-12) do not correctly define the scattering amplitude which determines the cross section of equation (3-13). This can be seen by considering the projection $\langle \underset{\sim}{\psi_0} \mid \Psi_I \rangle$ as $r \to \infty$. This quantity should yield only $\underset{\sim}{G_0}$ in the limit. However, the continuum states of the target will also contribute. The same is true for all inelastic channels. In all practical applications, the expansion (3-15) is truncated before the inclusion of continuum states is necessary and this problem does not arise.

51. P. G. Burke, S. Ormande, and W. Whitaker, Phys. Rev. Letters, 17, 800 (1966); Proc. Phys. Soc. (London), 92, 319 (1967).

52. P. G. Burke, J. W. Cooper, and S. Ormande, Phys. Rev. Letters, 17, 345 (1966).

53. B. L. Moiseiwitsch and S. J. Smith, Rev. Mod. Phys., 40, 238 (1968).

54. S. Khashaba and H. S. W. Massey, Proc. Phys. Soc. (London), 71, 574 (1958).

55. (a) H. S. W. Massey and B. L. Moiseiwitsch, Proc. Roy. Soc. (London) 227, 38 (1954); (b) 258, 147 (1960).

56. The usual Born approximation becomes the Born-Oppenheimer one for indistinguishable particles. This was first pointed out in reference (5).

57. D. G. Truhlar, D. C. Cartwright, and A. Kupperman, Phys. Rev. 1968 (in press).

58. (a) V. I. Ochkur, Soviet Physics - JETP 18, 503 (1964) {Zh. Eksperim. i Teor. Fiz. 45, 734 (1963)}
(b) V. I. Ochkur and V. F. Bratsev, Opt. Spectry. USSR, 19, 274 (1965). {Opt. i Spectroskopiya, 19, 490 (1965b).}
(c) V. I. Ochkur and V. F. Bratsev, Soviet Astron. A J 9, 797 (1966). {Astron. Zh., 42, 1035 (1965a).}

59. R. A. Bonham, J. Chem. Phys., 36, 3260 (1962).

60. H. Bethe, Ann. der Physik, 5, 325 (1930).

61. M. Born and J. R. Oppenheimer, Ann. der Physik, 84, 457 (1927).

62. M. R. H. Rudge, Proc. Phys. Soc., 85, 607 (1965); 86, 763 (1965).

63. Y. N. Demkov, Variational Principles in the Theory of Collisions (Pergamon Press, London, 1963), pp. 97-102.

64. O. Bely, Il Nuovo Cimento, 49, 66 (1967).

65. L. D. Landau and E. M. Lifshitz, Quantum Mechanics, second edition (Pergamon Press, Oxford, 1965), (a) p. 553, (b) p. 411.

66. D. C. Cartwright, Ph.D. Thesis, California Institute of Technology, 1967.

67. K. J. Miller and M. Krauss, J. Chem. Phys., 48, 2611 (1968).

68. S. Trajmar, D. C. Cartwright, J. K. Rice, R. T. Brinkman, and A. Kuppermann, J. Chem. Phys. 1968 (in press). A copy of this paper can be found in Appendix III.

69. S. P. Khare [Phys. Rev. 149, 33 (1966)] has calculated the DCS for excitation of the B and C states of H_2 at 25 KeV incident energy including exchange. However, the effect of exchange is negligible at this incident energy.

70. K. L. Bell, H. Eissa, and B. L. Moiseiwitsch, Proc. Phys. Soc. (London), 88, 57 (1966).

71. D. J. T. Morrison and M. R. H. Rudge, Proc. Phys. Soc. (London), 91, 565 (1967).

72. A theoretical discussion of the applicability of the Born approximation has been presented by H. S. W. Massey [Rev. Mod. Phys., 28, 199 (1956)] while an experimental

test was carried out by S. M. Silverman and E. N. Lassettre [J. Chem. Phys., 40, 1242 (1964)].

73. H. G. M. Heideman and L. Vriens, J. Chem. Phys., 46, 2911 (1967).

74. H. B. Dwight, Tables of Integrals and Other Mathematical Data, (The Macmillan Company, New York (1961)): (a) p. 132, (b) p. 235.

75. Reference (2b), p. 18.

76. D. C. Cartwright and A. Kuppermann, Phys. Rev., 163, 86 (1967).

77. Reference (2b), p. 200.

78. Reference (2b), p. 203.

79. Reference (2b), p. 193.

80. Reference (2c), p. 629.

81. A. Streitwieser, Molecular Orbital Theory for Organic Chemists (John Wiley and Sons, Inc., New York, 1961): (a) p. 207, (b) p. 33, (c) p. 165, (d) p. 10, (e) p. 16.

82. C. Reid, J. Chem. Phys., 18, 1299 (1950).

83. D. F. Evans, J. Chem. Soc., 1735 (1960).

84. See references (10), (35a), (36c), and this research section 5.7.

85. R. S. Mulliken, J. Chem. Phys., 3, 375 (1935).

86. J. D. Roberts, Molecular Orbital Calculations (W. A. Benjamin, Inc., New York, 1962), p. 42.

87. H. H. Brongersma, Ph.D. Thesis, FOM - Institute for Atomic and Molecular Physics, Amsterdam, 1968.

88. I. C. Percival and M. J. Seaton, Proc. Cambridge, Phil. Soc., 53, 654 (1957).

89. H. Wayland, Differential Equations Applied in Science and Engineering (D. Van Nostrand Company, Inc., Princeton, 1957), p. 199.

90. For example, see reference (31) and this research, sections 5.2-5.7.

91. Compare the angular distributions of reference (32) with those of (31). This effect has been noted in this research, sections 5.2-5.7.

92. (a) A computer program for the calculation of these symbols is available from: R. S. Gaswell and L. C. Maximon, "Fortran Programs for the Calculation of Wigner 3_j, 6_j, and 9_j Coefficients for Angular Momenta $\leq$ 80" NBS Technical note 409, November 15, 1966, Superintendent of Documents, Government Printing Office, Washington, D. C. 20402 (40 cents).

(b) A compilation of these symbols for angular momenta ≤ 8 is given by M. Rotenberg, R. Bivans, N. Metropolis, and J. K. Wooten, Jr., The 3_j and 6_j Symbols (Technology Press, Cambridge, 1959).

93. P. S. Hoeper, W. Franzer, and R. Grysta, Phys. Rev., 168, 50 (1968).

94. R. B. Leighton, Principles of Modern Physics (McGraw-Hill Book Company, Inc., New York, 1959), (a) p. 356, (b) pp. 350 ff.

95. W. B. Nottingham, Phys. Rev., 55, 203 (1939).

96. H. Boersch, J. Geiger, and H. Hellwig, Physics Letters, 3, 64 (1962).

97. W. Legler, Z. Physik, 171, 424 (1963).

98. S. N. Foner and B. H. Nall, Phys. Rev., 122, 512 (1961).

99. E. M. Clarke, Can. J. Phys., 32, 764 (1954).

100. A. Ll. Hughes and J. H. McMillen, Phys. Rev., 34, 291 (1929).

101. P. Marmet and L. Kerwin, Can J. Phys., 38, 787 (1960).

102. E. M. Purcell, Phys. Rev., 54, 818 (1938).

103. K. R. Spangenberg, Vacuum Tubes (McGraw-Hill Book Company, Inc., New York, 1948).
(a) This effect is discussed in chapter 8, (b) Chapt. 4.

104. J. R. Pierce, Theory and Design of Electron Beams, Second ed. (D. Van Nostrand Book Co., New York, 1934) (a) Chapt. 9, (b) Chapt. 8.

105. K. Spangenberg and L. M. Field, Elec. Comm., 21, 194 (1943).

106. J. A. Simpson and C. E. Kuyatt, J. of Res. of NBS, 67C, 279 (1963).

107. J. A. Simpson and C. E. Kuyatt, Rev. Sci. Instr., 34, 265 (1963).

108. E. A. Soa, Jenaer Jahrbuch, 1, 115 (1959).

109. D. B. Langmuir, Proc. IRE, 25, 977 (1937).

110. C. E. Kuyatt, Lectures at the National Bureau of Standards, Washington, D. C. (April-May, 1967).

111. See, for example, reference (94), p. 409.

112. E. R. Peck, Electricity and Magnetism (McGraw-Hill Book Company, Inc., New York, 1953), pp. 441-442. We have used formulae 12.102 and 12.109 and have assumed a total power of 50,000 watts emanating from a transmitter located about $2\frac{1}{2}$ kilometers from the apparatus.

113. M. Pirani and J. Yarwood, Principles of Vacuum Engineering (Chapman and Hall, London, 1961), Chapter 1.

114. C. Kittel, Introduction to Solid State Physics, Second ed. (John Wiley and Sons, Inc., New York, 1956), Chpt. 10.

115. W. B. Nottingham, Phys. Rev., 49, 78 (1936).

116. A. R. Hutson, Phys. Rev., 98, 889 (1955).

117. G. G. Belford, A. Kuppermann, and T. E. Phipps, Phys. Rev., 128, 524 (1962).

118. J. A. Simpson and C. E. Kuyatt, J. Appl. Phys., 37, 3805 (1966).

119. See for example, W. Hume-Rothery, The Metallic State (The Clarendon Press, Oxford, 1931), pp. 148-157.

120. See for example, J. A. Simpson and U. Fano, Phys. Rev. Letters, 11, 158 (1963).

121. G. E. Chamberlain, J. A. Simpson, S. R. Mielczarek, and C. E. Kuyatt, J. Chem. Phys., 47, 4266 (1967).

122. For example, the DCS for elastic scattering varies as q^{-4}, while that for optically dipole-allowed transitions varies as q^{-14} for large q^2 ($q^2 = k_o^2 + k_n^2 - 2k_o k_n \cos\theta$, see section 3 for the definitions of k_o and k_n). Refer to E. N. Lassettre [J. Chem. Phys., 43, 4479 (1965)] for a further discussion of this "Born approximation" behavior.

123. This phenomenon is adequately discussed in references (124) through (126) and will not be reiterated here.

124. E. B. Jordan and R. B. Brode, Phys. Rev., 43, 112 (1933).

125. C. L. Critchfield and D. C. Dodder, Phys. Rev., 75, 419 (1949).

126. R. J. Carbone, E. N. Fuls, and E. Everhart, Phys. Rev., 102, 1524 (1956).

127. R. T. Brinkman, private communication.

128. A detailed discussion of this approximation is given by J. D. Craggs and H. S. W. Massey, Handbuch der Physik, ed. by S. Flügge (Springer-Verlag, Berlin, 1959), Vol. 37, p. 314.

129. For example, refer to the work of Lassettre and coworkers[14,15] and Simpson[26,28].

130. For example, refer to the work of Doering[36] and Kuppermann[35].

131. S. M. Silverman and E. N. Lassettre, J. Chem. Phys., 44, 2219 (1966).

132. C. E. Moore, "Atomic Energy Levels," Vol. 1, National Bureau of Standards, Circular No. 467 (U. S. Government Printing Office, 1949), p. 4.

133. J. Todd, Survey of Numerical Analysis (McGraw-Hill Book Company, Inc., New York, 1962), p. 48.

134. This decrease can be understood from the data of reference (43) which show that the total cross section for excitation of the 2^3P state is lower at 26 eV than at 34 eV.

135. G. E. Chamberlain and H. G. M. Heideman, Phys. Rev. Letters, 15 (1965).

136. F. R. Gilmore, J. Quant. Spectr. Rad. Transfer, 5, 369 (1965).

137. W. Benesch, J. T. Vanderslice, S. G. Tilford, and P. G. Wilkinson, Astrophys. J., 143, 236 (1966).

138. Y. Tanaka, M. Ogawa, and A. S. Jursa, J. Chem. Phys., 40, 3690 (1964).

139. Such a comparison can be found in reference (17c).

140. K. Takayanagi and T. Takahashi, Report of Ionosphere and Space Research in Japan, 20, 357 (1966).

141. P. H. Krupenie, "The Band Spectrum of Carbon Monoxide," NBS reference data series, US NBS, 5, 1 (1966).

142. E. N. Lassettre, A. S. Berman, S. M. Silverman, and M. E. Krasnow, J. Chem. Phys., 40, 1232 (1964).

143. E. N. Lassettre and S. M. Silverman, J. Chem. Phys., 40, 1256 (1964).

144. S. M. Silverman and E.N. Lassettre, J. Chem. Phys., 41, 3727 (1964).

145. A. Skerbele, V. D. Meyer, and E. N. Lassettre, J. Chem. Phys., 44, 4069 (1966).

146. R. W. Nicholls, J. Quant. Spectry. and Radiative Transfer, 2, 433 (1962).

147. E. N. Lassettre and S. A. Francis, J. Chem. Phys., 40, 1208 (1964).

148. E. N. Lassettre and E. A. Jones, J. Chem. Phys., 40, 1222 (1964).

149. G. J. Schulz, Phys. Rev., 112, 150 (1958).

150. C. E. Kuyatt, S. R. Mielczarek, and J. A. Simpson, Phys. Rev. Letters, 12, 293 (1964).

151. J. Geiger, Z. Physik, 181, 413 (1964).

152. E. Hutchisson, Phys. Rev., 37, 45 (1931).

153. The discrepancies between relative intensitites observed via electron impact and those observed optically have been used to propose the existence of a forbidden transition in ethylene by Ross and Lassettre(23).

154. G. H. Dieke, J. Mol. Spectry., 2, 494 (1958).

155. Reference (9a). Note that the $A^3\Sigma_u^+$, $a^1\Pi_g$ and $C^3\Pi_u$ state assignments in figure 5 of this reference are incorrect as pointed out by Brongersma and Oosterhoff(11).

156. C. K. Ingold and G. W. King, J. Chem. Soc., 1953, 2702 (1953).

157. This point is discussed by Dowell and Sharp[12].

158. T. Nakayama and K. Watanabe, J. Chem. Phys., 40, 558 (1964). (1050Å to 2000Å.)

159. As in the previous cases, $C^{DD}_{\nu\nu 0}$ changes too slowly with angle to account for this ratio behavior. At E_0 = 25 eV, $C^{DD}_{10}(\theta = 0°) \cong .95$ while $C^{DD}_{10}(\theta = 70°) \cong 1.00$.

160. Reference (2c), p. 516.

161. Reference (2c), p. 26.

162. Reference (2b), p. 337.

163. References (12) through (15) of C_2H_2 preprint, also R. J. Buenker and S. D. Peyerimhoff., J. Chem. Phys., 48, 354 (1968).

164. W. C. Price, Phys. Rev., 47, 44 (1934). (1050 - 1520Å.)

165. P. G. Wilkinson, J. Mol. Spec., 2, 387 (1958). (1280 - 1520Å.)

166. P. G. Wilkinson, Can. J. Phys., 34, 643 (1956).

167. T. H. Dunning and V. McKoy, J. Chem. Phys., 47, 1735 (1967).

168. A. Lubezky and R. Kopelman, J. Chem. Phys., 45, 2526 (1966).

169. A summary of this work has been presented by P. G. Wilkinson and R. S. Mulliken, J. Chem. Phys., 23, 1895 (1955).

170. R. S. Mulliken, J. Chem. Phys., 33, 1596 (1960).

171. First observed in liquid ethylene by Reid[82] and then later by Evans[83] in ethylene-oxygen mixtures.

172. Reference (2c), p. 533 and p. 629.

173. W. C. Price and W. T. Tutte, Proc. Roy. Soc., 174A, 207 (1940).

174. M. Zelikoff and K. Watanabe, J. Opt. Soc. Amer., 43, 756 (1953).

175. Except, of course, for the N → T transition, which is spin-forbidden, and the N → V one which is masked by the much stronger N → R transition.

176. Ross and Lassettre[23] suggest a ^1A_g assignment for this state. However, M. Yaris, A. Moscowitz, and R. S. Berry, "On the Low-Lying Excited States of Mono-Olefins," (to be published) present plausible arguments for the $^1B_{1g}$ designation.

177. A low-lying "singlet → singlet transition" at 6.5 eV was reported by Kuppermann and Raff[35]. Since this feature has not been observed by any other investigator (not even by P. S. Wei [Ph.D. Thesis, California Institute of Technology, 1967] on an improved version of the Kuppermann-Raff apparatus), it is considered a spurious result.

178. This ratio was measured from the lower resolution (FWHM ≈ 0.1 eV) spectrum of reference (26).

179. Ross and Lassettre[23] did note the qualitative agreement, i.e., the intensity at 7.45 eV was greater than at 7.28 eV in the work by Simpson[26]. The discussion of the expected energy dependence given in reference (23) will not be repeated here.

180. Recall that for N_2, the X → $E^3\Sigma_g^+$ and X → $^1\Sigma_g^+$ transitions were observed at relatively high impact energies and $\theta \approx 0°$, leading Lassettre (see section 5.3) to an erroneous

assignment of the E state. A similar situation may exist in this case.

181. M. B. Robin, R. R. Hart, and N. A. Kuebler, J. Chem. Phys., 44, 1803 (1966).

PROPOSITION I

An infrared absorption experiment is proposed to measure directly transitions between the translational energy levels of H_2 molecules dissolved in liquid rare gases. The selection rules for such transitions are derived assuming isotropic harmonic oscillator wave functions and a quadrupole-induced dipole interaction potential.

The induced infrared absorption spectra of H_2 in the liquid and solid state[1], foreign gas mixtures[2], and solutions[3-5] have exhibited broad absorption features ($\nu_{\frac{1}{2}} \sim 100\ cm^{-1}$) on the high and low energy side of the fundamental vibrational absorption line, Q_Q. These absorptions, Q_R and Q_P, had been attributed to summation and difference tones, $\nu_o \pm \nu_\kappa$, where ν_o is the vibration frequency of the hydrogen molecule and $h\nu_\kappa$ is the continuum of kinetic energies of the relative motion of the absorbing molecule and its nearest neighbors[1].

Recently Ewing and Trajmar[4] have assigned the Q_R and Q_P features in the induced infrared absorption spectra of H_2 and D_2 in liquid argon to vibration-translation combination bands involving changes in the quantized translational energy levels of H_2 (or D_2) in solution. If the vibrational and translational quantum numbers are v and n, respectively; Q_P arises from the transition $v' = 1,\ n' = 0 \leftarrow v'' = 0,\ n'' = 1$; Q_Q from $v' = 1,\ n' = 0 \leftarrow v'' = 0,\ n'' = 0$; and Q_R from $v' = 1,\ n' = 1 \leftarrow v'' = 0,\ n'' = 0$ (there is no change in the rotational quantum number). Assuming a cell model of the liquid state and

that the potential interaction of the solute (H_2 or D_2) with its solvent cage is $V = \frac{1}{2}kr^2$ (isotropic harmonic oscillator) where r is the displacement of H_2 from the center of the cage and k is the interaction force constant, they predict

$$[\nu_{Q_R} - \nu_{Q_Q}]_{H_2} = \sqrt{2}\,[\nu_{Q_R} - \nu_{Q_Q}]_{D_2} . \qquad (1)$$

Their experimental results agree with this interpretation.

Rather than attempt to characterize the translational energy levels available to H_2 (or D_2) in solution from the vibrational-rotational spectra, an experiment is proposed to observe directly, in the far-infrared ($\nu \geq 50\ cm^{-1}$), transitions between these translational levels for H_2 molecules in their ground electronic, vibrational, and rotational states. This information would be of use in determining intermolecular potentials and in understanding the quantum effects which influence the thermodynamics of these systems[6,7].

The selection rules for translational transitions are determined by the dipole matrix elements

$$\langle \mu_i \rangle \equiv \langle \psi^*_{N'} | \mu_i | \psi_{N''} \rangle \quad . \qquad (2)$$

μ_i is the component of the induced dipole moment function μ along the i^{th} coordinate axis (x, y, or z) and the ψ_N are assumed to be isotropic harmonic oscillator wave functions[8].

$$\psi_N = \Phi_{n\ell}(r)\, Y_{\ell m}(\theta, \varphi) \tag{3}$$

where

$$\Phi_{n\ell} = N_{n\ell}\, L_p^{\alpha}(\rho^2)\, \rho^{\ell}\, e^{-\rho^2/2} \quad ,$$

$$p = \tfrac{1}{2}(n - \ell) \; , \; \alpha = \ell + \tfrac{1}{2},$$

$$\rho = \left[\frac{4\pi^2 M k}{h^2}\right]^{\frac{1}{4}} r \quad ,$$

$L_p^{\alpha}(\rho^2)$ is the associated Laguerre polynomial, $Y_{\ell m}$ is the spherical harmonic, $N_{n\ell}$ is a normalization constant, and M is the mass of H_2. If we assume that the dipole moment induced in the rare gas system is due to the effect on the rare gas of the permanent quadrupole moment of H_2, then

$$\mu(R) \cong \frac{K}{R^4} \quad .^{(9)} \tag{4}$$

R is the distance separating H_2 and the nearest solvent molecule and K is a constant depending on the solvent but independent of H_2 orientation. To calculate the total induced dipole of this solute-solvent interaction, we must average (4) over the cell (refer to figure 1).

Consider an H_2 molecule displaced a distance r from the center of a spherical cage of radius a. The S nearest neighbor solvent molecules are assumed to be uniformly distributed

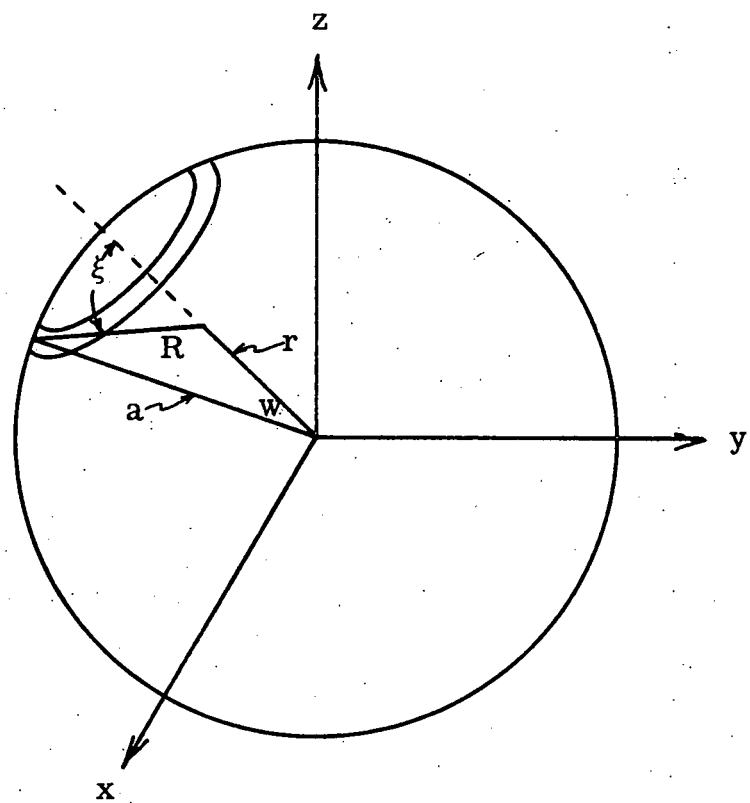

Figure 1. Coordinate system used for the calculation of the selection rules.

over the cavity wall. The dipole induced along R due to the fraction of molecules in the ring of area $2\pi a^2 \sin w\, dw$ is

$$d\mu_R = \frac{SK}{4\pi a^2} \left[\frac{2\pi a^2 \sin w\, dw}{R^4} \right] . \tag{5}$$

The moment induced along r by these molecules is

$$d\mu_r = \cos \xi \, d\mu_R . \tag{6}$$

Then, the total dipole moment induced along r by all of the surrounding molecules is

$$\mu_r = \frac{SK}{2} \int_{w=0}^{\pi} \frac{\cos \xi \sin w}{R^4} \, dw . \tag{7}$$

Changing variables and performing the integration over R yields

$$\mu_r = \frac{2\,SK}{3\,a^5} \left[\frac{r}{(1 - r^2/a^2)^2} \right] . \tag{8}$$

The component of μ_r along a space fixed coordinate axis (μ_i of equation (2)) is

$$\mu_i = \alpha_i(\theta, \varphi)\, \mu_r(r) \tag{9}$$

where α_i is the i^{th} direction cosine of the coordinate system.

The induced dipole matrix elements for transitions from the ground translational state $n'' = m'' = \ell'' = 0$ are

$$\langle \mu_i \rangle = \langle \Phi^*_{n'\ell'} \mu_r \Phi_{oo} \rangle \langle Y_{\ell'm'} \alpha_i(\theta,\varphi) Y_{oo} \rangle \quad . \qquad (10)$$

The "r" integral is in general non-zero, but the "θ,φ" one is zero unless $\ell' = 1$. This can only occur for $n' = 1, 3, 5$, etc.[8]. Translational transitions of $n'' = 0 \rightarrow n' = 2, 4, 6$, etc. are forbidden.

It is suggested that the initial experiments be done with H_2 dissolved in liquid argon to compare with experimental work already done[4]. It would then be of interest to examine heavier (Kr, Xe) and lighter solvents (Ne, He). In the argon systems the experimentally observed ($\nu_{Q_R} - \nu_{Q_Q}$) which have been assigned to the $n'' = 1 \leftarrow n' = 0$ transition are on the order of 100 cm^{-1}. To cover the desired spectral region (50 cm^{-1} to 1000 cm^{-1}) there are commercial instruments available[10]. A block diagram of a possible arrangement is shown in Figure 2. The entire optical path, except for the sample itself, should be kept under high vacuum to eliminate water vapor, which absorbs strongly in the far-infrared. Diamond is a good transparent window material in this region and, if 1 to 2 mm thick, has the required mechanical strength to hold a vacuum. All windows, mirrors, and gratings should be coated with a material such as turpentine soot to decrease the transmission of visible and near-infrared light. A convenient cell length for the study of vibrational-rotational transitions in dilute solutions of liquid H_2 was 0.5 meters[4]. Since the magnitude of the induced dipole allowing the pure translational transitions is not known, it is difficult to

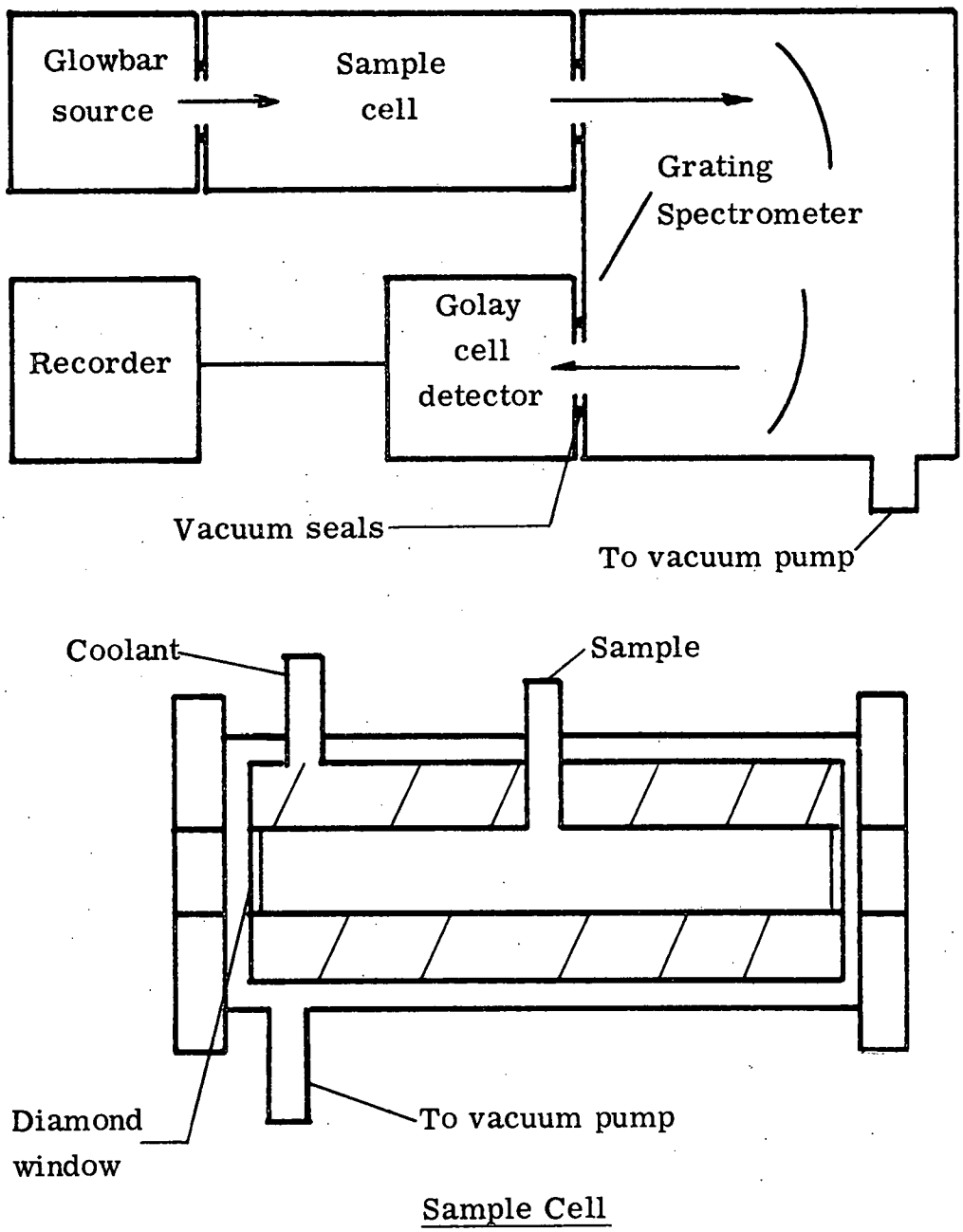

Figure 2. Experimental arrangement.

estimate the required cell length. Assuming an intensity 1/10 of that in the vibration-translation combination bands, a cell of approximately 5 meters is required. The cell dimensions could be reduced with no decrease in optical path length by using gold mirrors at each end of the cell for multiple reflections.

Since this proposition was first advanced, H_2 vibration-translation combination bands have been observed in liquid neon[11] and rotation-translation combination bands have been seen in liquid argon[12]. Because of the complications introduced by the attendent vibrational or rotational transitions, these further studies[11, 12] point out the desirability of direct observation of the translational transitions.

REFERENCES

1. H. P. Gush, W. F. J. Hare, E. T. Allin, and H. L. Welsh, Can. J. Phys., 38, 176 (1960).
2. D. A. Chisholm and H. L. Welsh, Can. J. Phys., 32, 291 (1954).
3. M. O. Bulanin and N. D. Orlova, Opt. Specty., 11, 298 (1961).
4. G. E. Ewing and S. Trajmar, J. Chem. Phys., 41, 814 (1964).
5. H. Vu, M. R. Atwood, and E. Staude, Compt. Rend., 257, 1771 (1963).
6. H. Volk and G. Halsey, J. Chem. Phys., 33, 1132 (1960).
7. M. Simon, Physica, 29, 1079 (1963).
8. J. Powell and B. Crasemann, Quantum Mechanics (Addison-Wesley Publishing Co., Inc., Reading, Mass., 1961).
9. J. Van Kranendonk, Physica, 17, 968 (1951).
10. R. A. Smith, F. E. Jones, and R. P. Chasman, The Detection and Measurement of Infrared Radiation (Oxford University Press, London, 1957).
11. G. E. Ewing and S. Trajmar, J. Chem. Phys., 42, 4038 (1965).
12. G. W. Holleman and G. E. Ewing, J. Chem. Phys., 47, 571 (1967).

PROPOSITION II

It is proposed that the techniques of low-energy, variable angle, high-resolution electron impact spectrometry be applied to the investigation of the polarization of light emitted from helium atoms excited via electron-impact at incident energies near threshold. One possible experimental arrangement is suggested and the expected signal level is calculated.

In 1926 Skinner[1] observed that various lines emitted when an electron beam struck a low-pressure mercury sample were polarized parallel or perpendicular with respect to the beam. Subsequently, Skinner and Appleyard[2] investigated the variation of this polarization with electron velocity in mercury. In this study and later ones on helium[3,4] the observed percent polarization at 90° (P) with respect to the electron beam had a value close to zero at or just above the threshold energy for the excitation and rose to a maximum value at higher energy[5].

$$P = 100\,(I^{\parallel} - I^{\perp})/(I^{\parallel} + I^{\perp}) \qquad (1)$$

$I^{\parallel}$ and $I^{\perp}$ are the emitted light intensities at 90° polarized parallel and perpendicular to the beam axis, respectively. In the case of D states of helium, the rise to maximum takes place within the energy spread of the electron beams used, about 1 eV. Theoretical investigations, however, predicted that polarizations in many cases should be as high as 100% at threshold[6]. Recently, McFarland[7] has attributed the failure of experimental verification of theory to

radially directed electrons elastically scattered from the electron beam. In his refined experiments, the electron energy resolution was about 0.1 eV and the threshold polarization measurements approached the theoretically expected magnitudes.

It is proposed that the techniques of low-energy, variable angle, high-resolution electron impact spectrometry be applied to the measurements of polarization effects near threshold in helium. High resolution ($\Delta E = \pm$ 0.03 eV) is quite important near threshold as evidenced by the calculated variation in polarization with energy of Lyman-alpha due to collisional 1s → 2p transitions in H[5]. As the energy of the electron beam approaches threshold from above, the polarization P dips sharply at about 0.1 eV above threshold and then rises to about 45% at threshold. In other cases, the percent polarization is theoretically predicted to be a maximum at threshold and a sharply decreasing function of beam energy a little above threshold (for example He $3^1D \rightarrow {}^1P$)[6]. These low energy dips were not observed in the earlier work of McFarland and Soltysik[4] due to poor electron energy resolution.

To help determine if high-resolution variable angle investigations are feasible, the expected signal intensities will be computed. Assume a simple three energy level system; an initial level "a" (usually the ground state), an upper level "b" populated by electron collision, and a final level "c" reached after photon emission. If Q_{ab} is the total cross-section for electron-impact excitation of level b; N_e and N_a are the number densities of the electron beam and

the particles in state a, respectively; and v_e is the velocity of the electron beam, the transition rate from a to b equals $v_e N_e N_a Q_{ab}$. Assuming that the only method of deexcitation of state b is through spontaneous photon emission (note that this assumption ignores stimulated emission, cascade effects, and collisional energy transfer in the gas) and equating the rate of excitation to the rate of emission imply that the total number of photons emitted per cc per sec (I_T) equals $v_e N_e N_a Q_{ab}$. If i and A are the electron beam current (electrons/sec) and cross-sectional area, respectively, the number of photons originating in a volume V emitted into a given solid angle $S(\theta, \varphi)$ per second is

$$I_p(\theta, \varphi) = \frac{i N_a V Q_{ab}}{A} S \frac{3(100 - P\cos^2 \theta)}{4\pi (300 - P)} , \qquad (2)$$

and

$$I_T = \int I_p(\theta, \varphi)\, d\Omega .$$

With the following estimates of the various parameters in a typical experiment:

$N_a = 3.2 \times 10^{13}$ particles/cc (10^{-3} torr at 300°K)

$Q_{ab} = 10^{-16}$ cm^2

$V/A = 10^{-2}$ cm

$P = 20$ percent

$S = 10^{-2}$ steradians

$\theta = 90°$

$$i = 6 \times 10^{10} \text{ electrons/sec}$$

equation (2) implies that $I_p(\theta) = 1.6 \times 10^3$ photons/sec. If the photons pass through a filter of 50% transmission and are detected by a photomultiplier of 20% efficiency there would be about 160 counts/sec. This is a practical level for standard counting techniques.

A schematic representation of a possible experimental arrangement is shown in figure 1. Although Smit[8] has verified the angular distribution law (equation 2) in helium, Fite and Brackman[9] have noted some discrepancies in atomic hydrogen. Thus, it is imperative to check this angular distribution at higher resolution. This would require the direct measurement of P at a given energy and the measurement of the variation in $I_p(\theta)$ with angle at this same energy. A polaroid filter could be used to determine $I^{\parallel}$ and $I^{\perp}$. Then subsequent measurements of P (at different impact energies) could be made by determining $I_p(\theta)$ at two different angles and applying the known distribution law.

There are a number of refinements in the method, such as cooling the photomultiplier, phase sensitive detection, and circular grids to reduce the effects of radially scattered electrons which may be required.

Since this proposition was first suggested, McFarland[10] has reinvestigated the polarization of the helium 4922 Å radiation as a function of incident energy. He used a cross-beam configuration which eliminated many of the previous experimental uncertainties.

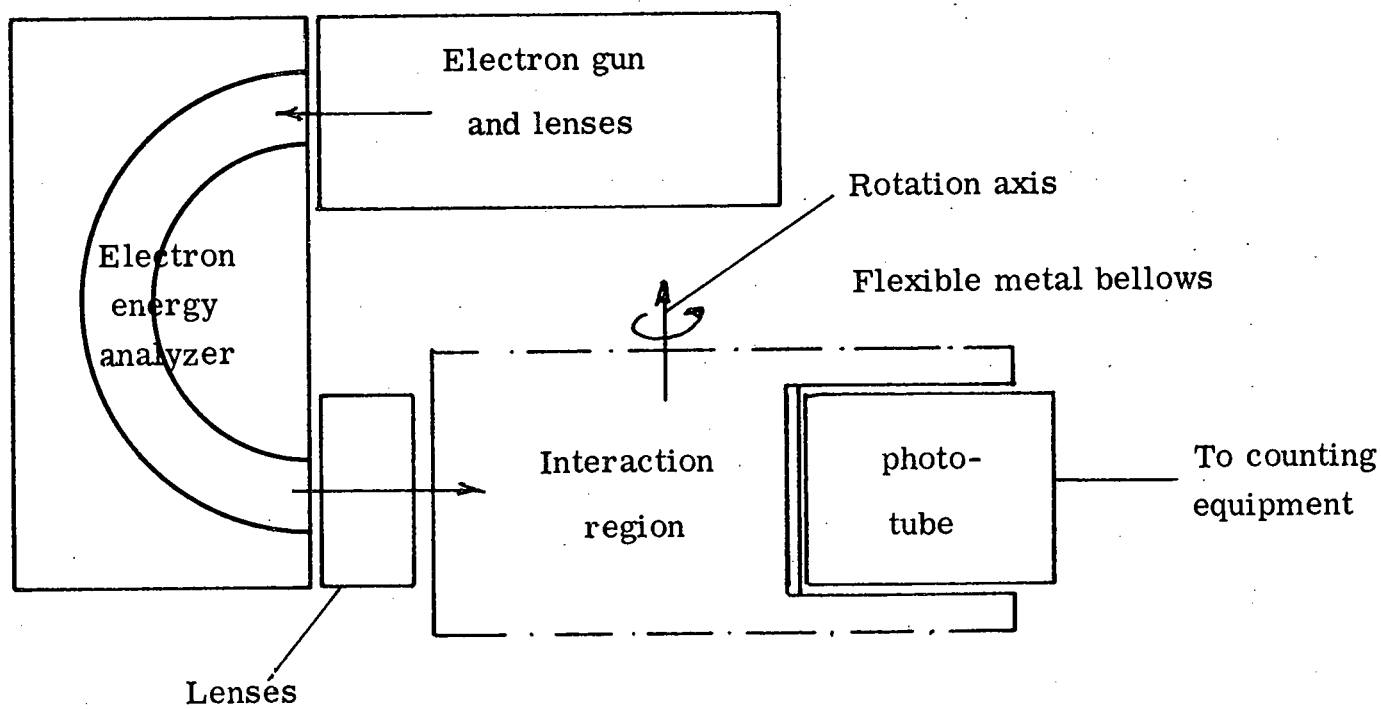

Figure 1. Experimental arrangement.

Although his experimentally determined threshold polarization agreed well with the theoretical value, a near threshold minimum was observed--a feature that has not been predicted by theory. However, these experiments[10] were performed at a fixed angle (90°) under low resolution ($\Delta E \approx 0.2$ eV). More detailed studies, as a function of angle and with better resolution, would still be of interest.

REFERENCES

1. H. W. B. Skinner, Proc. Roy. Soc. London, A112, 642 (1926).
2. H. W. B. Skinner and E. T. S. Appleyard, ibid, A117, 224 (1927).
3. R. H. McFarland and E. A. Soetysik, Phys. Rev., 128, 1758 (1962).
4. R. H. McFarland and E. A. Soltysik, Phys. Rev., 127, 2090 (1961).
5. D. W. O. Heddle and M. J. Seaton, Atomic Collision Processes, Proc. of the Third Int. Conf on the Phys. of Elec. and Atomic Collisions, 137 (1964).
6. I. C. Percival and M. J. Seaton, Phil. Trans., 251, 113 (1958).
7. R. H. McFarland, Phys. Rev., 133, 986 (1963).
8. J. A. Smit, Physica, 2, 104 (1935).
9. W. L. Fite and R. T. Brackman, Phys. Rev., 112, 1157 (1958).
10. R. H. McFarland, Phys. Rev., 156, 55 (1967).

PROPOSITION III

An experiment is proposed to measure the vibration-rotation infrared absorption of the 2326 cm^{-1} asymmetric stretching fundamental in H_3^+ produced in a microwave discharge of H_2. The conditions for which the concentration of H_3^+ is a maximum are discussed and an estimate of the pertinent experimental parameters is given.

In a recent article Huff and Ellison[1] have calculated the fundamental vibration frequencies and absorption intensities of H_3^+ using a theoretically obtained potential energy surface and associated electronic state wavefunctions. Although the existence of H_3^+ was established by Bleakney[2] in 1930, there is very little experimental data available[3-5]. Thus, an experiment is proposed to measure the vibration-rotation infrared absorption of the 2326 cm^{-1} asymmetric stretching fundamental in H_3^+ produced in a microwave discharge of H_2 to provide some experimental results to compare with recent theory[1,6].

Following the notation of Huff and Ellison, the integrated molar absorption coefficient, A″, can be expressed as;

$$A'' = (1/\ell C) \int \ell n[I_o/I(\nu)]\, d\nu \qquad (1)$$

where ℓ is the cell path length in centimeters; C is the number of moles per liter of H_3^+; I_o and $I(\nu)$ are the incident and transmitted intensities, respectively; ν is the frequency in wavenumbers; and A″ is calculated[1] to be 7069 darks. The integration is over all frequencies of the vibration-rotation band.

From these calculations we can estimate the feasibility of an absorption experiment. To get an approximate idea of the H_3^+ ion density needed (N), assume $I(\nu)$ has an average value of I_{av} and a band width of 50 cm^{-1} and that $I_{av}/I_o = .95$ results in a detectable absorption. Performing the integral in equation (1), one finds that;

$$\ell N = 2.1 \times 10^{17} \text{ ions/cm}^2 \qquad (2)$$

A microwave discharge in H_2 at pressures greater than a few mm Hg initially produces H^+ and H_2^+. After a millisecond the predominating ionic species are H_2^+ and H_3^+ with most of the H^+ gone (p. 577)[7]. Typical ion densities in moderate power microwave discharges range from 10^9 to 10^{12} ions/cc (p. 560)[7]. The average power (P_{av}) that must be supplied by the oscillating electric field per unit volume to sustain a given total ion density (N_i) is given as[8];

$$P_{av} = \frac{\frac{1}{2} c N_i (X_o e)^2}{m (c^2 + w^2)} \qquad (3)$$

where e and m are the electronic charge and mass, respectively; c is the collision frequency; X_o and w are the amplitude and frequency, respectively, of the applied field. This formula applies in cases for which c is greater or equal to w; i. e., for frequent electron collisions with the gas molecules for each oscillation of the electric field. This condition will prevail in the proposed experiment since pressures on the order of 100 mm Hg and microwave frequencies

of about 1000 Mc/sec are suggested. Goodyear and von Engel[9] report $c = 2.3 \times 10^{8}$ sec^{-1} at 30 microns pressure and 400°K in H_2. At 100 mm Hg and 400°K, c would be approximately 7×10^{11} sec^{-1}. With $w/2\pi$ equal to 1000 Mc/sec (10^{9} sec^{-1}), c is greater than w and the formula (3) applies. Using Goodyear and von Engel's value of $X_o = 1.8$ volts/cm as representative of microwave sources, and substituting the values of the various parameters into equation (3) implies that the power necessary to sustain a discharge of 10^{14} ions/cc is approximately 0.075 watts/cc. If much higher electron (ion) densities are attempted by increased power input, the probable result is more H^+ formation as observed in high electron density spark discharges (10^{17} electrons/cc) rather than an increased H_3^+ density (pp. 501-502)[7]. Varney[10] indicates that at pressures above 1 mm Hg the preponderant ionic species measured by mass spectrographic tests is H_3^+. Assuming N of relation (2) is on the order of 10^{14} ions/cc, the required path length ℓ is 21 meters.

At this stage we can make an estimate of the apparatus required. The reflectivity of silver for radiation of 2300 cm^{-1} can be 98%[11]. If 55 reflections are made there will be about 33% of the incident IR source radiation transmitted, which should be sufficient. The physical cell length needed is then about .4 meters. If the cell cross-section is circular with a radius of 1.8 cm (cross-sectional area of 10^{2} cm^{2}) the volume would be 4,000 cc and the required power would be 300 watts. Suitable microwave sources are commercially available to supply this power but a cavity to contain the sample cell would have to be designed.

Figure 1 is a schematic representation of a possible experimental arrangement. At the wattages anticipated, the sample tube and gas will heat up and radiate in the IR. To discriminate between this IR signal and the source signal, a phase sensitive detection system should be used. The output of the Nernst glower could be chopped by a rotating sectored disc before entering the sample cell. The frequency of rotation can be monitored by a photo-cell and only the component of the detector signal in phase with the photo-cell output would be recorded. There are many commercial IR spectrometers and phase sensitive detection circuits available for this application.

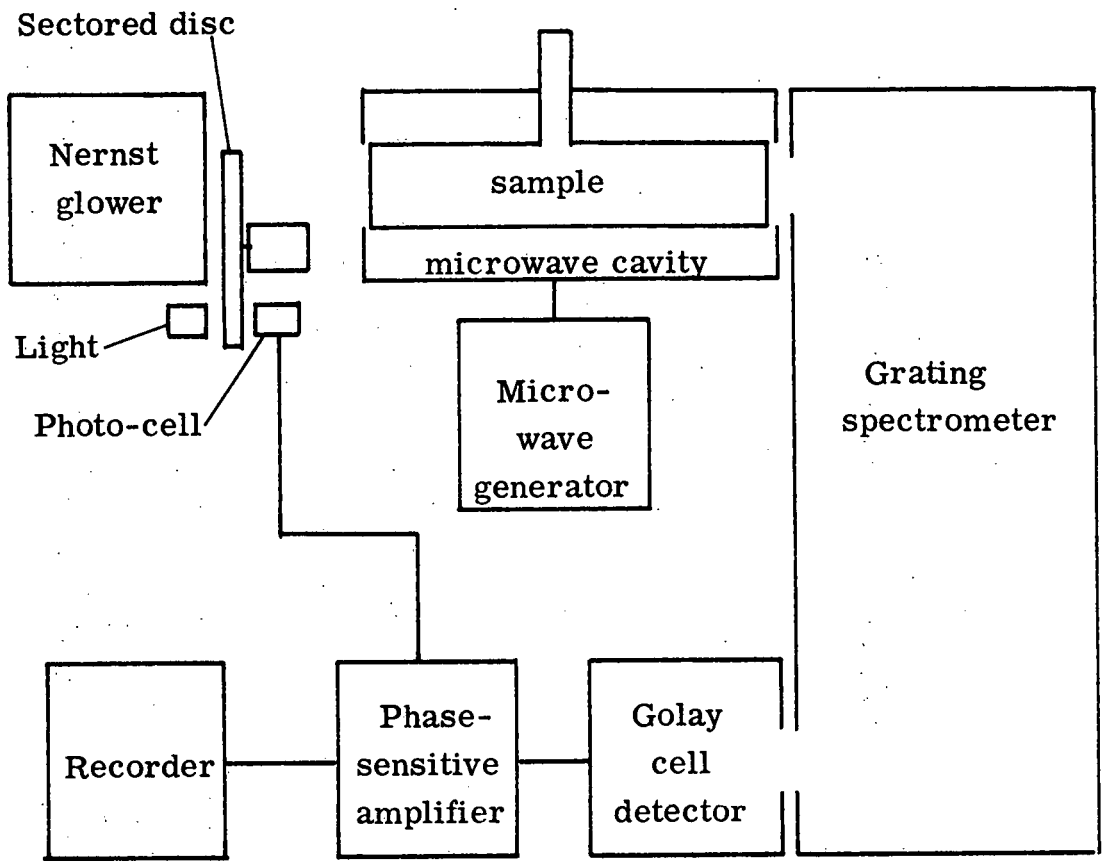

Figure 1. Experimental arrangement

REFERENCES

1. N. T. Huff and F. O. Ellison, J. Chem. Phys., 42, 364 (1965).
2. W. Bleakney, Phys. Rev., 35, 1180 (1930).
3. D. P. Stevenson, J. Chem. Phys., 29, 282 (1958).
4. R. N. Varney, Phys. Rev. Letters, 5, 559 (1960).
5. J. A. R. Samson and G. L. Weissler, U. S. Dept. Com. Office Tech. Serve. PB Report 45, (1961).
6. R. E. Christoffersen, J. Chem. Phys., 41, 960 (1964).
7. L. B. Loeb, Basic Processes of Gaseous Electronics (University of California Press, Berkeley, Calif., 1955).
8. G. Francis, Ionization Phenomena in Gases (Butterworths, London, 1960) p. 87.
9. C. C. Goodyear and A. von Engel, Proc. of Fifth Int. Conf. on Ionization Phenom. in Gases, I, 203 (1961).
10. R. N. Varney, ibid., p. 43.
11. R. A. Smith, F. E. Jones, and R. P. Chasmar, The Detection and Measurement of the Infrared Radiation (Oxford University Press, London, 1957).

PROPOSITION IV

It is proposed that an ion cyclotron resonance mass spectrometer be utilized to investigate the photoionization of gaseous alkali metals (particularly cesium) by light at wavelengths longer than those corresponding to the ionization potential with and without added gases (particularly NH_3).

It has been known for a long time that gaseous cesium can be photoionized by photons which have an energy less than that corresponding to the atomic ionization potential[1,2]. This early work indicated that the ionization mechanism is as follows:

$$Cs\,(6S) + h\nu \rightarrow Cs^*(nP) \qquad (1)$$

$$Cs^* + Cs \rightarrow [Cs\,Cs]^* \rightarrow Cs_2^+ + e^- . \qquad (2)$$

Lee and Mahan[3] have shown that an additional ionization process probably should be considered when $n \geq 12$,

$$Cs^*(nP) + Cs \rightarrow Cs^+ + Cs^- . \qquad (3)$$

Recently, it has been observed[4] that the addition of ammonia vapor alters the photoionization spectrum of cesium by decreasing the ion current for wavelengths longer than 3400 Å and increasing it for shorter ones. This has led Williams and Naiditch[4] to propose an ionization mechanism analogous to that of (2), i.e.,

$$Cs^*(nP) + NH_3 \rightarrow [Cs\,NH_3]^* \rightarrow Cs\,NH_3^+ + e^- . \qquad (4)$$

It should be pointed out that in none of these experiments have any of the ions produced been positively identified. In most cases[1,2,4] the total ion current was measured, while in one case[3] ions of different mobilities (presumably Cs_2^+ and Cs^+) were detected. Thus, it is proposed that the photoionization of gaseous cesium (and other alkali metals) with and without added gases be studied using an ion cyclotron resonance mass spectrometer[5] to detect and identify the ionic species. This method of detection enables one to unambiguously identify all of the ions formed and to monitor their currents independently. Such studies can be used to confirm or deny the ionization mechanisms already suggested.

In order to calculate the rate of formation of a particular ion, a few additional processes must be considered.

$$Cs^* \rightarrow Cs + h\nu \tag{5}$$

$$Cs^* + NH_3 \rightarrow Cs + NH_3^* \tag{6}$$

where (5) and (6) represent spontaneous emission and electronic energy transfer, respectively. The rate of Cs^* formation (due to reaction (1)) is proportional to the incident photon flux ρ times the Cs concentration ([Cs]). The net rate of Cs^* formation (considering only reactions (1) through (6)) is

$$\frac{d[Cs^*]}{dt} = \rho B[Cs] - A[Cs^*] - (k_2 + k_3)[Cs^*][Cs]$$

$$- (k_4 + k_6)[Cs^*][NH_3]$$

where A and B are the Einstein transition probabilities[6] of spontaneous emission and absorption, respectively, and k_2 through k_6 are the rate constants associated with reactions (2) through (6). Under steady state conditions, the net formation rate of Cs^* is zero which implies a concentration of

$$[Cs^*] = \frac{\rho B[Cs]}{A + (k_2 + k_3)[Cs] + (k_4 + k_6)[NH_3]} .$$

Thus, the Cs_2^+, Cs^+ (Cs^-), and $CsNH_3^+$ ion currents will be given by

$$I(Cs_2^+) = k_2[Cs^*][Cs]$$

$$= \frac{\rho B k_2 [Cs]^2}{A + (k_2 + k_3)[Cs] + (k_4 + k_6)[NH_3]}$$

$$I(Cs^+) = \frac{k_3}{k_2} I(Cs_2^+) \quad , \text{ and}$$

$$I(CsNH_3^+) = \frac{k_4}{k_2} [NH_3][Cs]^{-1} I(Cs_2^+) \quad .$$

k_3/k_2 and k_4/k_2 can then be determined from measurements of these ion currents. Further, if the Cs_2^+ ion current when $[NH_3] = 0$ is denoted $I_o(Cs_2^+)$, then

$$\frac{I_o(Cs_2^+)}{I(Cs_2^+)} = 1 + \frac{(k_4 + k_6)[NH_3]}{A + (k_2 + k_3)[Cs]}$$

$$= 1 + \frac{(k_4/k_2 + k_6/k_2)[NH_3]}{A/k_2 + (1 + k_3/k_2)[Cs]} \quad .$$

The measurement of I_0/I as a function of $[Cs]$ and $[NH_3]$ can then be used to determine A/k_2 and k_6/k_2. (Note that in reality A includes the deexcitation of Cs^* by wall collisions as well as spontaneous emission.) The k's are expected to be slowly varying functions of temperature but to depend strongly on the particular Cs^* excited state. In particular, the investigations already mentioned indicate that k_4 has an apparent energy threshold at 3400Å while k_2 has one at 3888Å.

The apparatus required to perform these experiments is for the most part commercially available. The usual ion cyclotron resonance spectrometer cell[5] must be modified to allow its operation at elevated temperatures ($\sim 200°C$). Also, the electron beam ionizer should be replaced by a suitable light source (a high-pressure mercury lamp, for example) and a monochromator.

REFERENCES

1. F. L. Mohler and C. Boeckner, J. Res. Natl. Bur. Std., 5, 51 (1930).
2. F. L. Mohler and C. Boeckner, J. Res. Natl. Bur. Std., 5, 399 (1930).
3. Y. Lee and B. H. Mahan, J. Chem. Phys., 42, 2893 (1965).
4. R. A. Williams and S. Naiditch, J. Chem. Phys., 47, 343 (1967).
5. J. D. Baldeschwieler, Science,159, 263 (1968).
6. G. Herzberg, Spectra of Diatomic Molecules (Second Edition, D. Van Nostrand, Inc., 1950), p. 20.

PROPOSITION V

An experiment is proposed to measure the energy distribution of electrons thermionically emitted from single crystals of tungsten in order to rationalize theory and experiment. A number of suggestions to correct inadequacies of prior investigations are given.

The increasing interest in electron scattering phenomena has led to a reexamination of the energy profiles of electron beams from thermionic sources. From the assumptions of the free electron theory of metals[1], the current distribution is expected to be[2a]

$$I(E)\,dE = \frac{4\pi me}{h^3} e^{-W_f/kT} E\, e^{-E/kT}\, dE \quad . \qquad (1)$$

IdE is the current carried by electrons in the energy range $E \rightarrow E + dE$, h is Planck's constant, e and m are the electron charge and mass, respectively, W_f is the work function of the metal, k is Boltzmann's constant, T is the cathode temperature, and E is the electron energy. The integral of (1) over all energies E gives the Richardson-Dushman equation for the total temperature limited current

$$I_T = \frac{4\pi me}{h^3} (kT)^2 e^{-W_f/kT} \quad . \qquad (2)$$

Equation (2) has been found to be a valid description of thermionic emission when written in the form

$$I_T = KT^2 e^{-W_f/kT} \qquad (3)$$

where K is an experimentally determined parameter for a given metal[1b].

However, experimental attempts to verify even the shape of the distribution given by equation (1) have not been successful. Hutson[3] observed an apparent "reflection coefficient" at the surface of single crystals of tungsten which resulted in a measured deficiency of low energy electrons. On the other hand, Simpson and Kuyatt[4] have noted an anomalous broadening of the distribution (1) as a function of beam current which appears to increase the relative number of low energy electrons. Although the experimental arrangements of these two investigations are basically similar (i.e., a thermionic cathode followed by an energy analyzer), there are a number of differences in the cathode preparation and operation and method of energy analysis which may significantly affect the results. It is therefore proposed that systematic experimental measurements of the electron energy distribution from a thermionic source be made in an attempt to clear up this somewhat muddled situation.

There are a number of restrictions on the experimental arrangement which are necessary in order to eliminate as many of the complicating factors as possible from the previous investigations[3,4]. These requirements and the methods proposed for obtaining them are outlined below. Figure 1 shows the proposed experimental set up.

Planar, indrectly heated, single crystals of tungsten will be used as the thermionic emitter. Robinson[5] has described a simple

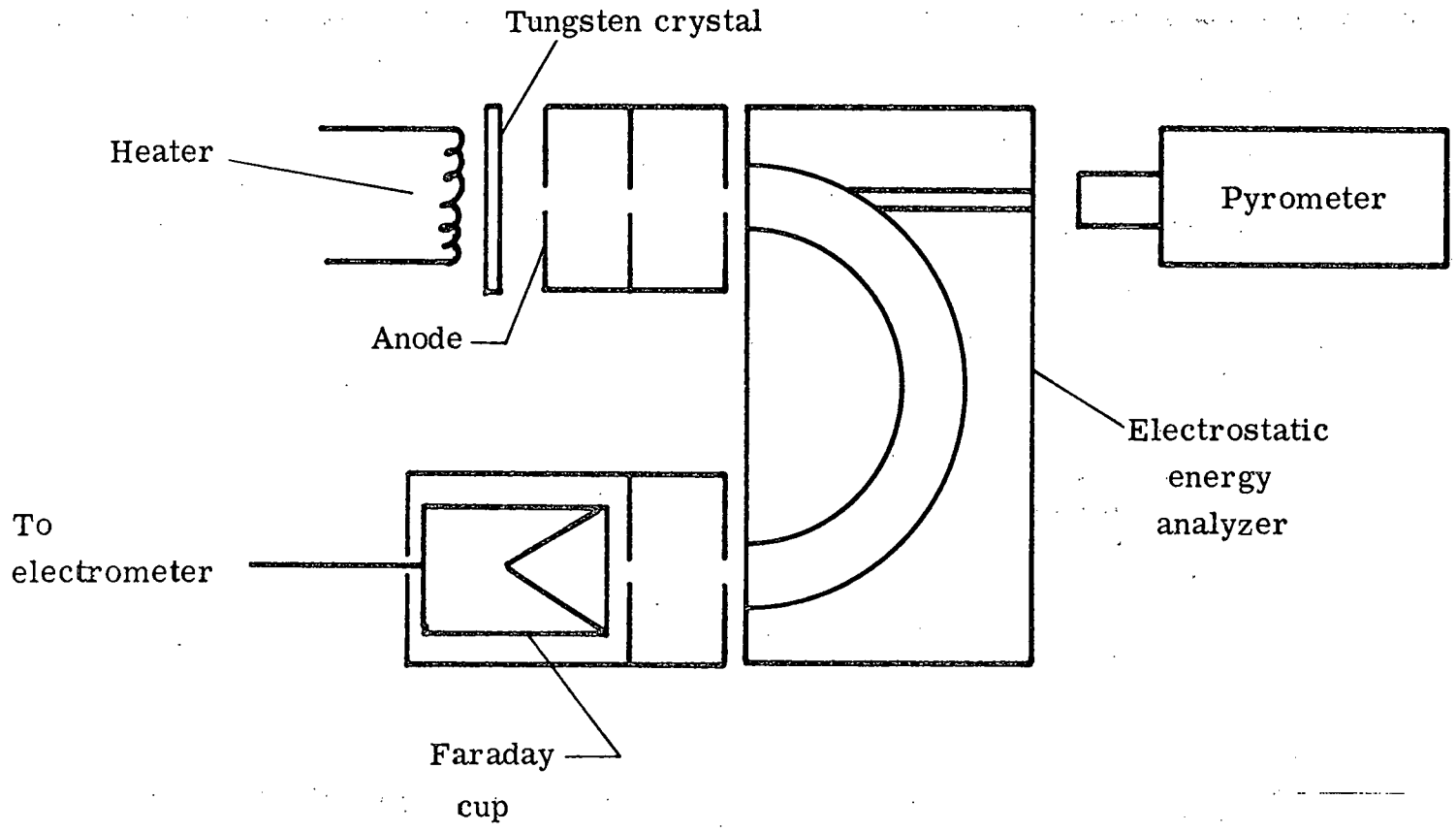

Figure 1. Experimental arrangement

procedure for obtaining such crystals and the particular exposed crystal face can be determined by X-ray scattering[6]. The use of indirect heating will eliminate the possibility of IR drops in the source. Also, it is imperative that a means of measuring the crystal temperature be provided. Commercial optical pyrometers are available with an accuracy of $\frac{1}{2}\%$ (10°K @ 2000°K).

The electron gun itself will consist of the tungsten source (cathode) and an aperture (anode). The potential between the cathode and anode provides the necessary draw-out voltage to direct the electron beam into an energy analyzer. The gun can be operated under space-charge or temperature limited conditions depending on the value of this potential.

The electron gun is followed by two apertures, equi-potential with the anode, and a hemispherical electrostatic energy analyzer[2b]. The apertures are needed to collimate the beam before its entrance into the analyzer. The region between the anode and analyzer is kept free of electric fields to eliminate the possibility that lens effects may distort the electron energy distribution. Likewise, magnetic shielding can be provided by Helmholtz coils[2c].

The analyzer is followed by two apertures (equi-potential with the anode) and a Faraday cup current collector. The energy profile of the beam can be obtained by recording the current reaching the Faraday cup versus the voltage across the hemispheres with all other voltages constant. This method of sweep has the disadvantage that the resolution is a function of the electron energy. This is not

a serious handicap since that function is known[2d].

Finally, the electron source and analyzer are enclosed in a high vacuum chamber (residual pressure less than 10^{-7} torr) to eliminate any interference from ionization or gas scattering phenomena.

Let the experimentally determined energy profile be $I_{exp}(E)$ and the "real" one be $I_{real}(E)$. Then

$$I_{exp}(E + U) \cong C I_{real}(E)$$

(provided the resolution of the analyzer is adequate) where C is an energy independent constant and U is a contact potential correction (generally unknown) that represents a shift in the energy origin but not a change in shape. Since T is known, I_{exp} can be compared with the theoretical prediction for I_{real} (i.e., equation (1)) simply by normalizing them to the same peak position (and height). These experimental energy distributions should be obtained for $E = 0$ to $E \gg kT$ as a function of the cathode temperature, total beam current, space charge conditions in the gun, and draw-out voltage.

There is an additional experimental complication that has been ignored in all previous investigations--the production of low energy secondary electrons by electron collisions with the apertures. Since the importance of this effect is not known, it is suggested that several sets of apertures, with different secondary electron yield characteristics[7], be used in the apparatus. In this way, distortions in the measured electron energy distribution due to

aperture scattering might be identified.

REFERENCES

1. R. B. Leighton, Principles of Modern Physics (McGraw-Hill Book Company, Inc., New York, 1959), (a) pp. 352-357, (b) p. 357.
2. J. K. Rice, Ph.D. Thesis, California Institute of Technology, 1969; (a) section 4.4.3.1, (b) sections 4.1.1 and 4.2.4.3, (c) section 4.1.3.2, (d) section 4.1.1.2, equations (4-19) and (4-29).
3. A. R. Hutson, Phys. Rev., 98, 889 (1955).
4. J. A. Simpson and C. E. Kuyatt, J. Appl. Phys., 37, 3805 (1966).
5. C. S. Robinson, Jr., J. Appl. Phys., 13, 647 (1942).
6. M. J. Buerger, Crystal Structure Analysis (John Wiley and Sons, Inc., New York, 1960).
7. E. W. McDaniel, Collision Phenomena in Ionized Gases (John Wiley and Sons, Inc., New York, 1964), pp. 658-670.